In-situ turbulence observations in the stratospheric wind and temperature field

Dissertation
in Atmosphärenphysik

Andreas Schneider

Universität Rostock Traditio et Innovatio

LEIBNIZ-INSTITUT FÜR ATMOSPHÄREN PHYSIK IAP

In-situ turbulence observations in the stratospheric wind and temperature field

Dissertation

zur

Erlangung des akademischen Grades

doctor rerum naturalium (Dr. rer. nat.)

der Mathematisch-Naturwissenschaftlichen Fakultät

der Universität Rostock

vorgelegt von

Andreas Schneider,

geb. am 26. 07. 1979 in Marburg,

wohnhaft in Kühlungsborn

Dieser Forschungsbericht wurde als Dissertation von der
Mathematisch-Naturwissenschaftlichen Fakultät der Universität Rostock angenommen.

Gutachter:	Prof. Dr. Franz-Josef Lübken (Leibniz-Institut für Atmosphärenphysik) Prof. Dr. Marvin A. Geller (Stony Brook University, New York, USA)
eingereicht am:	28. 08. 2015
verteidigt am:	11. 12. 2015

urn:nbn:de:gbv:28-diss2016-0023-4

Abstract

Knowledge of stratospheric turbulence is still limited, but important for the atmospheric energy balance and the mixing of trace species. A new balloon-borne instrument which measures turbulent fluctuations in wind and temperature with unprecedented vertical resolution has recently been developed at the Leibniz-Institute of Atmospheric Physics.

In this thesis, the instrument and therewith the data quality have been improved significantly. New flights have been performed. Features of observed dissipation rates are explained by atmospheric background conditions. Dissipation rates are compared to Thorpe analyses of radiosondes. The assumption needed for such an evaluation is checked and found not to be fulfilled. Kinetic dissipation rates computed from simultaneous wind and temperature measurements are inconsistent and reveal potential problems with the turbulence theory used for the evaluation.

Zusammenfassung

Stratosphärische Turbulenz ist bislang wenig verstanden, aber wichtig für die atmosphärische Energiebilanz und den Transport von Spurenstoffen. Am Leibniz-Institut für Atmosphärenphysik ist unlängst ein neues ballongetragenes Instrument entwickelt worden, das turbulente Fluktuationen in Wind und Temperatur mit bis dahin unerreichter vertikaler Auflösung misst.

Im Rahmen dieser Arbeit sind das Instrument und dadurch die Datenqualität signifikant verbessert worden. Neue Flüge sind durchgeführt worden. Charakteristiken gemessener Dissipationsraten werden durch atmosphärische Hintergrundbedingungen erklärt. Dissipationsraten werden mit einer Thorpe-Analyse von Radiosonden verglichen. Die Voraussetzung für die Anwendbarkeit einer solchen Auswertung wird überprüft und falsifiziert. Aus gleichzeitigen Messungen von Wind- und Temperaturfluktuationen ermittelte kinetische Dissipationsraten sind inkonsistent und weisen auf mögliche Probleme der für die Auswertung verwendeten Turbulenztheorie hin.

Contents

1 Introduction

The Earth's atmosphere is a very complex system which is highly non-linear and coupled. Time and time again new unexpected features are discovered. Complicated cross-relations can result in unintuitive phenomena. For instance, the lowest temperatures on Earth are found in the polar *summer* near 85 km altitude, although the Sun is shining 24 hours per day. Obviously, this cannot be caused by solar irradiation. Rather it is connected to large-scale dynamics driven by waves known as the Brewer-Dobson circulation, which results in an upwelling at the summer pole and thus adiabatic cooling. In the Antarctic, this temperature minimum is even lower (down to 100 K) and also at higher altitudes than expected, as recently observed by Lübken et al. [2014]. To date, no model can reproduce this behaviour without changing the gravity wave spectrum which has side effects in the stratosphere.

The basic system is understood. Usually the atmosphere is vertically structured according to the temperature gradient. Figure 1.1 shows a typical temperature profile for mid-latitude conditions. The lowermost layer is mostly heated from the Earth's surface, thus temperatures decrease with height. It is called *troposphere* from the Greek word for "change", because turbulent mixing plays an important role. Here the weather pattern takes place. It ends at roughly 8 km in the Arctic and 18 km near the equator at a level which is called *tropopause*. Thereafter, the temperature gradient is near zero or even positive, primarily due to the absorption of ultraviolet solar radiation by ozone. Due to the stable stratification this layer is called *stratosphere*. Above the *stratopause* at ~50 km height temperature decreases again due to the lack of heating. This layer is called *mesosphere*, from the Greek meso, "in between". A temperature minimum, which is called *mesopause*, is reached between roughly 80 km and 100 km depending on season. It entails the lowest temperatures on

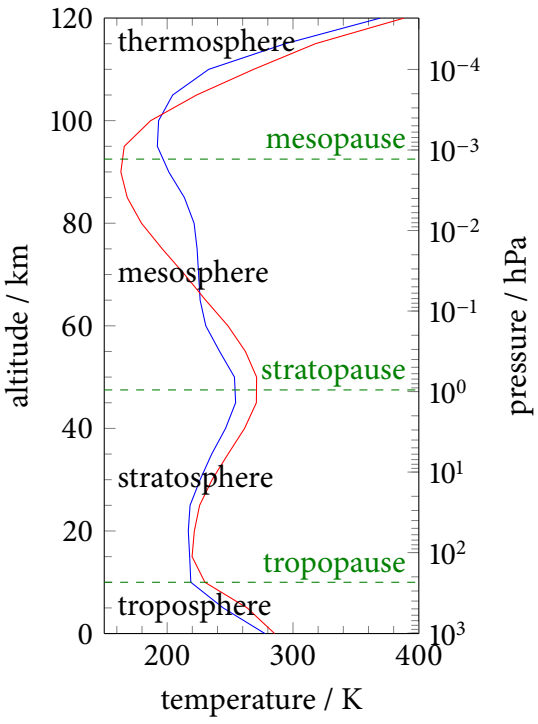

Figure 1.1: Mean temperature structure of the atmosphere for summer (red) and winter (blue) conditions at 50°N. Data from Fleming et al. [1988].

Earth. Further upwards the *thermosphere* begins with a steep increase in temperature due to the absorption of high-energy ultraviolet radiation by photodissociation of molecules and stripping of electrons from atoms.

The primary effect that leads to the thermal structure is the absorption of solar irradiation. The structure is modified by dynamical effects. The most important one is the Brewer-Dobson circulation mentioned above. Basically it consists of an upwelling at the tropics, two branches of meridional poleward flux in the lower and upper stratosphere, upwelling in the summer mesosphere, and downwelling in the winter mesosphere and stratosphere, and a flux from summer pole to winter pole in the mesosphere. That upwelling or downwelling results in adiabatic cooling or heating, respectively.

Another factor of the global energy budget is breaking gravity waves, which cause turbulence and dissipation into heat. Gravity waves are typically generated in the troposphere and propagate upwards. Due to decreasing pressure, the amplitude increases with altitude. When the wave-induced temperature gradient exceeds the adiabatic lapse rate, the wave breaks. This typically occurs in the mesosphere. However, some waves already break in the stratosphere, e. g. due to wave filtering which generally occurs when the phase speed equals the background wind. These breaking waves deposit their momentum and energy via the accompanying turbulence and dissipation. This modifies the energy flux from the troposphere to the mesosphere. The amount of energy dissipated in the stratosphere is largely unknown. Due to the stable stratification it has been assumed to be small. However, as the measurements from this work show, energy dissipation in the stratosphere is larger than expected. The actual extent of dissipation directly influences the global energy distribution. Moreover, turbulence is important for the mixing of trace species.

The lack of knowledge about stratospheric turbulence for the most part originates from technical challenges. The dissipation occurs on very small scales of centimetres or millimetres. These scales cannot be resolved by remote sensing techniques, such as radars (see Wilson [2004] for an overview), lidars [Smalikho et al., 2005] and satellites [Gavrilov, 2013, Sofieva et al., 2007]. In-situ observations are performed in the troposphere with aircraft [Schumann et al., 1995, Bögel and Baumann, 1991, Gultepe and Starr, 1995], helicopter [Siebert et al., 2007], tethered balloons [Frehlich et al., 2003] or unmanned aerial vehicles (UAV) [Balsley et al., 2015], and in the mesosphere with sounding rockets [e. g. Lübken, 1992, Giebeler et al., 1993]. In the stratosphere balloon-borne measurements were performed in the 1970s and 1980s by Barat [1982b]. His instrument resolved most of the inertial subrange, which was a huge achievement at that time. However, the vertical resolution was limited by the technical feasibility at that time. Clayson and Kantha [2008] proposed to use standard radiosondes for turbulence measurements, but as is shown in this work, these devices cannot detect most turbulent layers due to their limited vertical resolution.

To close the gap, a new balloon-borne instrument for high-resolution measurements of turbulent dissipation was developed at the IAP. It is called LITOS (Leibniz Institute Turbulence Observations in the Stratosphere). First results show that much more turbulence is present in the stratosphere than previously assumed (in terms of turbulent fraction). Turbulent heating

rates reach up to a few Kelvin per day for thin (roughly 10 m) layers. This is in the same order as typical solar heating rates in the lower stratosphere [Brasseur and Solomon, 1986, Fig. 4.19b]. Thus stratospheric turbulence is more important than previously assumed. High-resolution observations as performed by LITOS are necessary to detect the full extent.

Before the beginning of this work, one masters thesis [Sumińska, 2008] and one PhD thesis [Theuerkauf, 2012] had been performed on LITOS (the latter was finished while the work on this thesis had already begun). A measurement system with one-channel data acquisition was present. The applicability of the Constant Temperature Anemometer and Constant Current Anemometer systems in the environment of a balloon flight had been checked with laboratory experiments by Theuerkauf [2012]. Two flights with large balloons (namely BEXUS 6 and BEXUS 8) and a few flights with small balloons had been performed. However, data quality from the small platform was poor, and no information on gondola movements or the influence of the gondola on the measurement was available. Theuerkauf [2012] wrote software to infer profiles of kinetic dissipation rates from the raw data using Fourier techniques. These methods were reimplemented, improved and extended within this work. Data evaluation by Theuerkauf [2012] concentrated on the two BEXUS flights mentioned above. She performed statistics on turbulent layer thickness and separation, examined profiles of energy dissipation rates and the relation to the Richardson number. She also looked at gravity wave breaking and Kelvin-Helmholtz instabilities as possible sources of the observed turbulence.

Several questions had not been tackled. As mentioned above, the potential modification of the geophysical flow by the gondola system was yet to be examined. A comparison to the Thorpe evaluation of radiosondes, a method that was becoming popular at that time, had not been performed. The thermal dissipation rate had not been looked at. Furthermore, LITOS results had not been complemented by other data such as model simulations or radars. That is where this work set in.

During the final phase of this work, a second masters thesis was porformed on LITOS [Söder, 2014]. It concentrated on technical aspects of the small payload. Particularly, Söder [2014] integrated the measurement system in the spherical payload that had been decided to use after the wind tunnel experiments described in Section 3.4.

This thesis is structured as follows: First basic concepts of turbulence theory needed for the analysis of the measurements are shortly introduced in Chapter 2. Particularly, the concept of dissipation is physically motivated. Chapter 3 describes the instrument used for this study. The methods to extract turbulence data from the raw data are described in Chapter 4. Beside describing the spectral method for high-resolution measurements by LITOS, an error analysis is given. Furthermore, a method to extract dissipation rates from standard radiosondes, a variant of the so-called Thorpe analysis, is explained, as LITOS results are compared with such an evaluation. Geophysical results are detailed in Chapter 5. This includes the relation of dissipation rates to atmospheric background parameters, an intercomparison of different flights, as well as a comparison to model simulations and to radiosonde analyses from the same gondola. Furthermore, the relation between kinetic and thermal dissipation is considered. Finally, all results are summarised in Chapter 6, and an outlook is given. The appendices contain a summary of statis-

tical theory of turbulence and a derivation of the fitting function for experimental spectra (Appendix A), a new construction of wavelets for the continuous wavelet transform (Appendix B), and a description of tests of the attitude reconstruction for the balloon gondola (Appendix C).

2 Basics of turbulence

2.1 Introduction

Turbulence is a complex phenomenon. Although considerable progress was made in the last fifty years, it is still far from being completely understood. To date, no rigorous definition of turbulence has been found. Thus it is worthwhile to examine some basic properties, as summed up, e. g., in Mathieu and Scott [2000, Section 1.1]. To this end, it is illustrative to look at a simple example. Figure 2.1 presents visualisations of turbulence generated by a grid which shows many typical characteristics. It is easy to see that the flow is *random*. This is one of the most important features of turbulence. The details are unpredictable, but statistical properties are supposed to be reproducible. Besides, turbulence *contains a wide range of different scales*. When zooming in on the fluctuations, more fluctuations on smaller scales appear and so on, until on the smallest scales the distribution is smooth. Figure 2.1 also shows that turbulent flow is *rotational*, i. e. it is characterised by vorticity. Typically the vorticity has large variations at small scales. Furthermore, it is a *continuum phenomenon* and intrinsically *three-dimensional*. Moreover, turbulence *dissipates energy*, i. e. kinetic energy is irreversibly converted into heat. Section 2.2 elaborates on this topic. Finally, turbulence is *diffusive*, i. e. it rapidly disperses material and heat (mixing). Turbulent transport is an important factor, e. g., for the mixing of trace species.

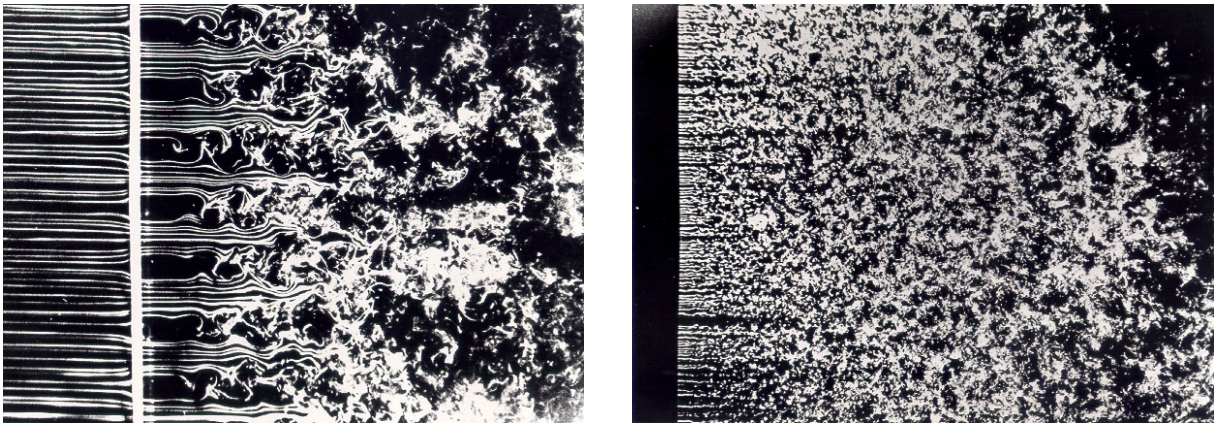

Figure 2.1: Homogeneous turbulence behind a grid. Photographs by Thomas Corke and Hassan Nagib from `http://fdrc.iit.edu/research/nagibResearch.php` (vis 10 Jul 2015).

An important parameter of a flow is the *Reynolds number*

$$Re := \frac{u\ell}{\nu} \tag{2.1}$$

where u is a characteristic velocity, ℓ a characteristic length and ν the kinematic viscosity. It describes the ratio of inertial to viscous forces. Viscosity damps the tendency to instability, thus a high Reynolds number is essential for turbulence [Mathieu and Scott, 2000, Section 1.1].

Based on observations, Richardson [1922, p. 66] realised that "big whirls have little whirls that feed on their velocity, and little whirls have lesser whirls and so on to viscosity—in the molecular sense." This conjecture is nowadays known as the energy cascade and widely accepted. Energy is fed into the cascade on large scales, therein transported to smaller scales, and dissipated at the smallest scales.

An inverse energy cascade in which energy is transported from small to large scales exists in so-called two-dimensional turbulence [Salmon, 1998, Section 4.8], a topic completely different from the three-dimensional case discussed in this work. Quasi two-dimensional turbulence is important in quasigeostrophic flow.

The large range of turbulent scales can be divided into regimes based on different dominating physical processes. As hinted above, the smallest scales are dominated by viscous forces. Those are called *viscous subrange*. In the atmosphere, buoyancy forces play a major role at large scales; this is called the *buoyancy subrange*. If the Reynolds number is large enough, a new range of scales appears where energy is neither brought into the system nor taken out of it, only transported to smaller scales via the cascade. This region is called the *inertial subrange*. More on the different subranges can be found in Appendix A, especially in Section A.4.

Measurements, e. g. the one shown in Figure 2.2, show that turbulence typically consists of *fluctuations* around a mean flow. The velocity does not deviate greatly from the mean for long periods of time [Pope, 2000, Section 1.1]. Thus it is convenient to separate the turbulent fluctuations from the background mean flow. For any measurable quantity a (e. g. velocity $a = u$ or temperature $a = T$), one writes

$$a = \langle a \rangle + a' \tag{2.2}$$

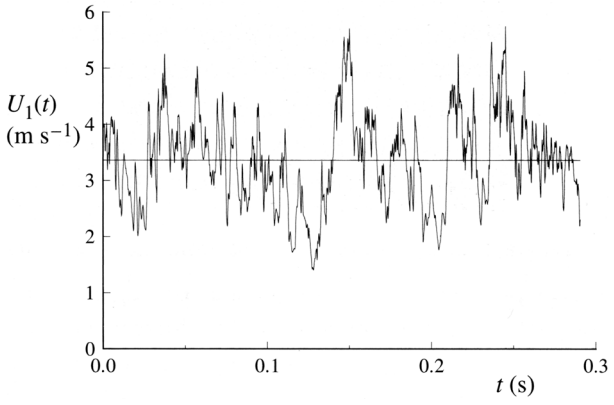

Figure 2.2: Time series of the axial component of velocity $U_1(t)$ on the centreline of a turbulent jet from the experiment of Tong and Warhaft [1995]. Figure taken from Pope [2000, Fig. 1.3].

where $\langle \cdot \rangle$ denotes an ensemble average and the prime designates the fluctuations defined by (2.2). This concept is known as Reynolds decomposition. The mean is independent of the actual realisation of the flow, while the fluctuations represent the random nature of turbu-

lence and are thus of main interest [Mathieu and Scott, 2000, Section 2.4].

In the remainder of this chapter, the concepts needed for the evaluation of experimental data from LITOS are introduced. First, Section 2.2 illustrates what dissipation is and how it is related to entropy. Afterwards, the essential concepts of the statistical treatment of turbulence needed for the determination of energy dissipation rates are very briefly introduced in Section 2.3. A more detailed treatment and a derivation of the spectral function that is fitted to experimental data can be found in Appendix A.

2.2 Dissipation

One of the central concepts used in this thesis is dissipation, as this is what LITOS measures. Thus it is important to understand what dissipation is. To this end, some fundamentals are shortly reviewed. The concept described below relating dissipation to entropy is hardly known among experimenters, but is important to understand the nature of dissipation.

Typographically, vectors are denoted in bold face and tensors in sans-serif. A flow is described by the velocity $\boldsymbol{u}$, its temperature T, pressure p, density ρ, and kinematic viscosity ν. The acceleration due to gravity is $\boldsymbol{g} = -\nabla\phi$, where ϕ is the gravitational potential. As usual in fluid dynamics, the treatment is based on continuum mechanics because all scales are much larger than the molecular structure of matter. Einstein's summation convention is used, i. e. repeated indices imply summation.

The evolution of the flow is governed by the Navier-Stokes equations. The first one in the set is the momentum equation (deduced from Newton's second law)

$$\frac{\mathrm{d}\boldsymbol{u}}{\mathrm{d}t} = \frac{\partial \boldsymbol{u}}{\partial t} + \boldsymbol{u}\cdot\nabla\boldsymbol{u} = -\frac{1}{\rho}\nabla p + \frac{1}{\rho}\nabla\cdot\boldsymbol{\mathsf{F}} - \nabla\phi \tag{2.3}$$

[Lange, 2002, (2-19), (2-51)]. The terms on the right-hand side describe strain, shear and gravitational forces. $\boldsymbol{\mathsf{F}}$ is called deformation tensor and describes the response due to strain and shear forces. The second equation of importance is the continuity equation (based on mass conservation)

$$\frac{\mathrm{d}\rho}{\mathrm{d}t} + \nabla\cdot\boldsymbol{u} = \frac{\partial\rho}{\partial t} + \nabla\cdot(\rho\boldsymbol{u}) = 0. \tag{2.4}$$

Using the Frobenius product $\boldsymbol{\mathsf{A}}\cdot\cdot\boldsymbol{\mathsf{B}} := a_{ij}b_{ij}$, the set is completed by the equation for the internal energy per unit mass e_i (based on the first law of thermodynamics)

$$\frac{\mathrm{d}e_\mathrm{i}}{\mathrm{d}t} = \frac{\partial e_\mathrm{i}}{\partial t} + \boldsymbol{u}\cdot\nabla e_\mathrm{i} = \frac{1}{\rho}\boldsymbol{\mathsf{F}}\cdot\cdot\nabla\boldsymbol{u} - \frac{1}{\rho}p\nabla\cdot\boldsymbol{u} - \frac{1}{\rho}\nabla\cdot\boldsymbol{J}_Q \tag{2.5}$$

[Lange, 2002, (2-56)]. $\boldsymbol{J}_Q$ is the heat flux. The three terms on the right hand side describe the change of internal energy due to friction, pressure work and transport.

To infer a budget of kinetic energy per unit mass $e_\mathrm{k} = \boldsymbol{u}^2/2$ and potential energy ϕ, the momentum equation (2.3) is multiplied with $\rho\boldsymbol{u}$ to yield after simple modifications

$$\frac{\partial\rho(e_\mathrm{k}+\phi)}{\partial t} = \nabla\cdot\left(\rho\boldsymbol{u}(e_\mathrm{k}+\phi) - \boldsymbol{u}p - \boldsymbol{u}\cdot\boldsymbol{F}\right) + p\nabla\cdot\boldsymbol{u} - \boldsymbol{F}\cdot\cdot\nabla\boldsymbol{u}. \tag{2.6}$$

The first term on the right hand side denotes transport. The second and third terms are already known from the internal energy equation (2.5) where they are present with different sign. Pressure work accounted for by the second term is the reversible conversion between inner energy and kinetic energy. Frictional dissipation of kinetic energy to inner energy quantified by the third term is an irreversible process. Thus the *kinetic energy dissipation rate* of the total flow ε_t is defined

$$\varepsilon_\mathrm{t} := \frac{1}{\rho}\boldsymbol{F}\cdot\cdot\nabla\boldsymbol{u}. \tag{2.7}$$

Not only kinetic energy is dissipated, but also heat. However, that cannot be seen in the energetics. Thus, entropy is considered. A budget equation of entropy per unit mass s is deduced from the Gibbs relation (neglecting water vapour, ions, etc. as those play no role in the stratosphere)

$$T\rho\frac{\mathrm{d}s}{\mathrm{d}t} = \rho\frac{\mathrm{d}e_\mathrm{i}}{\mathrm{d}t} + p\rho\frac{\mathrm{d}v}{\mathrm{d}t} = \rho\frac{\mathrm{d}e_\mathrm{i}}{\mathrm{d}t} + p\nabla\cdot\boldsymbol{u} \tag{2.8}$$

[Lange, 2002, (2-57)], where v is the volume per unit mass. The second equality uses the continuity equation $\rho\frac{\mathrm{d}v}{\mathrm{d}t} = \nabla\cdot\boldsymbol{u}$. Inserting the internal energy equation (2.5) yields

$$0 \le \frac{\mathrm{d}s}{\mathrm{d}t} = \frac{1}{T}\underbrace{\frac{1}{\rho}\boldsymbol{F}\cdot\cdot\nabla\boldsymbol{u}}_{=\varepsilon_\mathrm{t}} - \frac{1}{T}\underbrace{\frac{1}{\rho}\boldsymbol{J}_Q\frac{\nabla T}{T}}_{=:-\tilde{\chi}_\mathrm{t}} - \frac{1}{\rho}\nabla\cdot\boldsymbol{J}_Q \tag{2.9}$$

[similar to Gaßmann and Herzog, 2014, (17)]. The inequality is the second law of thermodynamics. Due to Onsager's theory, the vector type and tensor type quantities have to be separately non-negative [Lange, 2002, Section 1.10(a)]. The first term describes the entropy production due to irreversible conversion of kinetic energy to inner energy by friction. The condition $\varepsilon_\mathrm{t} \ge 0$ also poses a constraint to the deformation tensor $\boldsymbol{F}$. The second term describes the entropy production due to thermal diffusion, i. e. irreversible conversion of available inner energy to unavailable inner energy. This is also a type of dissipation. The non-negativity condition together with dimensional reasoning implies $\boldsymbol{J}_Q = -c_p\rho\alpha\nabla T$, where α is the thermal diffusivity. Thus the *thermal dissipation rate* of the total flow is defined as

$$\tilde{\chi}_\mathrm{t} := -\frac{1}{\rho}\boldsymbol{J}_Q\frac{\nabla T}{T} = \alpha\frac{c_p}{T}(\nabla T)^2. \tag{2.10}$$

Altogether, entropy production is given by the sum of kinetic energy dissipation, thermal dissipation, and transport. $\varepsilon_\mathrm{t} \geq 0$ and $\tilde{\chi}_\mathrm{t} \geq 0$ is a direct consequence of the second law of thermodynamics.

In many textbooks on turbulence, e. g. Mathieu and Scott [2000], Pope [2000], Tatarskii [1971], the flow is assumed to be incompressible, i. e. $\nabla \cdot \boldsymbol{u} = 0$. This is permissible if "the characteristic velocities are small compared to the velocity of sound c and the ratio of the characteristic length scale over which the velocity changes markedly to the time needed for this change to occur is also small compared to c" [Tatarskii, 1971, p. 46]. For the evaluation of the LITOS data, the dissipation rate is computed in windows of a few metres altitude, for which density does not change significantly. Typical velocities are in the order of $1\,\mathrm{m\,s^{-1}}$ which is much smaller than c. Thus the flow may be treated as incompressible. In that case the deformation tensor reduces to a much simpler form and thus the kinetic energy dissipation rate to

$$\varepsilon_\mathrm{t} = \frac{1}{\rho}\boldsymbol{F} \cdot\cdot \nabla \boldsymbol{u} = \frac{\nu}{2}\left(\frac{\partial u_i}{\partial x_j} + \frac{\partial u_j}{\partial x_i}\right)^2, \tag{2.11}$$

where ν is the kinematic viscosity.

As mentioned in the introduction to this chapter, it is common practice in turbulence theory to decompose quantities into a mean and a fluctuating part, the so-called Reynolds decomposition. The fluctuations are supposed to contain the turbulent part of the flow and represent the random nature. Dissipation is one of the key characteristics of turbulence. Thus it is important to look at what the decomposition effects to dissipation. Inserting the decomposition for velocity

$$u_i = \langle u_i \rangle + u_i' \tag{2.12}$$

[Mathieu and Scott, 2000, eq. (3.2)] into (2.11) and averaging the resulting equation yields

$$\langle \varepsilon_\mathrm{t} \rangle = \underbrace{\frac{\nu}{2}\left(\frac{\mathrm{d}\langle u_i \rangle}{\mathrm{d}x_j} + \frac{\mathrm{d}\langle u_j \rangle}{\mathrm{d}x_i}\right)^2}_{=:\varepsilon_\mathrm{m}} + \underbrace{\frac{\nu}{2}\left\langle\left(\frac{\mathrm{d}u_i'}{\mathrm{d}x_j} + \frac{\mathrm{d}u_j'}{\mathrm{d}x_i}\right)^2\right\rangle}_{=:\langle\varepsilon_\mathrm{f}\rangle} \tag{2.13}$$

[Mathieu and Scott, 2000, (4.25)]. The mixed terms vanish due to Reynolds' postulate [Lange, 2002, Section 6.1], particularly because $\left\langle \langle u_j \rangle u_j' \right\rangle = 0$. That means the overall dissipation ε_t nicely splits into a mean and a fluctuating component ε_m and $\langle \varepsilon_\mathrm{f} \rangle$, respectively. Usually the turbulent kinetic energy dissipation is much larger than the one of the mean flow,

$$\varepsilon_\mathrm{m} \ll \langle \varepsilon_\mathrm{f} \rangle \tag{2.14}$$

[Mathieu and Scott, 2000, (4.29)] because the gradients of the fluctuations are much larger than those of the slowly varying mean. Thus it is convenient to study the energy dissipation of the

fluctuations only. That is what is usually denoted as the dissipation rate, i. e.

$$\boxed{\varepsilon := \langle \varepsilon_\mathrm{f} \rangle = \frac{\nu}{2} \left\langle \left(\frac{\mathrm{d}u_i'}{\mathrm{d}x_j} + \frac{\mathrm{d}u_j'}{\mathrm{d}x_i} \right)^2 \right\rangle \quad \text{(kinetic energy dissipation rate for fluctuations)}}. \tag{2.15}$$

This nomenclature is used from this point onwards. The definition is consistent with Tatarskii [1971, §10].

Looking at the thermal dissipation, one sees that $\langle (\nabla T)^2 \rangle = (\nabla \langle T \rangle)^2 + \langle (\nabla T')^2 \rangle$ similarly splits into a mean and fluctuating part with $(\nabla \langle T \rangle)^2 \ll \langle (\nabla T')^2 \rangle$. Additionally, the temperature fluctuations are much smaller than the mean, $T' \ll \langle T \rangle$. Thus, the thermal dissipation

$$\langle \tilde{\chi}_\mathrm{t} \rangle \approx \underbrace{\frac{c_p}{\langle T \rangle} \alpha (\nabla \langle T \rangle)^2}_{=:\tilde{\chi}_\mathrm{m}} + \underbrace{\frac{c_p}{\langle T \rangle} \alpha \left\langle (\nabla T')^2 \right\rangle}_{=:\langle \tilde{\chi}_\mathrm{f} \rangle} \tag{2.16}$$

also decomposes into shares for the mean flow and the fluctuations, $\tilde{\chi}_\mathrm{m}$ and $\langle \tilde{\chi}_\mathrm{f} \rangle$, with $\tilde{\chi}_\mathrm{m} \ll \langle \tilde{\chi}_\mathrm{f} \rangle$. Therefore, the mean dissipation of temperature *fluctuations*, $\langle \tilde{\chi}_\mathrm{f} \rangle$, is considered only. In order to be consistent with the textbook of Tatarskii [1971], previous works by Theuerkauf [2012] and Lübken [1993], and numerical simulations by Werne and Fritts [2001], Fritts et al. [2015], the *thermal dissipation of temperature fluctuations* χ (denoted as N in the first three of the aforementioned works) is defined as

$$\boxed{\chi := \alpha \left\langle (\nabla T')^2 \right\rangle = \langle \tilde{\chi}_\mathrm{f} \rangle \, \frac{\langle T \rangle}{c_p} \quad \text{(thermal dissipation rate for fluctuations)}} \tag{2.17}$$

[cf. Tatarskii, 1971, (13.25)], although it does not have the dimensions of a dissipation.

In the literature dissipation rates are also given in the form of heating rates due to turbulent dissipation

$$\frac{\mathrm{d}T}{\mathrm{d}t} = \varepsilon / c_p. \tag{2.18}$$

In this form the heating due to turbulent dissipation can easily be compared to that, e. g., due to solar irradiation.

2.3 Statistical theory and spectral analysis

In the previous section, the concept of dissipation was physically motivated and defined. The definition contains the derivatives of the fluctuations, which have to be computed at the smallest scales, the so-called Kolmogorov microscale $\eta := \sqrt[4]{\nu^3/\varepsilon}$ [e. g. Mathieu and Scott, 2000, (7.37)], because only at these scales the distribution is smooth (cf. Section 2.1). η is in the order of mil-

limetres and below. Both spatially and temporally (when applying Taylor's hypothesis to observe the spatial derivatives) the resolution of LITOS is not sufficient to include η for all cases. More important, the fluctuations at those scales are below the measurement noise. Thus the dissipation rate is not directly measurable, and a separate theory has to be used.

As mentioned in the introduction to this chapter, turbulent fluctuations have a random character. That suggests to tackle the problem with statistical methods. The velocity fluctuations $\boldsymbol{u}'(\boldsymbol{x}, t)$ and temperature fluctuations $T'(\boldsymbol{x}, t)$ are treated as random fields. A measurement is one realisation of the random process.

Based on Tatarskii [1971], Lübken [1993] established a theory for the extraction of turbulence parameters for temperature and density fluctuations, which Theuerkauf [2012] extended for velocity fluctuations. A complete derivation including the discussion of some implicit assumptions not mentioned by the original authors is given in Appendix A, together with an introduction to the statistical theory of turbulence. Here, only the most essential results are summarised.

If the statistics of a field is independent of time, it is called *stationary*. Moreover, if the statistical properties do not depend on the location in space, it is *homogeneous*, and if the statistics are independent of the direction in space, it is called *isotropic*. All three of these properties are assumed hereafter. This is permissible because small scales are considered, see below. That causes the *temporal correlation function*

$$B_{ij}^{(\mathrm{t})}(\boldsymbol{x}, t, \tau) := \left\langle u_i'(\boldsymbol{x}, t+\tau) u_j'(\boldsymbol{x}, t) \right\rangle \tag{2.19}$$

[Tatarskii, 1971, (2.7)] to be independent of $\boldsymbol{x}$ and t, i. e. dependent on τ only. This reduction of the number of variables together with a decorrelation assumption enables a Fourier transform

$$W(\omega) := \frac{1}{2\pi} \int_{-\infty}^{\infty} B^{(\mathrm{t})}(\tau)\, \cos(\omega\tau)\, \mathrm{d}\tau \tag{2.20}$$

[Tatarskii, 1971, (2.16)]. The sine term vanishes because $\boldsymbol{B}^{(\mathrm{t})}$ is an even function. W is called the *temporal spectrum*.

Lübken and Hillert [1992, (4)] used a Heisenberg type spectrum spanning the inertial and viscous subranges

$$W(\omega) = C^2 \frac{\Gamma\left(\frac{5}{3}\right) \sin\left(\frac{\pi}{3}\right)}{2\pi u_\mathrm{b}} \frac{(\omega/u_\mathrm{b})^{-5/3}}{\left(1 + \left(\frac{\omega}{u_\mathrm{b} k_0}\right)^{8/3}\right)^2} \tag{2.21}$$

where C^2 is the so-called structure function constant, u_b denotes the balloon ascent velocity and k_0 the breakpoint between the inertial and viscous subranges. For velocity fluctuations, $C^2 = a_\mathrm{v}^2 \varepsilon^{2/3}$ [Kolmogorov, 1941a, (23)], and for temperature fluctuations $C^2 = a_\mathrm{T}^2 \frac{\chi}{\varepsilon^{1/3}}$ [Obukhov, 1949, (21)], where a_v^2 and a_T^2 are constants. The spatial scale $l_0 = 2\pi/k_0$ corresponding to the breakpoint

is called *inner scale*. It is related to the dissipation rate by

$$l_0 = c_{l_0} \sqrt[4]{\frac{\nu^3}{\varepsilon}} \tag{2.22}$$

[e. g. Tatarskii, 1971, (12.4)], where c_{l_0} is a constant depending on the type of fluctuations considered.

Theuerkauf [2012, (B.13)] derived for velocity fluctuations

$$c_{l_0,\mathrm{v}} = 2\pi \left(\frac{9\Gamma(5/3)\sin(\pi/3)}{16} a_\mathrm{v}^2 \right)^{3/4} \tag{2.23}$$

(see Appendix A.5 for details of the derivation). The value of a_v^2 is usually determined from measurements. Theuerkauf [2012, Appendix B] used $a_\mathrm{v}^2 = 2.0$ [Bertin et al., 1997, (8); Antonia et al., 1981, p. 580; Pope, 2000, p. 194] yielding

$$c_{l_0,\mathrm{v}} = 5.7. \tag{2.24}$$

This value for $c_{l_0,\mathrm{v}}$ is used for the evaluation performed in this thesis. The empirical constant a_v^2 can also be determined with renormalisation group analysis techniques. Yakhot and Orszag [1986, (2.62)] obtained for the Kolomogorov constant in the inertial-range energy spectrum $C_\mathrm{K} = 1.617$, which results in $a_\mathrm{v}^2 = 2.13$ and thus, using (2.23), $c_{l_0,\mathrm{v}} = 5.98$. In contrast, Hocking [1985, Section 4] gave $c_{l_0,\mathrm{v}} = 12.8$; however, he noted that "l_0 is not exactly the point on the spectrum where a break in slope would occur [e. g., Hill and Clifford, 1978, figure 1]; the break in slope occurs at a spatial scale of between 2 and 4 times l_0." The break is just what is needed for the fit to a measured spectrum. As the value (2.24) is derived to represent the kink in the spectrum, it seems more realistic for the use at hand.

The different values of the constant $c_{l_0,\mathrm{v}}$ vary by a factor of ~2.2. Due to the $c_{l_0,\mathrm{v}}^4$ dependence of the inversion of (2.22), that results in a systematic uncertainty in ε of a factor of ~25! When disregarding the value by Hocking [1985] because that does not lead to an l_0 corresponding to the point in the spectrum where the kink occurs, the uncertainty is 5 % in l_0 or 20 % in ε.

For temperature fluctuations Theuerkauf [2012, (A.23)] deduced

$$c_{l_0,\mathrm{T}} = 2\pi \left(\frac{9\Gamma(5/3)\sin(\pi/3)}{16 Pr_\mathrm{mol}} a_\mathrm{T}^2 \right)^{3/4}, \tag{2.25}$$

where $Pr_\mathrm{mol} := \nu/\alpha$ is the molecular Prandtl number which describes the relation between kinematic viscosity ν and molecular diffusion coefficient α. With $a_\mathrm{T}^2 = 1.74 \times 2$ [Lübken, 1992, (37)] (the factor 2 is the normalisation factor f_α from Lübken [1992]) and $Pr_\mathrm{mol} = 0.73$ [Lübken, 1993, Appendix A] she obtained

$$c_{l_0,\mathrm{T}} = 10.9, \tag{2.26}$$

the value used in this thesis. Wilson et al. [2014, Section 3.3.4] used $a_\mathrm{T}^2 = 3.2$ for the structure function constant, which, using (2.25), results in $c_{l_0,\mathrm{T}} = 10.3$, i. e. quite similar to the value derived by Theuerkauf [2012]. Hill and Clifford [1978, (7)] gave a different value of $c_{l_0,\mathrm{T}} = 7.4$. The different values of $c_{l_0,\mathrm{T}}$ cause an uncertainty in ε of a factor of ~4.7. When disregarding the value by Hill and Clifford [1978] (the l_0 obtained with it does not correspond to the kink in the spectrum, see above), the uncertainty is 6 % in l_0 or 25 % in ε.

When inserting the definition of the structure function constant C^2 into (2.21), one sees that the resulting equation depends on both l_0 and ε. Therefore ε is eliminated by using (2.22). The resultant formula for velocity fluctuations

$$W(\omega) = a_\mathrm{v}^2 \left(c_{l_0,\mathrm{v}}^4 \frac{\nu^3}{l_0^4} \right)^{2/3} \frac{\Gamma(\frac{5}{3}) \sin(\frac{\pi}{3})}{2\pi u_\mathrm{b}} \frac{(\omega/u_\mathrm{b})^{-5/3}}{\left(1 + \left(\frac{\omega}{u_\mathrm{b}(2\pi/l_0)}\right)^{8/3}\right)^2} \tag{2.27}$$

has only l_0 as free parameter, and that for temperature fluctuations

$$W(\omega) = a_\mathrm{T}^2 \, \chi \left(c_{l_0,\mathrm{T}}^4 \frac{\nu^3}{l_0^4} \right)^{-1/3} \frac{\Gamma(\frac{5}{3}) \sin(\frac{\pi}{3})}{2\pi u_\mathrm{b}} \frac{(\omega/u_\mathrm{b})^{-5/3}}{\left(1 + \left(\frac{\omega}{u_\mathrm{b}(2\pi/l_0)}\right)^{8/3}\right)^2} \tag{2.28}$$

has only l_0 and χ as free parameters, because the balloon ascent velocity u_b and the kinematic viscosity ν are known from the radiosonde measurement. Thus l_0 (and therewith ε) and χ can be obtained by fitting to measured spectra. Especially, l_0 is mainly determined by the spatial scale where the break between inertial and viscous subrange is located (there is an additional weak l_0 dependency of the structure function constant C^2). The thermal dissipation rate χ is a linear factor in the structure function constant C_T^2 and thus the temperature spectrum (2.28), therefore it is specified by the level of the absolute value of the PSD.

The breakpoint between inertial and buoyancy subranges is called *outer scale*. Ozmidov [1965] deduced an outer scale representing the vertical size of the largest eddies in stably stratified fluid by finding the scale where the turbulent kinetic energy equals the buoyancy energy,

$$\varepsilon^{2/3} L_\mathrm{O}^{5/3} / L_\mathrm{O} \propto E_\mathrm{turb} = E_\mathrm{pot} \propto N^2 L_\mathrm{O}^2.$$

Therewith he obtained

$$L_\mathrm{O} = c_{L_\mathrm{O}} \sqrt{\frac{\varepsilon}{N^3}} \tag{2.29}$$

with a constant c_{L_O} near unity. This scale is called *Ozmidov scale*. Geller [1972, Appendix 2] incurred a similar result by finding the scale where turbulent and buoyancy acceleration are equal. As the spatial scales in measured spectra are below L_O, the assumption of isotropy is justified. The constant c_{L_O} is often set to 1 [e. g. Gavrilov et al., 2005, Clayson and Kantha, 2008, Wilson et al., 2014]. The Ozmidov scale plays a role in extracting turbulence parameters from radiosonde measurements, a method detailed in Section 4.2.

3 Measurement technique

The instrument used in this study is described in this chapter. First, the general measurement principle is illustrated. Then the gondola system of the balloon-borne instrument is specified in detail. The last two sections discuss potential disturbances of the measurement by the instrument itself. These can be caused by gondola motions which create spurious apparent winds or by the gondola form altering the geophysical flow. After experimenting with different payload shapes, the one inducing the least disturbances is chosen.

3.1 General measurement principle

On large scales, i. e. in the buoyancy subrange and part of the inertial subrange, wave motions superpose the turbulent fluctuations. Thus it is favourable to measure at small scales where only turbulent motions are present. For the precise determination of the energy dissipation rate, the resolution has to be better than the inner scale l_0. $l_0 = c_{l_0} \sqrt[4]{\nu^3/\varepsilon}$, (2.22), scales with the kinematic viscosity $\nu = \mu/\rho$ which in turn is the dynamic viscosity μ scaled by density ρ. The dynamic viscosity is defined by the resistance to shear and does not change greatly. Due to the exponential decrease of density with altitude and because the height dependence of the dissipation rate is weaker [cf. Lübken, 1997, Figure 9; Haack et al., 2014, Figure 7], the inner scale increases with height. Typical values are centimetres in the troposphere and metres in the mesosphere. The coverage of the full spectrum down to these small scales can only be performed with in-situ techniques.

Moreover, atmospheric turbulence is very intermittent [e. g. Salmon, 1998, Frisch, 1995]. To resolve changes in energy dissipation at scales in the order of 1 m with spectral methods, a window of that length has to contain enough data points that the spectrum covers several orders of magnitude of spatial scales. This is necessary to resolve both the inertial and viscous subrange in order to enable a meaningful fit of a turbulence model to the data (cf. Section 4.1.1).

In-situ platforms suitable for the stratosphere are balloons or high altitude aircrafts. The latter cannot reach the middle stratosphere, are very expensive and typically operate at high speeds which is unfavourable for the resolution of very small scales and velocities. Thus balloons have been chosen as platform. A new balloon-borne instrument for the in-situ measurement of turbulence in wind and temperature called LITOS (Leibniz Institute Turbulence Observations in the Stratosphere) was designed at IAP to fulfill the requirements named above. To this end, sensitive wind and temperature sensors are installed on the gondola of the balloon. A standard meteorological radiosonde (details see below) records the atmospheric background. The distance

between balloon and gondola is typically 100 m to 150 m to be out of the wake of the balloon. To prevent influences from the gondola, the sensors are mounted on booms, and the radiosonde is attached either 30 m below the gondola or between balloon and gondola.

Since most of the area exposed to wind of the whole system comprises the balloon, the gondola is advected with the mean wind in the altitude of the balloon $\overline{u(z+h)}$, where z denotes the altitude of the gondola, h the distance between balloon and payload, and the overbar a cross-section weighted average over the height of the balloon. Thus the wind sensor measures the apparent horizontal wind $u_a(z)$ given as the difference between the true wind $u(z)$ at the altitude of the gondola and the velocity of the balloon $\overline{u(z+h)}$, as indicated in Figure 3.1. Since only wind fluctuations u' are needed for the turbulence analysis, and because $\overline{u(z+h)}$ contains only large-scale motions that are included in $\langle u \rangle$, knowledge of u_a is sufficient. u' is extracted from u_a by subtracting a linear trend or a spline, see Section 4.1.

The wind sensor is a constant temperature anemometer (CTA), which consists of a thin wire

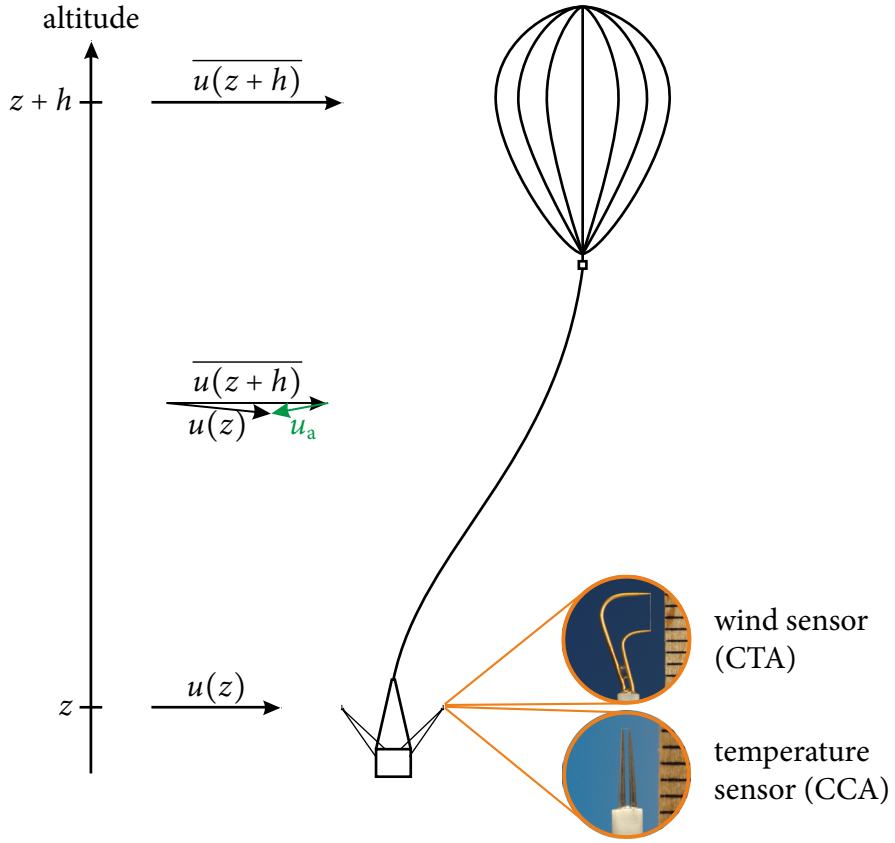

Figure 3.1: General measurement principle of LITOS. z denotes the altitude of the sensor(s), h the distance between balloon and gondola, u horizontal wind velocity, the overbar a cross-section weighted average over the height of the balloon, and u_a the apparent wind. In the photographs of the CTA and CCA sensors, the ticks on the ruler are millimetres.

of 5 µm diameter and 1.25 mm length held at a constant temperature. This is performed by incorporating the wire as one leg of a Wheatstone bridge. The anemometer's principle of operation is based on the cooling effect of the air flow penetrating the wire. The amount of heat taken away corresponds to wind velocity. Thus, the latter is given by the voltage required to keep the wire's temperature constant. The principle is described in detail by Bruun [1995] and Durst [2008].

The wire's orientation designates its spatial sensitivity. As indicated in Figure 3.1, probes with the wire oriented vertically are used for LITOS in order to measure the horizontal wind component while being insensitive to the vertical component. The prongs that support the wire imply a preferred flow direction from opposite the prongs (from the right side in Figure 3.1). If the prongs lie upstream, the measurement can be disturbed.

CTA sensors are standard for laboratory measurements, and whole textbooks are devoted to this topic [e. g. Bruun, 1995]. However, LITOS is the first instrument to apply them on a balloon. The applicability in such an environment has been examined in a previous study [Theuerkauf et al., 2011]. The lower pressure limit has been estimated to ~1 hPa (~45 km). Laboratory experiments on the dependence of the CTA response on pressure and temperature have been performed. CTA sensitivity decreases with decreasing pressure (increasing altitude), but also with increasing wind velocity. The impact on the dissipation rate is not straightforward. Theuerkauf et al. [2011] showed for a representative example that within the altitude section of a window length (up to ~25 m) the change in sensitivity is small enough not to influence the spectrum. The limiting factor for the detection of dissipation rates is the number of data points in the fit rather than the sensor sensitivity, cf. Section 4.1.1.

The evaluation of the CTA data depends on the spectral form but not on the absolute values (see Section 4.1); therefore the anemometer voltage is directly used for the analysis, and a calibration of the CTA system is not necessary. Such a calibration to infer wind velocities from the anemometer voltage would indeed be difficult because it has to be performed in a laboratory for known velocities under the same ambient conditions (pressure, temperature) as the measurement [see Theuerkauf et al., 2011]. Conditions of a balloon flight, where pressure varies within several orders of magnitude and temperature changes by ~80 K, are very difficult to simulate in a wind tunnel.

The constant temperature anemometry system by Dantec Dynamics is used for LITOS. The Dantec Dynamics 55P31 gold-plated wire probe is specified up to frequencies of 90 kHz at standard pressure (~1000 hPa), the MiniCTA 54T30 Wheatstone bridge with a frequency response of 10 kHz. With a mean balloon ascent rate of 5 m s^{-1}, a sampling frequency of 8 kHz has been selected to obtain a sub-millimetre vertical resolution. Thus, the inner scale of turbulence is resolved for most cases. Only for very large dissipation rates the inertial subrange extends to the Nyquist limit.

The temperature sensor is a constant current anemometer (CCA). It consists of a thin wire of 1 µm diametre and 0.4 mm length, which is basically operated as a resistance thermometer (despite its name "anemometer"). As the current is kept konstant, the output voltage is directly proportional to temperature. Due to the very low heat capacity of the wire and the low current, a sampling rate of 8 kHz is applied.

Theuerkauf [2012, Section 3.2] tested the impact of pressure and wind on the CCA measurement. No influence could be detected within the tested range of −40 °C to 20 °C and 0 m s^{-1} to 35 m s^{-1} in the climate chamber and 5 hPa to 1000 hPa in the pressure chamber. Thus she concluded that the system can be used without restriction for stratospheric soundings.

For the BEXUS 8 flight, a Dantec Dynamics 90C20 temperature module with a 55P31 wire probe has been used. Due to the large weight of the module, it was replaced by another one with lower weight for the BEXUS 12 flight, namely the 1745 constant current anemometer system manufactured by TSI Corporation with 1260A-T1.5 probes (wire diameter 3.8 µm, wire length 1.3 mm). However, that Wheatstone bridge turned out to have too large a noise.

The sensors are moved vertically through the atmosphere by the rising balloon. Neglecting the vertical wind compared to the ascent velocity, a spatial measurement (more specifically an altitude profile) is obtained. With Taylor's frozen field hypothesis this enables the computation of spatial spectra without knowing the absolute wind velocity. Those spectra are needed for the derivation of ε. During the floating phase there is no such known movement through the ambient air, thus turbulence evaluation is impossible without absolute wind measurement.

As mentioned above, the atmospheric background is observed by a meteorological radiosonde (Vaisala RS92), which measures temperature, pressure, humidity and background wind in a standardised way with a sampling time of 2 s, i. e. a vertical resolution of 10 m. The accuracy (according to the data sheet) is 0.5 K, 1 hPa, 1 %RH and 0.15 m s^{-1}, respectively. The device has an onboard telemetry which transmits the data to a ground station.

3.2 Gondola system

The LITOS experiment exists in two versions. One was flown on large (~100 kg) payloads together with other experiments within Balloon EXperiments for University Students (BEXUS) and allowed for a larger weight. That way more sensors can be flown, and instruments can be added for tests. The drawback is that the launch location and time is very limited (it takes place at Kiruna, Sweden in autumn) and cannot be influenced by the experimenters. Thus, a small stand-alone version was developed which can be flown with a weather balloon from every radiosonde station at all times. In order to keep this version simple and avoid complex licensing procedures with air safety authorities, the overall payload weight is limited to 5 kg. Both systems are described in the following subsections.

3.2.1 Gondola system for large payloads (BEXUS)

Balloon EXperiments for University Students (BEXUS) is a programme run by the German Aerospace Center (DLR) and the Swedish National Space Board (SNSB). It allows university students to carry out experiments on stratospheric research balloons. A payload of up to ~100 kg is launched with a 12 000 m^3 balloon from Esrange Space Center, Kiruna, Sweden (67° 53' N,

21° 04' E). That allows more weight and therefore more sensors than with a small payload. The LITOS experiment was flown three times with BEXUS: on BEXUS 6, 8 and 12 in 2008, 2009 and 2011, respectively. The first two flights are already described by Theuerkauf [2012] so that here the focus lies on BEXUS 12.

Esrange provides the flight train including balloon, a cutter, a parachute, the Esrange Balloon Service System (EBASS) used for altitude control and flight termination, an Argos GPS and air traffic control Transponder (AGT), a radar reflector, and a gondola into which the experiment is integrated using defined interfaces [Persson et al., 2010]. Infrastructure offered by Esrange also includes a telemetry system called E-Link that can be used by the experiments. Figure 3.2 shows a sketch of the flight train of BEXUS 12.

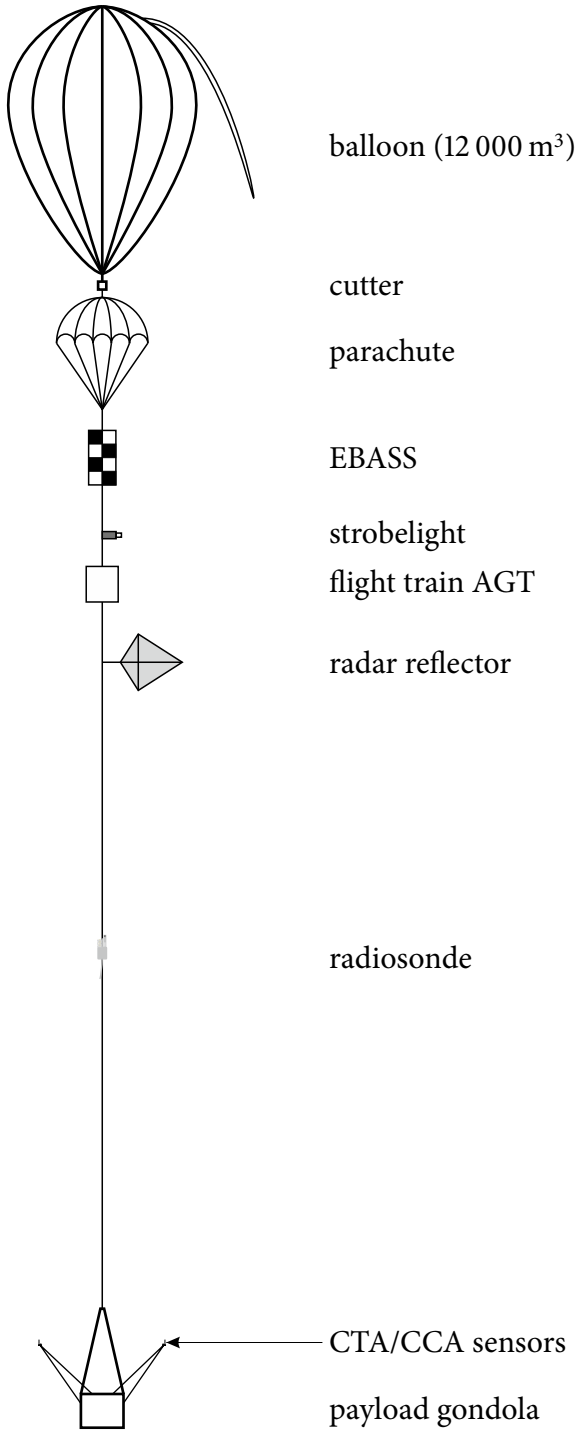

Figure 3.2: Flight train of BEXUS 12. Drawing according to Persson et al. [2010].

The LITOS experiment for BEXUS 12 was designed to be redundant because the fragile probes might break during the launch procedure. Two CTA sensors (Dantec Dynamics' MiniCTA system 54T30 with gold-plated wire probes 55P31) and three CCA sensors (TSI Corporation's Model 1745 CCA Wheatstone bridges with 1260A-T1.5 probes) were installed. All five were sampled with standalone dataloggers developed by Reimesch Communications that were already used for the BEXUS 6 and 8 flights. New booms supporting the sensors were designed that put the probes further away from the gondola compared to BEXUS 8 and 6. The actual construction was performed by a student of mechanical engineering. One CTA sensor produced data with good quality that are the basis for the geophysical results presented in Chapter 5. The data acquisition device of the other one had a failure so that the data is corrupt. The Wheatstone bridge of the new light-weight CCA system turned out to have a high non-Gaussian

noise level which is exceeded only by very large temperature fluctuations. Additionally the data are affected by electronic disturbances in form of large spikes, which were generated by a coupling of the CCA bridge to the data acquisition via the joint voltage supply. Therefore the CCA data from BEXUS 12 are not used in this thesis.

Additionally, a three-dimensional CTA probe (Dantec Dynamics 55P91) was tested which consists of three CTA wires arranged so that all three wind components can be measured. The aim was to check the assumption of isotropy. Exact temporal correlation of all three channels is important; thus a new electronics board which can acquire three channels at once was developed within the Bachelor thesis of Andreas Roloff [Roloff, 2011]. Regrettably, it had a high inherent noise in the same order as the wind fluctuations. Nevertheless, information can be extracted with spectral analysis. For instance, several turbulent layers and clearly calm regions have been identified. However, due to the low signal to noise ratio many spectra are not identifiable as turbulent or calm which prevents automatic data evaluation. Thus the data of the three-dimensional CTA sensor are not considered further in this thesis.

To prevent gondola-induced disturbances, the wind and temperature sensors were mounted on booms attached to the outside of the gondola (see photograph in Figure 3.3). A radiosonde was incorporated in the flight train, i. e. placed between balloon and gondola. Separate IAP developed control electronics coordinated the whole experiment and transmitted housekeeping data via the E-Link telemetry system provided by Esrange. All data were stored on SD cards, as the payload was recovered with a helicopter. The overall experiment weight was 25 kg.

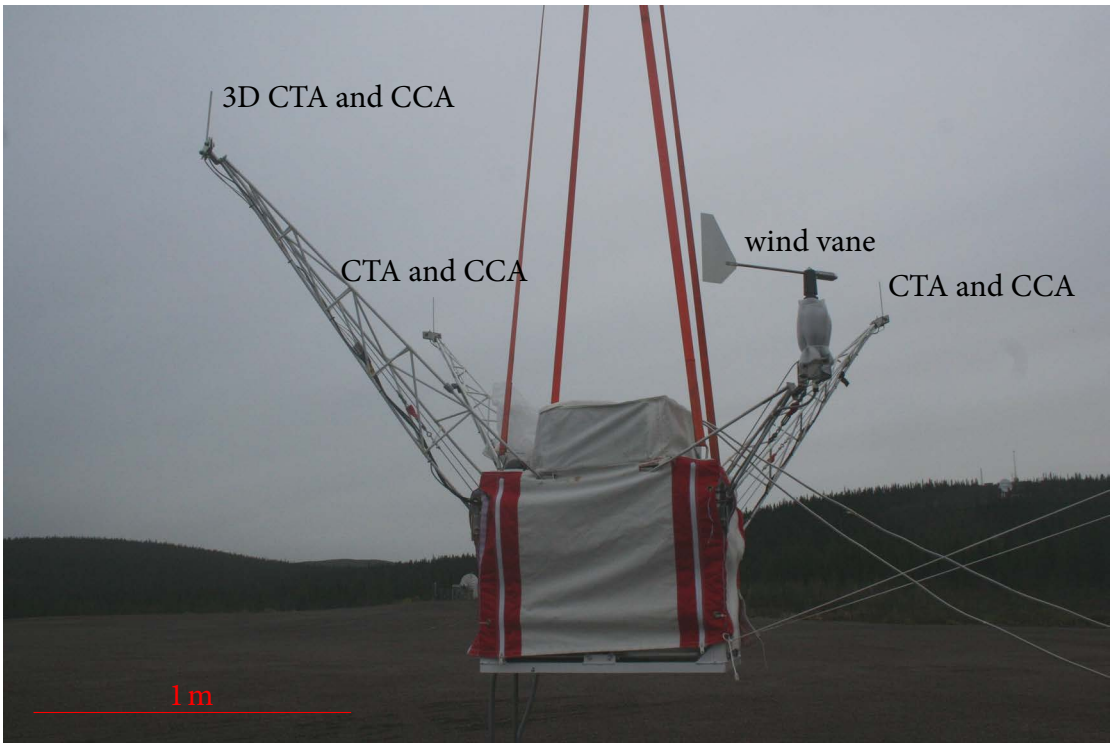

Figure 3.3: Photograph of the BEXUS 12 gondola just before launch on 27th September 2011

3.2.2 Gondola system for small payloads

The BEXUS campaigns have the disadvantage that place and time of the launch are fixed and cannot be influenced by the experimenter. Furthermore, the experiment has to go through a one year long review process similar to what is usual in space projects. Thus participating in BEXUS is laborious and inflexible. The launch of a large balloon outside of BEXUS would be very expensive. In order to get flexible flight opportunities, a small version of LITOS was developed which can be launched with a weather balloon from every radiosonde station. To date, several launches from Kühlungsborn (54° 07' N, 11° 46' E) and Sodankylä (67° 22' N, 26° 38' E) were performed.

In contrast to BEXUS, where infrastructure is provided, for the small payload everything has to be cared for by the experimenter. This includes balloon, parachute, packaging, and recovery system. For the latter, a GPS tracker (NAL Research 9601-DGS-LP) which transmits the position via Iridium satellite network is used. The tracker can be complemented with a radio beacon with frequency 150 MHz. All equipment is packed in styrofoam boxes to protect it during impact and to provide some thermal isolation. Details are given in the following subsections. Air traffic regulations limit the overall weight to be flown without complex licensing and safety procedures to 5 kg. After subtracting the mass of the recovery system, parachute, unwinders, etc., roughly 3 kg remain for the instrument itself. Taking into account Wheatstone bridges, data acquisition and batteries, the number of sensors is constrained to one or two.

First version: cubic payload

Initially (i. e. before the beginning of this work), the main experiment consisted of one CTA sensor with Wheatstone bridge, data acquisition (Reimesch Communications), separate housekeeping electronics with attitude sensors, and batteries; it was packed in a cubic styrofoam box of 35 cm width and 30 cm height. Figure 3.4 shows a photograph. A camera was included to give a visual impression of the attitude. The probe support sticks out on the top of the box. To orient the box such that the CTA is oriented towards the wind (cf. Section 3.1), a wind vane is attached to the gondola. The orientation is desired due to the sensor's directional change in sensitivity. Two 50 m unwinders provide distance to the balloon to be out of its wake. The tracking system is placed in a separate box directly below the balloon. The radiosonde hangs below the main instrument with another 30 m unwinder. The left side of Figure 3.5 shows a sketch of the flight train.

First flights yielded large gondola movements (see Section 3.3). Apart from prominent pendulum displacements, fast turns were observed. These could be reproduced in laboratory pendulum tests of the gondola on a 3 m cord: the payload makes sudden 180° turns in mid-movement while swinging back because a threshold velocity has to be exceeded for the wind vane to work. In order to prevent those movements, two additional large wind vanes were added (see photograph in Figure 3.6). In fact rotation and particularly quick turns were greatly reduced (see Section 3.3). However, due to the large area exposed to wind pendulum motions were still quite large. To further reduce the motions and because of wind tunnel results (see Section 3.4), a new payload form was designed.

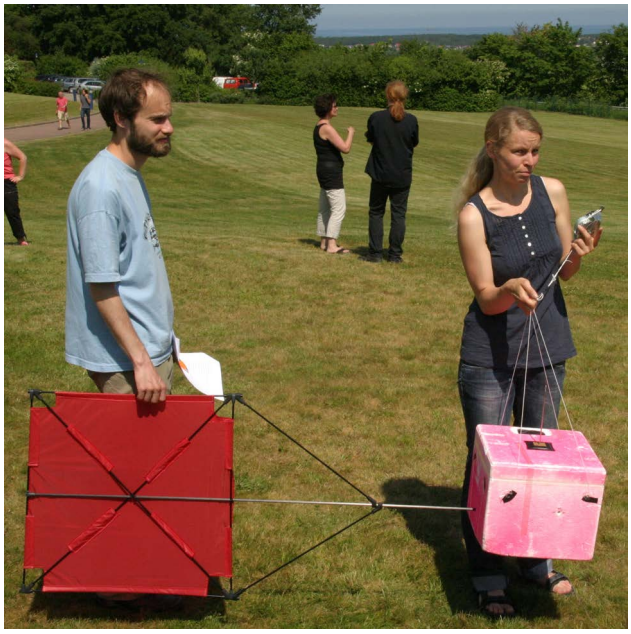

Figure 3.4: Photograph of the initial LITOS payload in a cubic box with one windvane, launched on 1st July 2010 from Kühlungsborn

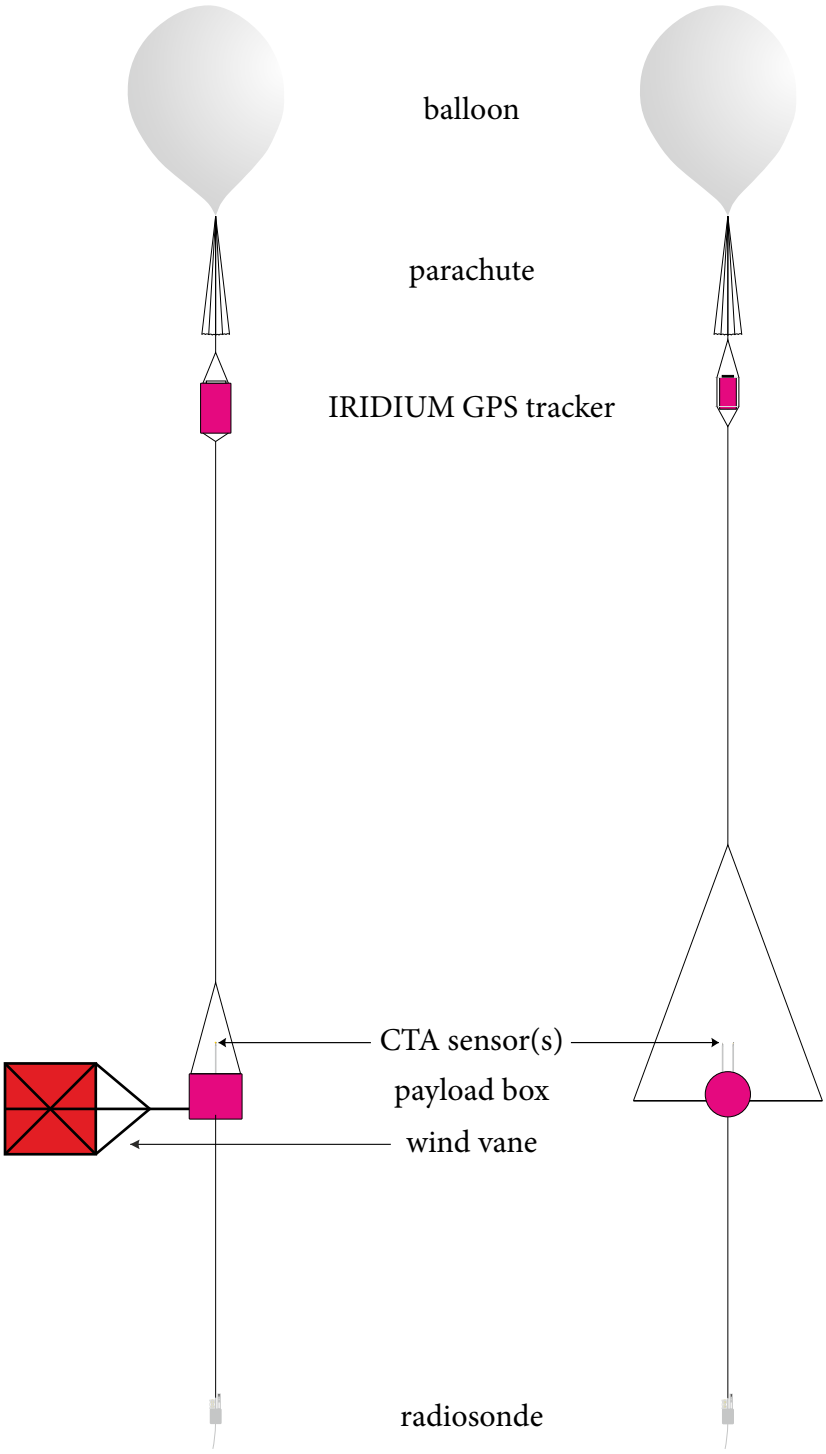

Figure 3.5: Flight train for the small payload. Left: first version with cubic box. Right: second version with spherical box.

Figure 3.6: Photograph of the LITOS payload with three large windvanes, launched on 25th February 2011 from Kühlungsborn

Second version: spherical payload

Due to the problems with the cubic payload mentioned above and the results from the wind tunnel experiments described in Section 3.4, it was proposed by the author to change the gondola to a spherical shape. The idea is to minimise the area exposed to wind. Later, simulations with a simplified model performed by Söder [2014] confirmed that this is the best approach. The integration of the components into the spherical styrofoam box was performed by Söder [2014]. To further suppress movements, Söder [2014] added rods sticking out of the gondola for the suspension to increase the lever arm. The right side of Figure 3.5 shows a drawing of the new design, Figure 3.7 a photograph. First flights confirm that gondola movements have decreased, see Section 3.3 for details.

Concurrently, a new data acquisition electronics has been developed in-house based on the student-developed board flown with BEXUS 12. It can sample two CTA/CCA simultaneously so that the number of sensors can be increased to 2 while respecting the weight limit and solving previous problems with the synchronisation of the data encountered at BEXUS. The electronic noise was reduced to ~1 mV which is similar to the noise level of the CTA Wheatstone bridge. Additionally, the board features a real time clock (RTC) to simplify merging the data with that of the radiosonde and a new attitude sensor (ADIS16407) which combines a three-axial gyroscope, a three-axial temperature-compensated accelerometer, a three-axial magnetometer and a pressure sensor in one chip.

Figure 3.7: Photograph of the spherical LITOS payload launched on 20th November 2014 from Kühlungsborn. The cubic styrofoam box is not part of the payload, but is used for handling on the ground.

3.3 Gondola movements

Gondola movements during flight are not restricted to slow pendulum motions, but also include large accelerations, e. g. due to wind forcing. Such a behaviour can be seen, e. g., on films from video cameras flown with the payload. Those motions induce spurious apparent winds and thus disturb the measurement. That problem had not been examined before this work. In order to estimate the impact, the attitude is to be reconstructed. That is a standard problem in avionics, where the Attitude Heading Reference System (AHRS) determines the orientation along the principal axes (see Figure 3.8). Basically, there are two alternatives: measuring the attitude with respect to an external reference (e. g. the Sun or the magnetic field) or an inertial measurement. The latter has the main problem that small errors accumulate [Wertz, 1978, Section 1.3]. Thus, typically data from several sensors are combined with a Kalman or similar filter [Wertz, 1978], although in principle the attitude can be reconstructed by integrating a rotation measurement.

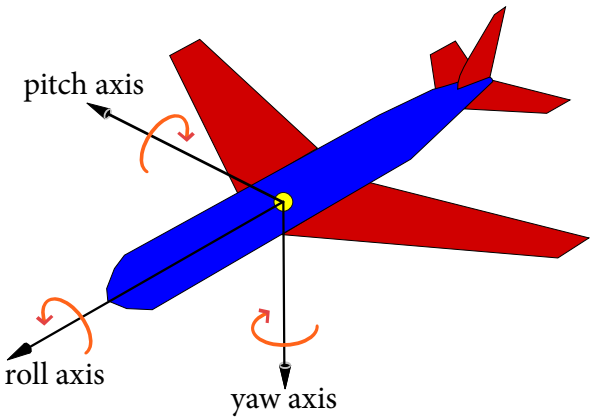

Figure 3.8: Aircraft principal axes. Image source: Wikipedia

In many low-cost environments, three-dimensional rotation, acceleration and magnetometer sensors are used [e. g. Kraft, 2002, Claussen, 2008]. The estimation from the gyroscope is corrected by the measurements of the other sensors. Specifically, the acceleration sensor is assumed to measure mainly gravity and thus used to correct the roll and pitch angles but provides no information on the yaw angle. Similarly, the magnetic field direction provides information on the yaw angle but not on the roll angle.

On the LITOS payload, rotation, acceleration and magnetometer sensors have been included (cf. Section 3.2). A temperature-induced drift of the measured acceleration in the first version of the sensor (ADIS16350) and possible tilted mounting are corrected. To reconstruct the gondola attitude, the algorithm developed by Claussen [2008] has been chosen for its simplicity. Expected movements are mainly pendulum motions, thus displacement and azimuth angles as defined in Figure 3.9 are computed. The gyroscope is specified with a noise of $0.6\,^\circ\,\mathrm{s}^{-1}$ RMS, so the accuracy of the attitude is expected to be 1° to 2° at best. The error is difficult to quantify because the algorithm has complex inherent dynamics. To test the method, the data acquisition box was put in known attitudes in the laboratory and additionally exposed to pendulum motions using a 3 m string and known initial displace-

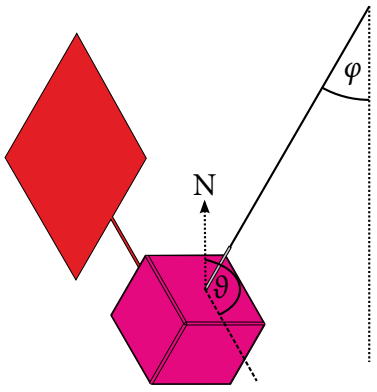

Figure 3.9: Definition of the displacement angle φ and the azimuth angle ϑ

ments. The known attitudes were reproduced with the expected accuracy given above, and the oscillation period differed by ~0.1 s to the theoretical one[1] of 3.5 s and to the measurement with a stop watch for 10 periods. The details are given in Appendix C.

As described in the previous section, there are four types of gondolas: the large payload (BEXUS) and three shapes of the small payload (cubic with one wind vane, cubic with three wind vanes, and spherical). For each type a representative flight has been selected. For these four flights the displacement angle φ and the azimuthal angular velocity $\dot{\vartheta}$ are plotted in Figures 3.10, 3.11, 3.12 and 3.13, respectively.

For the heavy BEXUS payload, the displacement angle is in the order of the accuracy of the attitude measurement, i. e. it hung "like a stone" without significant pendulum motions (Figure 3.10, left panel). Concurrently the gondola slowly rotated around the yaw axis (middle panel) with an angular velocity typically below 4.5 ° s^{-1} (right panel), i. e. a 360° turn lasts ≥ 80 s. As can be seen in the middle panel, there was no preferred direction. These slow movements take place on much larger time scales than the CTA and CCA measurement which they are thus assumed not to affect.

In contrast, the first version of the small payload made large pendulum motions reaching dis-

1 assuming a mathematical pendulum with small displacements, i. e. $T = 2\pi\sqrt{\frac{l}{g}}$, where l is the length of the cord and g the acceleration of gravity

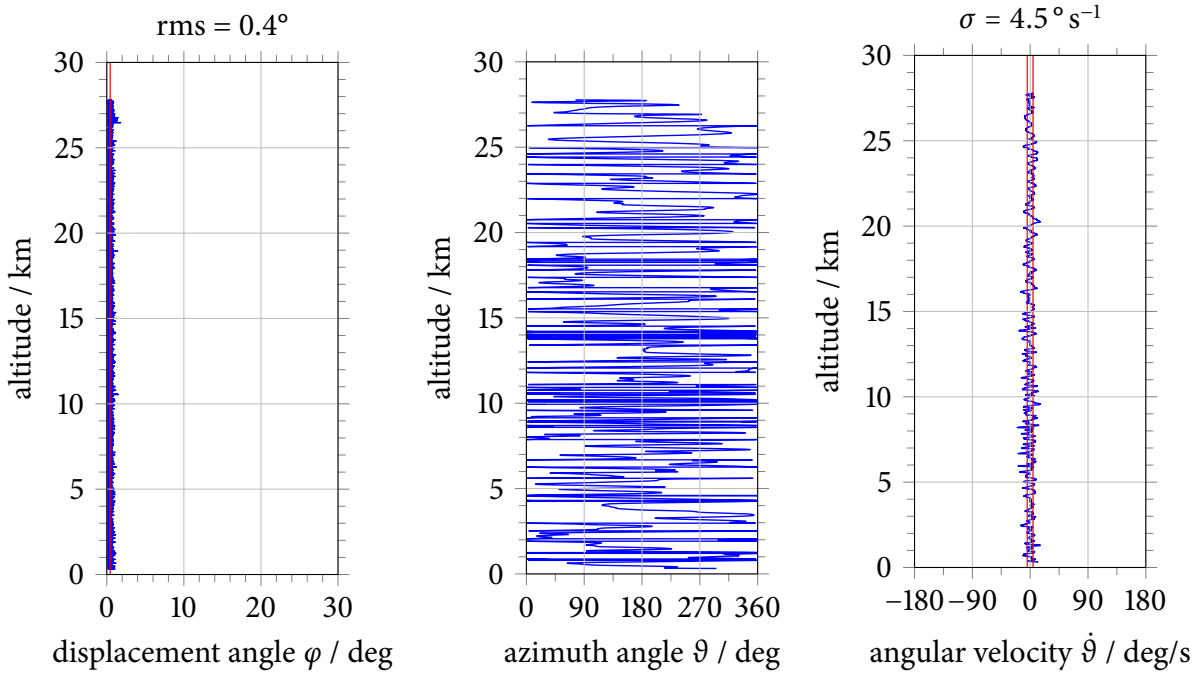

Figure 3.10: Attitude for the BEXUS 8 flight launched at Kiruna at 10th November 2009. Left: displacement angle (blue) and rms (red). Centre: azimuth angle. Right: rotation around the azimuth axis (blue) and mean plus/minus one standard deviation (red).

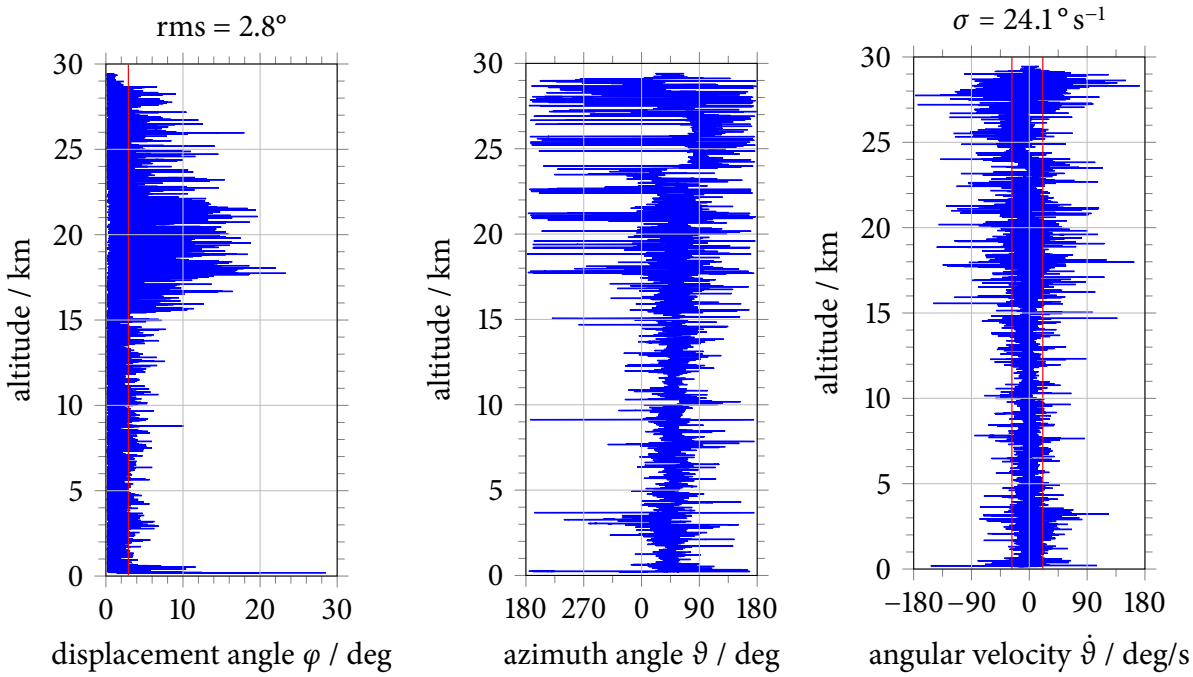

Figure 3.11: Same as Figure 3.10, but for the cubic payload with one windvane launched at Sodankylä at 5th August 2010.

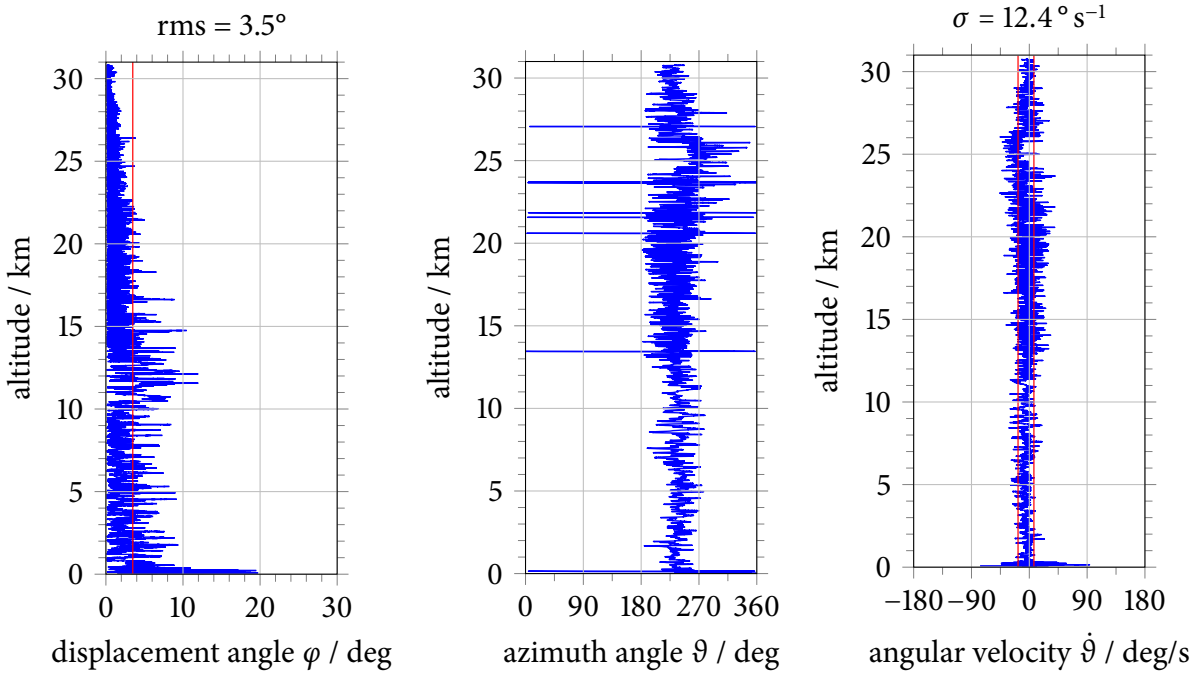

Figure 3.12: Same as Figure 3.10, but for the cubic payload with three large windvanes launched at Kühlungsborn at 25th February 2011.

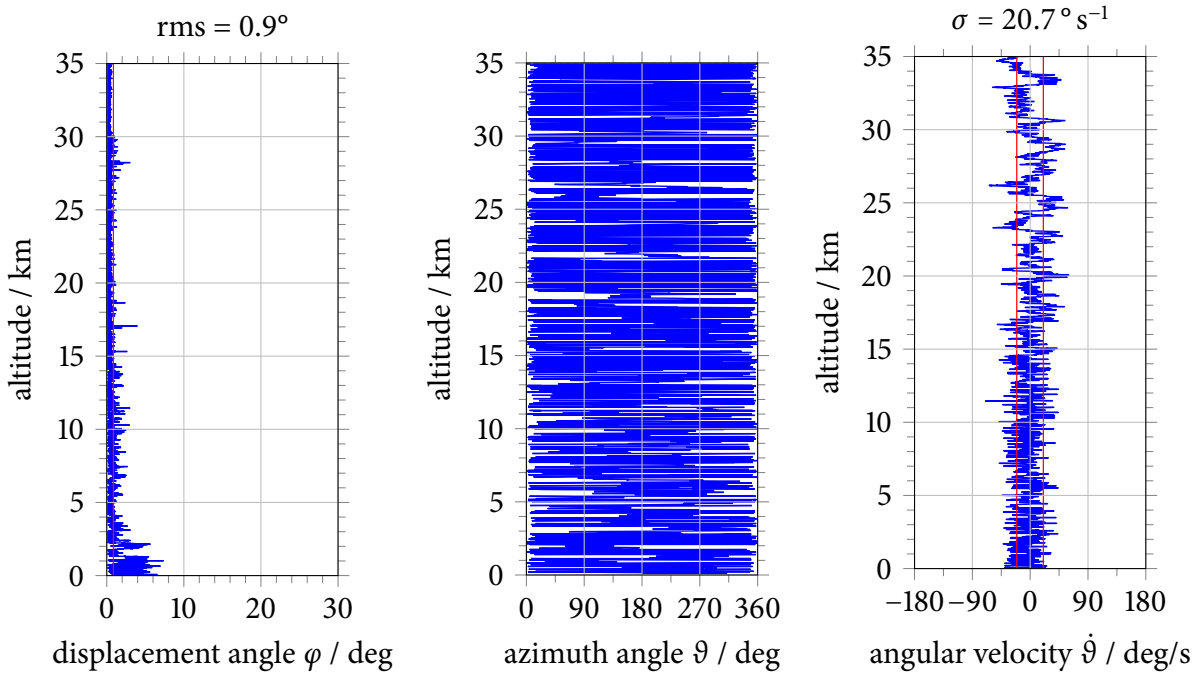

Figure 3.13: Same as Figure 3.10, but for the spherical payload launched at Kühlungsborn at 20th November 2014.

placements of up to ~20° (Figure 3.11, left panel). Additionally, some fast turns in azimuth angle were observed (centre panel), featuring large angular velocities (right panel). These are explained as follows: When the gondola swings back in pendulum motion, the wind vane turns it 180°. But due to the velocity threshold needed for the wind vane to work, that does not happen at the extrema but in mid-movement, i. e. at first the gondola moves with the wind vane at front. Such motions have been reproduced in laboratory tests with the payload hanging on a 3 m cord. Thus the single wind vane does not have the desired effect, but introduces additional problems. When zooming in (see Figure 3.14) it can be seen that the movements of the payload were quite quick which comes along with large accelerations. These induce apparent wind fluctuations which disturb the CTA measurement. Only limited sections of the sounding are usable, and any semi-automatic evaluation of the data is prohibited.

The next approach was to prevent quick movements by greatly increasing the area exposed to wind in order to use its breaking effect. In fact, the large wind vanes effectively prevented rotation: the rms of $\dot{\vartheta}$ is halved in comparison to the gondola with one wind vane (see Figure 3.12, centre and right panels). Moreover, there were less pendulum motions with less amplitude, and they were less quickly (right panel, see also Figure 3.14). Due to the lower acceleration, the data is disturbed less, even though the rms of the displacement angle φ is larger. Apart from the still relatively large pendulum angles, the payload with the large wind vanes is bulky and difficult to handle.

The new spherical payload was designed to behave as similar to the heavy BEXUS payload

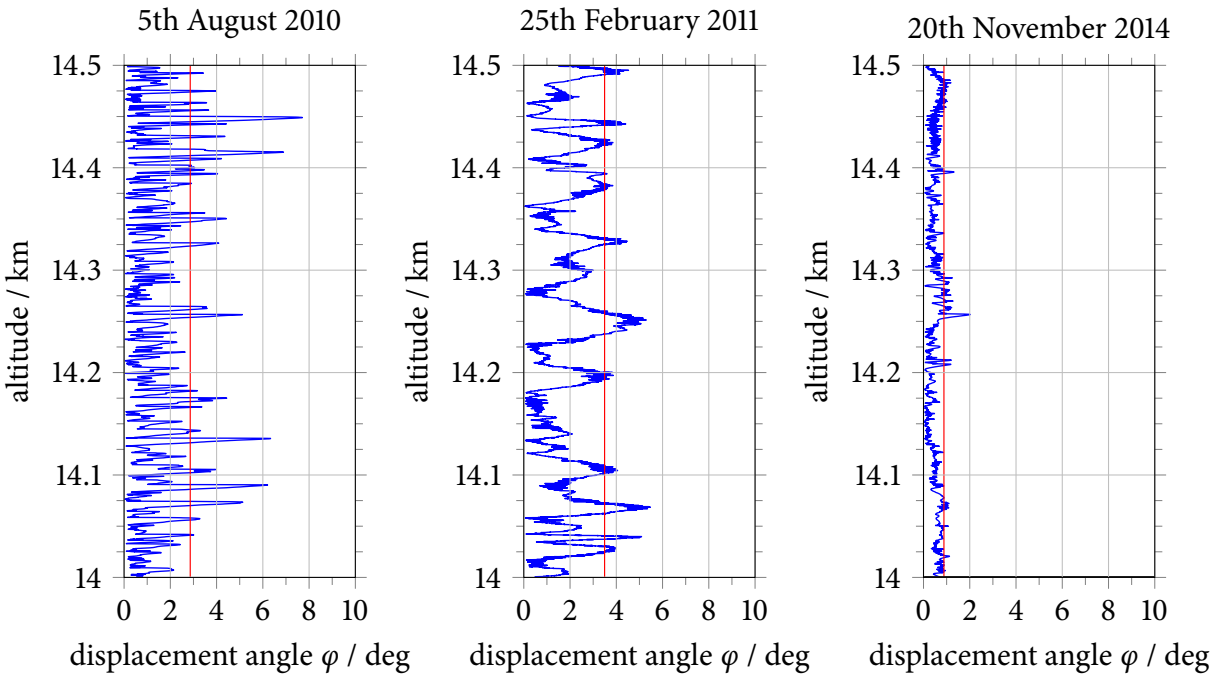

Figure 3.14: Detailed plot for the displacement angle for flights with different small gondolas. Left: cubic payload with one wind vane. Centre: cubic payload with three large wind vanes. Right: spherical payload. The red vertical line in each panel shows the rms (over the whole flight).

as possible, i. e. the ratio between the area cross-section and weight was reduced as much as possible. Furthermore, the suspension was changed by Söder [2014] to rods sticking out of the gondola to increase the lever arm. As can be seen in Figure 3.13 (left panel), that resulted in much less pendulum motions, which are similar to BEXUS and in the order of the accuracy of the measurement, after initial movements induced by the launch procedure have subsided. The huge improvement compared to the cubic shape is particularly visible in the detailed plot in Figure 3.14. As a drawback rotation has greatly increased (centre panel of Figure 3.13); it is much faster than for BEXUS due to the much lower inertia of the small gondola. On the other hand, the movement is smooth without large accelerations (right panel) because the form has no preferred direction; thus the disturbance of the measurement is small. The spherical form gave the best data from a small payload so far.

To compare the behaviour of the different gondolas quantitatively, the root mean square (rms) has been computed for the displacement angle and the standard deviation for the azimuth angular velocity. Those two quantities are presented in Figure 3.15. The BEXUS platform with its large weight has the best performance, both for pendulum motions (rms = 0.4°) and rotation ($\sigma = 4.5\,^\circ\,\mathrm{s}^{-1}$). For the small payload, the first version has the worst performance with large pendulum motions with rms = 2.8° and fast rotation ($\sigma = 24.1\,^\circ\,\mathrm{s}^{-1}$). The new spherical form with its higher weight to area ratio is a tremendous improvement with pendulum motions with rms = 0.9°, i. e. only slightly inferior to BEXUS. The rotation with $\sigma = 20.7\,^\circ\,\mathrm{s}^{-1}$ is also lower than

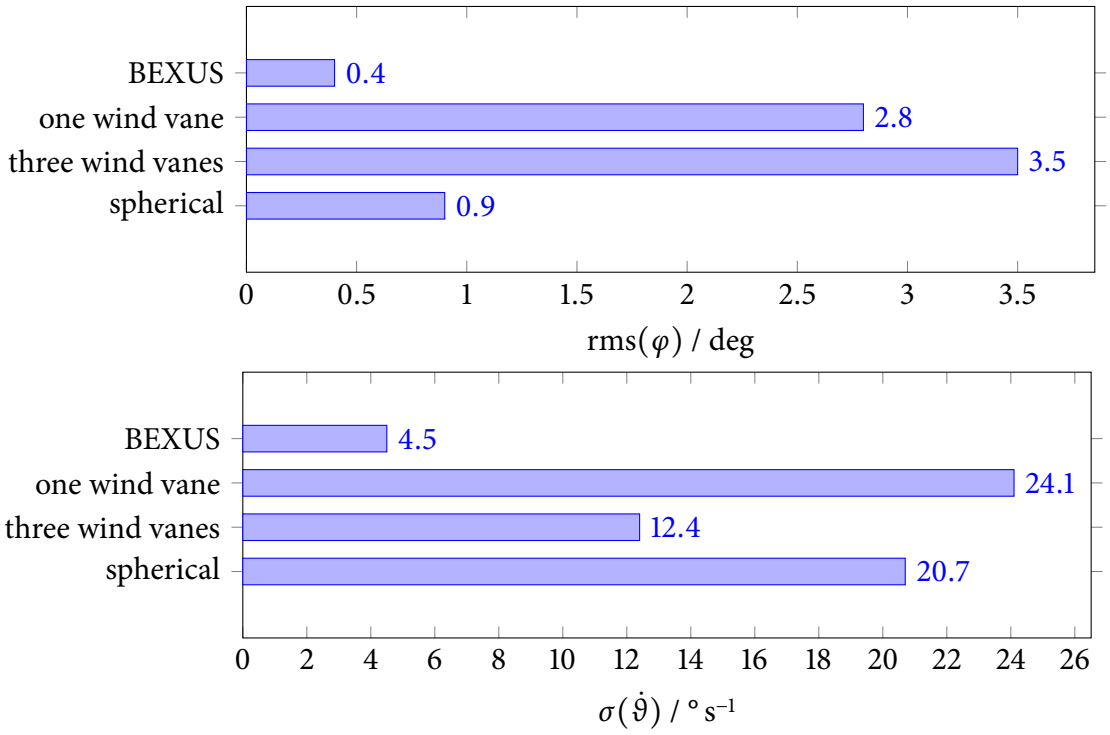

Figure 3.15: Comparison of the movements of the different types of gondolas. Top: rms of the displacement angle φ. Bottom: standard deviation of the azimuth angular velocity $\sigma(\dot{\vartheta})$.

for the first version, but still significantly larger than for BEXUS. The best azimuth orientation is observed for the payload with large wind vanes, where the absolute orientation mostly remains within a band of ~ 90°. The angular velocities with $\sigma = 12.4\,°\,s^{-1}$ are higher than for BEXUS, but still lowest for the small payload. However, it is bulky and difficult to handle. It should also be kept in mind that the smoothness of the motions is very important, but is not covered by the parameters rms and σ.

Summarising, the new spherical shape of the payload results in a vast reduction of spurious motions of the gondola; especially large accelerations were reduced. For that reason data quality has significantly improved.

3.4 Wind tunnel experiments

The turbulence measurement can also be disturbed by the modification of the geophysical flow by the gondola itself. For example, turbulence can be generated when air flows over the edge of the box. Such effects on LITOS had not been examined before this work. In order to check the influence of the gondola system on the measurement, wind tunnel experiments were performed at the facilities of the Chair of Fluid Dynamics at the University of Rostock (LSM) in March 2011.

To this end, a 1:3 model of the gondola at that time (i. e. the cubic form with one wind vane) was built from aluminium, yet a real CTA sensor was placed at the scale location to enable a real measurement (cf. photographs in Figure 3.16). The model was exposed to a laminar flow with constant velocity, and the flow was examined for several gondola attitudes.

For a qualitative view, the flow was made visible with smoke. For this experiment the wind tunnel was operated at $1\,\mathrm{m\,s^{-1}}$. This corresponds to a Reynolds number of ~6500, i. e. typical conditions at ~20 km altitude. Larger wind velocities (representative of conditions, e. g., near

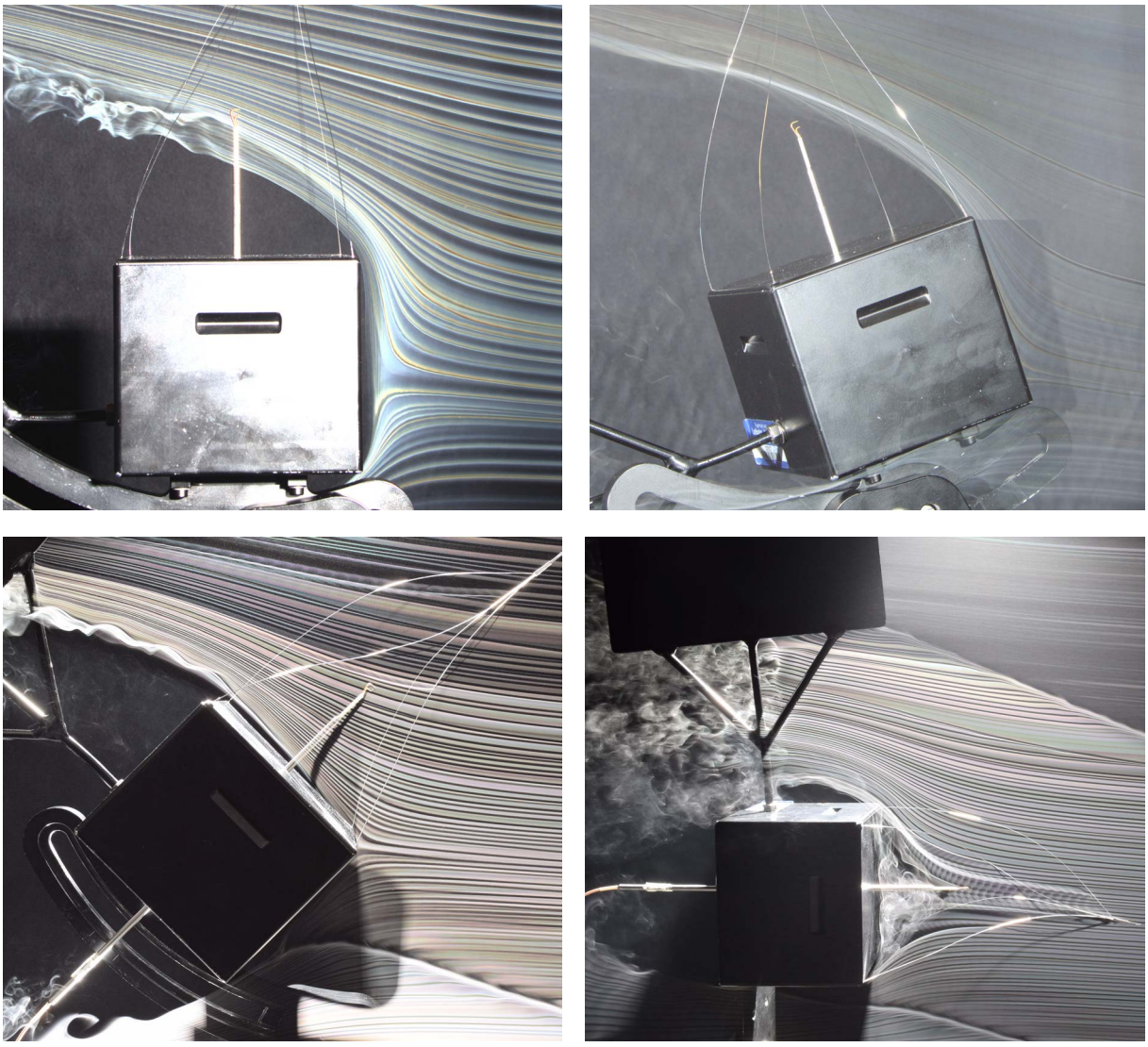

Figure 3.16: Streamline photographs of the Reynolds-scaled model of the cubic LITOS payload with pitch angles of 0° (top left), 15° (top right), −45° (bottom left) and −90° (bottom right). Roll and yaw angles are 0°. The laminar flow velocity was $1\,\mathrm{m\,s^{-1}}$, which corresponds to a Reynolds number of ~6500, i. e. typical conditions at ~20 km altitude.

ground) have not been realised because too large velocities dissipate the smoke (i. e. the streamlines are no more visible). Figure 3.16 shows photographs for pitch angles of 0°, 15°, −45° and −90°. Roll and yaw angles are 0°. The photographs show that the streamlines are bent by the cube. If the pitch angle is larger than ~15°, the CTA can either measure turbulence induced by the flow over the edge of the gondola or air shadowed by the edge (top right panel), and thus not the atmospheric flow. If the pitch angle approaches −90°, the sensor is in the stagnation area of the cube (bottom right panel).

Of particular interest is the wire response. As a worst case estimate, an experiment was conducted to quantify for which angles of attack gondola-induced turbulence from flow over the edge is observed. The model was tilted around the pitch and roll axes in 5° steps between −5° and 45° for yaw angles of 0°, 20°, and 45°. For each position a 10 s time series of the CTA voltage was recorded with a sampling rate of 30 kHz using a Wheatstone bridge and A/D converter system provided by LSM. The wind tunnel was operated at 6 m s^{-1} which corresponds to 2 m s^{-1} for the real gondola near ground; that is in the order of a typical horizontal apparent wind during flight.

As an estimation of the intensity of turbulence, the mean of the power spectral density between 90 Hz and 300 Hz is plotted colour-coded in dependence of pitch and roll angle for yaw angles of 0° and 45° in Figure 3.17. It is quite low for angles less than ~20° (laminar flow on the wire) and strongly increases for larger angles (flow over the edge of the box).

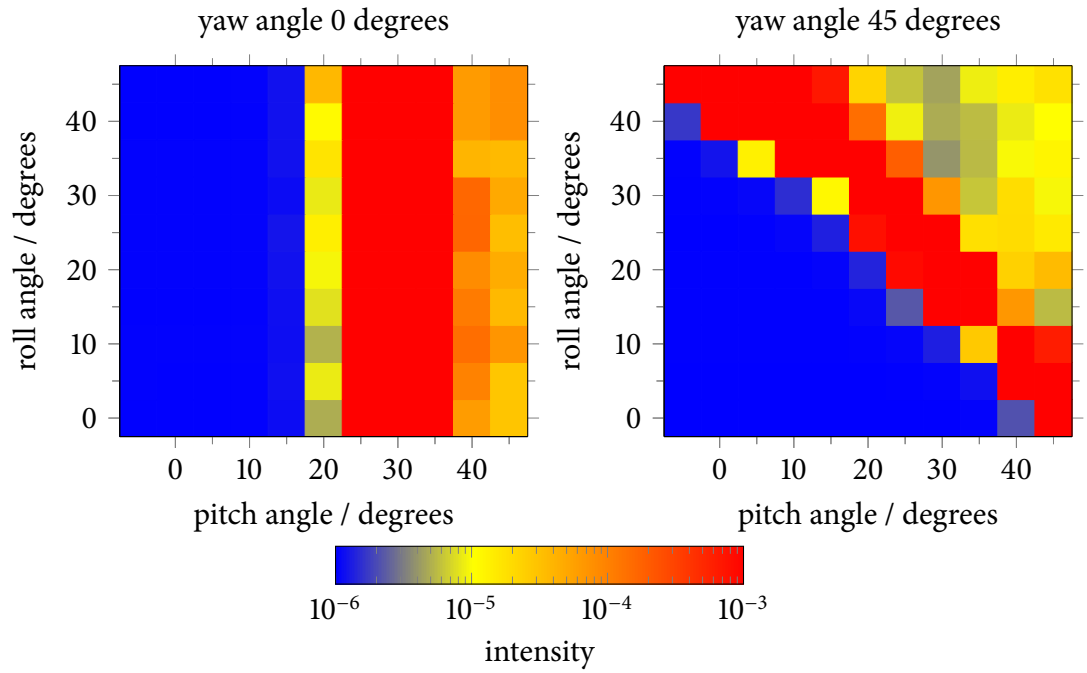

Figure 3.17: Mean of the power spectral density between 90 Hz and 300 Hz as a measure of the intensity of turbulence in dependence of the pitch and roll angle for a yaw angle of 0° (left) and 45° (right) of the gondola model.

During flight the flow has a typical angle of attack of ~−80° (5 m s^{-1} ascent rate, ~1 m s^{-1} wind shear) (not shown in Figure 3.17). That means normally the flow is not affected by the gondola. Nevertheless, during large pendulum motions as described in the previous section, disturbances cannot be excluded. As a consequence, the payload form was changed in order to affect the flow less. Since during flight the angle of attack cannot be controlled, a spherical form has been chosen because it has no preferred direction.

To enable a direct comparison of both shapes, the streamlines have been visualised for the new payload form, too. Figure 3.18 shows photographs for the same angles of attack as Figure 3.16 depicts for the cubic payload (excluding −90°). For the new shape the streamlines are bent less and are closer to the body; the flow is affected much less. Especially, while for the cubic form it is strongly dependent on the angle of attack whether the measurement is disturbed by the gondola or not, the spherical form does not have such a dependence. Therefore the spherical shape is preferred over the cubic one.

As shown in Section 3.3, the payload shape without edges and wind vanes results in calmer flight. That means that the performance of the new spherical payload is best for both attitude and possible modification of the geophysical flow. Turbulence data from the spherical payload is shown in Section 5.4.

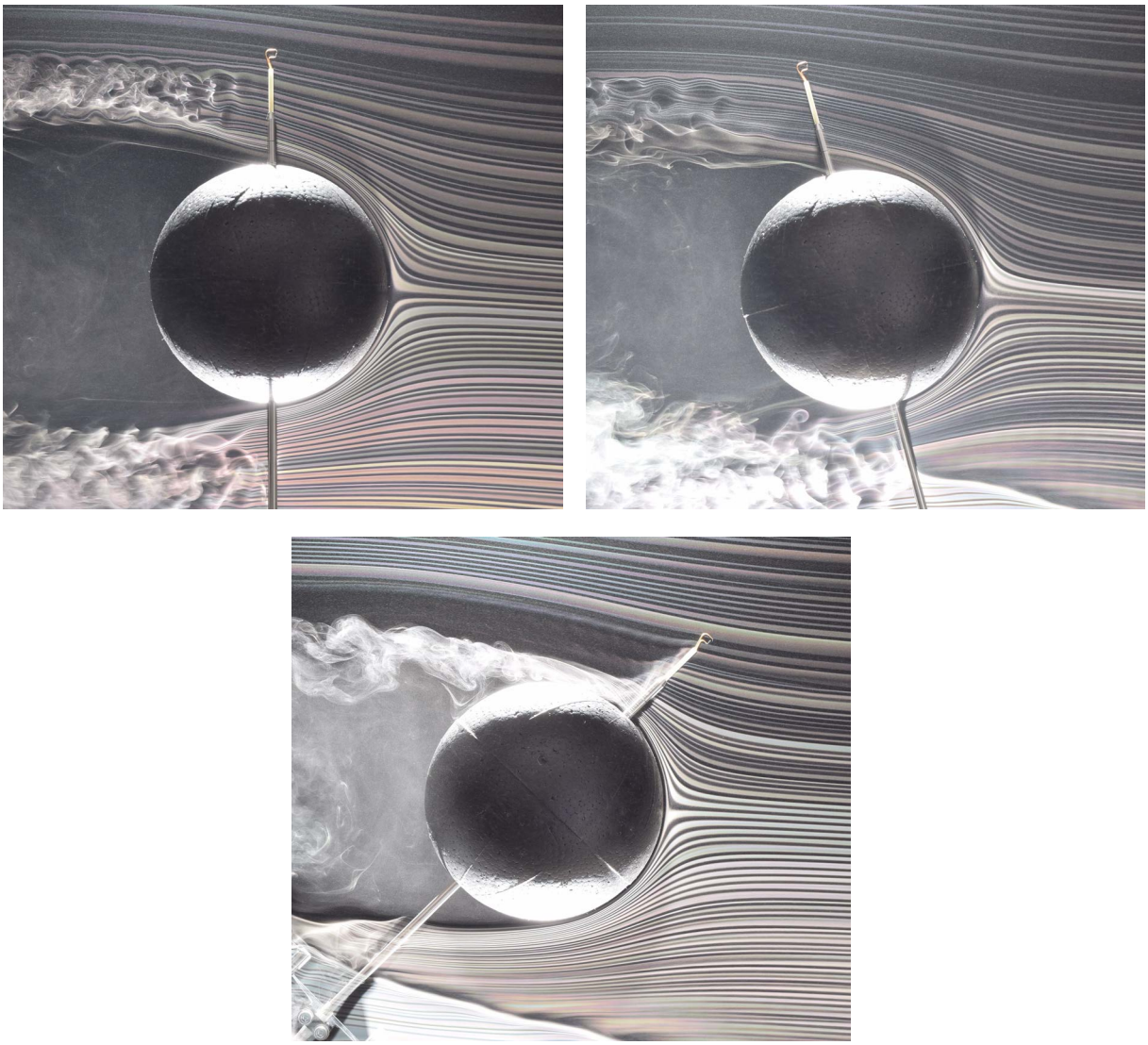

Figure 3.18: Streamline photographs of the Reynolds-scaled model of the spherical LITOS payload with pitch angles of 0° (top left), 15° (top right), and −45° (bottom). The laminar flow velocity was 1 m s^{-1}.

4 Data analysis technique

In this chapter it is specified how the geophysical parameters interpreted in the next chapter are obtained from the raw data measured by the instrument described in the last chapter. Particularly, the energy dissipation rate ε is of interest. The method to derive ε from wind or temperature fluctuations with spectral analysis is detailed in Section 4.1, and errors are analysed. Furthermore, in Section 4.2 a method used in the literature to infer energy dissipation rates from standard radiosondes is outlined. The results from both methods are compared in Chapter 5. Section 4.3 briefly describes the setup for model simulations used for the interpretation of the geophysical background during the BEXUS 8 and BEXUS 12 flights.

4.1 Determination of the energy dissipation rate with spectral analysis

As mentioned at the beginning of Section 2.3 on page 10, a direct computation of ε with definition (2.15) is not feasible, because it contains the derivatives of the velocity which has to be computed at the Kolmogorov microscale where the atmospheric fluctuations are below the instrumental noise level. Therefore an indirect method with spectral analysis is used.

The temporal spectrum (2.20) is the Fourier transform of the autocorrelation function (2.19) of velocity or temperature fluctuations with respect to the time variable. Thus (in view of the Wiener-Khinchin theorem) it is the power spectral density (PSD) of the velocity or temperature fluctuations. Therefore, the spectrum W in the form given in (2.27) or (2.28) can be fitted to the power spectrum of measured wind or temperature fluctuations, respectively. To this end, the inner scale of turbulence needs to be resolved. LITOS is designed to perform that for typical stratospheric conditions.

As noted in Section 3.1, LITOS does not measure absolute velocities, because the calibration of the CTA sensor for all possible ambient conditions in the troposphere and stratosphere is not feasible. However, the effect of the calibration on the PSD is mainly a scaling of the absolute value, but the derivation of the energy dissipation rate does not depend on the absolute value of the PSD, only on identifying the position of the bend between inertial and viscous subrange. Thus an additional multiplicative fit parameter which covers the unknown calibration is introduced for velocity fluctuations. Theuerkauf [2012, Appendix C] examined the impact of CTA sensor sensitivity on the PSD and found it negligible.

For temperature fluctuation, no such problem arises because the calibration of the CCA sensor does not depend on pressure or wind velocity. The thermometer voltage is converted to temper-

ature prior to data analysis. This step is important to obtain reasonable values of the thermal dissipation rate χ from the fit, because χ crucially depends on the absolute value of the PSD.

There are different possibilities to obtain the power spectrum from the measurements. On the one hand, after the choice of a suitable window, the periodogram $\hat{W}$ as an estimation of the power spectrum can be computed directly with Fourier methods. The periodogram is called an estimation of the true PSD because only one realisation of a stochastic process is observed. Details are given in Section 4.1.1. On the other hand, power spectral densities can also be computed with wavelets [e. g. Torrence and Compo, 1998]. Section 4.1.3 covers this topic. For the evaluation in Chapter 5, the Fourier method is used because the noise level detection is more stable.

4.1.1 Spectral analysis using Fourier technique

Figure 4.1 shows an example of wind and temperature fluctuations from the BEXUS 8 flight. Large-scale motions have been removed by subtracting a spline. Large fluctuations, e. g. between ~16 086 m and 16 152 m, represent turbulence. The small amplitudes of ~2 mV or ~0.1 K, respectively, e. g. from 16.06 to 16.08 km, are due to instrumental noise and correspond to a calm region. Theuerkauf [2012, Section 4.2] used the magnitude of the fluctuations to identify turbulent regions and inferred statistics of layer thickness and distance.

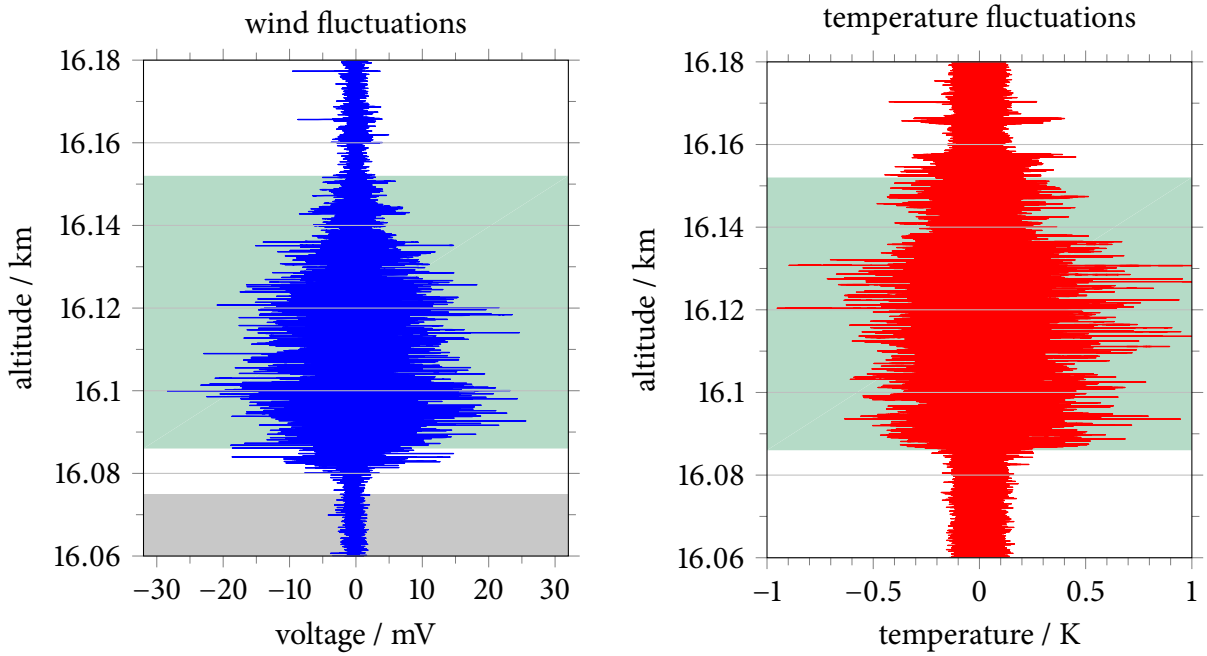

Figure 4.1: Example of measured wind (left) and temperature (right) fluctuations from the BEXUS 8 flight. An amplitude of $\lesssim 2$ mV or 0.1 K, respectively, corresponds to instrumental noise. The green shading marks turbulent regions for which the power spectral density is shown in Figure 4.2. The grey shading marks the non-turbulent region for which the spectrum is shown in Figure 4.4. The vertical knot distance of the smoothing spline subtracted to extract the fluctuations is 0.1 m.

For the turbulent layer from 16 086 m to 16 152 m (shaded green in Figure 4.1) the periodogram $\hat{W}$ is computed with a von Hann window after the removal of a linear trend. Please note that the detrending is different than the spline removal shown in the raw data plot in Figure 4.1. The resulting PSD is smoothed with a (linear) running average over 31 data points. The averaging reduces the uncertainty in the power spectrum estimate [DelSole and Tippett, 2014]. The resulting spectra are shown in Figure 4.2 (blue and red curves in the top and bottom panels, respectively). The grey dotted lines mark the 95 % confidence levels computed as described by DelSole and Tippett [2014]. A $-5/3$ slope describing an inertial regime and the transition to the viscous subrange with -7 slope are identified. The -7 slope is not reached due to noise and the smoothing procedure, as can be seen with artificial spectra (cf. the description of artificial spectra at the end of Section 4.1.2). However, it is only important to locate the kink in order to determine l_0. The part at spatial scales smaller than $\sim 10^{-2}$ m with approximately constant PSD corresponds to the instrumental noise level. As the transition between inertial and viscous subrange is resolved, the turbulence model (2.27) or (2.28), respectively, can be fitted to the data. Prior to fitting, the instrumental noise level has to be detected and the fitting range adapted accordingly. The PSD value of the noise level (green horizontal line in Figure 4.2) is estimated from the median of the PSD between a third of the sampling frequency, $f_s/3$, and the Nyquist frequency, $f_s/2$. This high-frequency part of the spectrum typically shows instrumental noise only. The median is robust to potential disturbances in form of spikes. The small-scale end of the fit range is then chosen as the spatial scale where the PSD first falls below the noise level (starting from large scales), because aside from small-scale fluctuations the PSD typically decreases with increasing frequency until the noise level is reached. The large-scale fit limit is set arbitrarily to 2 m spatial scale; this is well within the inertial range even for very small dissipation rates. The noise level is subtracted from the periodogram before fitting. PSD values that are below the noise level (i. e. negative after noise level subtraction) are omitted. In Figure 4.2 the fit curve has an apparent positive curvature (i. e. it "bends" towards higher PSD values) at the small-scale end (particularly visible in the top panel). This is due to the added constant offset of the noise level to the fit function prior to plotting. To show that this artefact of the depiction is not present in the fit, the velocity spectrum from Figure 4.2 (top panel) is displayed with subtracted noise level in Figure 4.3, i. e. as used for performing the fit. Therein the fit function always has negative curvature.

The fit is performed with logarithmic data. Let $W_{l_0,\chi}$ denote the theoretical spectrum (2.27) or (2.28), which depends on frequency $\omega = 2\pi f$ and the parameter l_0 and χ. Please remember that for velocity fluctuations an additional multiplicative factor is added to (2.27) to care for the unknown calibration. For simplicity, this constant is also called χ in this section, but has no physical meaning—in contrast to χ from temperature fluctuations which denotes the thermal dissipation rate. The fit parameter $(a, b) := (\log l_0, \log \chi)$ are obtained by fitting the function $x \mapsto \bar{W}_{a,b}(x) := \log W_{10^a,10^b}(10^x)$ to the measured data $(x, y) = (\log 2\pi f, \log \hat{W})$, where f denotes frequency and log the logarithm to the base 10. To this end, the standard χ^2 measure

$$\sum_{i=1}^{N} \frac{(\log \hat{W}_i - \log \bar{W}_{\log l_0,\log \chi}(10^{\log f_i}))^2}{\sigma_i^2} \tag{4.1}$$

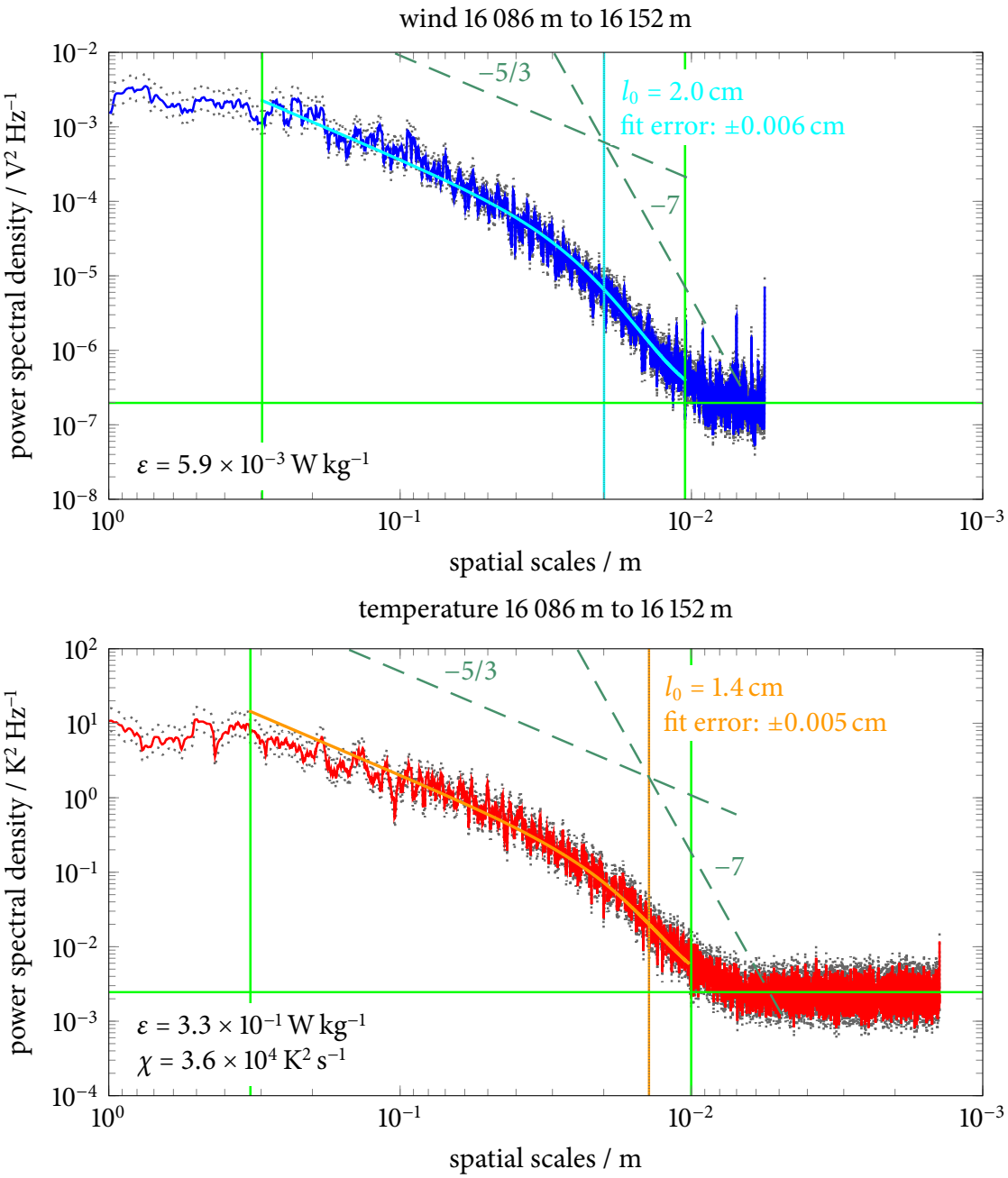

Figure 4.2: Example of spectrum and fit for the determination of the dissipation rate for velocity (top) and temperature (bottom) fluctuations. The blue and red curves, respectively, show the measurements, the grey dotted lines the 95 % confidence interval. The cyan and orange curves show the fits of the Heisenberg model to the measured spectra, the vertical lines of the same colour indicate the inner scale l_0. The green dashed lines visualise slopes of −5/3 and −7 to guide the eye. The light green horizontal and vertical lines show the detected noise level and the fit limits, respectively.

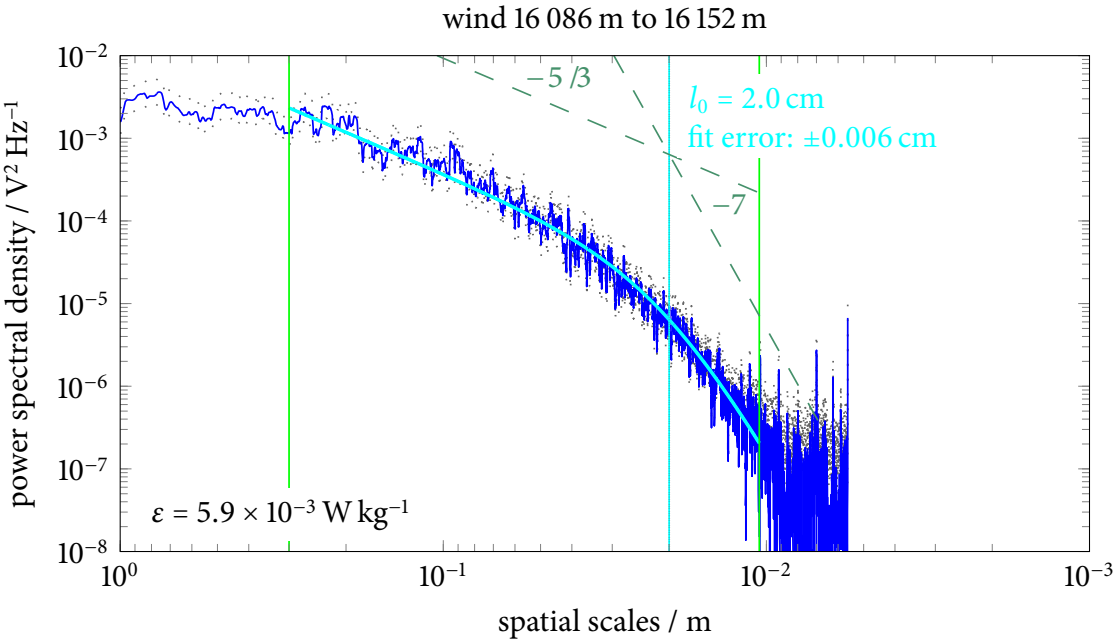

Figure 4.3: Example of the spectrum of velocity fluctuations from Figure 4.2, top panel with noise level subtracted, i. e. as used for performing the fit. Curves and lines as in Figure 4.2.

[James and Winkler, 2004; Eadie et al., 1971, Section 8.4] is minimised with CERN's MINUIT software, where $\hat{W}_i$ is the observed periodogram at frequency f_i, σ_i the standard deviation of the measurement $\log \hat{W}_i$, and N the number of data points in the spectrum. The measurement error σ_i is dealt with in the next section. The symbol χ^2 should not be confused with the thermal dissipation rate χ. The fit result for the examples is shown in Figure 4.3 as cyan curve and in Figure 4.2 in the top and bottom panel as cyan and orange curve, respectively.

In the example, the resultant dissipation rates from wind and temperature fluctuations disagree by roughly a factor of 55. This is more than the uncertainty of the ε determination which is roughly a factor of 4 (see next subsection). The relation between ε values obtained from wind and temperature measurements is discussed in Section 5.3.

The procedure contains several improvements compared to that used by Theuerkauf [2012]. The methods to detect the noise level and choose the fit range were modified. The fit algorithm used by Theuerkauf [2012] (MATLAB's lsqcurvefit function which minimises a different quantity than MINUIT) does not return a fit error and does not depend on the input error, thus it was replaced. Additionally to the new features, the performance of the fit is better.

In order to obtain an altitude profile of energy dissipation, a sliding window of 5 m altitude with 50 % overlap is used, i. e. the resulting profile has a vertical resolution of 2.5 m. For each window, the periodogram is computed with a Hann window after the removal of a linear trend, the spectrum is smoothed and the fit of the turbulence model is performed as described above. Then a set of criteria is applied to sort out non-turbulent spectra which manifest as bad fits. An

example of a non-turbulent spectrum (from the calm region shaded grey in Figure 4.1) is shown in Figure 4.4. The criteria are:

(a) The noise level estimation fails.

(b) The inner scale l_0 is outside the fit range.

(c) ε has an implausible value ($\varepsilon < 0$ or $\varepsilon > 100\,\mathrm{W\,kg^{-1}}$).

(d) The mean logarithmic absolute difference between fit and data is larger than a threshold of 0.4.

(e) l_0 is larger than a threshold of a 25th of the window length. For such large inner scales the fit is dominated by too few data points. This kind of criterion describes a technical minimum and was introduced by Söder [2014, Section 4.2].

The criteria are extended compared to those used by Theuerkauf [2012]. For spectra that are sorted out, ε is set to zero. Figure 4.5 depicts a part of the ε profile from velocity fluctuations of the BEXUS 8 flight. The shading marks the layer that is shown in Figures 4.1, 4.2, and 4.3.

Oboukhov [1962] and Kolmogorov [1962] hypothesised that dissipation rates follow a lognormal distribution. This supposition was later derived more rigorously by Gurvich and Yaglom [1967] by using Kolmogorov's breakage theory [Kolmogorov, 1941b] and introducing a scale-similarity law for ε. Basically, the volume averages $\bar{\varepsilon}_j$ in a nested set of volumes V_j with $V_{j+1} \subset V_j$

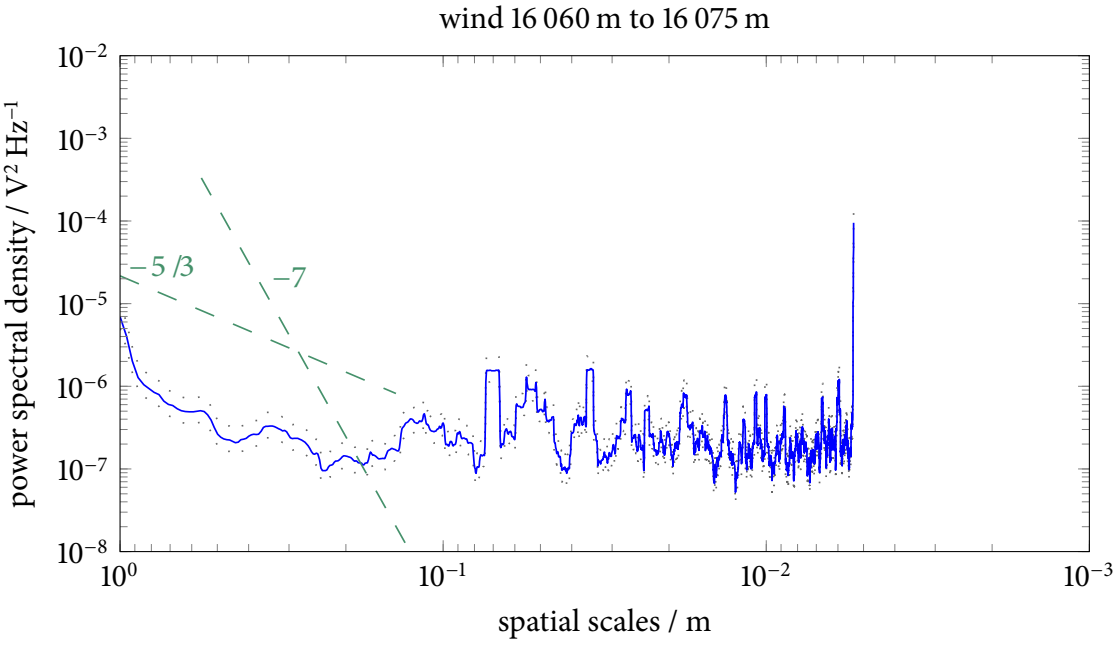

Figure 4.4: Example of a spectrum of a non-turbulent region

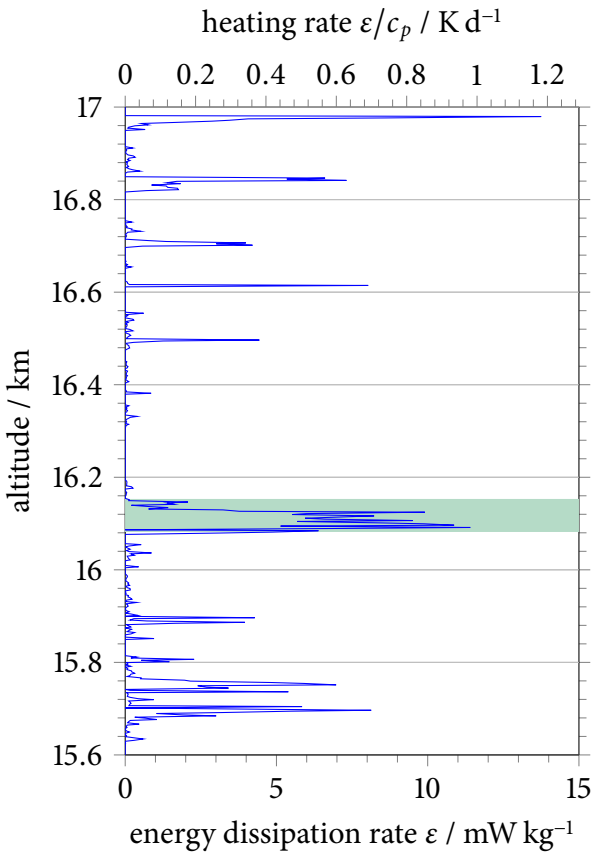

Figure 4.5: Part of the altitude profile of energy dissipation from velocity fluctuations for the BEXUS 8 flight. The shading marks the layer that is shown in Figures 4.1, 4.2, and 4.3.

are considered, and the random variables $\bar{\varepsilon}_j$ are assumed to be mutually independent and identically distributed so that the central limit theorem can be applied. See Yamazaki and Lueck [1990, Section 2] for a review of the theory. The distribution was experimentally confirmed, e. g., by measurements in the boundary layer by Freytag [1978]. According to Ulrich Schumann (DLR) [private communication], it is a quality criterion for a measurement of atmospheric dissipation rates to reproduce that distribution. Figure 4.6 show histograms of dissipation rates for the tropospheric and stratospheric measurements of the BEXUS 12 flight. In the stratosphere, the data shows good agreement with a lognormal distribution. In the troposphere, however, an additional "shoulder" at small rates is present. The cause for this feature is yet unknown and has to be further investigated.

The importance of the criterion (e) for a well-behaved distribution of ε is illustrated in Figure 4.7. Especially for BEXUS 8, a second band with very small dissipation rates appears which mainly consists of bad fits. These are filtered out by the criterion (e) (grey area in the plot).

Turbulent layers are determined from the ε profile by finding connected sections where none of the criteria listed above applies, i. e. where $\varepsilon > 0$. In order to care for outliers from bad spectra

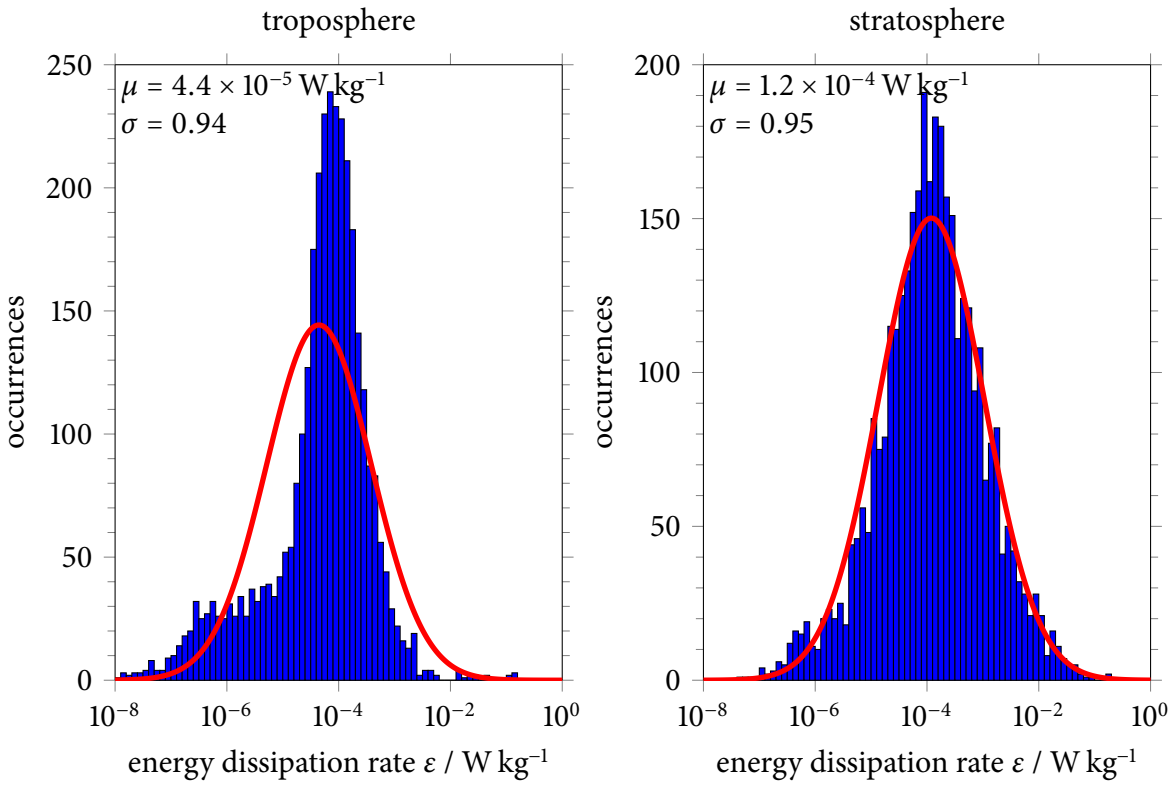

Figure 4.6: Histograms of tropospheric (left) and stratospheric (right) dissipation rates obtained with a 5 m window from the measurements of BEXUS 12. The red curves show most likely normal distributions of the logarithmic ε data.

caused by disturbances, layers separated by only one non-turbulent window (i. e. data point in the profile) are treated as one.

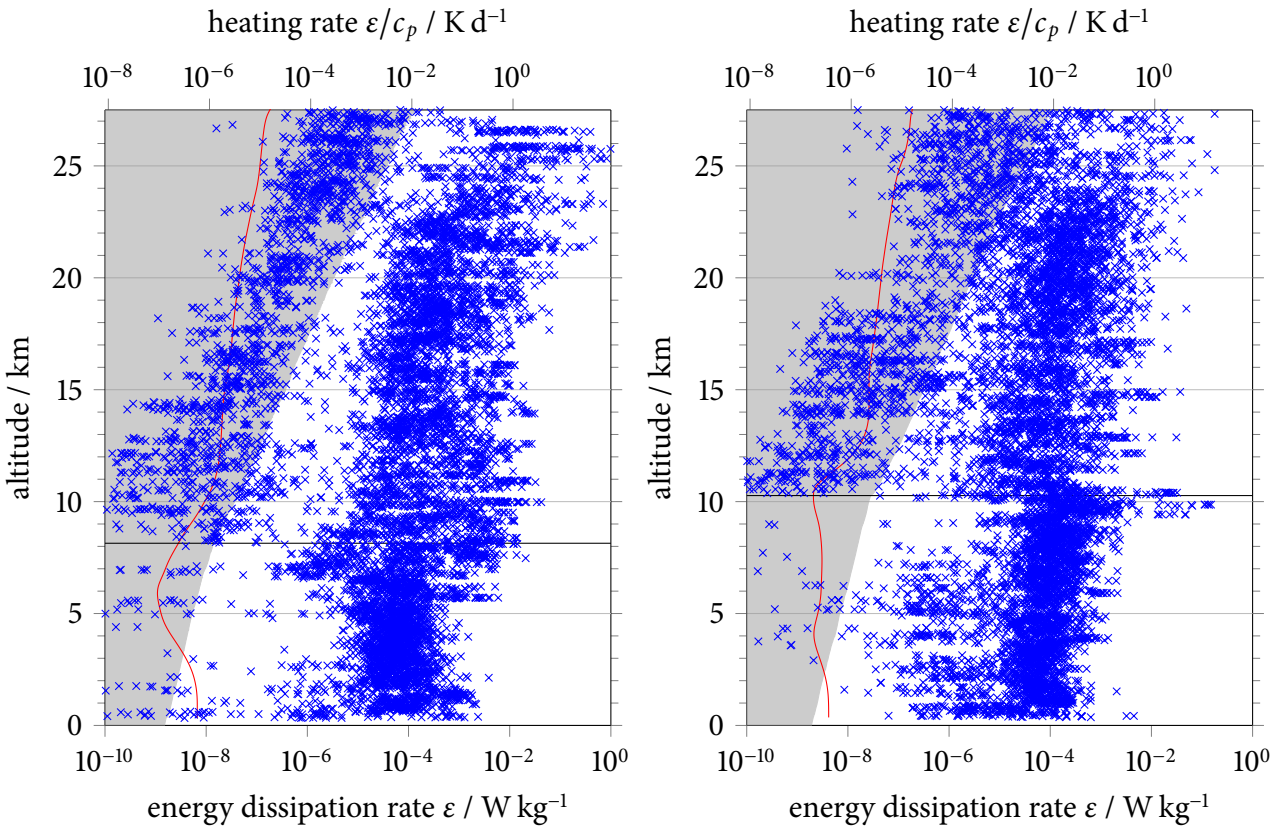

Figure 4.7: Altitude profiles of dissipation rates for the BEXUS 8 (left) and BEXUS 12 (right) flights before application of the criterion (e) for the technical minimum. The grey shading marks those data points that will be eliminated by the criterion. The red curve shows the theoretical minimum by Lübken [1993].

4.1.2 Error analysis

For the fit (4.1) the measurement noise variance σ_i^2 of the *logarithmic* PSD is needed, but its estimation proves difficult. In principle, a statistical treatment of the logarithmic data is necessary, but some integrals arising in this context cannot be solved with elementary methods. However, as will be shown later the statistical error is much smaller than the error resulting from the choice of the fit range. To circumvent the difficulty in computing σ_i^2, it is helpful to notice that the confidence intervals (in linear space) are proportional to the PSD. Thus the logarithm of the ratio of the upper confidence interval to the PSD is additive in logarithmic space, and it does not depend on frequency. That leads to the idea to use it as input error σ_i for the fit. This is not equal to the variance of the logarithmic data but should be in a similar order of magnitude.

Now the error for the result for the inner scale l_0 is analysed, which has not been done before for this method. The resulting fit error in l_0 for the example in Figure 4.2 is ±0.006 cm and ±0.005 cm

for the top and bottom panel, respectively. The interval is much smaller than expected, in fact so small that in the figure it is inside the thickness of the line marking l_0. Similar small fit errors are generally observed. Of course, the fit error crucially depends on the absolute value of the measurement error σ_i used as input for the fit, which is not known precisely, see above.

Error due to the choice of the fit limits and the noise level subtraction

In practice, however, the error resulting from other sources, e. g. the choice of the noise level or the fit limits, is much larger than the statistical error which manifests as fit error. This will be illustrated with an example of a typical spectrum. Since many spectra are similar, the results are representative for most cases. The fit limits and the noise level subtraction are individually varied and the impact on the fit result is quantified.

First the dependence of the fit result for the inner scale on the choice of the small-scale fit limit is considered as shown in Figure 4.8. By eye, the transition between geophysical signal and constant instrumental noise level is visible, but due to the oscillations in the PSD and the numerous possibilities for disturbances, the automatic procedure described in the last subsection does not always find the optimal result. To estimate the error, the small-scale fit limit is varied by

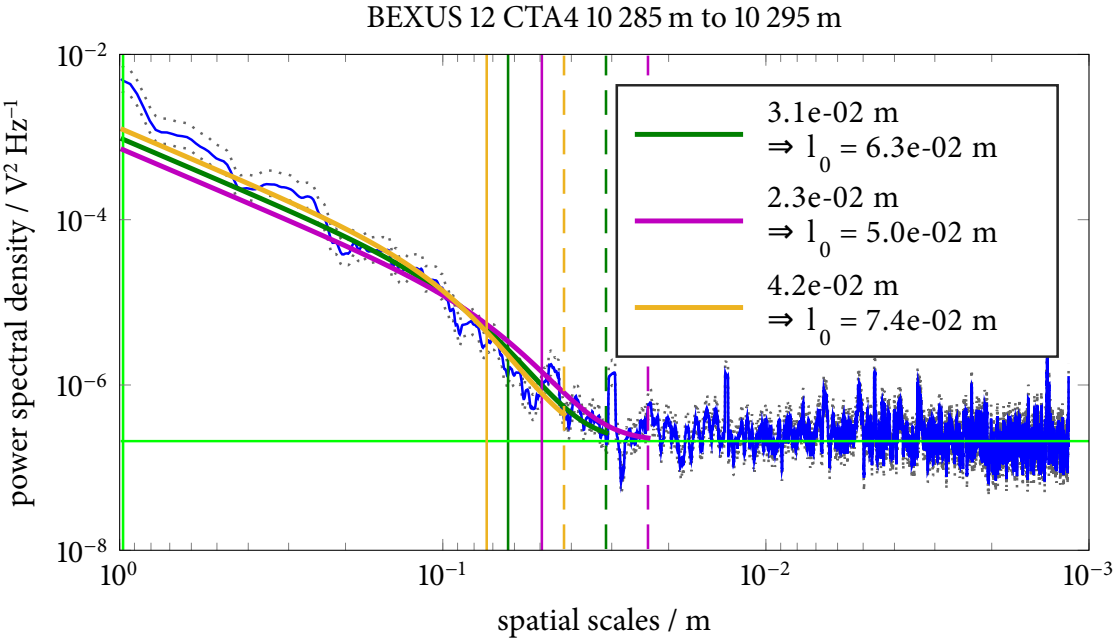

Figure 4.8: Dependence of the fit on the variation of the small-scale fit limit. The blue curve denotes the measured spectrum. The dark green dashed line shows the default choice of the small-scale fit limit while the magenta and yellow ones correspond to a lower or higher one. The solid curves of the same colour represent the respective fit and the solid vertical lines the corresponding inner scale. The light green lines mark the default large-scale fit limit and noise level.

35 % and the respective fits are performed. The variation is chosen by eye as what would still be an appropriate choice of the point where the spectrum enters the noise level band. The dark green curve represents the default choice as described in the last subsection. If the limit is at too small a scale, the fit extends to the region with approximately constant PSD (noise), but such a behaviour is not described by the fit function. (The apparent positive curvature of the fit function at the small-scale end is due to the depiction with added noise level, see previous section, particularly Figures 4.2 and 4.3.) That leads to a fit that does not describe the data very well (magenta curve in Figure 4.8). If the limit is too far at large scales, the fit range is shortened and potentially the transition in the spectrum representing the inner scale is not completely within the range any more (orange curve). The results for the inner scale l_0 vary by ~20 %, much more than the statistical fit error. In terms of ε, that corresponds to roughly a factor of 2.

To quantify the dependence on the choice of the large-scale fit limit, that limit is varied by a factor of 5. Similar to the case above, the variation is chosen by eye as what is still well within the inertial subrange. The resulting fits are presented in Figure 4.9. Mostly, the slope of the spectrum does not change very much at the large scales resolved for typical window lengths. Additionally, the density of data points on a logarithmic frequency scale is much smaller on large scales than on small scales; thus the fit is affected less by the large scales. Hence the expected impact on the fit result is low. This is confirmed by the example where the variation of l_0 is only about 7 %. That corresponds to ~20 % in ε.

Finally, the influence of the noise level subtraction is discussed. The noise level is a band with

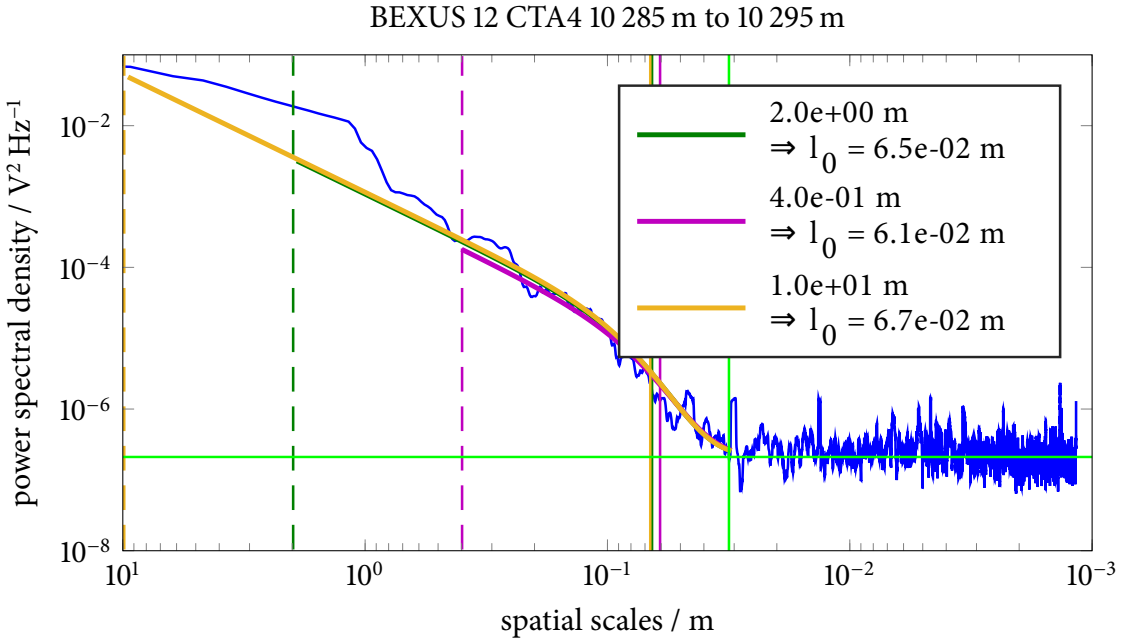

Figure 4.9: Dependence of the fit on the variation of the large-scale fit limit. Analogous to Figure 4.8, but the three colours dark green, magenta and yellow mark three variations of the large-scale fit limit.

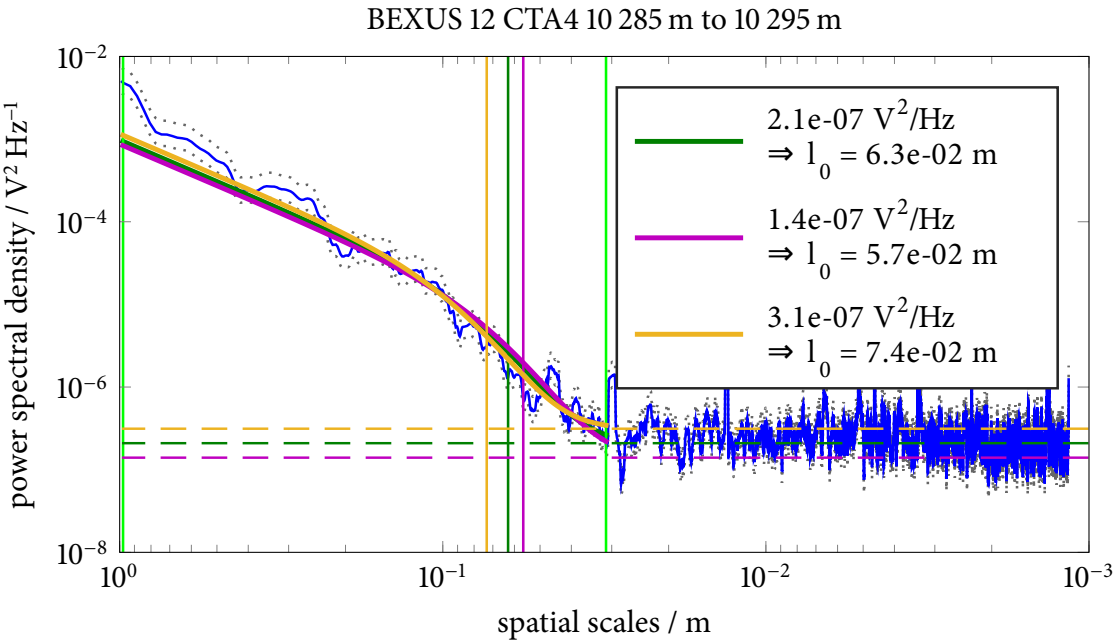

Figure 4.10: Dependence of the fit on the variation of the subtraction of the noise level. The green, magenta and orange curves represent the fits obtained for the noise level subtraction shown with the dashed horizontal lines of the same colour. The respective solid vertical lines visualise the resulting inner scales. The light green vertical lines mark the fit range.

a thickness of roughly half an order of magnitude with irregular varying boundaries. Thus the choice of the noise level value is not unique. Figure 4.10 shows the fit results for three choices. The green curve represents the default choice of the median between $f_s/3$ and $f_s/2$ described in the last subsection. The magenta and orange curves correspond to 50 % lower or higher ones, respectively. The amount of the variation was chosen visually as what still describes the noise level band. The impact on l_0 is ~20 %. This corresponds to roughly a factor of 2 in ε.

Altogether, due to the described variation in noise level and fit limits, l_0 varies between 4.0 cm to 7.8 cm, i. e. by ~40 % compared to the default choice. This results in an uncertainty in ε of a factor of 7!

Error analysis using artificial spectra

The approach presented above does not consider the inherent dynamics of the automatic routines for the noise level detection and the choice of the fit limits. Thus another approach is used to get an impression of the impact of these routines. Artificial spectra are generated by adding noise to theoretical spectra with random l_0; those are processed just like the measured ones, and the obtained l_0 and ε are compared to the original ones. Generally, the theoretical spectrum is disturbed by a combination of measurement noise and atmospheric variability due to the fact that only one realisation of a random process is observed. The instrumental noise is modelled

by Gaussian white noise. The atmospheric part is in principle unknown, thus it has been chosen such that the artificial spectra are similar to the measured ones. The choice is a normal distributed noise with standard deviation proportional to the PSD value.

An example is shown in Figure 4.11. From 100 000 realisations, disregarding those ~10 % where the fit is sorted out due to the criteria named in Section 4.1.1, a mean absolute value of relative error in ε of roughly 1.5 is obtained. For 90 % of those realisations, the relative error is below 0.9, and for 95 % it is below 1.9. Figure 4.12 presents a histogram of the relative error for all realisations. The largest obtained error was 15 000 due to the incorrect detection of the small-scale fit limit, but there are only a few outliers with a relative error above 4. The mean relative error in l_0 is larger than 0, as is the median. That means that the retrieval gives by trend too large an inner scale and thus too small a dissipation rate. That is respected in the histogram for the error in ε by the fact that most values lie below 0. The median is −0.4. The mean error, however, is positive due to few outliers with much too large ε.

Summing up, a relative error in the dissipation rate ε of roughly 1.5 is expected due to the imprecise choice of noise level and fit limits. Some sporadic spectra are likely to have a greater error (outliers). When looking at the ratio of determined and theoretical values, the geometrical mean error in ε is a factor of 4.

Moreover, the uncertainty in the constant c_{l_0} in (2.22) results in an additional possible bias in ε, see Section 2.3.

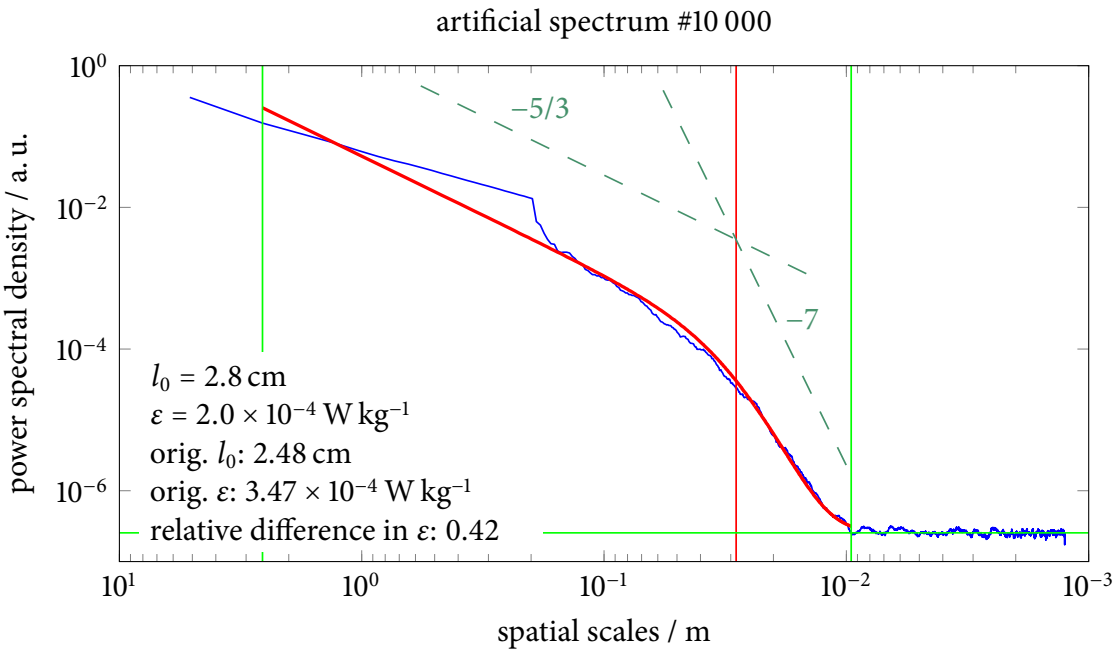

Figure 4.11: Example of an artificial spectrum used for a sensitivity study to estimate the error in l_0 and ε. The blue curve shows the spectrum, the red one the fit, the vertical red line the inner scale, and the green lines are as in Figure 4.2.

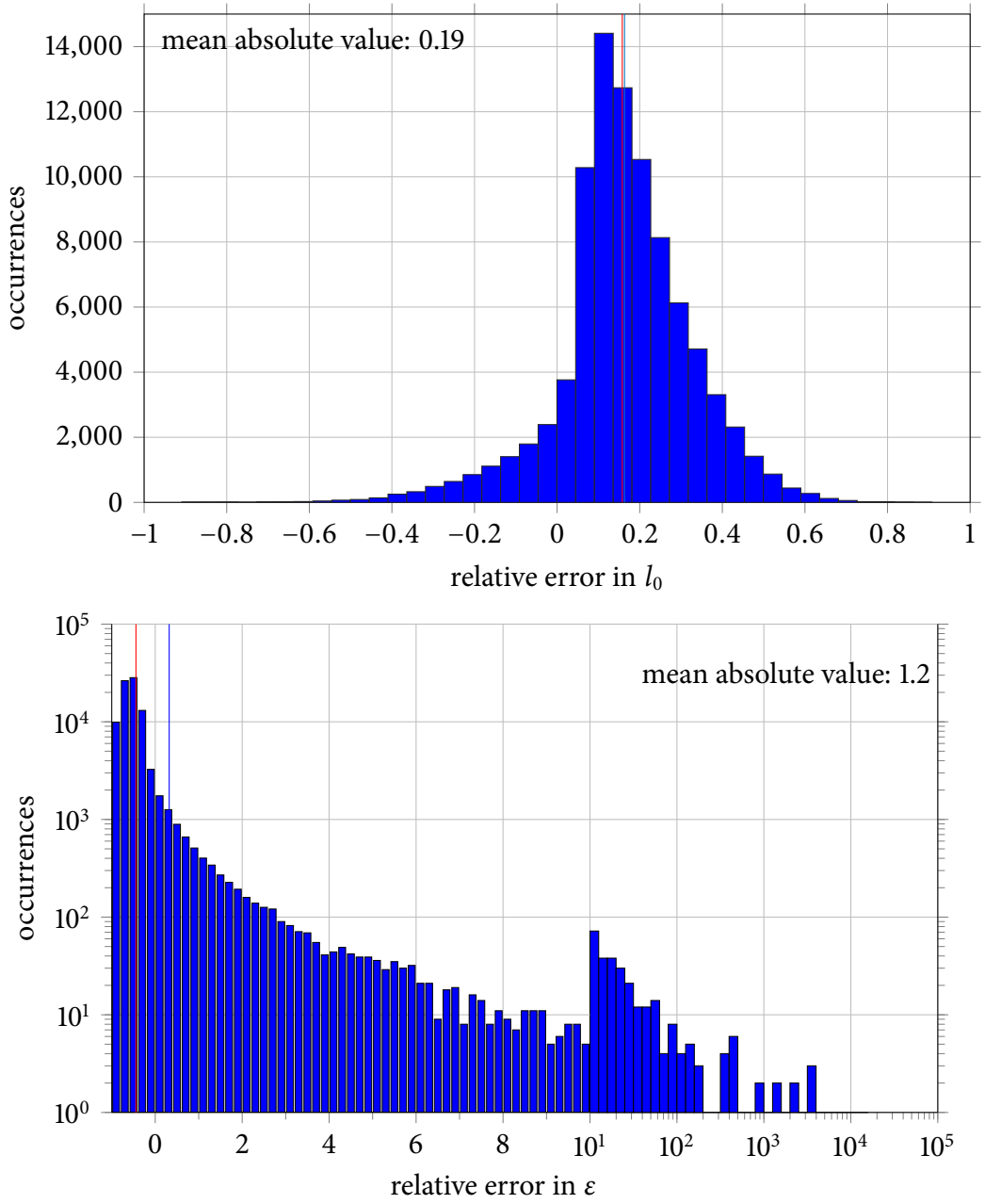

Figure 4.12: Relative error of l_0 (top) and ε (bottom) obtained for 100 000 artificial spectra with random l_0. The blue vertical line shows the mean, the red one the median. In the bottom panel, the error scale changes from linear to logarithmic at a value of 10 in order to include outliers.

4.1.3 Spectral analysis using wavelets

As mentioned before, the power spectral density can also be computed with wavelets. After the choice of an analysing wavelet ψ, the *continuous wavelet transform* (CWT)

$$\mathcal{W}u(a,b) := |a|^{-1/2} \int_{-\infty}^{\infty} u(t)\, \psi\left(\frac{t-b}{a}\right) \mathrm{d}t \tag{4.2}$$

[Daubechies, 1992, (1.2.1)] decomposes the signal u into a time-frequency representation in dependence of the wavelet scale a and the time shift b. The *wavelet power* is defined as

$$|\mathcal{W}u(a,b)|^2 \tag{4.3}$$

[Torrence and Compo, 1998, Section 3d]. The wavelet power comprises a power spectral density in dependence on frequency *and* time (respective space). A further advantage compared to the windowed Fourier technique is that the support of the wavelet

$$\operatorname{supp}\psi := \{t \in \mathbb{R} : \psi(t) \neq 0\}$$

(which is comparable to the window size in windowed Fourier analysis) scales with wavelet scale a, so that for fine scales only *local* details are resolved. Wavelet scale a is connected to frequency f via

$$f(a) = \frac{f_\mathrm{c}}{a} \tag{4.4}$$

[analogous to Torrence and Compo, 1998, Section 3h], where f_c is the centre frequency of the analysing wavelet.

Figure 4.13 shows the wavelet power spectrum for the BEXUS 12 flight computed with the analysing wavelet (B.3) with $\nu_0 = 6$ after removal of a running average. The thin horizontal lines of higher PSD make the thin layers directly visible. Remember that for larger dissipation rates, the power spectrum drops below the noise level at smaller scales (i. e. higher frequencies). For instance, above ~10 km the spatial scale where the PSD first reaches the noise level (dark blue in the colour code) drops to larger spatial scales. This corresponds to a drop in dissipation rate as described in Section 5.1. The peaks on very small spatial scales of a few millimetre correspond to high-frequency electronic disturbances. Those do not affect the data evaluation because they are well outside the fit range.

A magnified part from 9.8 km to 10.3 km is depicted in Figure 4.14 for better visibility of the details. It demonstrates the advantage of the time-frequency representation that allows the identification of turbulent layers without the choice of a window.

In order to obtain energy dissipation rates, the *global wavelet spectrum* for a given altitude window is computed which consists of the mean of the wavelet power over altitude (i. e. time)

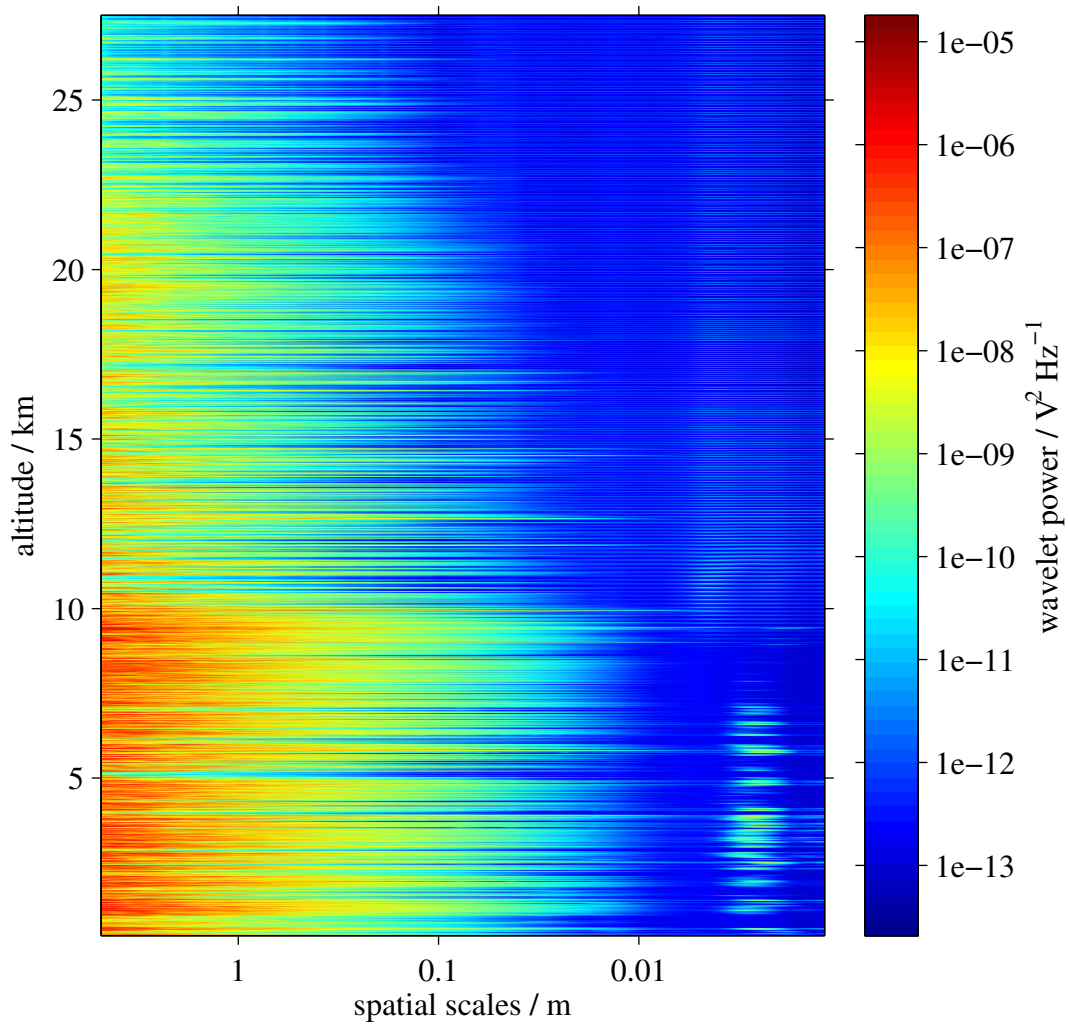

Figure 4.13: Wavelet power spectrum colour-coded in dependence of altitude and spatial scales for the BEXUS 12 flight. Generally, stronger turbulence means that the PSD drops to the noise level at smaller scales, thus the intermittency featuring thin turbulent layers is visible in the figure.

[Torrence and Compo, 1998, Section 5a]. A turbulence model can be fitted to such a spectrum similarly than for Fourier spectra (see Section 4.1.1). An example is presented in Figure 4.15. An advantage compared to the Fourier spectrum is that the data points are equally spaced in logarithmic frequency space. That means that the fit is equally determined by all scales and not dominated by the small scales as in the Fourier case.

A problem with wavelet spectra is that the noise level detection does not work reliably, although a few alternative methods using the derivative of a spline fit have been tested. Potentially, that can be solved by new methods, e. g. with overlapping linear fits; however, that is outside the scope of this work. Thus, the Fourier analysis is used for the evaluation shown in Chapter 5.

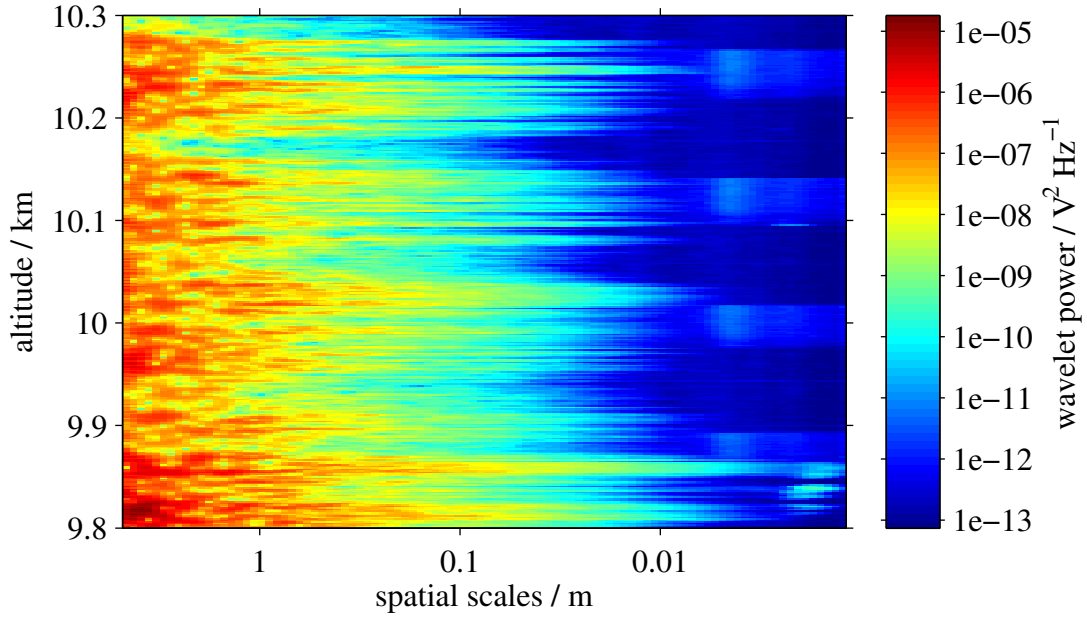

Figure 4.14: Magnification of the wavelet power spectrum from 9.8 km to 10.3 km for the BEXUS 12 flight. It shows that by using wavelet techniques the extent of turbulent layers is visible without having to chose a window.

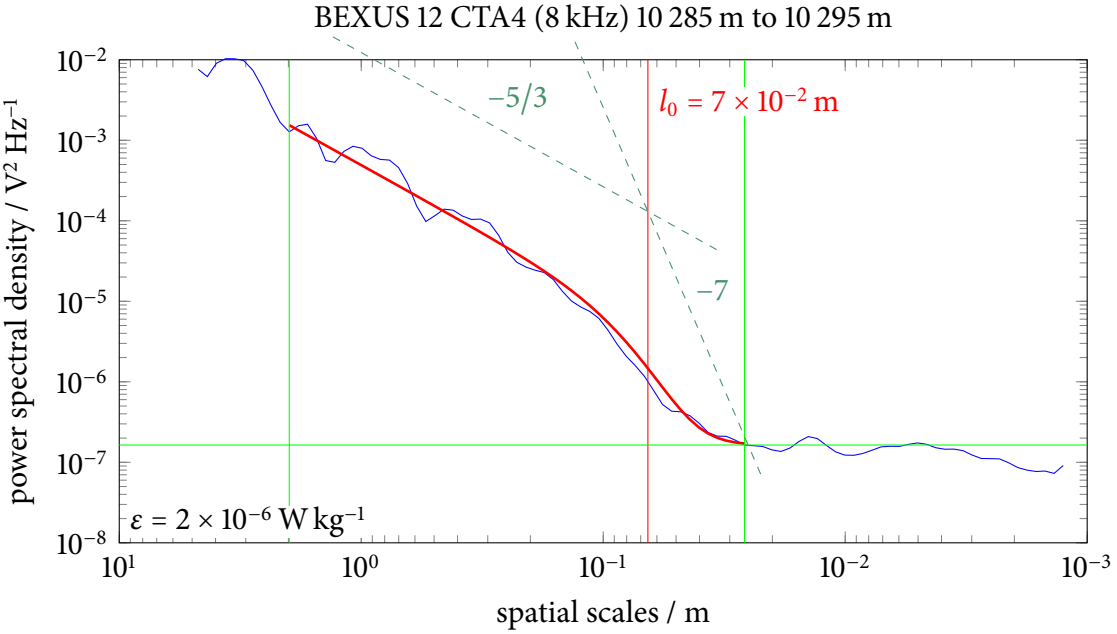

Figure 4.15: Global wavelet power spectrum for the altitude range 10 285 m to 10 295 m (blue curve) with fit of the turbulence model (2.27) (red curve). The red vertical line shows the resulting inner scale l_0, the other lines are as in Figure 4.2.

4.2 Thorpe analysis

Recently, turbulence studies with standard radiosonde data were published. Those sondes have a vertical resolution of roughly 10 m, i. e. much larger than that of LITOS, cf. Section 3.1. For that kind of analysis, Thorpe's method has been used. In order to compare this approach with the high-resolved measurements of LITOS, it is applied to the data of radiosondes on LITOS flights. The method and necessary data processing are described below. Results using this method and a comparison to those from spectral analysis are shown in Section 5.5.

4.2.1 Basic principle

Thorpe [1977] proposed a simple method for the indirect measurement of turbulence in oceans and lakes, which was adapted to the atmosphere by Luce et al. [2002] and Clayson and Kantha [2008]. It uses static instabilities as a proxy. Stability can be measured by the gradient of the potential temperature $\Theta := T\left(\frac{p_{\mathrm{ref}}}{p}\right)^{R/c_p}$, where $p_{\mathrm{ref}} = 1000\,\mathrm{hPa}$ is a reference pressure, $R = 287\,\mathrm{J\,kg^{-1}}$ the specific gas constant for dry air and $c_p = 1003\,\mathrm{J\,kg^{-1}\,K^{-1}}$ the specific heat capacity of air at constant pressure. In a stably stratified atmosphere, Θ is a monotonously increasing function of altitude. If, locally, the potential temperature has a negative gradient, a static instability is at hand. Such an instability drives natural convection and turbulence, although it need not be the original driving process, but could be created, e. g., by three-dimensional wind-shear. Since turbulent motions tend to remove the gradient in potential temperature, the method cannot detect turbulence at late stages.

The essential idea of the Thorpe method is to compare an observed vertical profile of potential temperature to an equivalent stable one which is obtained by sorting. That means that by changing the order of the data points air parcels are moved upwards and downwards to yield a statically stable profile with monotonously increasing potential temperature. This is easiest (although not necessarily [Thorpe, 2005, p. 176]) done on data sampled on an equidistant altitude grid $z_j = j\,\Delta z$, $j \in I_n := \{1, \ldots, n\}$, where n is the number of data points in the measurement and Δz the sample altitude step. The measured potential density profile is denoted by Θ_j, $j \in I_n$.

Figure 4.16 demonstrates the sorting process. Let $s : I_n \to I_n$ denote the permutation describing the sorting process, i. e. the sorted profile is referred to by $(\Theta_{s(j)})$. The difference between measured and sorted profile in potential temperature, $S_{\mathrm{T}}(j) := \Theta_j - \Theta_{s(j)}$, is called *Thorpe signal*. The altitude difference between observed and sorted profile, $D_{\mathrm{T}}(j) := z_j - z_{s(j)} = (j - s(j))\Delta z$, defines the *Thorpe displacement* at level z_j.

Instabilities are detected using the cumulative sum of the Thorpe displacement, $\sum_{j=1}^{k} D_{\mathrm{T}}(j)$ [Wilson et al., 2010, Section 3]. It is zero on statically stable sections, as in that case the profile is already sorted. Additionally, it is never positive. To verify that fact, let $s : I_n \to I_n$ be any permutation and $k \leq n$ arbitrary. Since the sum of the first k natural numbers is the minimum of the sum of any k different natural numbers in I_n, it follows that

$$\sum_{j=1}^{k} j \leq \sum_{j' \in s^{-1}(\{1,\ldots,k\})} j' = \sum_{j=1}^{k} s(j).$$

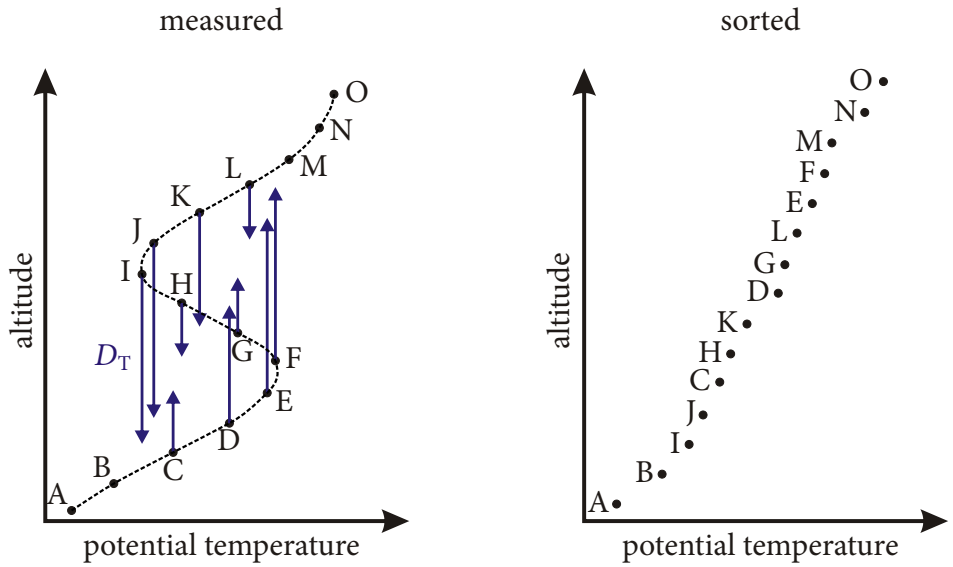

Figure 4.16: The sorting algorithm used to create a stable potential temperature profile (right) from a measured one (left). The points, A–O, represent the discrete measured values of potential temperature Θ_j at their respective levels z_j. Those between B and M are statically unstable in the sense that there is denser fluid above or less dense below them, even though the density only decreases with altitude between F and I. The vertical arrows show the displacements D_T in z required to re-sort the observed potential temperature profile into the statically stable order shown in the right panel. The sorting conserves mass but not potential energy. Figure and caption adapted from Thorpe [2005, Fig. 6.2].

This is equivalent to the assertion with s being the sorting permutation. Thus, a layer with $\sum_{j=1}^{k} D_T(j) < 0$ between points with $\sum_{j=1}^{k} D_T(j) = 0$ can be identified as an inversion in potential temperature.

The root-mean-square (rms) of the Thorpe displacements D_T, taken "over vertical scales that exceed the maximum local estimates of D_T" [Thorpe, 2005, p. 176], here over the considered instability [Wilson et al., 2010, p. 978], is called *Thorpe length*

$$L_T := \mathrm{rms}(D_T). \tag{4.5}$$

It describes the mean vertical length where heavier fluid is above lighter one.

Thorpe [1977, Section 4] proposed the rms displacement (4.5) to be a measure of the outer vertical scale of turbulence. The idea is that the overturning scale is connected to the vertical size of the largest eddies in stratified flow [Thorpe, 2005, p. 175], which is known as Ozmidov scale L_O, (2.29). This results in the assumption that both length scales are proportional to each other, i. e.

$$L_T = c_{TO} L_O \tag{4.6}$$

with a constant c_{TO}. Inserting the definition (2.29) for the Ozmidov scale,

$$L_{\mathrm{O}} = c_{L_{\mathrm{O}}} \sqrt{\frac{\varepsilon}{N^3}},$$

where the constant $c_{L_{\mathrm{O}}}$ is usually set to 1 [e. g. Gavrilov et al., 2005, Clayson and Kantha, 2008, Wilson et al., 2014], and solving for ε gives

$$\varepsilon = c_{\mathrm{TO}}^2 \, L_{\mathrm{T}}^2 \, N^3. \tag{4.7}$$

The background buoyancy frequency N is best taken from the sorted profile [Dillon, 1982, Section 3]. An imaginary N would result in a negative and imaginary dissipation rate, which is unphysically. The constant c_{TO}^2 is mostly taken from oceanographic measurements as only few studies in the atmosphere are available. Its value varies over several orders of magnitude in the literature. With LITOS, the dissipation rate ε is measured directly so that the assumption can be checked and the constant be determined. The results are found in Section 5.5. Moreover, the dissipation rates obtained from both methods are compared (where $c_{\mathrm{TO}}^2 = 0.3$ is used for the Thorpe evaluation as by Clayson and Kantha [2008]).

If water vapour reaches saturation, static stability is lower than for dry air due to the release of latent heat from condensing water during upwards motion [Wilson et al., 2013]. As a remedy, for saturated regions a moist-conservative potential temperature is used instead of the dry potential temperature. This is relevant in the troposphere only.

Instrumental noise can create artificial negative gradients in the potential temperature data. To distinguish these from real inversions, a statistic test according to Wilson et al. [2010, 2011] is applied. Basically it consists of comparing the range of the measured data in a detected layer with the range of a pure noise sample.

The details of the data processing are described in the next subsection.

4.2.2 Data processing and measurement noise of radiosonde data

For the radiosonde evaluation the data processing by Wilson et al. [2011] is used which is described in this subsection.

Just before reaching floating altitude the ascent rate of the balloon is very variable, and sometimes the balloon even descends for a short time. Thus prior to data processing, radiosonde data from above 25 km altitude is cut off in order to eliminate disturbances from that transition phase.

Due to slight variations in ascent velocity, the data come at irregular altitude levels. So first of all, the data are resampled to a regular vertical grid. Assuming hydrostatic equilibrium, the measured altitude difference is

$$\Delta z_i^{\mathrm{M}} := z_{i+1}^{\mathrm{M}} - z_i^{\mathrm{M}} = -\frac{R T_i^{\mathrm{M}}}{g} \frac{\Delta P_i^{\mathrm{M}}}{P_i^{\mathrm{M}}} \tag{4.8}$$

where $R = 287\,\mathrm{J\,kg^{-1}\,K^{-1}}$ is the specific gas constant for dry air, $g = 9.81\,\mathrm{m\,s^{-2}}$ the acceleration of gravity, T_i^{M} the measured temperature and $\Delta P_i^{\mathrm{M}} := P_{i+1}^{\mathrm{M}} - P_i^{\mathrm{M}}$ the measured pressure difference at level i. The superscript M stands for "measured". The mean ascent rate is $\Delta z := \langle \Delta z_i^{\mathrm{M}} \rangle_i$, which is taken as new regular sampling step because this choice is associated with minimal interpolation. The corresponding regular altitude grid is $z_i^{\mathrm{R}} := z_1^{\mathrm{M}} + i\Delta z$. The superscript R stands for "resampled".

Although the balloon is ascending, due to measurement noise the observed pressure difference ΔP_i^{M} is not always negative. Therefore a cubic least square spline fit is performed, yielding a monotonous pressure profile P_i^{A}. The superscript A stands for "approximated". The spline is evaluated at z_i^{R} yielding a resampled pressure profile P_i^{R}. The temperature T_i^{M} is resampled to the regular grid with linear interpolation leading to a profile T_i^{R}. From this dataset, the potential temperature

$$\Theta_i := T_i^{\mathrm{R}} \left(\frac{P_{\mathrm{ref}}}{P_i^{\mathrm{R}}} \right)^{R/c_p} \tag{4.9}$$

is computed.

To care for saturation effects in the troposphere, saturated regions are identified with the method described by Zhang et al. [2010]. A layer is regarded as saturated, if the relative humidity exceeds an altitude-dependent threshold RH_{min} within the whole layer and if additionally somewhere within the layer $RH \geq RH_{\mathrm{max}}$. The thresholds RH_{min} and RH_{max} are piecewise linear functions of altitude defined by Zhang et al. [2010]. As the relative humidity of radiosondes is computed with respect to liquid water, it is corrected for $T < 0\,^{\circ}\mathrm{C}$. To this end, RH is multiplied by the ratio $e_{\mathrm{w}}/e_{\mathrm{i}}$ of the saturation pressure of water vapour over liquid water e_{w} and over ice e_{i}. e_{i} is estimated by the empirical expression

$$e_{\mathrm{i}} = \frac{1\,\mathrm{hPa}}{100} \exp\left(28.9074 - \frac{6143.7\,\mathrm{K}}{T} \right) \tag{4.10}$$

[Murphy and Koop, 2005, (2); Wilson et al., 2013, (9)], and e_{w} by the WMO recommended formula[1]

$$\begin{aligned} \log_{10} e_{\mathrm{w}} =& 10.79574\,(1 - 273.16\,\mathrm{K}/T) - 5.02800 \log_{10}(T/273.16\,\mathrm{K}) \\ &+ 1.50475 \cdot 10^{-4}\,(1 - 10^{-8.2969(T/273.16\,\mathrm{K}-1)}) \\ &+ 0.42873 \cdot 10^{-3}\,(10^{4.76955(1-273.16\,\mathrm{K}/T)} - 1) \\ &- 2.2195768 + \log_{10}(1013.25) \end{aligned} \tag{4.11}$$

[Goff, 1957, (6)], where e_{w} and e_{i} are in Hectopascal. The left panel in Figure 4.17 visualises the difference between original and corrected relative humidity and its impact on the detection of moist layers for the BEXUS 12 flight.

1 cf. note on `http://cires.colorado.edu/~voemel/vp.html` (vis 10 Jul 2015)

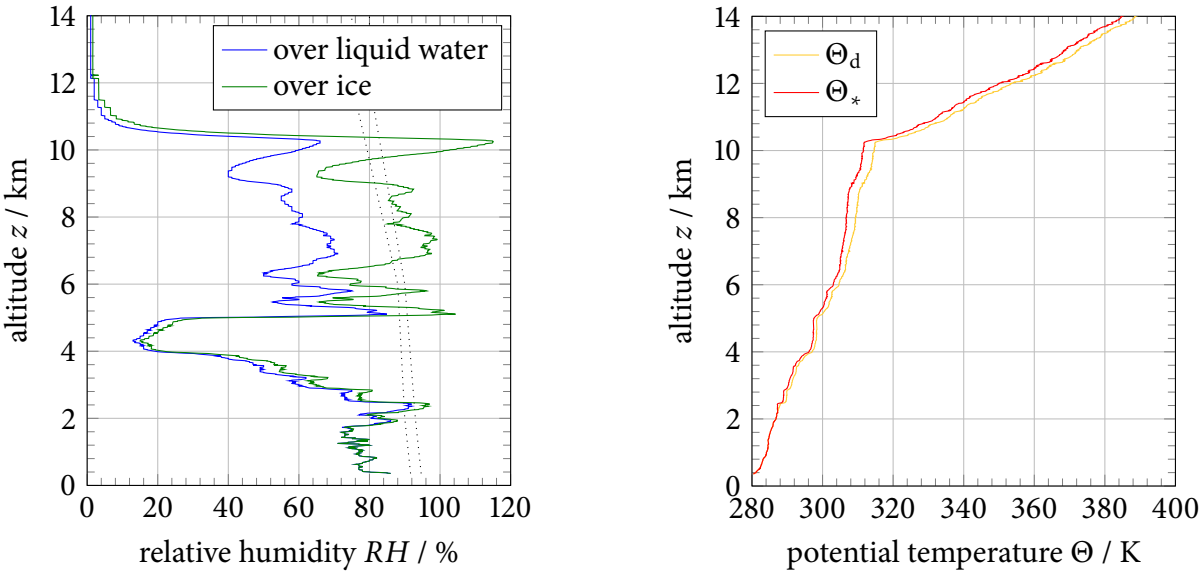

Figure 4.17: Left: Relative humidity for the BEXUS 12 flight. The blue curve shows the original radiosonde measurement while the green one includes the correction for saturation over ice for temperatures below the frost point. The grey dotted lines denote the thresholds RH_{min} and RH_{max}. Right: Dry (orange) and composite (red) potential temperatures for the BEXUS 12 flight.

In order to treat moist layers, a few new quantities have to be introduced. The water vapour mixing ratio is denoted q_{v}, the liquid water or ice mixing ratio q_{l}, the saturation mixing ratio q_{s}, and $q_{\mathrm{w}} = q_{\mathrm{l}} + q_{\mathrm{s}}$ is the total water mixing ratio. The mixing ratio is related to the relative humidity by $RH \approx \frac{q_{\mathrm{w}}}{q_{\mathrm{s}}}$. $c_{p\mathrm{d}} = 1003\,\mathrm{J\,kg^{-1}\,K^{-1}}$ and $c_{pv} = 2080\,\mathrm{J\,kg^{-1}\,K^{-1}}$ are the specific heats at constant pressure for dry air and water vapour, respectively, $c_{\mathrm{w}} = 4182\,\mathrm{J\,kg^{-1}\,K^{-1}}$ is the specific heat for liquid (or ice) water, $L_{\mathrm{V}} = 2\,500\,000\,\mathrm{J\,kg^{-1}}$ is the latent heat of vaporisation of liquid water or ice, and $\gamma \approx 0.622$ is a constant. Using the moist saturated lapse rate

$$\Gamma_{\mathrm{m}} = \frac{g}{c_{p\mathrm{d}}}(1+q_{\mathrm{w}})\left(1+\frac{c_{pv}q_{\mathrm{s}}+c_{\mathrm{w}}q_{\mathrm{l}}}{c_{p\mathrm{d}}}+\frac{\gamma L_{\mathrm{V}}^2 q_{\mathrm{s}}}{c_{p\mathrm{d}}RT^2}\left(1+\frac{q_{\mathrm{s}}}{\gamma}\right)\right)^{-1} \tag{4.12}$$

[Wilson et al., 2013, (8)], a moist Brunt-Väisälä frequency is computed via

$$N_{\mathrm{m}}^2 \approx \frac{g}{T}\left(\frac{\partial T}{\partial z}+\Gamma_{\mathrm{m}}\right)\left(1+\frac{L_{\mathrm{V}}q_{\mathrm{s}}}{RT}\right)-\frac{g}{1+q_{\mathrm{w}}}\frac{\mathrm{d}q_{\mathrm{w}}}{\mathrm{d}z} \tag{4.13}$$

[Wilson et al., 2013, (7)]. Now, the composite potential temperature is calculated via

$$\Theta_*(j) = \Theta_*(j-1)\left(1+N_i^2(j-1)\frac{\Delta z}{g}\right) \tag{4.14}$$

where inside saturated layers $N_i^2 = N_\mathrm{m}^2$ is the moist buoyancy frequency, and outside $N_i^2 = N_\mathrm{d}^2 = \frac{g}{T}\left(\frac{\mathrm{d}T}{\mathrm{d}z} + \frac{g}{c_p}\right)$ the usual dry buoyancy frequency. The right panel of Figure 4.17 shows the dry potential temperature Θ_d and the composite potential temperature Θ_* for the BEXUS 12 flight.

Although the gradient of the potential temperature is reduced by incorporating moisture effects (see right panel of Figure 4.17), the correction is small, and it makes no difference in the number of significant layers for the BEXUS flights. In contrast, Wilson et al. [2013, Section 4] reported a great impact for flights from Shigaraki MU Observatory (Japan, 34° 51' N, 136° 06' E). Moisture seems to play less a role in the cold arctic atmosphere.

As mentioned before, artificial inversions can be created by measurement noise. Thus, after the detection of inversions with the cumulative Thorpe displacement $\sum_{j=1}^{k} D_\mathrm{T}(j)$ (see previous subsection), a statistical test is performed for each layer. For an inversion from z_i to z_{i+k-1}, i. e. of size k data bins, the measured range of potential temperatures $W_k := \max\{\Theta_j : i \le j \le i+k-1\} - \min\{\Theta_j : i \le j \le i+k-1\}$ is compared to that of a pure noise sample which consists of k independent, identically distributed Gaussian random variables with standard deviation σ_Θ. The choice of the measurement noise σ_Θ is discussed below. If $w_p(k)$ is the p percentile of the range of the pure noise sample, the layer is noise-induced (i. e. not significant) with a p confidence level if

$$\frac{W_k}{\sigma_\Theta} < w_p(k) \tag{4.15}$$

[Wilson et al., 2010].

Wilson et al. [2011] proposed a simple method to estimate the instrumental noise σ_Θ from the variation of the data itself. Basically, the mean variation between subsequent data points is treated as noise.

The paper is not explicit about the handling of the pressure. Since P^R is smoothed with a spline, it makes no sense to use it to estimate the measurement noise. Thus, in this work the procedure is applied to the resampled temperature data T^R and the logarithm of the *unsmoothed* pressure resampled at the equidistant grid. First, the profile is split into segments of ~200 m altitude. In each segment, a linear trend is removed, and the measurement noise standard deviation σ is set to the standard deviation of the first differences of the data after trend removal divided by $\sqrt{2}$. That is, if T_seg is the temperature within a segment and l_T a linear fit, then

$$\sigma_T = \sqrt{\mathrm{var}(\mathrm{diff}(T_\mathrm{seg} - l_T))/2}$$

where $\mathrm{diff} : x(j) \mapsto x(j+1) - x(j)$ denotes the first difference operator. The resulting noise profile is smoothed with a least square spline approximation. An example for the BEXUS 12 flight is shown in Figure 4.18. Naturally, the result depends on the choice of the grid for the spline. For the potential temperature, the noise is found with Gauß' law of error propagation,

$$\sigma_\Theta = \Theta\sqrt{\left(\frac{\sigma_T}{T}\right)^2 + \left(\frac{R}{c_p}\frac{\sigma_P}{P}\right)^2} \approx \Theta\frac{\sigma_T}{T} \overset{(4.9)}{=} \sigma_T\left(\frac{P_\mathrm{ref}}{P}\right)^{R/c_p} \tag{4.16}$$

where the approximation neglects the noise on pressure which is much smaller than the one on temperature (see Figure 4.18 and Section 3.1).

This method of noise estimation treats all variation at scales in the order of the sampling length (roughly 10 m) as measurement noise. However, these scales are also affected by geophysics. For example, small overturns on scales of a few 10 m (which is the typical width of turbulent layers as measured by LITOS, see Section 5.1 or Theuerkauf [2012, Section 4.2]) increase the detected noise level. Thus the estimated measurement noise might be larger than the true one. On the other hand, sensor noise on scales larger than the sampling length is not covered.

The average of first differences of the potential temperature data scaled by the noise defines the mean trend-to-noise ratio (tnr)

$$\overline{\zeta} := \frac{\langle \mathrm{diff}\, \Theta_i \rangle_i}{\sigma_\Theta} \tag{4.17}$$

[Wilson et al., 2011, (5)]. If it is too low (typically smaller than 1), a denoising procedure is required, which consists of a weighted running average (with a Hamming window) with m data points followed by a downsampling with factor m [Wilson et al., 2010, Section 4c]. It increases the tnr by a factor of $m^{3/2}$.

For BEXUS 8 the tnr is $\overline{\zeta} = 0.55$, and thus a denoising with $m = 3$ is necessary. 37 of 95 layers

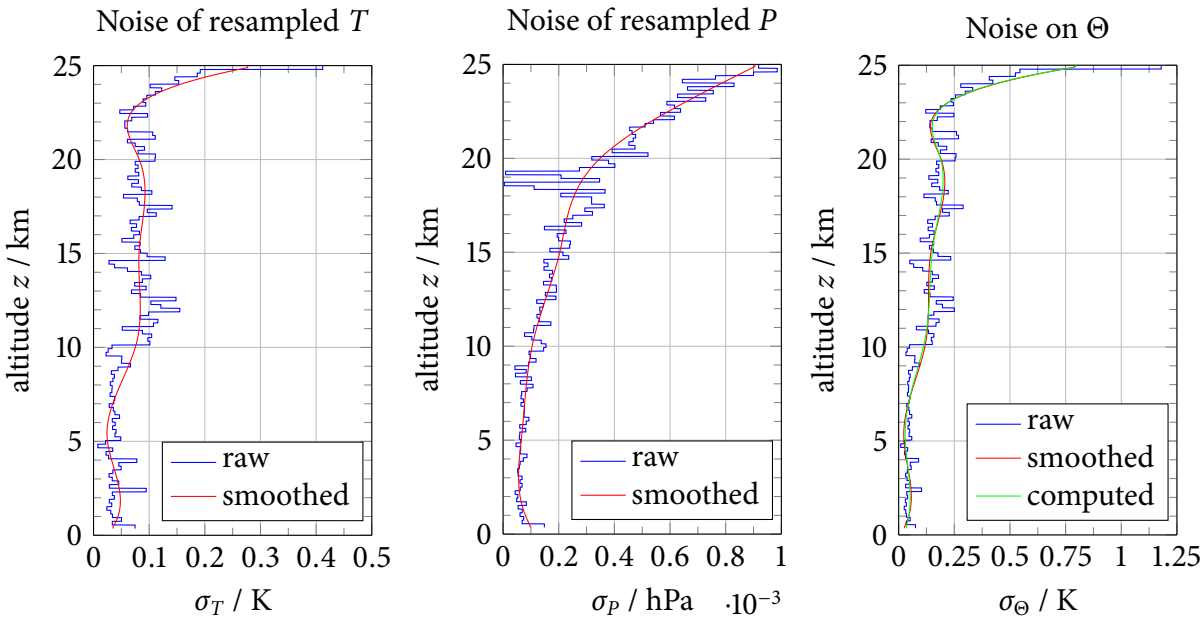

Figure 4.18: Vertical profiles of the estimated noise level according to Wilson et al. [2011] for the BEXUS 12 flight (radiosonde data prior to downsampling). The blue curves show the estimates in each altitude segment, the red curve the smoothing spline fit. The green curve in the right panel is computed with (4.16) with the smoothed σ_T.

(39 %) are significant. For BEXUS 12 the tnr is $\overline{\zeta} = 0.89$, and a denoising is performed with $m = 2$. Only 10 of 121 layers (~8 %) are significant. As discussed in Section 5.5, that results in a turbulent fraction of only 21 % (8 %) for BEXUS 8 (BEXUS 12), however 70 % (55 %) of the turbulent layers observed by LITOS are thinner than the vertical resolution of the (downsampled) radiosonde. That highlights the importance of measuring on small scales.

For each layer the Thorpe length L_T is computed, and therewith the energy dissipation rate ε using (4.7). The Thorpe length for significant and non-significant layers for the BEXUS 12 flight is plotted in Figure 4.19.

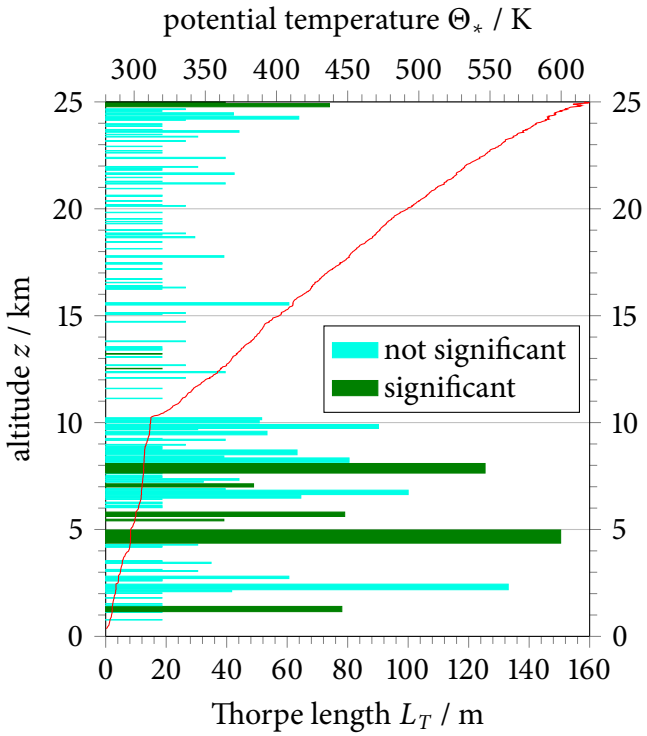

Figure 4.19: Thorpe lengths for the BEXUS 12 flight. The red curve shows the corresponding (composite) potential temperature Θ_*

In Section 5.5, the Thorpe length is compared to the Ozmidov scale obtained from the dissipation rates measured by LITOS averaged over the respective layer. In that way, the assumption of proportionality between both length scales is checked, and values of the constant c_TO^2 are computed. Moreover, results for the energy dissipation rate from both methods are compared.

4.3 WRF model

In order to study the atmospheric background conditions and the role of gravity waves during the BEXUS 8 and BEXUS 12 flights, simulations with the Weather Research and Forecasting (WRF) model, version 3.4 were performed by Johannes Wagner (University of Innsbruck). The

Advanced Research WRF (ARW) core was used which integrates the nonhydrostatic, fully compressible Euler equations on terrain following vertical η coordinates [Skamarock et al., 2008]. Vertically 131 η levels are used with vertical distance varying from 50 m near the surface to about 600 m at the model top at 1 hPa (about 41 km). The horizontal grid uses a stereographic projection centred at 70.4°N, 10°E. The computational domain consists of an outer domain (d1) with 350×300 grid points and an inner domain (d2) with 343×226 grid points. The domain configuration can be seen in Figure 4.20. Initial and boundary conditions are supplied by European Centre for Medium-Range Weather Forecasts (ECMWF) operational analysis on 137 model levels with a temporal resolution of 6 hours.

In Section 5.2, data are visualised as maps on model levels and altitude sections through the launch point (as marked by the green line in Figure 4.20).

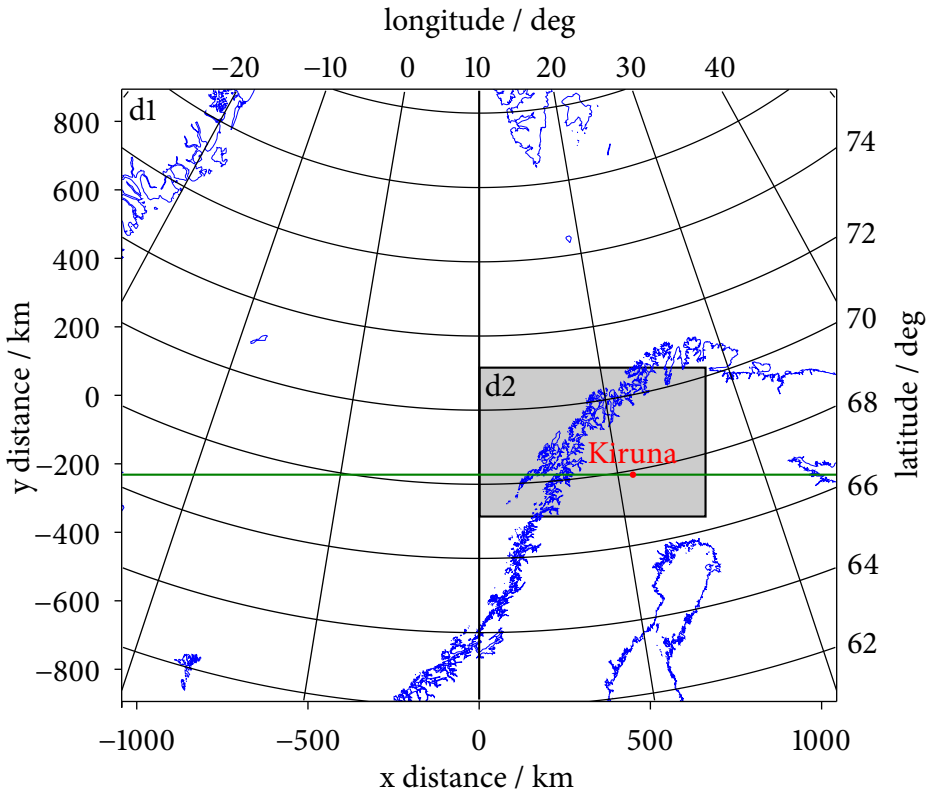

Figure 4.20: Domain configuration for the WRF model runs performed for the BEXUS 8 and BEXUS 12 flights. The large domain d1 consists of the whole map, while the small domain d2 is marked by a grey shading. The green line marks where altitude sections through the launch point are plotted.

5 Geophysical results

Geophysical results obtained within this study are described in this chapter. First, in Section 5.1 turbulence observations during the BEXUS 12 flight from 2011 are presented and related to the atmospheric background conditions measured by the radiosonde. Then that flight is contrasted to the earlier flight BEXUS 8 in Section 5.2. To classify the observations in the geophysical context, model simulations driven by reanalysis data are used. In Section 5.3 relations between dissipation rates measured by wind and temperature fluctuations as well as between kinetic and thermal dissipation are examined. Section 5.4 contains an overview of results obtained from flights with the small payload described in Section 3.2.2. Results from LITOS are compared with those of the Thorpe evaluation of radiosondes in Section 5.5; moreover, the main assumption for such an evaluation, namely a linear relation between Thorpe and Ozmidov length scales, is investigated.

5.1 The BEXUS 12 flight

The LITOS experiment was flown as part of the BEXUS 12 payload at 27th September 2011. See Section 3.2.1 for a description of the flight configuration and experiment details. The results for the turbulence evaluation (as described in Section 4.1) and their relation to the atmospheric background conditions measured by the radiosonde are given in this section.

The left panel of Figure 5.1 shows the temperature (red) and background horizontal wind (blue and green) as measured by the radiosonde. Excepting some small inversion layers, temperatures decrease up to the tropopause at 10.3 km. Directly above the tropopause a sharp increase in temperature is visible. Such kind of feature was first reported by Birner et al. [2002] and is now called tropopause inversion layer (TIL). Above ~12.6 km altitude temperatures slightly decrease. The wind field shows a reversal between ~6 km and 10 km in both components with a strong wind shear below the tropopause. This wind shear entails low Richardson numbers and correlates to highly increased dissipation (see below). Above the tropopause the wind field shows signatures of gravity wave activity with short wavelengths that have no obvious altitude-dependent structure.

The right panel of Figure 5.1 depicts the energy dissipation rate (blue crosses for turbulent regions, non-turbulent regions are left out). Lübken [1993, (3.146)] derived an estimate of the theoretical minimum of the dissipation rate

$$\varepsilon_{\min} \approx \nu N^2 \tag{5.1}$$

by requiring that the turbulent diffusion has to be larger than the molecular one because oth-

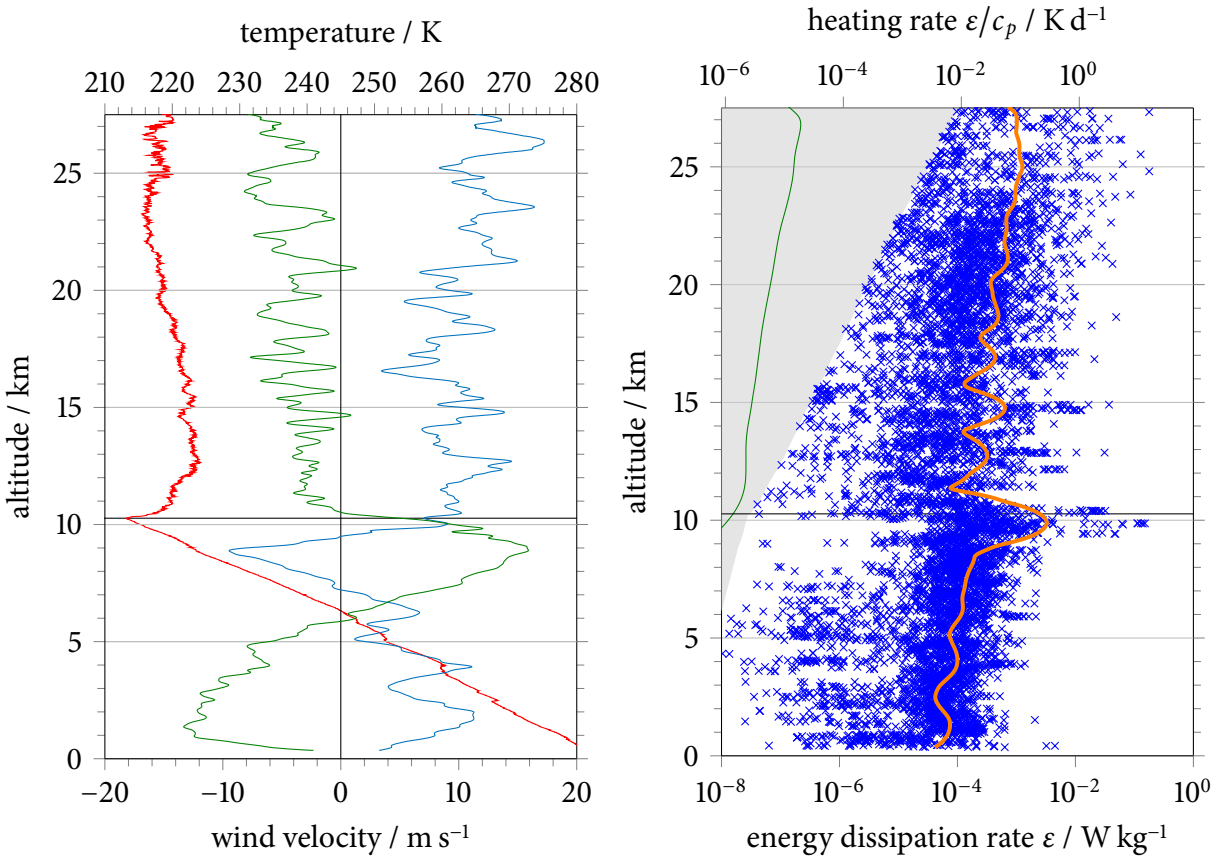

Figure 5.1: Left: Background zonal wind (blue), meridional wind (green) and temperature (red) measured by the radiosonde. Right: Energy dissipation rate (blue crosses) from wind fluctuations measured by LITOS. The orange curve shows a Hann-weighted running average over 2 km. The grey area marks the domain below the technical minimum (cf. Section 4.1.1), the green line the estimation of the theoretical minimum by Lübken [1993, (3.146)]. The horizontal black line in both plots marks the tropopause.

erwise molecular diffusion would destroy turbulent eddies immediately. Alternatively, (5.1) can be deduced from the condition that the size of a turbulent cell has to exceed the mean free path. The theoretical minimum (5.1) is marked in the right panel of Figure 5.1 by the green curve. It is well below the technical minimum (marked by the grey area in the figure), which is given in Section 4.1.1 in form of a maximum for the inner scale, $l_0 < L/25$, where L is the window length (here 5 m). The upper limit to l_0 is imposed to ensure that enough data points are within the fit range to enable a meaningful fit.

The dissipation rates show considerable scatter; within only a few 10 m ε varies over a few orders of magnitude. This represents the well-known intermittency of turbulence.

On the large scale, the dissipation rates evince an overall tendency to rise with altitude, excepting a step to smaller rates at ~10.5 km. The step is located directly above the tropopause. Thus part of it is attributed to the highly increased static stability in the tropopause inversion layer (TIL)

which suppresses turbulence. Since the retrieval of the dissipation rate is independent of the Brunt-Väisälä frequency N (see Section 4.1.1), the drop is not an artefact of the method. Moreover, the wind shear below the tropopause may have filtered a large fraction of the gravity wave spectrum so that further upwards less waves persist that can break and produce turbulence. Just below the step, i. e. at ~10 km altitude, a pronounced maximum in dissipation is found. It can be explained by this very gravity wave filtering. Furthermore, that turbulent layer correlates with high wind shear. Within the upper part of the TIL dissipation rates rise again, while above the TIL at ~12.6 km altitude another drop in dissipation occurs.

By eye, ε values in Figure 5.1 seem to accumulate near 10^{-4} W kg^{-1}. This is confirmed by the geometric mean value of the turbulent data bins of 7×10^{-5} W kg^{-1}, which represents the most frequent value of the lognormally distributed dissipation rates (cf. Section 4.1.1, especially Figure 4.6 on page 42). The arithmetic mean of all bins (including those where $\varepsilon = 0$) is 0.5 mW kg^{-1}, the median is 0.02 mW kg^{-1}. Table 5.1 gives averages for the tropospheric and stratospheric part. The values are larger in the stratosphere compared to the troposphere. A similar behaviour has been found by Theuerkauf [2012, Table 4.5] for the BEXUS 8 and BEXUS 6 flights. A more detailed comparison of BEXUS 12 and BEXUS 8 is found in Section 5.2. The averages of the dissipation rates are in a similar order of magnitude as typical values in the literature. A comparison to dissipation rates found in the literature is presented by Theuerkauf [2012, Section 4.4.3] and Söder [2014, Section 4.3].

Figure 5.2 shows the cumulative occurrence of dissipation rates. Typical solar heating rates in the lower stratosphere are in the order of 1 K d^{-1} [Brasseur and Solomon, 1986, Fig. 4.19b]. Comparable or higher turbulent heating rates are only reached for 1 % of the data bins (i. e. altitude windows classified as turbulent). 90 % have heating rates below 0.1 K d^{-1} which is negligible for the energy budget. Most values are in the order of 10^{-2} K d^{-1}, which corresponds to the mode of the distribution, the geometric mean.

During BEXUS 12, turbulence is observed in the whole altitude range. Overall, 85 % of the troposphere and 52 % of the lower stratosphere has been found to be turbulent (i. e. the spectrum was classified as turbulent, see Section 4.1.1). This is a much higher percentage than expected. However, one should keep in mind that some patches have very low dissipation rates. A comparison to radar measurements is given below.

Typically, turbulence occurs in thin layers. This can already be seen in the raw data, cf. Figure 4.1 on page 36. In order to obtain quantitative results, turbulent layers are identified as a collection of adjacent altitude windows with $\varepsilon > 0$; layers separated by only one non-turbulent

Table 5.1: Mean dissipation rates measured during the BEXUS 12 flight

	arithmetic mean	geometric mean	turbulent fraction
troposphere	0.4 mW/kg	0.04 mW/kg	85 %
stratosphere	0.6 mW/kg	0.1 mW/kg	52 %
whole flight	0.5 mW/kg	0.07 mW/kg	64 %

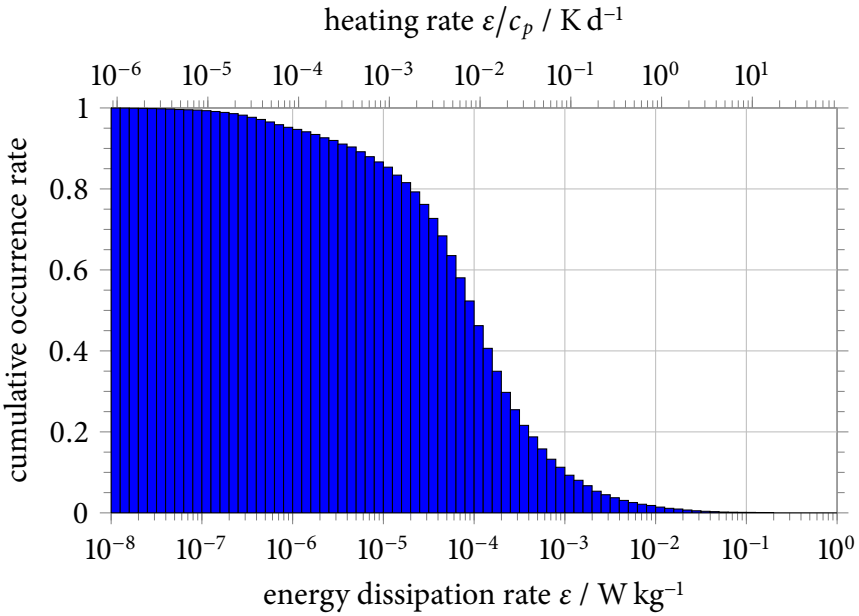

Figure 5.2: Cumulative occurrence of dissipation rates for the BEXUS 12 flight

bin are treated as one. Figure 5.3 shows the statistics of turbulent layers for BEXUS 12. Most frequent are very thin layers consisting of only one data bin. Towards larger thickness the occurrence decreases more or less monotonously. Only a few singular layers are larger than 100 m. The mean layer thickness is 41 m (cyan vertical line in the figure), the median is 18 m (green vertical line). The thickest layer is 570 m. In the troposphere, the average thickness is as large as 99 m, while in the stratosphere it is only 27 m.

Theuerkauf [2012, Section 4.2] used a cluster analysis of raw data to infer layer thickness. She found most layers between 10 m and 50 m with a mean thickness of 46 m for the BEXUS 8 flight and 38 m for the BEXUS 6 flight. Moreover, layers were generally thinner in the stratosphere than in the troposphere. These results are very similar to what is found for BEXUS 12 from the spectral method. Particularly, the mean layer thickness is nearly constant for all three BEXUS flights. The stability of these results independent of the evaluation method makes them even more reliable.

Radiosondes typically can reliably detect layers of 20 m thickness (two bins at 10 m vertical resolution, cf. Section 5.5). 55 % of the layers measured during BEXUS 12 are below that limit. That highlights the importance of high-resolution measurements. A detailed assessment of turbulence evaluation from radiosondes is given in Section 5.5.

Most layers are thinner than the typical vertical resolution of remote sensing instruments. An example at the lower end is the PROUST ST radar (located in France) with a range resolution of 30 m (red vertical line in Figure 5.3). 65 % of the layers are thinner than that value.

Using data from that radar, Wilson et al. [2005] estimated the turbulent fraction in the lower

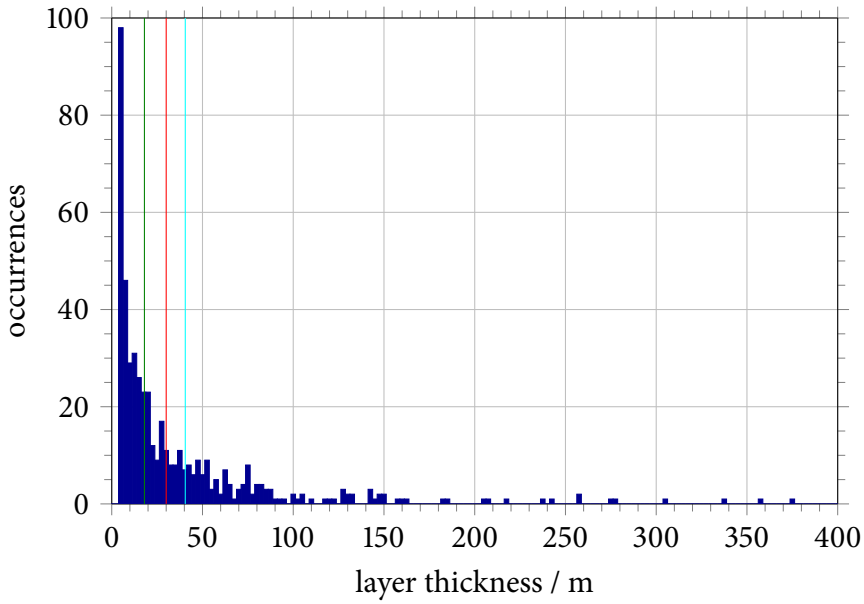

Figure 5.3: Statistics of turbulent layer thickness measured by LITOS. The cyan vertical line marks the mean layer thickness, the green one the median, and the red one the vertical resolution of the PROUST ST radar.

stratosphere between 10 % and 20 %. That is much less than the 52 % observed by LITOS. However, as mentioned above the radar has a range resolution of 30 m and measures dissipation rates between 10^{-5} W kg^{-1} and 10^{-3} W kg^{-1}. These rates are in the same order as the mean values observed by LITOS. 73 % of the stratospheric layers observed by LITOS are smaller than 30 m. Thus, according to the results from LITOS, the radar volume is mostly filled with a mixture of turbulent and non-turbulent air. Additionally, the detection limit is lower than for LITOS. Therefore it is not surprising that the turbulent fraction observed by the radar is much lower. When counting only layers thicker than 30 m with $\varepsilon > 10^{-5}$ W kg^{-1}, the turbulent fraction in the lower stratosphere according to LITOS is only 16 % which is comparable to the radar observations by Wilson et al. [2005] mentioned above.

In the literature, turbulence is often related to the Richardson number $Ri = N^2/S^2$, where $S = \left|\frac{\partial \boldsymbol{u}_\mathrm{h}}{\partial z}\right|$ is the vertical shear of horizontal wind and N the Brunt-Väisälä frequency. The Richardson number represents the ratio of buoyancy forces (which suppress turbulence) and shear forces (which generate turbulence). Miles [1961] and Howard [1961] showed that in a plane-parallel vertically stratified shear flow of an inviscid, non-heat-conducting, incompressible fluid instability (and thus turbulence) occurs for Richardson numbers below a critical one of $Ri_\mathrm{c} = 1/4$. This can be understood by considering the work needed for the exchange of two air parcels with altitude difference Δz, which is proportional to $\Delta z^2(Ri - 1/4)$ [Nappo, 2002, (6.18)]. Later, a value of $Ri_\mathrm{c} = 1$ was suggested [e. g. Canuto et al., 2001]. The Glossary of Meteorology of the American

Meteorological Society [Glickman, 2000, p. 188f] states[1] that the "value is usually taken as Ri_c = 0.25, although suggestions in the literature range from 0.2 to 1.0. There is also some suggestion of hysteresis, where laminar air flow must drop below Ri = 0.25 to become turbulent, but turbulent flow can exist up to Ri = 1.0 before becoming laminar" [cf. Galperin et al., 2007]. The Richardson criterion is commonly used in models to parametrise turbulence.

To examine the relation between turbulence and the Richardson number in the LITOS measurements, Ri is plotted in the right panel of Figure 5.4 with a linear axis below ¼ and a logarithmic one above. The critical number ¼ is shown as red line. Horizontal wind and potential temperature were smoothed prior to differentiation with a Hann-weighted running mean over 90 m in order not to dominate the derivative by measurement noise. The smoothing length has been chosen as the smallest one where the influence of the measurement noise is largely eliminated after experimenting with different values. Larger smoothing lengths tend to result less

1 Online version under `http://glossary.ametsoc.org/wiki/Critical_richardson_number` (vis 10 Jul 2015)

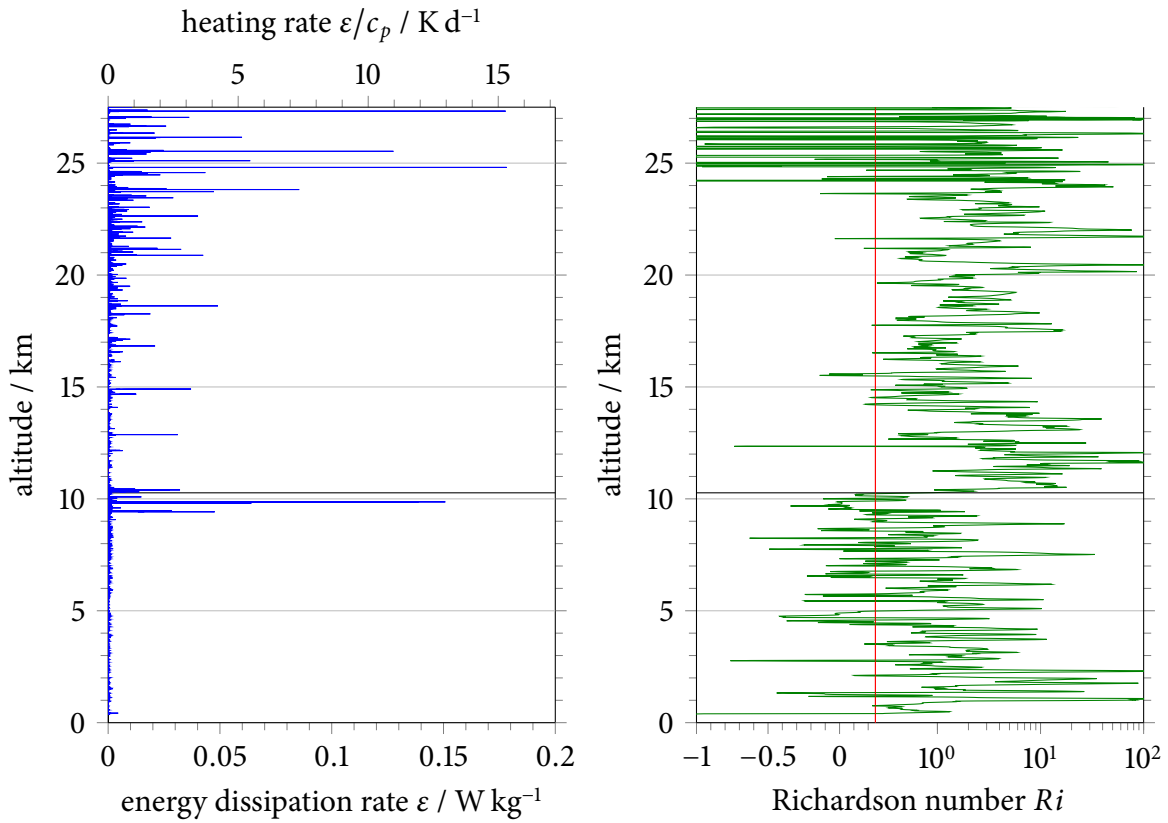

Figure 5.4: Energy dissipation rate (left) and Richardson number (right) for the BEXUS 12 flight. In the right panel, the Ri axis is split at ¼ into a linear and a logarithmic part. The red vertical line shows the critical Richardson number ¼. The black horizontal line marks the tropopause.

regions with $Ri < 1/4$. The left panel of Figure 5.4 presents the same ε profile as the right panel of Figure 5.1, but with a linear ε axis to emphasise the thin layer structure. Just below the tropopause, i. e. at ~10 km height, a large altitude region with low (even negative) Ri numbers is found which is correlated to high dissipation rates. As noted above, this region is marked by strong wind shear. Here, the Richardson criterion is fulfilled. However, there are many altitude regions with large Ri between 10 and 100 where there is also turbulence. Some examples are presented in Figure 5.5. It shows the altitude range from 11.4 km to 12.4 km, where the Richardson number is larger than 1 throughout. At 11.414 km, for instance, a peak in dissipation rate occurs at a maximum of the Richardson number of ~40. Similar behaviour is found at 11.77 km. Several other turbulent layers are correlated to minima of the Richardson number, e. g. at 11.509 km, near 12.03 km, 12.16 km and 12.32 km, although $Ri > 3$ for the whole range. Others are at altitudes where Ri has a gradient, e. g. at 11.60 km, 11.66 km and 11.93 km. Altogether, no clear relation between Richardson number and turbulence is found. A similar behaviour has already been reported by Theuerkauf [2012, Section 5.2] for the BEXUS 6 and 8 flights.

In this work, the Richardson number was computed on different scales than the dissipation rate, namely 90 m (the smoothing of the radiosonde data to eliminate noise dominating the

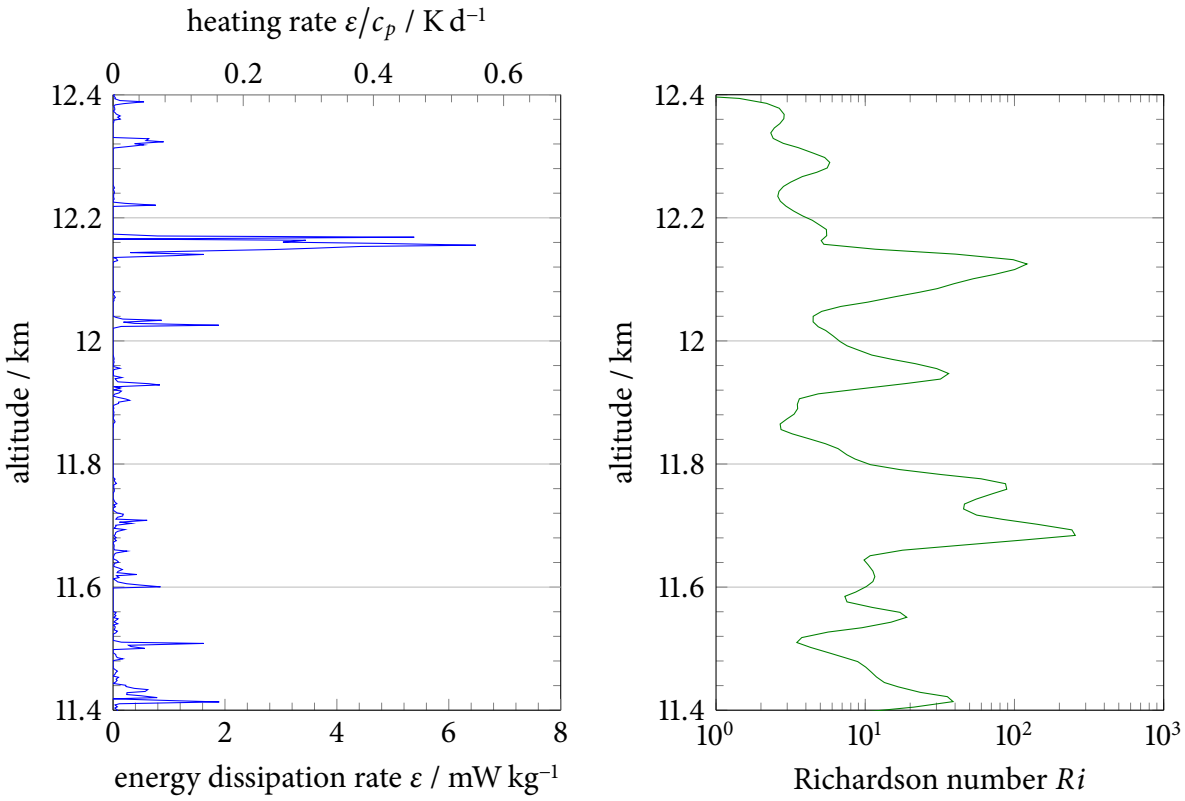

Figure 5.5: Energy dissipation rate (left) and Richardson number (right) for the altitude range 11.4 km to 12.4 km of the BEXUS 12 flight

derivative) versus 5 m (the altitude window length for ε computation). Such a comparison of different scales may be problematic.

Achatz [2005] performed simulations of stable and unstable gravity waves and found instability and onset of turbulence for Richardson numbers both smaller and larger than ¼. He noted that the theory of Miles [1961] and Howard [1961] is not applicable because the gravity wave phase propagation is slanted. In view of this comment it is not that surprising that the Richardson criterion is not fulfilled for the LITOS measurements because in the real atmosphere waves usually propagate inclined, i. e. the shear is not orthogonal to the altitude axis.

Turbulence is important for the mixing of trace species and heat. By analogy to molecular diffusion, that feature is usually described by an eddy diffusion coefficient. The idea is to parametrise the vertical heat flux by the vertical gradient of the mean temperature, i. e.

$$\langle w'T' \rangle = -K \frac{\mathrm{d} \langle T \rangle}{\mathrm{d}z}$$

[e. g. Panofsky and Dutton, 1984, (4.7.4)]. The eddy diffusion coefficient K has dimensions of length times velocity. A relation to the dissipation rate is given by

$$K = \beta \frac{\varepsilon}{N^2} \tag{5.2}$$

[Lilly et al., 1974, (8); Weinstock, 1978, (30)], where β is a constant. Fukao et al. [1994, (10)] expressed β as a function of the flux Richardson number

$$Ri_\mathrm{f} := \frac{\frac{g}{\langle \Theta \rangle} \langle \Theta' w' \rangle}{\frac{\mathrm{d}\langle u \rangle}{\mathrm{d}z} \langle u'w' \rangle},$$

namely $\beta = Ri_\mathrm{f}/(1 - Ri_\mathrm{f})$. A common choice is $Ri_\mathrm{f} = 0.2$ and thus $\beta = 0.25$ [Clayson and Kantha, 2008, Section 2].

Figure 5.6 depicts the eddy diffusivity obtained via (5.2) for the BEXUS 12 flight. Due to the proportionality to ε and because the variation of N^2 is much smaller than that of ε, the structure is similar to the one of the dissipation rate (right panel of Figure 5.1). That means K shows similar large intermittency. It varies between roughly 10^{-5} m^2 s^{-1} and 10^3 m^2 s^{-1}. The mean value is 2 m^2 s^{-1} and the geometric mean 0.1 m^2 s^{-1}. The jump at the tropopause is due to the dependency of (5.2) on N^2.

From older balloon measurements from the 1970s in France, Bertin et al. [1997] obtained values between roughly 10^{-4} and 10^0 m^2 s^{-1} within one large turbulent patch, see left panel in Figure 5.7. That confirms a large intermittency. The range of values is within the one observed by LITOS. The smaller scatter might be due to less vertical resolution and because only an altitude range of 300 m is covered. In other publications only averages are reported. Alisse et al. [2000] estimated K between 0.01 m^2 s^{-1} and 0.02 m^2 s^{-1} from selected turbulent patches measured with a balloon-borne instrument, which is compatible to the geometric mean of the LITOS measure-

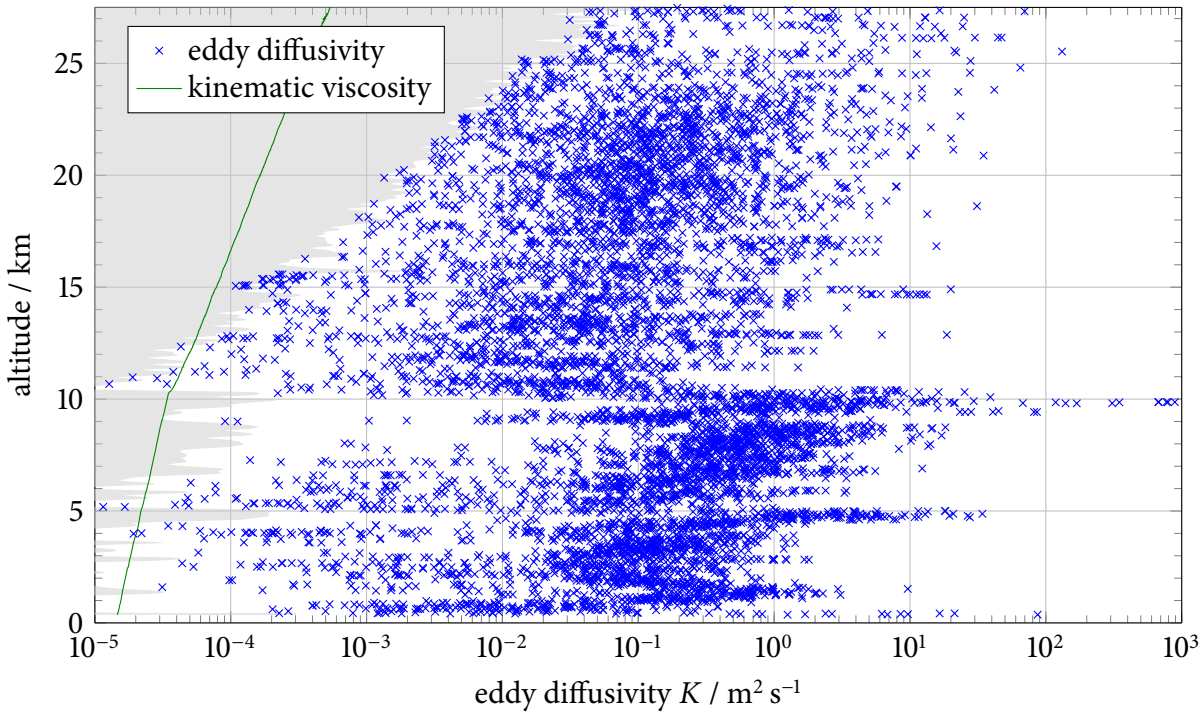

Figure 5.6: Eddy diffusion coefficients (blue crosses) for the BEXUS 12 flight computed via (5.2). The green line shows the kinematic viscosity. The grey area marks the domain below the technical minimum of LITOS.

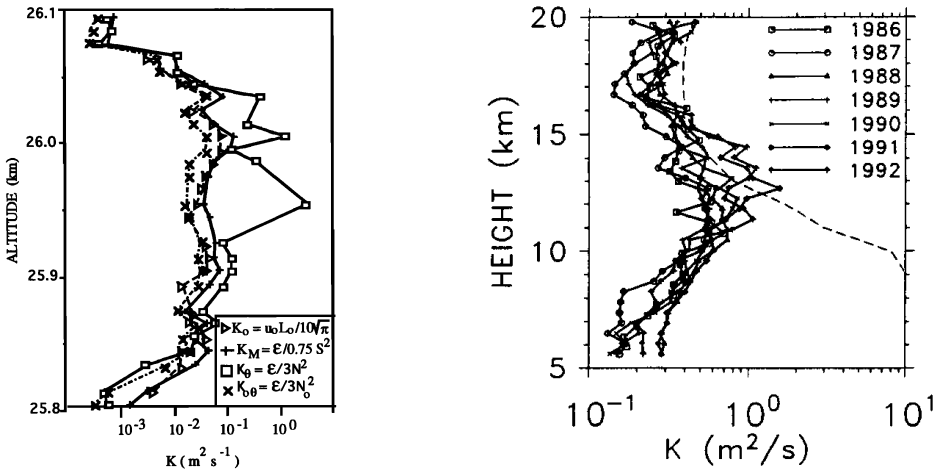

Figure 5.7: Eddy diffusivity measurements found in the literature. Left: Balloon measurement from 28th April 1978 [Bertin et al., 1997]. Right: Annual medians of MU radar data [Kurosaki et al., 1996].

ment, given the large variability. Lilly et al. [1974] observed a dependence on the underlying terrain in aircraft measurements between 14 km and 21 km altitude. They obtained mean values between 1×10^{-2} m^2 s^{-1} and 6×10^{-2} m^2 s^{-1}. Wilson [2004] summarised results from radar measurements. Mainly annual or seasonal medians were given, enabled by the fact that a radar can measure continuously. Exemplary results from Shigaraki, Japan (35° N, 136° E) are shown in the right panel of Figure 5.7. The values range roughly from 1×10^{-1} m^2 s^{-1} to 1 m^2 s^{-1}. Although those measurements took place at different geographic locations, they are consistent with the observations by LITOS.

Hocking [1985, Fig. 1] gave typical values of energy dissipation rates and buoyancy periods for the lower and middle atmosphere. Inserting these values for the lower stratosphere in (5.2) results in typical eddy diffusivities between 6×10^{-3} m^2 s^{-1} and 6×10^{-1} m^2 s^{-1}. The geometric mean observed by LITOS falls within this range, while the arithmetic mean is slightly larger. Turbulent transport seems to have been relatively large during BEXUS 12.

Summing up, turbulence was observed for 85 % of the troposphere and 52 % of the stratosphere and occured in thin patches of typically a few 10 m thickness. Energy dissipation rates are very intermittent in the range 10^{-8} W kg^{-1} to 10^{0} W kg^{-1} with an average of 5×10^{-4} W kg^{-1}. These results are compatible with earlier measurements by Theuerkauf [2012] and, when taking into account different instrumental sensitivities, with radar measurements by Wilson et al. [2005]. Similar to results by Theuerkauf [2012], no general relation between the occurrence of turbulence and the Richardson number is found; particularly, turbulence exists for large Ri of ~100. A pronounced peak in dissipation at roughly 10 km height is explained by a wind reversal in that altitude region, which produces turbulence by filtering gravity waves as well as directly by the shear of the background wind.

5.2 Comparison of the BEXUS 8 and 12 flights and relation to the background atmospheres

The LITOS experiment was previously flown (in a different configuration) on BEXUS 8 launched at 10th October 2009 from Kiruna. The flight took place at similar seasonal conditions as BEXUS 12. Results from this flight are described by Theuerkauf [2012]. Here, the BEXUS 8 and BEXUS 12 flights are compared.

Figure 5.8 presents profiles of dissipation rates for both flights, while Table 5.2 summarises the mean values. The background winds and temperatures measured by the radiosondes are contrasted in Figure 5.9.

Compared to BEXUS 8, during BEXUS 12 slightly more dissipation in the troposphere but considerably less dissipation in the lower stratosphere was observed. Furthermore, while for BEXUS 12 a pronounced maximum was observed below the tropopause (cf. last section), no outstanding peak was seen for BEXUS 8. This is consistent with the fact that in contrast to BEXUS 12 no noticeable wind shear or wind reversal was present during BEXUS 8 (Figure 5.9). That means

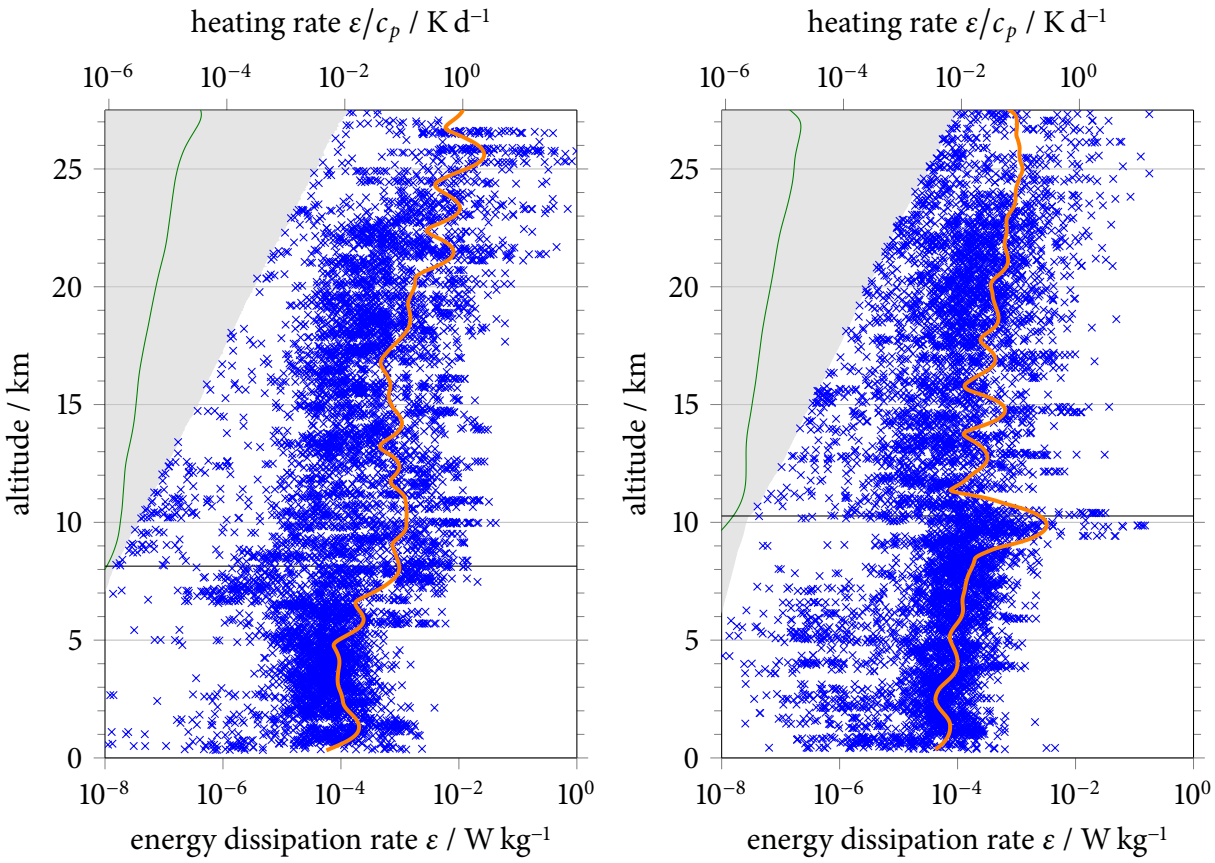

Figure 5.8: Energy dissipation rate (blue crosses) from wind fluctuations measured by LITOS on the BEXUS 8 (left) and BEXUS 12 (right) flights. The orange curve shows a Hann-weighted running average over 2 km. The grey area marks the domain below the technical minimum (cf. Section 4.1.1), the green line the estimation of the theoretical minimum by Lübken [1993, (3.146)]. The horizontal black line in both plots marks the tropopause.

Table 5.2: Mean dissipation rates and turbulent fraction for the BEXUS 8 and BEXUS 12 flights

		BEXUS 8	BEXUS 12
turbulent fraction / %	troposphere	90	85
	stratosphere	52	52
	whole flight	63	64
arithmetic mean ε / mW kg^{-1}	troposphere	0.2	0.4
	stratosphere	4	0.6
	whole flight	3	0.5
geometric mean ε / mW kg^{-1}	troposphere	0.05	0.04
	stratosphere	0.4	0.1
	whole flight	0.2	0.07

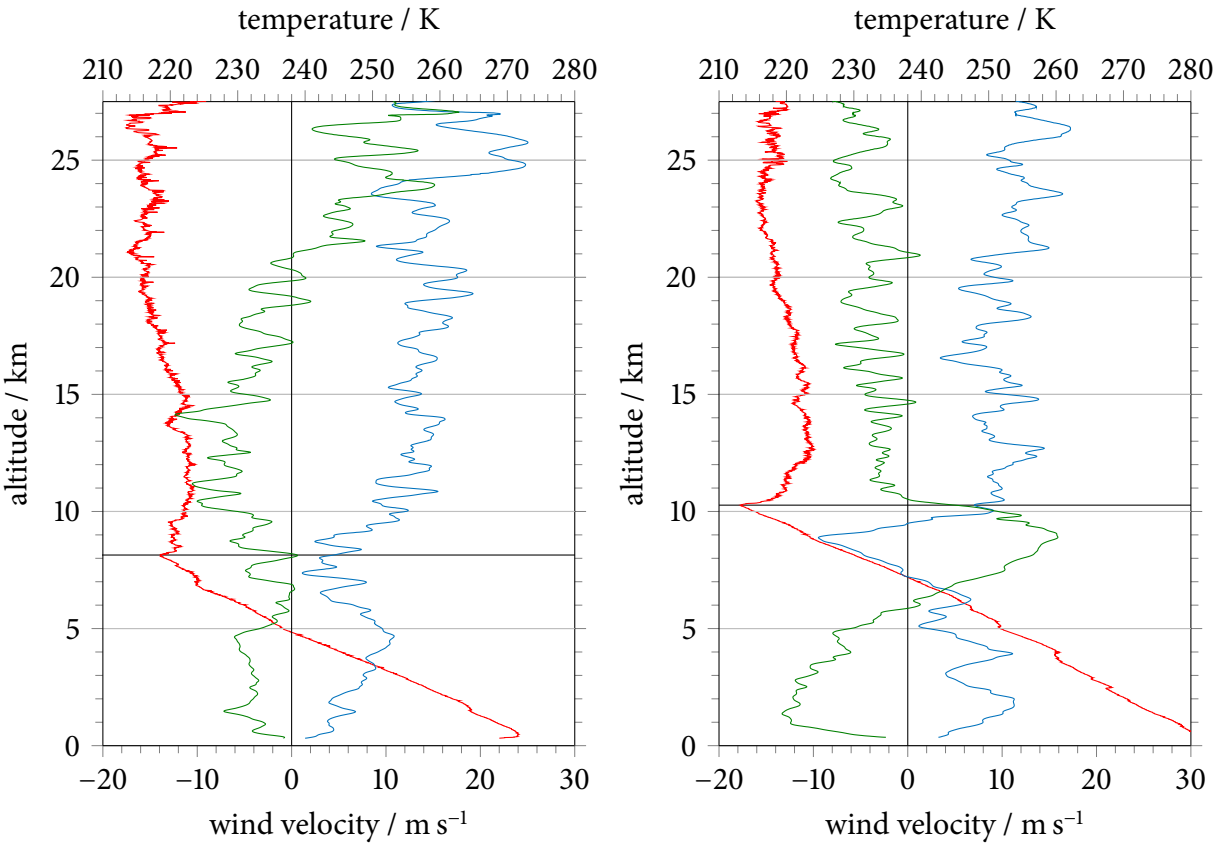

Figure 5.9: Background zonal wind (blue), meridional wind (green) and temperature (red) measured by the radiosondes on the BEXUS 8 (left) and BEXUS 12 (right) flights. The horizontal black line in both plots marks the tropopause.

that no enhanced dynamic instability was present, but also that gravity waves were not filtered below the tropopause and thus could propagate into the stratosphere and break there.

During BEXUS 8, dissipation rates only slightly decreased at the tropopause. The increase in stability does not seem to play a large role for turbulent intensity. In contrast, for BEXUS 12 the decrease in dissipation rate at the tropopause was very pronounced. But that drop is not for the whole part due to the increase in stability; it also coincides with the upper boundary of the layer with large wind shear and gravity wave filtering mentioned above.

To further study the relation of the measurements to the atmospheric background conditions, WRF model runs driven by ECMWF reanalysis data were performed by Johannes Wagner (University of Innsbruck) for both flights. Details of the model configuration can be found in Section 4.3. To get an overview, Figure 5.10 shows tropospheric winds at 850 hPa for the large domain (d1), while Figure 5.11 depicts an altitude section through the launch point (Kiruna).

During both flights, tropospheric westerly winds flowed over the Scandinavian mountains (Figure 5.10). These winds were stronger in 2011, however in 2009 the angle of attack to the

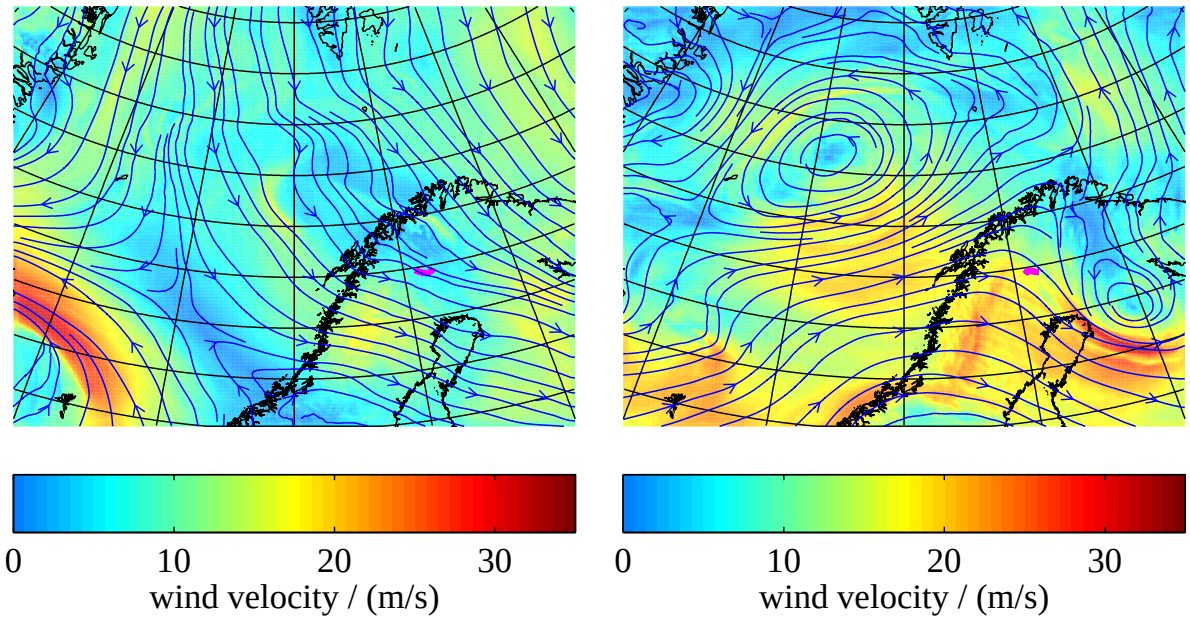

Figure 5.10: Horizontal winds at 850 hPa from WRF model output for 10th October 2009, 9:00 UT (left) and 27th September 2011, 18:00 UT (right) on the large domain (d1). The blue streamlines visualise the wind direction. The magenta lines show the trajectories of the BEXUS 8 and BEXUS 12 flights, respectively.

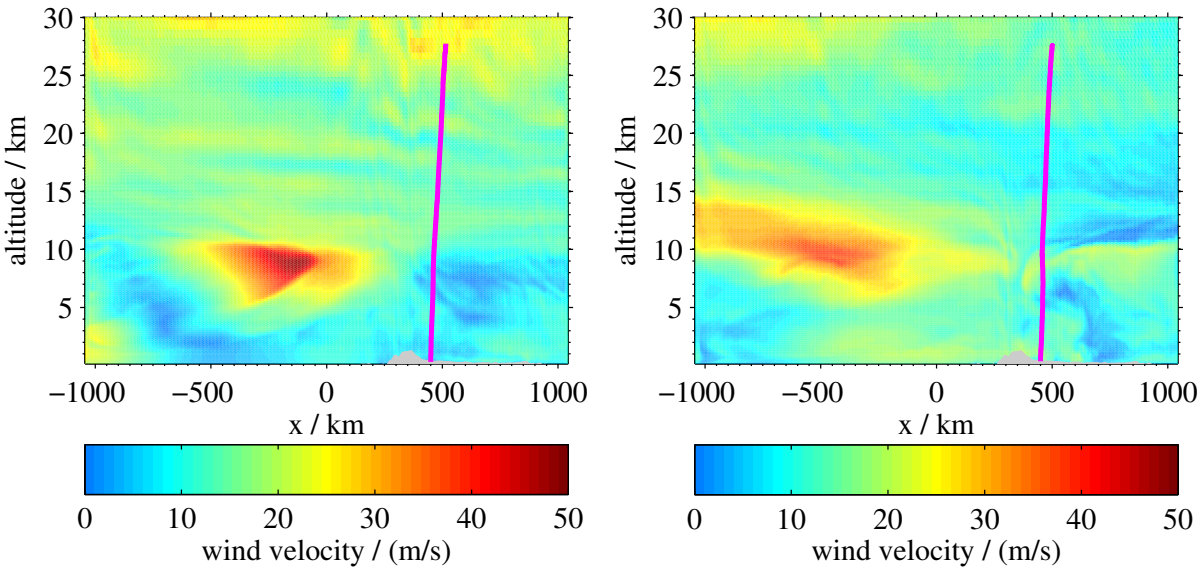

Figure 5.11: Horizontal wind velocity as altitude section through the launch point from WRF model output for 10th October 2009, 9:00 UT (left) and 27th September 2011, 18:00 UT (right) on the large domain (d1). The magenta lines show projections of the trajectories of the BEXUS 8 (left) and BEXUS 12 (right) flights, respectively.

mountains was nearly orthogonal while it was tilted in 2011. The resulting mountain wave activity can clearly be seen, e. g., in the vertical winds and the horizontal divergence; these quantities are plotted in Figure 5.12 and Figure 5.13, respectively. The small domain (d2) was chosen for these plots to make details visible. The wave activity is stronger in 2011, thus the larger wind velocity seems more important than the angle of attack.

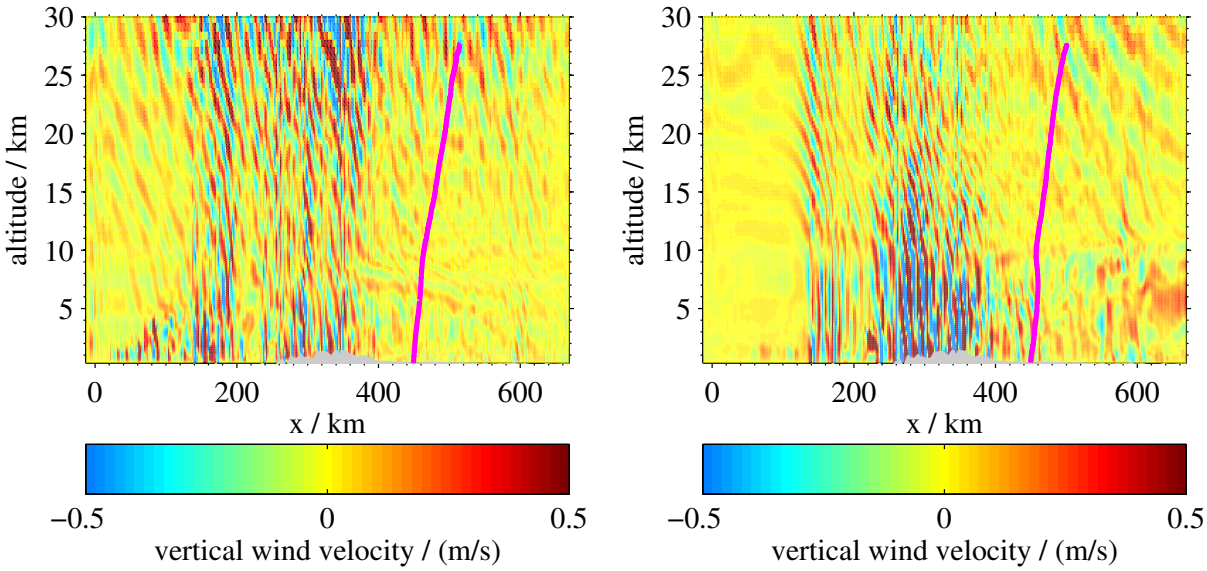

Figure 5.12: Same as Figure 5.11 but showing vertical winds on the small domain (d2).

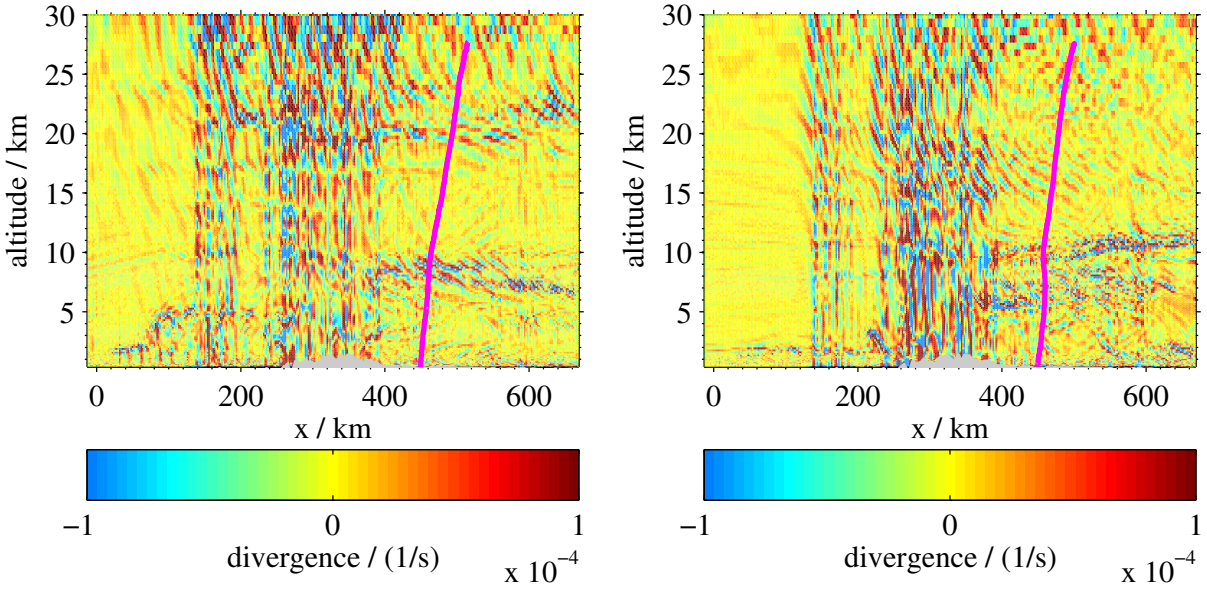

Figure 5.13: Same as Figure 5.12 but showing horizontal divergence.

Waves can also be generated by geostrophic adjustment. Figure 5.14 shows a wind map for 500 hPa. During BEXUS 12, bending streamlines are visible east of the flight trajectory. Wave signatures extending from that region to the eastern boundary of the Scandinavian mountains are visible in the divergence (right panel of Figure 5.13 between ~ x = 400 km and 600 km) and in the vertical wind. However, what fraction of these waves originates from geostrophic adjustment cannot be distinguished. Whatsoever, important is that the waves are there.

For 2009, bending streamlines are present northward of Kiruna, but wind velocities in that area are small. Thus geostrophic adjustment may have occurred only to a small extent, if any.

Waves can propagate over considerable distances and over considerable times. The waves seen in the horizontal divergence and the vertical winds may have originated hundreds of kilometres away and/or hours earlier. Whatsoever, the source is not important, only the presence of the waves.

To trigger turbulence, wave *breaking* is necessary. Such events are triggered by dynamic or convective instabilities or by wave-wave interactions [e. g. Fritts and Alexander, 2003]. However, only large-scale waves are resolved in WRF, and no information on wave breaking is available. But waves are the major source of instabilities and turbulence [Fritts et al., 2013, Section 1]. Therefore, the evaluation concentrates on relating wave activity to turbulence. Wave breaking is often observed accompanying the presence of waves.

In the case of 2011, as mentioned above wave activity is visible eastwards of the Scandinavian mountains where the balloon flew. It ceased to exist at ~10 km altitude (see right panels of Figure 5.12 and 5.13) which is consistent with wave filtering by the jet visible in the horizontal winds

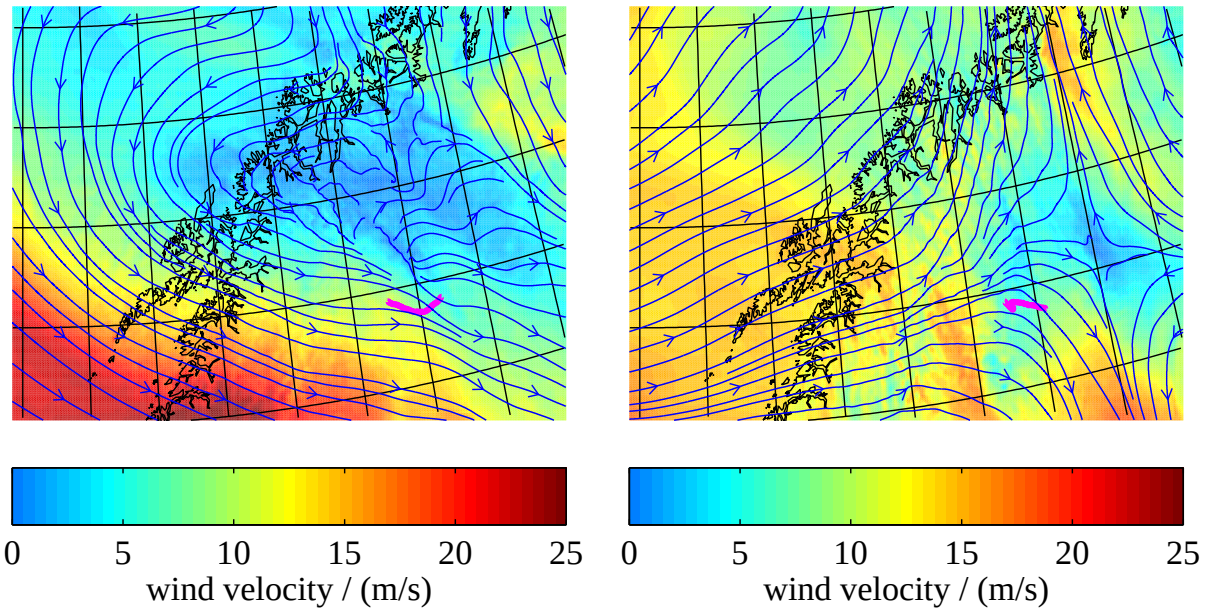

Figure 5.14: Same as Figure 5.10 but showing horizontal winds at 500 hPa for the small domain (d2).

in the right panel of Figure 5.11 (between x = 400 km and 1000 km). The wind reversal has also been measured by the radiosonde (right panel of Figure 5.9). The divergence additionally shows enhanced intensity just below ~10 km altitude (right panel of Figure 5.13). That fits with increased dissipation directly below the tropopause and the step to smaller rates directly above (right panel of Figure 5.8, cf. Section 5.1). New wave activity can be seen at ~15 km.

In the case of 2009, eastwards of the mountains near the flight trajectory smaller wave activity is present, but it extends throughout all altitudes (left panel of Figure 5.12). Consistently, no pronounced jet with wind reversal is present which could have filtered gravity waves (left panel of Figure 5.11). Again, the radiosonde winds show the same behaviour. Fittingly, no drop in the dissipation rate is observed.

All these findings confirm the analysis of the radiosonde data and nicely fit the measured dissipation rates. Higher tropospheric dissipation rates in 2011 come along with more wave activity (compare the left and right panels in Figure 5.12 or 5.13). Conversely, in the stratosphere the wave activity was weaker in 2011 compared to 2009 which results in lower dissipation rates observed by LITOS. That is consistent with the lack of filtering in 2009. However, no clear geophysical cause of the larger stratospheric wave activity can be identified in the WRF data. A hint is that in the stratospheric vertical winds (Figure 5.12) large scale (propagating) waves are visible for BEXUS 12 while a more chaotic behaviour (potentially breaking waves) is seen for BEXUS 8.

Turbulent kinetic energy (TKE) can also be retrieved from the WRF model output. Since this data is intended for use in the boundary layer, it can only be interpreted qualitatively in the upper troposphere and stratosphere. For BEXUS 12, the result is plotted in the left panel of Figure 5.15. The TKE peaks at ~10 km altitude which corresponds to the intense turbulent layer visible in the right panel of Figure 5.8. The fact that it is reproduced in WRF highlights the geophysical significance of that layer.

The model Richardson number (right panel of Figure 5.15) is mostly much larger than 1 (reaching values in the order of 10^9). Only for small regions Ri falls below 2 (coloured area) or even below ¼ (black contours). Here the event at ~10 km is marked as well. Additionally, low Richardson numbers are found between 6.8 km and 7.2 km and between 8.16 km and 8.66 km. At these altitudes, LITOS has observed turbulence, but the dissipation rates do not peak similar to ~10 km.

Summarising, several features, differences and similarities in dissipation measured during the BEXUS 8 and 12 flights can be explained from background meteorological conditions. Particularly, turbulence measured by LITOS is related to gravity wave activity observed in WRF simulations driven by reanalysis data. This hints at a connection between wave activity and wave breaking, e. g. by continuous breaking of a fraction of the waves throughout all altitudes.

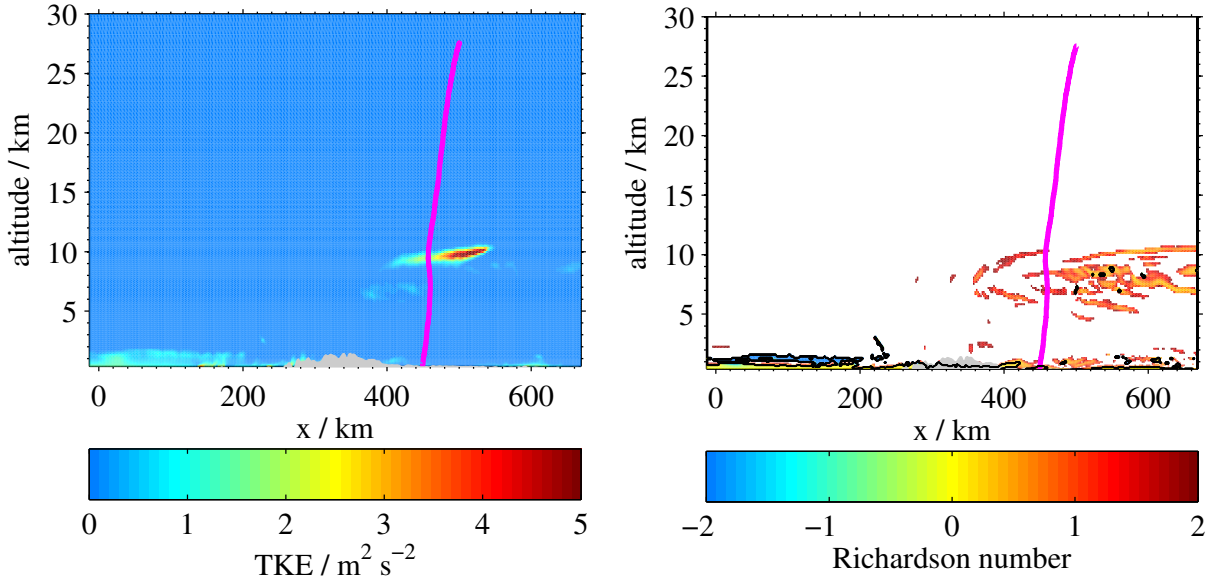

Figure 5.15: Altitude section through the launch point showing turbulent kinetic energy (TKE) (left) and Richardson number (right) from WRF model output for 27th September 2011, 18:00 UT at the small domain (d2). In the right panel, white marks $Ri > 2$ (with a mean of 1×10^9), and black contours mark $Ri \leq 1/4$. The magenta lines show projections of the trajectory of the BEXUS 12 flight.

5.3 Dissipation rates from wind and temperature measurements

Energy dissipation rates ε can be determined from wind as well as from temperature measurements. Theoretically, both should coincide if temperature is a valid tracer (i. e. the background temperature gradient is not equal to the adiabatic one). During BEXUS 8, data from both CTA and CCA sensors were acquired.

Theuerkauf [2012] analysed layer thickness and kinetic dissipation rates ε from both measurements. Using a cluster algorithm she found that turbulent layers in the temperature field are on average significantly thinner than those in the wind field. The mean layer thickness is 46 m for wind fluctuations, differing between 65 m in the tropopause region (7 km to 15 km) and 36 m in the stratosphere (15 km to 27.5 km). For temperature fluctuations the average width is 24 m and does not change significantly for both altitude regions (25 m versus 24 m). Partially these differences may be due to different instrumental sensitivity. The sensitivity of the CTA decreases with increasing altitude, while that of the CCA is independent of altitude. Furthermore, Theuerkauf [2012] notes that kinetic dissipation rates ε_T from temperature fluctuations are on average one to two orders of magnitude larger than those inferred from wind fluctuations (ε_v) "for unknown reasons" [Theuerkauf, 2012, Chapter 6].

Here, the relation of the dissipation rates from both measurements is examined using repro-

cessed data, i. e. the dissipation profiles were newly computed from the raw data using the new set of criteria listed in Section 4.1.1. Moreover, the thermal dissipation rate χ is considered. Due to the uncertainty in altitude assignment for both sensors, profiles computed with a 25 m window (instead of a 5 m one) are used for the comparison.

In the troposphere only few turbulent layers are observed in the temperature data (not shown), probably because the thermal lapse rate is close to the adiabatic one so that the turbulent fluctuations are very small (potentially lower than the measurement noise). In the stratosphere, the layer structure detected by the wind and temperature measurements is similar. Figure 5.16 shows an example of ε from wind (left panel) and temperature fluctuations (centre panel) for an altitude range from 12 km to 12.7 km. Most (strong) turbulent layers have been detected by both measurements (i. e. the spectrum is classified as turbulent), and also the variation of the magnitude of ε with altitude is similar. The correlation coefficient between ε_v and ε_T is 0.74. However, the absolute values differ by roughly one order of magnitude. This discrepancy has already been noted by Theuerkauf [2012].

For better comparison, the ratio of both dissipation rates for the whole flight is plotted in Figure 5.17. Only data bins where both sensors have observed turbulence are included. Apart from

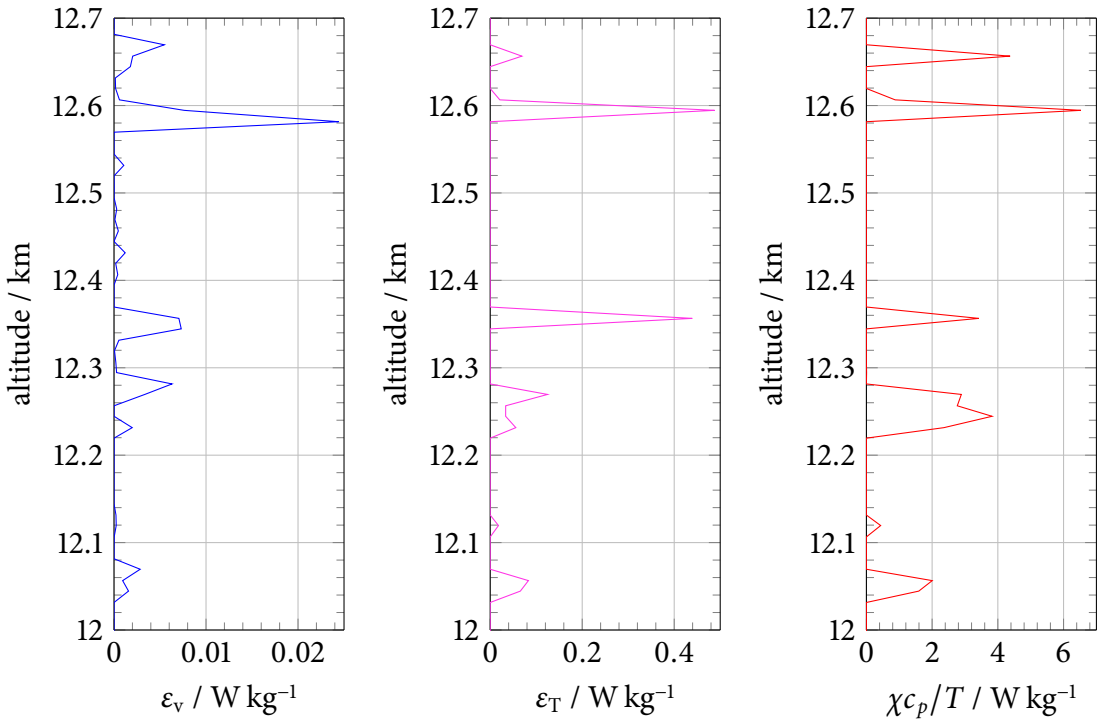

Figure 5.16: Altitude profile of dissipation rates for the BEXUS 8 flight for the range 12 km to 12.7 km: Kinetic dissipation rate from wind fluctuations (ε_v, left), kinetic dissipation rate from temperature fluctuations (ε_T, centre) and thermal dissipation rate $\chi\, c_p/T$ from temperature fluctuations (right). Please note the different scales of the dissipation axes of the three panels.

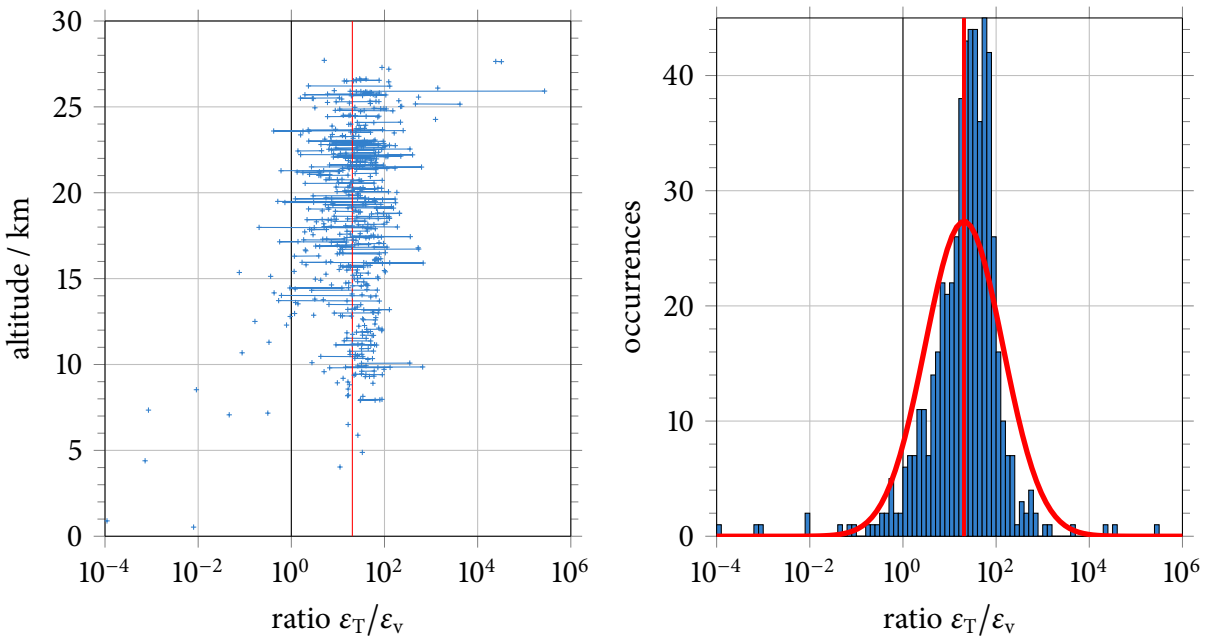

Figure 5.17: Ratio $\varepsilon_T/\varepsilon_v$ of kinetic dissipation rates obtained from temperature and wind measurements. Shown are an altitude profile (left) and a histogram (right). The red vertical line marks the geometric mean or most probable value, the red curve in the right panel the most probable normal distribution of the logarithmic data.

the lack of simultaneous layers in the troposphere already mentioned above, no pronounced altitude dependence of the ratio can be identified. The histogram shows a nearly lognormal distribution centred around 20, the geometric mean of the ratios. This offset suggests a systematic bias. It may originate from wrong values for the constants $c_{l_0,v}$ and $c_{l_0,T}$ in the formulas for determining ε from l_0, (2.22). The values for c_{l_0} depend on empirical constants such as the structure function constant which are not precisely known. Moreover, while Theuerkauf [2012] used a value for $c_{l_0,v}$ that is smaller than that of $c_{l_0,T}$, the values given by Hocking [1985] obey the opposite relation, i. e. $c_{l_0,v} > c_{l_0,T}$. Solely the ratio of the values for wind and temperature fluctuations used in this thesis, $c_{l_0,v}/c_{l_0,T}$, makes a difference of a factor of 13 in ε, cf. (2.24) and (2.26) in Section 2.3. See Section 2.3 for a discussion of the different values of c_{l_0}. Furthermore, the assumptions of isotropic, homogeneous and stationary turbulence might be not fulfilled.

The full width at half maximum of the distribution is 0.8 orders of magnitude. This is above the uncertainty estimated for the computation of ε in Section 4.1.2, which is roughly a factor of 4. That hints that the uncertainty determined in Section 4.1.2 may be underestimated, or there may be a systematic error. The assumptions of isotropy, homogeneity and stationarity might be not fulfilled. Another possibility is that the theoretical basis behind the evaluation method may need improvement. For instance, the form of the structure function is crucial for the determination of ε from temperature fluctuations. The structure function is deduced from dimensional analysis.

If in this deduction, for example, $\tilde{\chi} = \chi c_P/T$ would be used instead of χ (an obvious choice when taking into account the nature of dissipation discussed in Section 2.2), which has a different dimension, the results would be different.

Another point of interest is in the relation between the kinetic and thermal dissipation, ε and $\chi c_p/T$. The factor c_p/T is needed to obtain the dimensions of a dissipation and thus comparability, cf. (2.17) and (2.9) in Section 2.2. The thermal dissipation rate χ is obtained as second fit parameter from the fit of the turbulence model (2.28) to the spectrum of the observed temperature fluctuations, see Section 4.1. The thermometer voltages are converted to temperatures prior to the analysis to enable correct absolute values of the PSD. The right panel of Figure 5.16 displays part of the altitude profile of $\chi c_p/T$. Similarities to the kinetic dissipation rate ε (centre and left panels) are visible. The correlation between ε_T and $\chi c_p/T$ is as high as 0.77, that between ε_v and $\chi c_p/T$ only 0.56. The higher correlation in the first case is not surprising because the measurements of ε_v and χ are independent, while ε_T and χ are determined from the same spectrum. For example, when no significant temperature fluctuations are observed and thus the thermal spectrum is classified as non-turbulent, ε_T is zero, although velocity fluctuations and kinetic dissipation may be present.

To further investigate the relation between ε and χ, the ratio $\varepsilon_T/(\chi c_p/T)$ of kinetic and thermal dissipation rates measured by temperature fluctuations is presented in Figure 5.18. The altitude

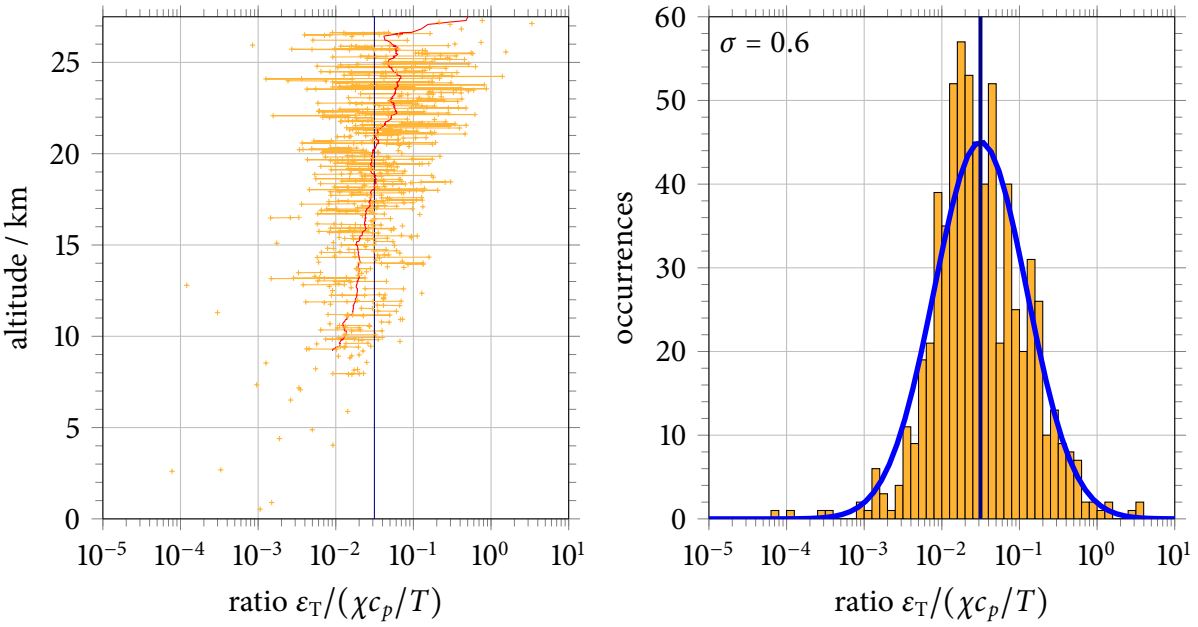

Figure 5.18: Ratio of kinetic and thermal dissipation rates ε_T and $\chi c_p/T$ measured by temperature fluctuations. Left: altitude profile (orange); the blue vertical line marks the geometric mean, the red curve a logarithmic running mean over 5 km. Right: histogram (orange); the blue curve marks the most likely normal distribution of the logarithmic data, the blue vertical line the most probable value.

profile (left panel) shows a small height dependence. As visualised by the logarithmic running mean (red curve), the ratio generally increases with altitude but stays below 1. The histogram (over all altitudes, right panel) shows a clear lognormal behaviour. A fitted lognormal distribution (blue curve) shows a good agreement to the data. The mode is 0.03 (vertical blue line), i. e. χ is typically larger than ε.

As mentioned above, both ε_T and χ are obtained from the same spectrum and are thus not completely independent. Therefore the relation between the kinetic dissipation rate from the wind measurement and the thermal dissipation rate (where χ is of course from the temperature measurement) is examined in Figure 5.19. The ratio $\varepsilon_v/(\chi c_p/T)$ shows a broader distribution than $\varepsilon_T/(\chi c_p/T)$ and resembles the lognormal distribution less well. There is no obvious altitude dependence of the ratio (left panel), in contrast to the relation of ε_T to $\chi c_p/T$ described above.

The statistics may be biased by the fact that bins with $\varepsilon = 0$ are not included; however, values of zero or infinity make no sense on a logarithmic scale. Furthermore, because ε_v and ε_T are correlated, the two statistics presented in Figure 5.18 and 5.19 are not fully independent. But due to the unclear relation both are considered.

To the author's knowledge, this is the first examination of measured kinetic and thermal dissipation rates. Thus comparison is possible only with model results.

Gaßmann [private comminication] finds in simulations with ICON-IAP that the kinetic dissipation typically peaks at slightly lower altitudes than the thermal dissipation. The reason is that vertical velocity components of turbulent motions increase the temperature difference to

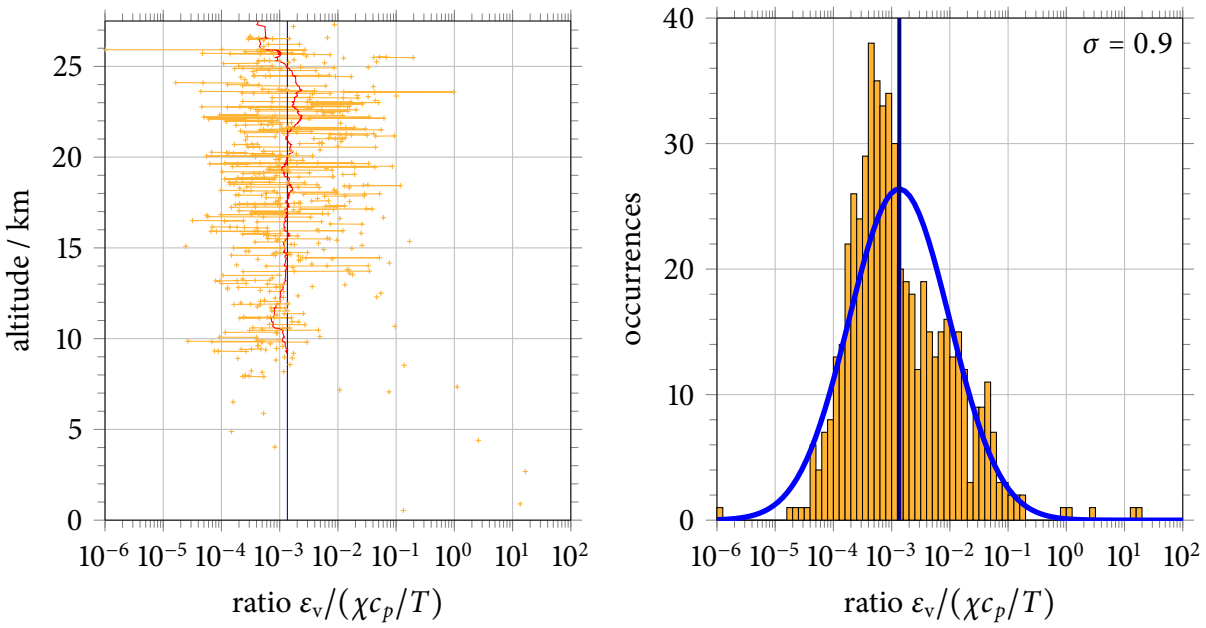

Figure 5.19: Same as Figure 5.18, but for the ratio of kinetic and thermal dissipation rates ε_v and $\chi c_p/T$ measured by wind and temperature fluctuations, respectively.

the level directly above which drives thermal dissipation.

In the LITOS data, χ and ε_T from temperature always peak at the same altitudes. An important reason is probably that both are obtained from the same spectrum. While that does not prescribe the relation in *magnitude*, no kinetic dissipation can be observed with this method where no significant temperature fluctuations are present, although wind fluctuations may be present. Such situations are commonly seen in the raw data. Thus mainly the comparison between ε_v and $\chi c_p/T$ is physically meaningful.

Layers in ε_v from the wind measurement in several cases start slightly below corresponding layers in χ (from the temperature measurement); examples in Figure 5.16 are the layers from 12.57 km to 12.61 km and from 12.33 km to 12.37 km. Such an offset in altitude can also be seen in the fluctuations, see e. g. Figure 4.1 on page 36. However, in several other cases layers in ε_v and χ start simultaneously, e. g. from 12.03 km to 12.08 km and from 12.22 km to 12.29 km in Figure 5.16.

Fritts and Wang [2013] compared ε and $Ri\chi$ of direct numerical simulations. The correlation between both fields is generally large, but "approximate spatial coherence does not imply that the dissipation fields exhibit similar responses". The degree of correspondence depends on event character and stage of evolution. Generally, the correlation is weak where strong mixing has occurred. Fritts et al. [2015, e. g. Fig. 9a, b] found for Kelvin-Helmholtz events that the thermal dissipation peaks at the outer portions of the KH billows while the kinetic dissipation typically peaks at the centre.

LITOS is expected to measure events of different origins and stages and thus varying correlations between both kinds of dissipation. In this light, a correlation coefficient of 0.56 between ε_v and $\chi c_p/T$ is within the expected margin.

Of course, one flight cannot resemble the whole story. Further investigations regarding this basic relationship are necessary. For instance, more flights with both sensors would be interesting.

In this section kinetic dissipation rates measured simultaneously with two different instruments, namely by wind and by temperature fluctuations, are compared. The values have a systematic offset of more than an order of magnitude and the ratio also scatters by nearly an order of magnitude. That hints that the value of the constants (2.24) and (2.26) may be incorrect, or at potential inconsistencies and limitations of the turbulence theory used for the evaluation.

Moreover, the first comparison of measured kinetic and thermal dissipation rates was performed. No clear relationship is found, but $\chi c_p/T$ typically is larger than ε.

5.4 Flights with the small payload

To date, three flights with the small LITOS payload are available that yielded high quality data. Those were launched at 27th March 2014, 6th June 2014 and 12th July 2015 from Kühlungsborn. The first two of these flights were already analysed and related to atmospheric background conditions based on Global Forecast System (GFS) model data by Söder [2014, Chapter 4]. Some

results are repeated here and some new ones added. The dissipation profiles shown below are reprocessed with the new set of criteria listed in Section 4.1.1.

A detailed description of the payload can be found in Section 3.2.2. The flight configuration contained two CTA sensors. For the latest flight one of them had the wire oriented horizontally.

Since both CTA sensors were only approximately 10 cm apart, Söder [2014] used the simultaneous measurement of turbulence with both sensors as compliance criterion. No such criterion is applied here in order to be comparable to the results of the BEXUS flights.

5.4.1 27th March 2014

A balloon with a spherical payload was launched from Kühlungsborn at 27th March 2014, 11:10 CET. The left panel of Figure 5.20 shows the atmospheric background conditions measured by the radiosonde. The wind field (blue and green curves for zonal and meridional components,

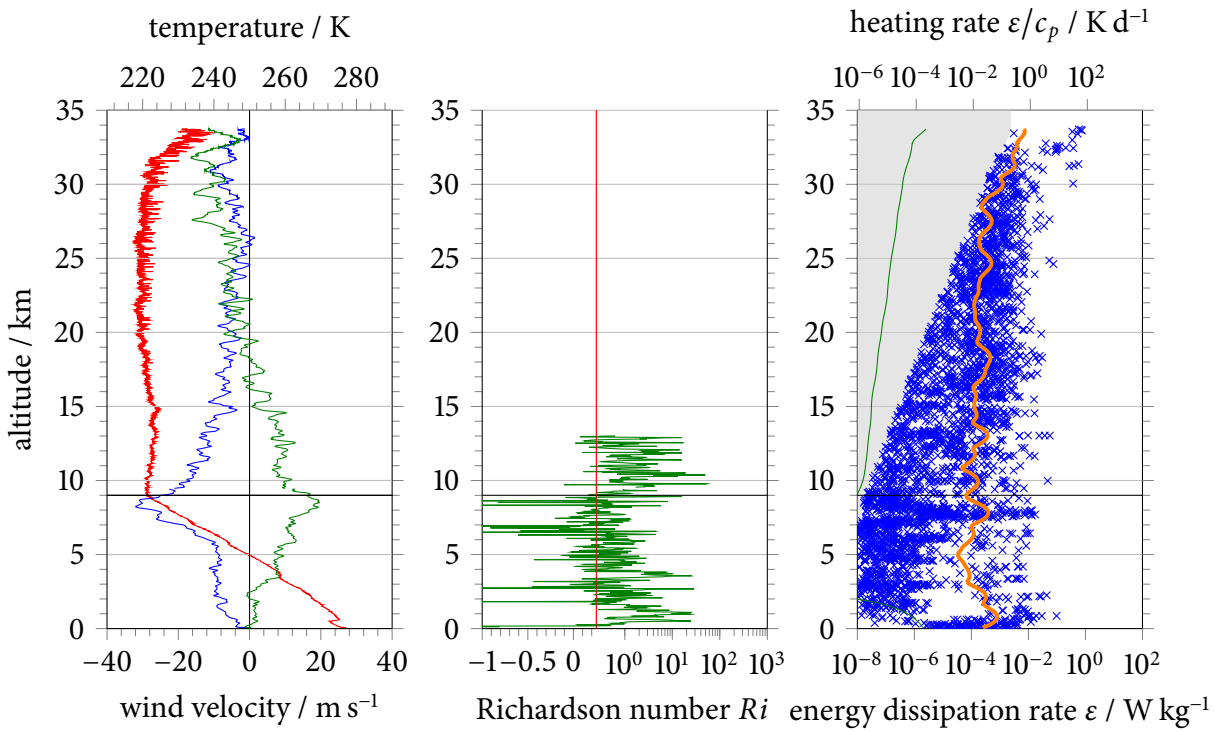

Figure 5.20: Results for the LITOS flight from 27th March 2014. Left: Background zonal wind (blue), meridional wind (green) and temperature (red) measured by the radiosonde. Centre: Richardson number with Ri axis split at ¼ into a linear and a logarithmic part. Right: Energy dissipation rates (blue crosses) from wind fluctuations measured by CTA sensor 1. The orange curve shows a Hann-weighted running average over 2 km. The grey area marks the technical minimum (cf. Section 4.1.1), the green line the estimation of the theoretical minimum by Lübken [1993, (3.146)]. The horizontal black line marks the tropopause.

respectively) reveals a relatively strong jet stream. Apart from that, only signatures of small-scale gravity waves can be seen. Temperatures (red curve) decreased up to the tropopause at 9 km, above which the lower stratosphere was more or less isothermal. Above ~30 km temperatures increased. The temperature measurement is disturbed (mainly in the stratosphere); the probable reason is radiation effects, because the radiosonde was incorporated in the main payload during this flight, cf. Söder [2014, Section 3.2.3]. Thus, evaluation involving derivatives of the temperature, e. g. the computation of Richardson numbers, is not possible for altitudes above ~13 km.

Dissipation rates (right panel) reached a maximum between ~7.5 km and 8 km. The maximum correlates with high wind shear (left panel) and entails relatively low Richardson numbers between approximately −0.2 and 1 (centre panel). Another, less pronounced maximum in ε is found from ~6 km to 6.5 km. Here Richardson numbers were in the same order and even lower down to −1.5. Similar to the BEXUS flights, a general increase of dissipation rates with altitude was observed on the large scale. Mean dissipation rates are 0.2 mW kg^{-1} in the troposphere and 0.9 mW kg^{-1} in the stratosphere. This is in the same order of magnitude as for the BEXUS 12 flight.

Turbulence is related to breaking gravity waves. Thus Söder [2014, Section 4.4] examined possible sources of such waves, namely flow over topography (mountains), geostrophic adjustment and convective generation. Although the mere existence of gravity waves is no cause of turbulence, as already mentioned in Section 5.2, they have to exist in order to break. Since no information about wave breaking is available, wave activity is considered.

As seen in the left panel of Figure 5.21, winds blew from eastern directions where no consider-

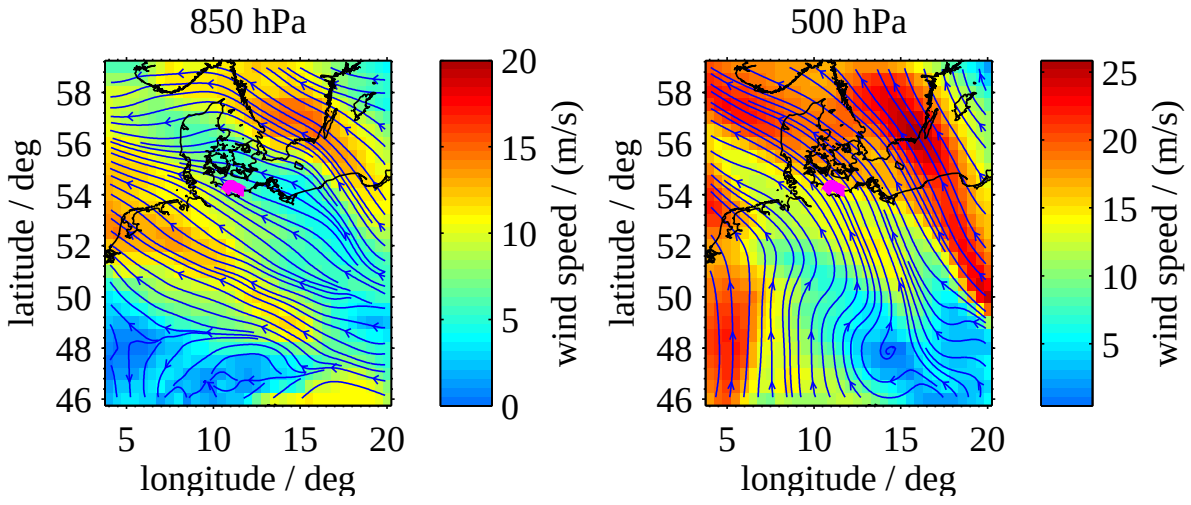

Figure 5.21: Horizontal winds at 850 hPa (left) and 500 hPa (right) from GFS run from 27th March 2014 6 UT, 6 h forecast. The blue streamlines visualise the wind direction. The magenta line in both panels shows a projection of the flight trajectory.

able mountains are located. Thus no significant mountain wave generation is expected. The flow at 500 hPa (right panel) was stable parallel from the south-south-east so that no geostrophic adjustment was possible. Convective available potential energies were very low (not shown). Söder [2014, Section 4.4] concluded that tropospheric gravity wave motion was low, but stratospheric activity may have been caused by strong wind shear near 500 hPa. The wind shear originated from the jet visible in the left panel of Figure 5.22 and potentially produced shear instabilities and turbulence.

The right panel of Figure 5.22 depicts an altitude profile of horizontal divergence. Such profiles were not considered by Söder [2014]. As mentioned in Section 5.2, this quantity is commonly used as a proxy for gravity waves. Wave-like structures are visible over the whole altitude region. This is no contradiction to few sources of waves described above because the waves may have propagated to Northern Germany from distant points.

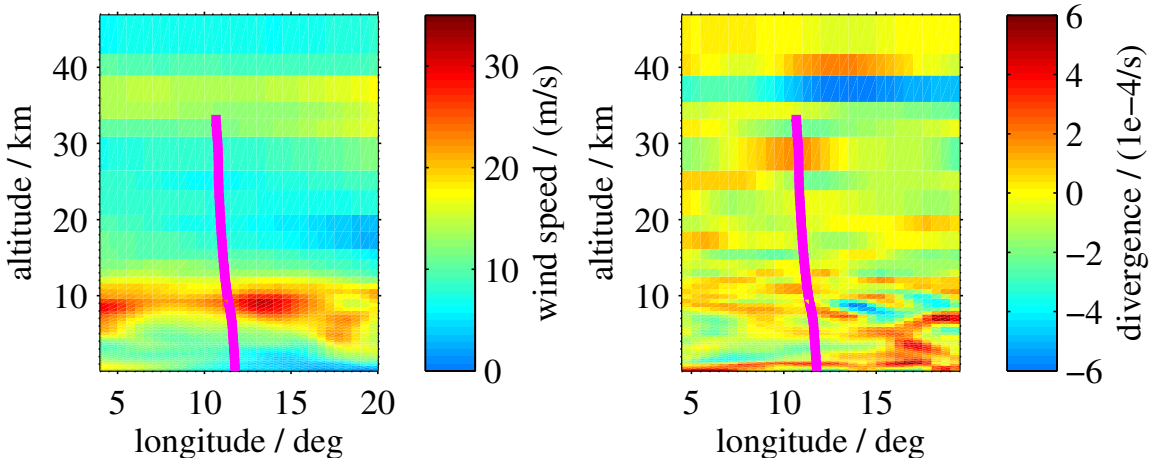

Figure 5.22: Horizontal winds (left) and horizontal divergence (right) as altitude section at 54° N from GFS run from 27th March 2014 6 UT, 6 h forecast. The magenta line in both panels shows a projection of the flight trajectory.

5.4.2 6th June 2014

During the flight launched at Kühlungsborn at 6th June 2014, 11:32 CEST, a new CTA Wheatstone bridge by Dantec Dynamics was tested. For comparison, a classical Wheatstone bridge was operated at the other channel. The result of the test is described in detail by Söder [2014]. Essentially, the new Wheatstone bridge has a large non-Gaussian noise, which makes signal analysis difficult. Thus only the results from the old Wheatstone bridge are analysed here.

The atmospheric background observed by the radiosonde is shown in the left panel of Figure 5.23. As for the previous flight, the radiosonde was incorporated in the payload and thus the temperature measurement disturbed by radiation effects. Temperatures decreased up to the

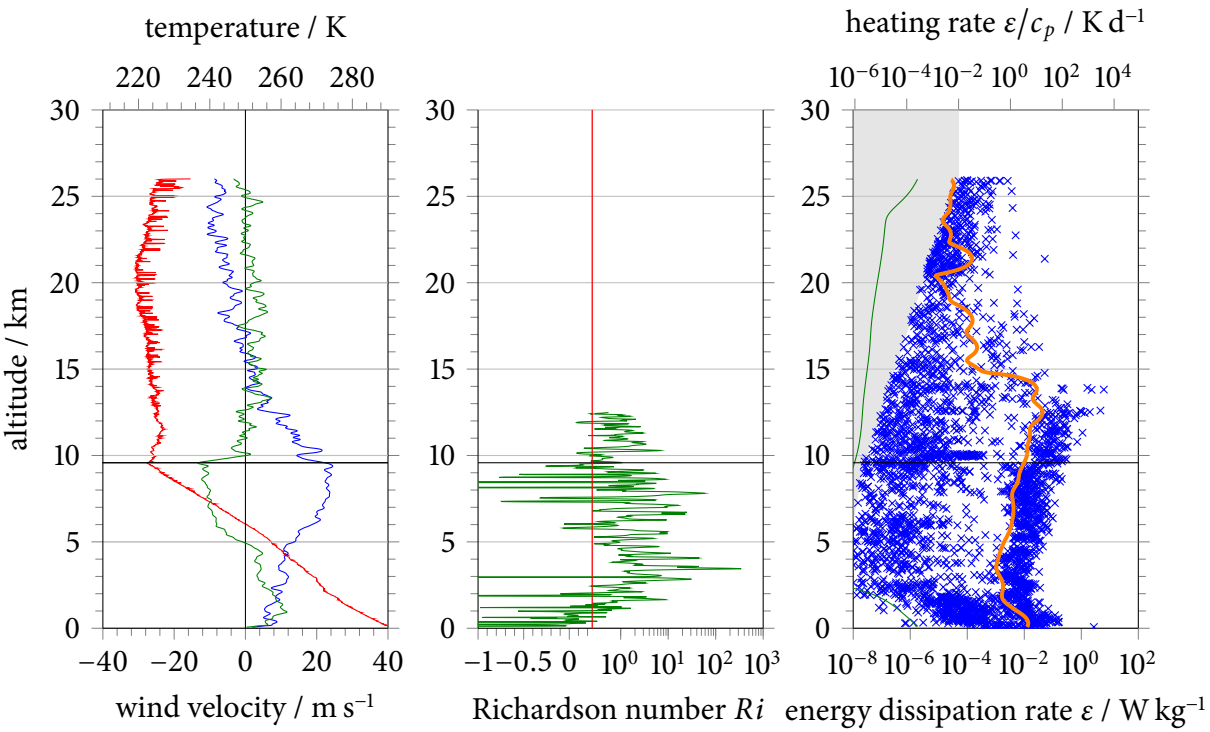

Figure 5.23: Like Figure 5.20, but for the flight at 6th June 2014. The dissipation profile (right panel) is based on the data from the old Wheatstone bridge.

tropopause, above which they did not change much. Winds came from south-western directions and were generally weak. The jet was also weaker than at 27th March. Directly above the tropopause a strong wind shear was present. However, due to the stable stratification at that altitude Richardson numbers were above ¼ (centre panel). Low Richardson numbers mainly appeared in the upper troposphere.

Dissipation rates were large below ~13 km altitude (right panel of Figure 5.23). Above they dropped to low values. This is visible in the running average (orange curve in the ε profile) and in the mean values: The mean dissipation rate from ground to 14 km is 11 mW kg^{-1}, the one above 14 km is only 0.1 mW kg^{-1}. Between the tropopause and 14 km the average is as high as 24 mW kg^{-1}, while in the troposphere it is 4 mW kg^{-1}

Atmospheric background conditions from GFS model data are depicted in Figure 5.24. Söder [2014, Section 4.4] noted that the northwards winds near ground nearly perpendicular to the German Central Uplands were a potential source of mountain waves (see left panel). Moreover, relatively high values of convective available potential energy (CAPE) of up to 1000 J kg^{-1} were present above Denmark and the Baltic, and even in northern Germany 200 J kg^{-1} were reached (not shown). Thus convective creation of gravity waves was likely. Furthermore, bending streamlines were present west of the flight path and near Denmark (right panel of Figure 5.24) which may have effected geostrophic adjustment. Due to this multitude of sources, Söder [2014, Sec-

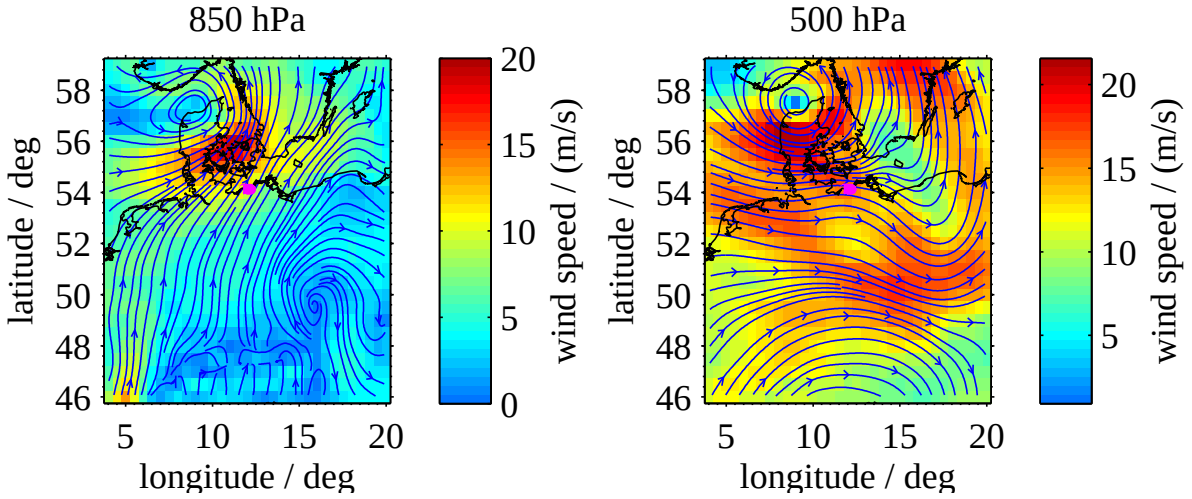

Figure 5.24: Like Figure 5.21, but for GFS run from 6th June 2014, 6 UT, 6 h forecast

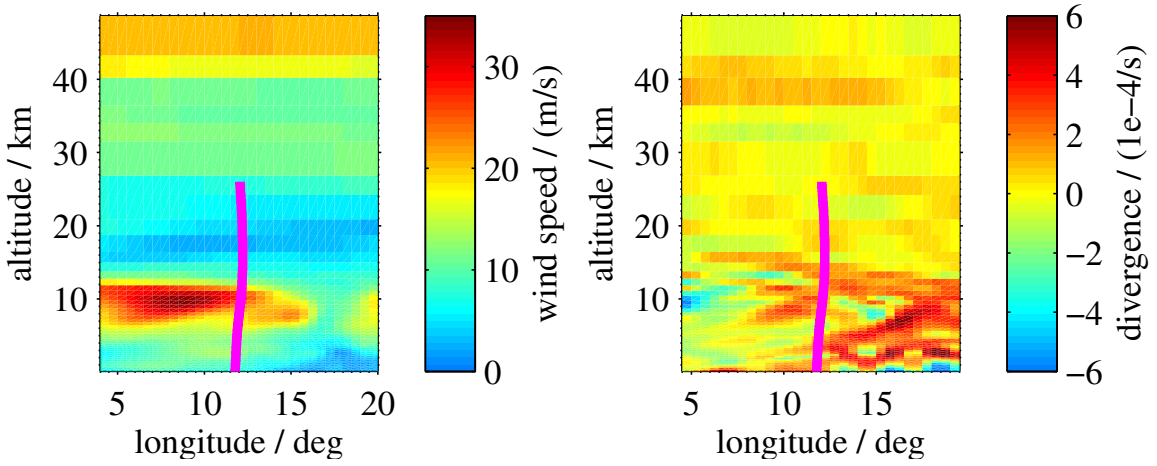

Figure 5.25: Like Figure 5.22, but for GFS run from 6th June 2014, 6 UT, 6 h forecast

tion 4.4] expected high wave activity which can explain the high dissipation rates observed by LITOS.

Wave activity is visible in the horizontal divergence (right panel of Figure 5.25). Wave-like structures are present below ~15 km altitude but become very weak above. This corresponds to the sharp drop in dissipation rate at that altitude.

The left panel of Figure 5.25 shows an altitude section of horizontal wind velocity. The jet was of similar extent than for the previous flight.

5.4.3 12th July 2015

At 12th July 2015, 00:01 CEST a small LITOS payload was launched at night time for the first time. The configuration contained two CTA sensors, thereof one with the wire oriented vertically as usual and the other one with the wire oriented horizontally. The idea for this configuration was to test the influence of the wire orientation.

The left panel of Figure 5.26 shows the background parameters measured by the radiosonde. Westerly winds prevailed up to ~18 km, whereas above ~19 km winds came from the east. This change in direction was not associated with a significant wind shear because velocities were small in that altitude region. A jet stream is visible at roughly 10 km. Superposed on the winds are small-scale gravity waves. Above the tropopause at 11.3 km altitude, temperatures did not change greatly up to ~20 km; higher up they increased.

The right panel of Figure 5.26 depicts the turbulent dissipation profile of the sensor with the wire oriented vertically (i. e. the same wire orientation as for the previous flights). It shows an overall tendency to increasing rates with altitude up to the tropopause. Above, mean rates drop, as, e. g., reflected in the weighted running mean (orange curve). From roughly 15 km upwards dissipation rates were low. So were winds (see left panel).

Turbulent fractions were 45 % in the troposphere and 8 % in the stratosphere and thus much

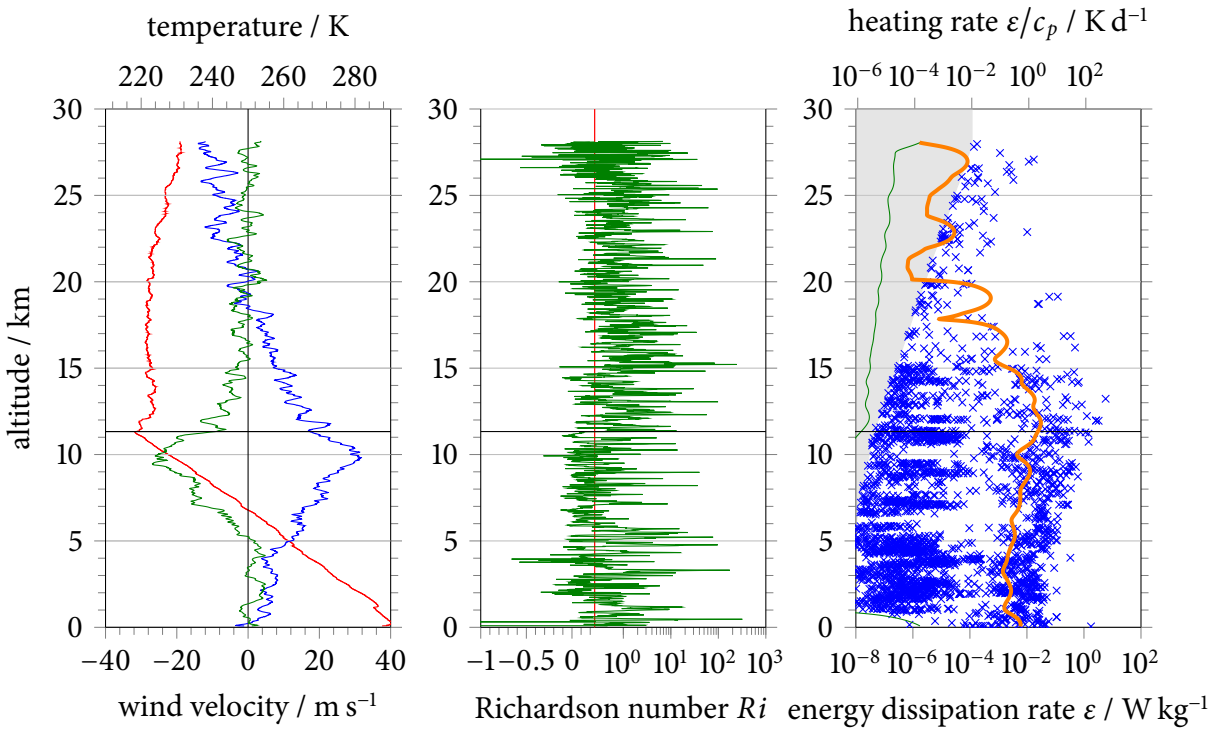

Figure 5.26: Like Figure 5.20, but for the flight at 12th July 2015. The dissipation profile (right panel) is based on the data from the sensor with the wire oriented vertically.

smaller than for the BEXUS flights (cf. Table 5.2 on page 71). Arithmetic averages of dissipation rates were 6 mW kg^{-1} in the troposphere and 4 mW kg^{-1} in the stratosphere, i. e. much higher than for BEXUS, especially in the troposphere. The large averages were mainly caused by some layers with very large dissipation rates. Geometric mean values were lower than for BEXUS with 0.01 mW kg^{-1} in the troposphere and 0.03 mW kg^{-1} in the stratosphere. When looking at averages below and above the drop visible in the profile, one obtains mean dissipation rates of 8 mW kg^{-1} below 15 km and only 0.3 mW kg^{-1} above. This is similar to the flight from June 2014.

Richardson numbers (centre panel of Figure 5.26) were small for most altitudes, even above 15 km where turbulent fractions and dissipation rates were low. No direct relation between Richardson number and turbulence is observed for the BEXUS flights as well, as noted in Section 5.1. A comparison to the other Kühlungsborn flights is not possible because for 27th March 2014 and 6th June 2014 the temperature data is disturbed.

Figure 5.27 shows wind maps from GFS model runs from 11th July 2015, 18:00 UT, 6 h forecast. At 850 hPa (left panel), winds came from the west and north west where the North German Plain is located, thus no mountain wave activity is expected. At roughly 70 hPa (ca. 20 km altitude) the winds reversed, but stayed at very low velocities. This can be seen in the altitude section shown in the left panel of Figure 5.28 and in the radiosonde measurement (left panel of Figure 5.26).

Another source of gravity waves is geostrophic adjustment. The right panel of Figure 5.27 shows horizontal winds at 500 hPa. Slightly bending streamlines can be seen west of the flight path over the North German Plain. These may have emitted gravity waves. Convective available potential energies are very low (< 1 J kg^{-1}, not shown). Gravity waves can also propagate considerable distances, so low generation does not necessarily imply low wave activity.

The right panel of Figure 5.28 depicts horizontal divergence. Wave-like structures are visible below ~15 km; above that altitude no wave activity can be seen any more. This coincides with high dissipation rates below ~15 km and low rates above.

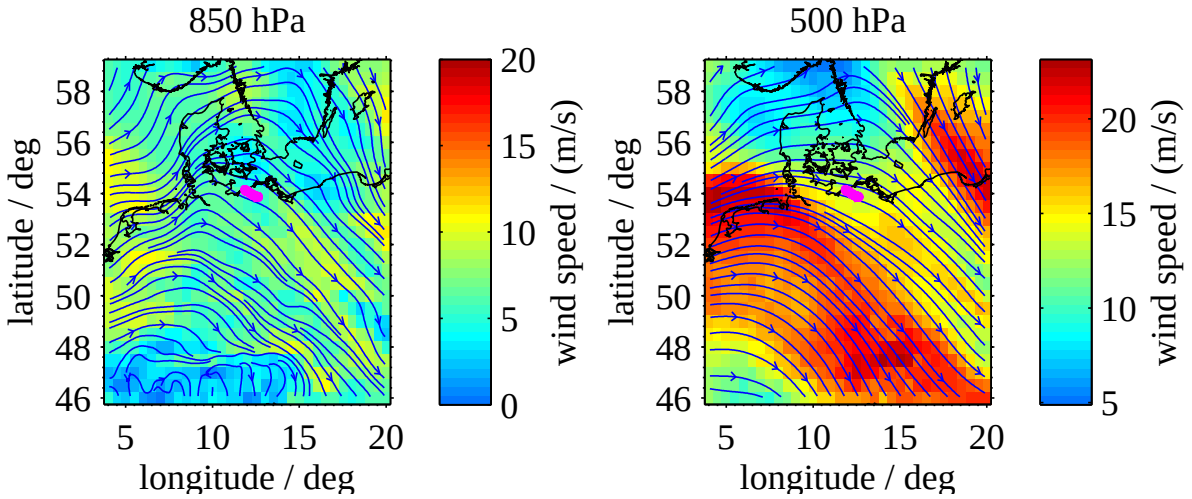

Figure 5.27: Like Figure 5.21, but for GFS run from 11th July 2015, 18 UT, 6 h forecast

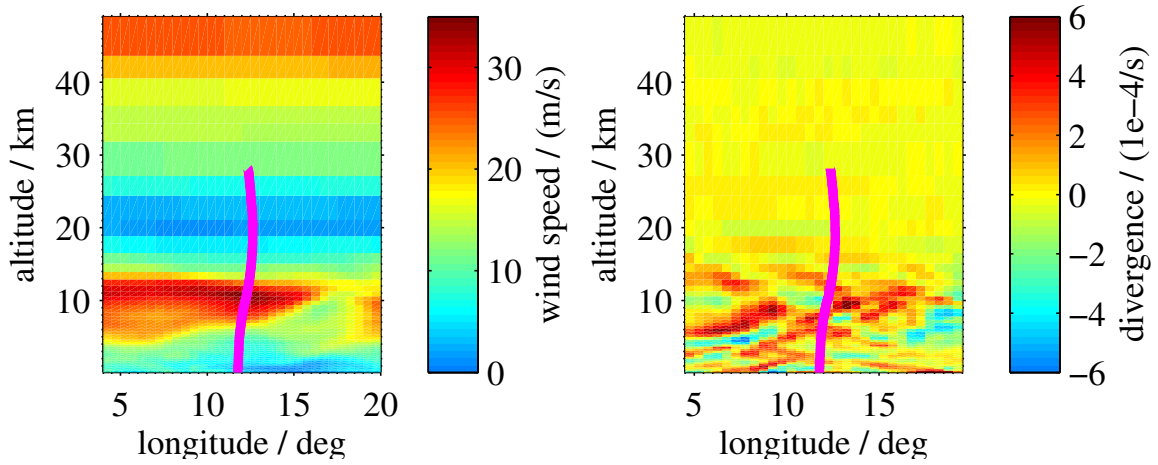

Figure 5.28: Like Figure 5.22, but for GFS run from 11th July 2015, 18 UT, 6 h forecast

5.4.4 Comparison of the Kühlungsborn flights

Table 5.3 shows a comparison of mean dissipation rates and turbulent fractions for the three flights from Kühlungsborn presented above. The flight at 6th June 2014 featured the highest occurrence rates and mean ε values. This corresponds to the largest number of potential gravity wave sources (mountain waves from the German Central Uplands, geostrophic adjustment and medium convective available potential energy).

At 12th July 2015, the turbulent fraction in the troposphere was similar while tropospheric dissipation rates were on average even higher. In the stratosphere, the lowest percentage of turbulence was detected. Average dissipation rates were smaller than at 6th June 2014, but still relatively large. Gravity waves were potentially generated by geostrophic adjustment, while no mountain wave or convective sources are visible. Waves may also have propagated from other places. Wave-

Table 5.3: Mean dissipation rates and turbulent fractions for the three flights from Kühlungsborn

		27 Mar 2014	6 Jun 2014	12 Jul 2015
turbulent fraction / %	troposphere	36	46	45
	stratosphere	20	19	8
	whole flight	24	29	23
arithmetic mean ε / mW kg^{-1}	troposphere	0.2	4	6
	stratosphere	0.9	7	4
	whole flight	0.7	6	5
geometric mean ε / mW kg^{-1}	troposphere	0.01	0.1	0.01
	stratosphere	0.08	0.05	0.03
	whole flight	0.02	0.08	0.01

like structures are visible in the horizontal divergence below ~15 km, while it is nearly constant above. This coincides with high dissipation below that altitude and low dissipation above.

The correlation between wave activity and turbulence hints at continuous wave-breaking throughout all altitudes. When the atmosphere is unstable (Richardson numbers are low, see centre panel of Figure 5.26), a fraction of the waves can break at all altitudes. In this situation turbulence (and dissipation) is indeed related to the occurrence of gravity waves.

Mean dissipation rates at 27th March 2014 were lowest for the three flights. This corresponds to the least sources of gravity waves. No drop in dissipation rate occurred near 15 km as for the other two flights, but medium rates persisted throughout the altitude range. This may be a seasonal effect and has to be further investigated.

When looking at all flights, one sees a clear relation between the occurrence of a drop in dissipation rate and a drop in the horizontal divergence: For the flight from 27th March 2014, wave-like structures in the horizontal divergence as well as medium dissipation rates both continue throughout all altitudes. For the other two flights, both quantities have a drop at roughly 15 km. This shows a clear correlation between dissipation and gravity wave occurrence and hints at continuous wave breaking as discussed above.

5.5 Comparison to Thorpe evaluation of radiosonde measurements

Recently, energy dissipation rates were obtained from standard radiosondes using Thorpe's method [e.g. Gavrilov et al., 2005, Clayson and Kantha, 2008, Kantha and Hocking, 2011]. The motivation behind that approach is to exploit existing measurements available for large geographical areas and several years. For such an evaluation a proportionality between the Thorpe and Ozmidov scales is assumed to infer dissipation rates via (4.7), see Section 4.2. This assumption comes from oceanography but was rarely checked in the atmosphere. With LITOS and a radiosonde on the same gondola, such a check is possible and was performed as described in this section.

When comparing results from LITOS and a Thorpe analysis, it should be kept in mind that both methods do not observe exactly the same thing: The Thorpe method uses (static) instabilities as a proxy, while LITOS measures turbulent motions directly. Not all turbulence is associated with static instabilities. Even if initially a negative potential temperature gradient may have occurred, it is removed by the turbulent motions which outlive the instability. Thus turbulence may still be active while the instability has already ceased. Such fossil turbulence cannot be observed by the Thorpe method, but may be measured by LITOS. On the other hand, within an instability turbulence may have not yet been developed. Such a layer is detected by the Thorpe method, but not by LITOS. Moreover, the retrieval of ε assumes fully developed turbulence, but the atmospheric turbulence may be in a stage where the assumed spectral form is not valid.

The author has already published the results presented in this section in a similar form in Schneider et al. [2015]. The difference is that in the paper a relaxed form of the significance test

by Wilson et al. [2010] has been used to get a better statistical basis, while here the rigorous form is applied.

The evaluation concentrates on data from the large payload (see Section 3.2.1) because that platform is less sensitive to disturbances. To date, three such flights have been performed, namely BEXUS 6, 8 and 12 in 2008, 2009 and 2011, respectively. For BEXUS 6, the radiosonde data are partly disturbed so that it is not considered in this work. At 12th July 2015 a first night-time flight with the small payload was performed from Kühlungsborn (see Sections 3.2.1 and 5.4.3). Data from this very recent flight is of high quality and thus also suitable for the analysis presented in this section.

The Thorpe analysis is performed as described in Section 4.2.2. Prior to the analysis, radiosonde data above 25 km are cut off to eliminate disturbances from the transition to the floating phase. For both BEXUS flights a denoising with downsampling factors of 3 and 2 for BEXUS 8 and 12, respectively, is necessary to obtain a sufficiently large mean trend-to-noise ratio (tnr) of 2.8 and 2.5, respectively. With a 95 % percentile, 37 of 95 (10 of 121) detected unstable layers for BEXUS 8 (BEXUS 12) are significant. For the Kühlungsborn flight the tnr is 1.3 and no denoising is necessary; 23 of 476 unstable layers are significant.

For BEXUS 8 (BEXUS 12), inversions are observed in 21 % (8 %) of the atmosphere. The mean layer thickness is 139 m (197 m). In the troposphere, 24 % (17 %) is turbulent with a mean layer thickness of 189 m (289 m). In the stratosphere, the turbulence fraction according to the Thorpe analysis is 19 % (2 %) with a mean layer thickness of 121 m (61 m). That means that compared to the troposphere there is less turbulence in the more stable stratosphere and layers are generally thinner.

Similar relations between tropospheric and stratospheric values are obtained by LITOS (cf. Sections 5.1 and 5.2, especially Table 5.2). As expected the turbulent fraction in the stratosphere is lower than in the troposphere, but altogether much more turbulence has been observed by LITOS compared to the radiosonde: For BEXUS 8 (BEXUS 12), 63 % (64 %) of the atmosphere below 25 km is turbulent! Layer widths are also smaller in the stratosphere compared to the troposphere, although with much smaller values than detected by the Thorpe method. That suggests that possibly radiosondes do not have the resolution to detect all turbulence. Particularly, the statistics of layer thickness presented in Section 5.1 shows that 55 % of the turbulent layers detected for BEXUS 12 are thinner than the resolution of the downsampled radiosonde of 20 m. For BEXUS 8, 70 % of the LITOS layers are thinner than 30 m (remember that the downsampling factor for the radiosonde data of this flight is 3). Taking into account that unstable layers have to span at least two data bins to be reliably detected, 84 % (72 %) of all LITOS layers for BEXUS 8 (BEXUS 12) are undetectable by the radiosonde.

The Ozmidov scale is computed directly from the dissipation rate ε measured by LITOS via (2.29), $L_\mathrm{O} = c_{L_\mathrm{O}} \sqrt{\varepsilon / N^3}$; the Brunt-Väisälä frequency $N = \sqrt{\frac{g}{\Theta} \frac{\mathrm{d}\Theta}{\mathrm{d}z}}$ is taken from the radiosonde measurement as it only slowly varies with altitude. It is computed from the *sorted* potential temperature profile instead of the original one because a background stratification is needed and an imaginary N would result in an imaginary and negative Ozmidov scale, which is unphysically

[Dillon, 1982, Sect. 3]. As mentioned in Section 4.2, the constant c_{L_O} is set to 1 [e.g. Gavrilov et al., 2005, Clayson and Kantha, 2008, Kantha and Hocking, 2011]. The result is visualised in Figure 5.29 for a small altitude range from 20 km to 21.1 km (blue curve). It shows substructures within layers, e. g. between 20.19 km and 20.34 km. Remember from Section 4.1.1 that ε is computed in 5 m windows with 50 % overlap. Conversely, the Thorpe scale (green bars) is a per-layer value by construction. The potential temperature (red curve) from which it is derived has a lower resolution than the L_O profile. LITOS reveals that layers detected by the Thorpe method actually are divided in patches with different dissipation. For example, a patch from 20.68 km to 20.72 km with relatively large dissipation rate is followed by small non-turbulent region from 20.72 km to 20.75 km, followed by another turbulent layer and so on, all within the same unstable layer observed by the radiosonde. Additionally, several layers measured by LITOS are not detected by the radiosonde at all, e. g. between 20.19 km and 20.34 km.

In order to compare the Thorpe and the LITOS methods, the dissipation rates measured by LITOS are averaged over the unstable layers detected by the Thorpe method. Such mean rates

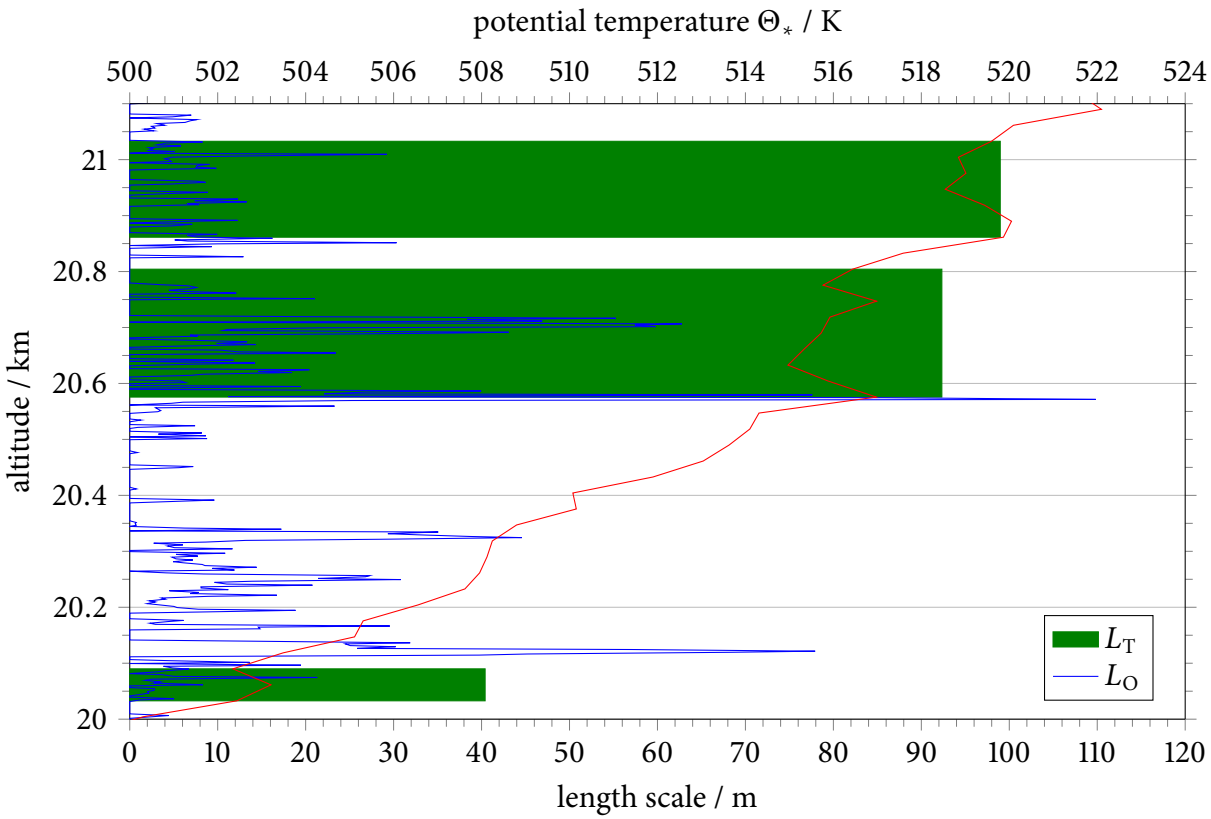

Figure 5.29: Zoom plot of Thorpe (green) and Ozmidov (blue) length scales for the BEXUS 8 flight. The red curve shows the potential temperature.

are denoted by $\overline{\varepsilon}$. Those layers where both methods detect turbulence, i. e. where $\overline{\varepsilon} > 0$, are selected. For BEXUS 8, 35 of the 37 significant layers (95 %) fulfil that criterion, for BEXUS 12 all 10 (100 %). On the other hand, only 113 of 489 (26 of 498) layers detected by LITOS, i. e. 21 % (5 %) intersect a significant Thorpe layer for BEXUS 8 (BEXUS 12). This is also reflected in the mean layer thickness. The mean thickness of LITOS layers is 40 m (41 m), that of LITOS layers intersecting a Thorpe layer 122 m (144 m). That means only thick layers are detected by the radiosonde with its relatively coarse resolution.

A mean Ozmidov scale is computed from $\overline{\varepsilon}$ (and the background Brunt-Väisälä frequency as mentioned before), $\overline{L_\mathrm{O}} := \sqrt{\overline{\varepsilon}/N^3}$. Figure 5.30 shows a plot of Ozmidov scale $\overline{L_\mathrm{O}}$ versus Thorpe scale L_T for the BEXUS 8 (green) and BEXUS 12 (magenta) flights as well as for the new Kühlungsborn flight from July 2015 (orange). Both length scales are of similar order of magnitude. For BEXUS 8, no obvious relation can be identified, particularly no proportionality. The correlation coefficient is 0.31. For BEXUS 12, the correlation is as high as 0.88 and an approximate proportionality may be present, but it is based on a very small sample. For the Kühlungsborn flight, the visual impression of the plot hints at a possible proportionality, however the correlation coefficient is only 0.29. Moreover, the value of the ratio $\overline{L_\mathrm{O}}/L_\mathrm{T}$ is clearly different for the Kühlungsborn flight and for the BEXUS flights. That hints that the relation may depend on

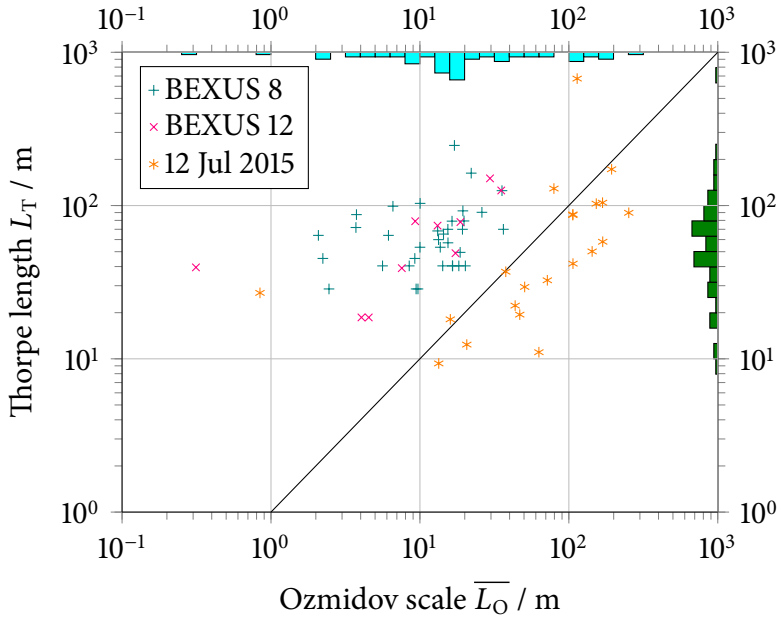

Figure 5.30: Thorpe length L_T vs. Ozmidov scale $\overline{L_\mathrm{O}}$ for BEXUS 8 (green), BEXUS 12 (magenta) and the July 2015 flight from Kühlungsborn (orange). The histograms show the distributions of $\overline{L_\mathrm{O}}$ and L_T, respectively, of all data points in the graph, i. e. of the composite data set of BEXUS 8, BEXUS 12 and the Kühlungsborn flight. The occurrence axes have a linear scale and are omitted for readability. Note that L_T is limited by the resolution of the (downsampled) radiosonde (~30 m for BEXUS 8, ~20 m for BEXUS 12, and ~10 m for the Kühlungsborn flight).

the geophysical situation. Whatsoever, taking into account all data points (i. e. all flights), the assumption of a general proportionality $L_T \propto L_O$, (4.6), needed for the conversion of Thorpe lengths to energy dissipation rates, is not fulfilled for the LITOS data.

The histograms in the top and in the right axes in Fig. 5.30 show the distributions for $\overline{L_O}$ and L_T, respectively, for the composite dataset of all data in the graph, i. e. of BEXUS 8, BEXUS 12 and the Kühlungsborn flight from 12th July 2015. The maximum for the Thorpe length is at larger scales than for the Ozmidov scale. The distribution of L_T is more dominated by the centre while the one of L_O is broader. This may be due to the higher sensitivity and dynamic range of LITOS compared to the radiosonde.

Recent studies question a proportionality between L_O and L_T even for the ocean. For example, direct numerical simulations by Smyth and Moum [2000] indicate that L_O/L_T is not constant but rather depends on the age of turbulence (their Fig. 15). Atmospheric simulations by Fritts et al. [2015] for breaking gravity waves and Kelvin-Helmholtz instabilities show very different spatial structures for L_O and L_T, see Figure 5.31. The ratio L_O/L_T would strongly depend on the place where the balloon flies through the field (compare e. g. $X' = 0.75$ and $X' = 0.85$). This contradicts a general proportionality between L_O and L_T.

Since a proportionality $L_T = c_{TO} L_O$ is widely assumed in the literature, further investigations

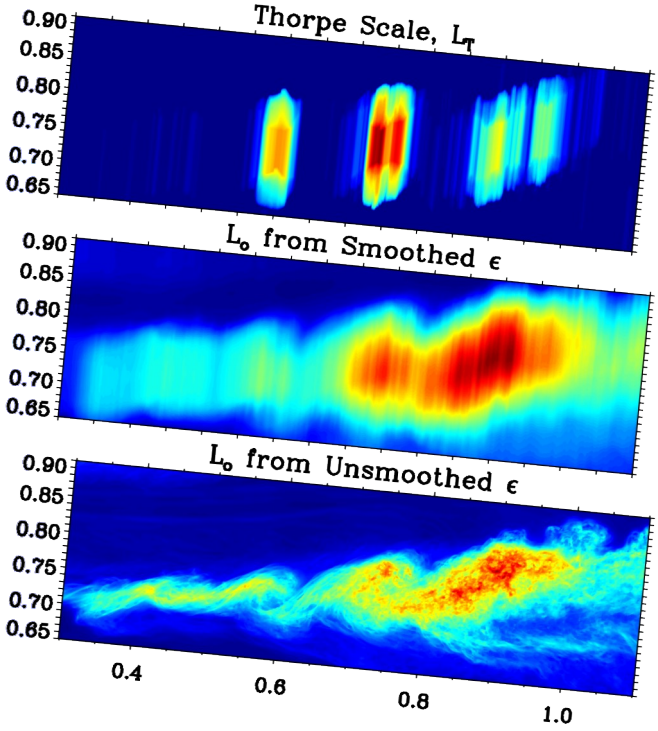

Figure 5.31: Results of a direct numerical simulation of a Kelvin-Helmholtz instability by Fritts et al. [2015, Figure 11] showing streamwise-vertical cross sections of L_T, and L_O assuming smoothed and local ε (top to bottom). Horizontal and vertical scales show the subdomain location in X' and Z'.

are necessary. The application to compute dissipation rates via (4.7), $\varepsilon = c_{\mathrm{TO}}^2 L_{\mathrm{T}}^2 N^3$, involves the value of the proportionality constant $c_{\mathrm{TO}}^2 = (\overline{L_{\mathrm{O}}}/L_{\mathrm{T}})^2$. However, knowledge about that value is very limited. Having measured both $\overline{L_{\mathrm{O}}}$ and L_{T} enables the computation of c_{TO}^2 for each layer. A histogram of the result for the two BEXUS flights is depicted in the left panel of Figure 5.32. It shows a broad distribution spanning more than two orders of magnitude. Taking into account the large scatter of the data points in Figure 5.30, this is not unexpected. Wijesekera et al. [1993, Section 3.1] found the distribution of the ratio $L_{\mathrm{T}}/L_{\mathrm{O}}$ to be lognormal, which implies $(L_{\mathrm{O}}/L_{\mathrm{T}})^2 = c_{\mathrm{TO}}^2$ to be lognormal as well. Thus a normal distribution is fitted to the logarithmic data with a most-likelyhood estimate (blue curve in the left panel of Figure 5.32). It shows a reasonable agreement to the data and is centred around 0.03 (blue vertical line). The same mode is obtained when treating both flights BEXUS separately.

The new night-time flight with the small payload performed from Kühlungsborn at 12th July 2015 shows a different relation with a most probable value of $c_{\mathrm{TO}}^2 = 1.6$ (right panel). This highlights that the ratio is highly variable.

The values for c_{TO}^2 used in the literature are in the order of 1. Clayson and Kantha [2008] incured 0.3 by reviewing oceanic measurements. Kantha and Hocking [2011] obtained $c_{\mathrm{TO}}^2 = 1.0$ by a comparison of radiosonde data to radar measurements. Gavrilov et al. [2005] used $c_{\mathrm{TO}}^2 = 1.32$ ($c_{\mathrm{TO}} = 1.15$) referring to a French thesis; this value was obtained from selected thick stratospheric layers (> 200 m) with statistically homogeneous turbulence. However, in those publications no data basis, distribution width or error is given. Wilson et al. [2014] reported a few case studies of turbulent layers in the troposphere detected simultaneously by radar and balloon; using their reported estimates of L_{T} and L_{O} leads to values of c_{TO}^2 between 0.1 and 1.6.

A comparison of those literature values to the most likely ones from LITOS yields a significant

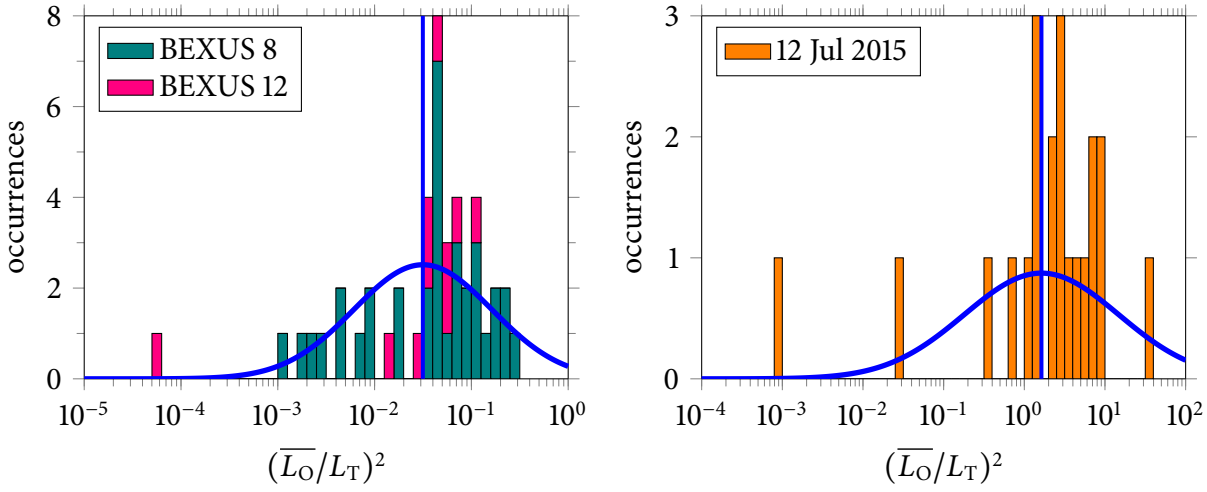

Figure 5.32: Statistics of the ratio $(\overline{L_{\mathrm{O}}}/L_{\mathrm{T}})^2$ for the BEXUS 8 and BEXUS 12 flights (left) and for the Kühlungsborn flight from 12th July 2015 (right). The blue curves show the most likely normal distributions for the logarithmic data, the vertical blue lines the most likely values of that distributions.

discrepancy for the BEXUS flights, while the results are compatible for the Kühlungsborn flight. That suggests a geophysical variability of c_{TO}^2. Due to the good agreement of the result from the Kühlungsborn flight and the literature values, a bias by the layer selection procedure or the different detection thresholds of LITOS and the radiosonde seems less likely.

A comparison of dissipation rates is different from comparing the length scales discussed above because the relation between the energy dissipation rate ε and the length scales involves the Brunt-Väisälä frequency (see (2.29) and (4.7)) as well as (for the Thorpe analysis) the value of the constant c_{TO}^2. As mentioned at the beginning of this section, several authors used the proportionality $L_{\mathrm{O}} \propto L_{\mathrm{T}}$ to obtain energy dissipation rates from radiosondes. In these cases, no information on the actual relation between L_{O} and L_{T} is available, thus a value for c_{TO}^2 has to be assumed. To compare such a method with LITOS, $\varepsilon_{\mathrm{Thorpe}}$ is computed accordingly with (4.7), $\varepsilon_{\mathrm{Thorpe}} = c_{\mathrm{TO}}^2 L_{\mathrm{T}}^2 N^3$, regardless of the results concerning the proportionality presented above. The proportionality constant is assumed to be $c_{\mathrm{TO}}^2 = 0.3$ as in Clayson and Kantha [2008]. Similar to the computation of the Ozmidov scale, N is taken from the sorted profile to prevent negative and imaginary dissipation rates which are unphysically.

Figure 5.33 compares altitude profiles of ε obtained with both methods for the BEXUS 8 flight.

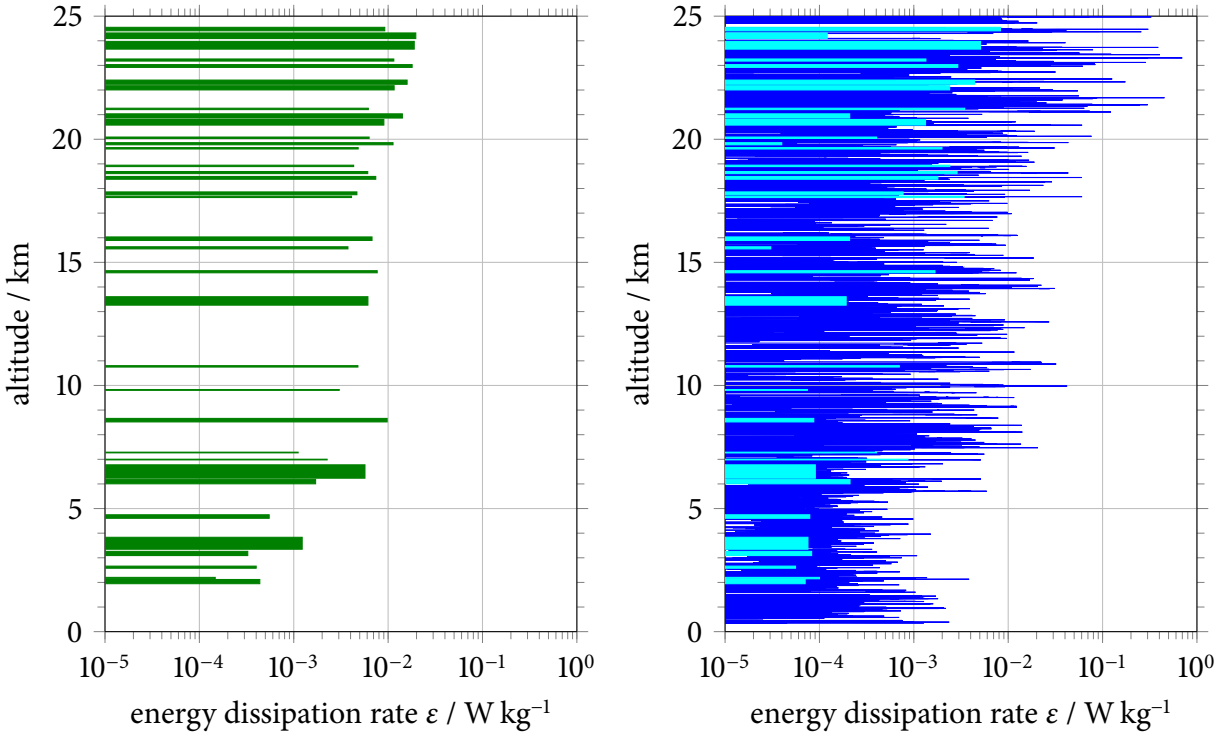

Figure 5.33: Energy dissipation rates obtained from Thorpe analysis of the radiosonde (left) and spectral analysis of the high-resolved wind measurement (right) for the BEXUS 8 flight. In the right panel, the blue curve shows ε in the full resolution, the cyan bars visualise averages over the unstable layers detected by the Thorpe analysis ($\overline{\varepsilon}$).

For LITOS, ε is shown in the full resolution (blue curve) as well as averaged over the layers detected by the Thorpe analysis ($\overline{\varepsilon}$, cyan bars). Many turbulent layers measured by LITOS are not observed by the radiosonde at all. These are not associated with a significant negative gradient of potential temperature on scales detectable by the radiosonde, which is necessary for detection by the Thorpe method. Those turbulent layers may be too thin to be observed with the relatively coarse vertical resolution of the radiosonde. Apart from that, as mentioned above not all turbulence is related to static instabilities. On the other hand, turbulence may have not yet been developed within an instability. Both methods do not detect exactly the same thing; the indirect observation of turbulence through static instabilities (as done by the Thorpe method) is somewhat different from measuring the turbulent motions directly (as done by LITOS).

Moreover, even for those layers observed by both instruments the difference is large. The left panel of Figure 5.34 depicts the ratio $\overline{\varepsilon}_{\mathrm{LITOS}}/\varepsilon_{\mathrm{Thorpe}}$ of the dissipation rates obtained by LITOS and by the Thorpe analysis of the radiosonde for BEXUS 8. For this flight, the dissipation rate measured by LITOS is always smaller than that from the Thorpe analysis. ε values deviate up to a factor of ~300. The geometric mean of the ratio is 9×10^{-2}. For the flight from 12th July 2015 (right panel of Figure 5.34) the deviation of both methods is not as large, and the ε value from

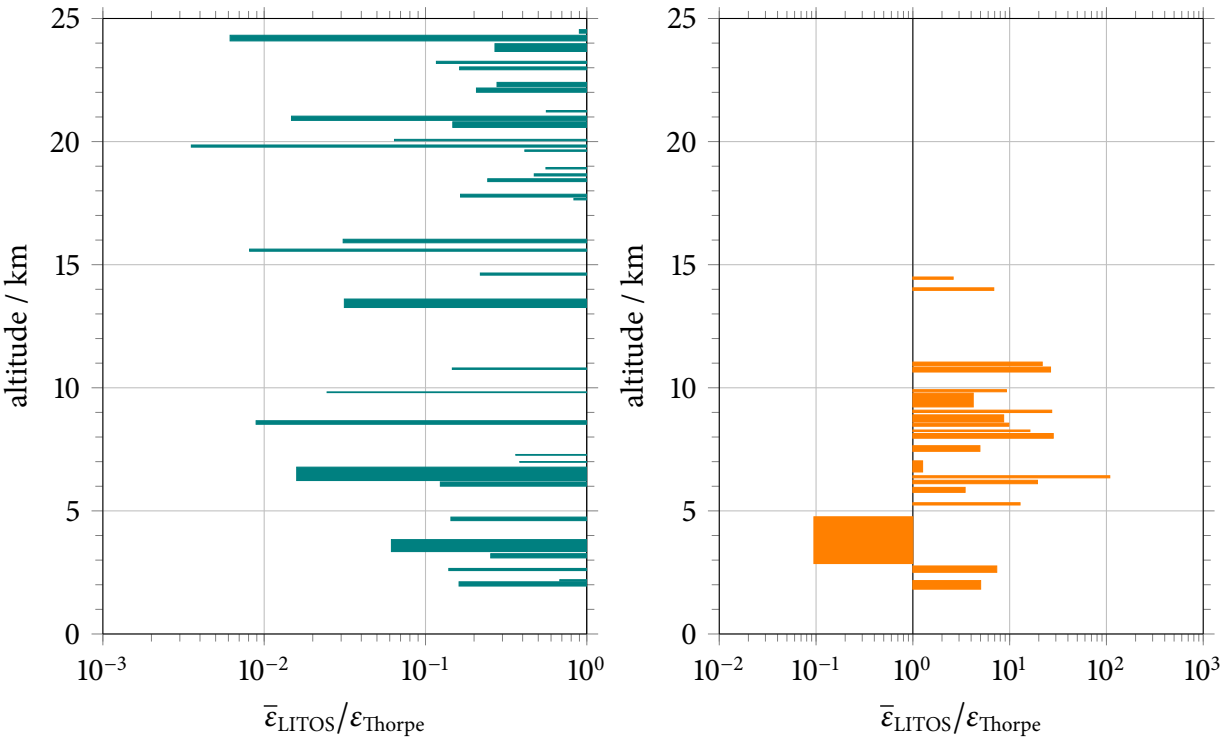

Figure 5.34: Ratio of dissipation rate obtained by LITOS and by the Thorpe evaluation of the radiosonde, $\overline{\varepsilon}_{\mathrm{LITOS}}/\varepsilon_{\mathrm{Thorpe}}$ for BEXUS 8 (left) and the Kühlungsborn flight from 12th July 2015 (right)

LITOS is higher than that from the radiosonde for some layers and lower for others.

The deviation in the ε values is connected to the deviation of the mean value of $c_{\mathrm{TO}}^2 = (\overline{L_{\mathrm{O}}}/L_{\mathrm{T}})^2$ from the literature value of 0.3 used in the radiosonde evaluation. With the most probable value, i. e. $c_{\mathrm{TO}}^2 = 0.03$ for BEXUS 8, the difference would be smaller. However, the intention of this section is the comparison with radiosonde evaluation as performed in the literature; for those applications no user-adapted value of c_{TO}^2 is available.

Mean dissipation rates for significant layers of the BEXUS 8 flight are 7 mW kg^{-1} (geometric mean: 4 mW kg^{-1}) from Thorpe compared to 1 mW kg^{-1} (geometric mean: 0.5 mW kg^{-1}) from LITOS. That means the averages differ by nearly an order of magnitude. The correlation coefficient between $\overline{\varepsilon}$ from LITOS and ε from Thorpe is 0.41. Table 5.4 shows a comparison of the mean values of both methods. In the troposphere the discrepancy is a factor of 10, while in the stratosphere it is smaller but still a factor of 4. This is, at least for the troposphere, above the uncertainty of the determination of ε from the spectra which is roughly a factor of 4.

It should be noted that the comparison involves two parameters: (a) evaluation method (Thorpe or spectral analysis) and (b) vertical resolution (low or high). The low-resolved Thorpe analysis is considered here because such an evaluation of radiosonde data has been proposed for extensive use [Clayson and Kantha, 2008, Love and Geller, 2012]. Please note that Love and Geller [2012] call 1 Hz (5 m) high resolution, while here it is called low resolution (compared to LITOS with 8 kHz). In principle, the Thorpe analysis can also be performed on data with higher resolution, as done, e. g., by Luce et al. [2002] for temperature data with a 50 Hz sampling rate; however, such data are rarely available compared to those of standard radiosondes. Furthermore, a kind of spectral analysis can be used to determine dissipation rates from relatively low-resolution wind data [Barat, 1982a], but this method depends on the absolute value of the wind velocity, which is not available for the LITOS measurements (see Section 3.1).

The analysis presented in this section only contains data from three flights, as this is what is available to date. The two BEXUS flights both took place at polar latitudes near autumn equinox, while the one with the small payload was at mid-latitudes during summer conditions. Of course they cannot represent the whole variability of the stratosphere. Nevertheless, although there are differences between the flights, such as dissipation rates being on average 1 order of magnitude higher for BEXUS 8 compared to BEXUS 12, these are not relevant for the results discussed above. More flights with LITOS are planned to broaden the data basis.

Table 5.4: Comparison of mean dissipation rates from Thorpe analysis of the radiosonde and spectral analysis of LITOS averaged over significant unstable layers for the BEXUS 8 flight

	Thorpe			LITOS		
	tropo	strato	all	tropo	strato	all
arithmetic mean ε / mW kg^{-1}	2	8	7	0.2	2	1
geometric mean ε / mW kg^{-1}	0.8	7	4	0.1	0.8	0.5

In this section the assumption for the extraction of dissipation rates by Thorpe analysis, a proportionality between Thorpe length L_T and Ozmidov scale L_O, was checked. No general proportionality is found in the LITOS data, but the relation is highly variable, potentially depending on the geophysical situation. Although an approximate proportionality may be present for some flights, the most probable value of the ratio $(L_O/L_T)^2$, the "constant" used in radiosonde analyses, varies by nearly two orders of magnitude for different flights. A comparison of a Thorpe analysis of radiosonde data as performed in the literature to results from LITOS shows that many turbulent layers observed by LITOS are not detected by the radiosonde. Indeed, for BEXUS 8, BEXUS 12, and the Kühlungsborn flight, 84 %, 72 %, and 88 %, respectively, of all layers observed by LITOS are thinner than the minimal layer width reliably detectable by the radiosonde (defined by two data bins of the radiosonde profile). That means standard radiosondes have too coarse a resolution to detect most turbulence.

6 Summary and outlook

In this work, the balloon-borne instrument LITOS for turbulence measurements in the stratosphere that was first developed by Sumińska [2008] and Theuerkauf [2012] has been significantly improved, and new flights with the instrument were performed and evaluated. Combining data of new and previous flights, the results from LITOS were compared with an evaluation method for radiosondes found in the literature, the so-called Thorpe analysis, and the essential assumption for extracting dissipation rates with that method was checked. Moreover, the first comparison of kinetic and thermal dissipation rates in the stratosphere was performed.

Technical development

On the technical side, a new data acquisition that eliminates potential problems with the temporal correlation of data of different sensors has been developed at the IAP. This board also includes inertial sensors. To reconstruct the attitude of the balloon, an algorithm combining measurements of rotation, acceleration and magnetic field has been implemented within this thesis.

To check the impact of the payload on the measurement, wind tunnel experiments were performed with a model of the small gondola at that time. The results of these experiments have lead to a new payload shape which is spherical instead of cubic. The much better performance of the new gondola was verified in the wind tunnel and with the evaluation of attitude measurements from flights with both payload shapes.

Furthermore, the first error estimation for the retrieval method of the dissipation rate ε was carried out. With retrievals of simulated spectra, the error in ε is estimated to roughly a factor of 4.

New flights

Several new flights were performed within this work. One flight on a large (12 000 m^3) balloon was conducted from Kiruna during Balloon EXperiments for University Students (BEXUS) 12. Due to the large weight of the gondola, that system has very few spurious motions and thus the best data quality.

Additionally, several flights with the new design of the small payload were carried out from Kühlungsborn. The flight behaviour (e. g. pendulum motions) and data quality are vastly improved compared to the previous design. Some minor issues with disturbances remain.

Geophysical results

The new measurements confirm a large intermittency of turbulence, which occurs in patches alternating with laminar regions. The boundaries between both are relatively sharp. Thin layers prevail with nearly monotonous decrease in occurrence with increasing thickness. The mean layer width for BEXUS 12 is 41 m. In the troposphere layers are on average significantly thicker with 99 m compared to the stratosphere with 27 m. The mean value is in very good agreement to the observations by Theuerkauf [2012] who obtained 46 m for the BEXUS 8 flight and 38 m for BEXUS 6 using a different evaluation method. She similarly found thinner and more frequent layers in the stratosphere compared to the tropopause region (7 km to 15 km).

Turbulent fractions measured by LITOS are large—85 % in the troposphere and 52 % in the stratosphere for BEXUS 12. Particularly in the stratosphere this is much more than expected. Most observed layers are thinner than the typical vertical resolution of remote sensing instruments. That means with finer resolution more turbulence can be detected. For a comparison with radar measurements by Wilson et al. [2005], the different sensitivity and vertical resolution of both instruments have to be taken into account. When considering only layers detectable by the radar, the LITOS results are compatible with a turbulent fraction of 10 % to 20 % obtained by Wilson et al. [2005].

Features in dissipation rates ε can be related to meteorological background conditions. For the BEXUS 12 flight, a sharp maximum in turbulent dissipation just below the tropopause at ~10 km altitude corresponds to high wind shears which entails low or even negative Richardson numbers. LITOS gives direct evidence for the dissipation associated with the dynamical instability. The wind shear is associated with a wind reversal that filters gravity waves. During previous BEXUS flights no such wind reversal and also no distinct peaks in dissipation rates were present, supporting the above interpretation.

Dissipation was observed even for large Richardson numbers Ri, confirming results by Theuerkauf [2012] that were based on two soundings only. That contradicts the classical criterion for dynamic instability, which states that turbulence exists for Ri numbers smaller than 1/4. Similarly, Achatz [2005] found in numerical simulations of gravity waves that instability and the onset of turbulence is independent of Ri.

Eddy diffusion coefficients computed from ε are in acceptable agreement to other stratospheric measurements considering the different resolutions of the instruments.

To further study the relations to the meteorological background conditions, Weather Research and Forecasting (WRF) model simulations for the BEXUS 8 and BEXUS 12 flights were provided by Johannes Wagner (University of Innsbruck). This is the first time that high-resolution stratospheric turbulence measurements were interpreted using accompagning high-resolution simulations. Gravity wave activity seen in WRF is clearly related to dissipation observed by LITOS. For instance, during BEXUS 12 wave activity was enhanced near 10 km and ceased to exist above. This is consistent with wave filtering and enhanced dissipation in this altitude region. LITOS for the first time provides a direct measurement of the dissipation associated with the (breaking) waves. The results also confirm that internal gravity waves are major contributors to instability

and turbulence [e. g. Fritts et al., 2013, Section 1].

During BEXUS 8 wind and temperature fluctuations were measured simultaneously. Dissipation rates from those independent observations, ε_v and ε_T, were compared. Both are expected to coincide since the same physical quantity is measured. For the evaluation, new dissipation profiles were computed from the original raw data. Rates obtained from both sensors are highly correlated, but, as already noted by Theuerkauf [2012], the absolute values differ by more than one order of magnitude. As was found in the present thesis, this is above the uncertainty in the determination of ε which is estimated to be roughly a factor of 4. That hints at potential inconsistencies and limitations of the turbulence theory used to extract the values, e. g. in the constants in the relation between inner scale l_0 and dissipation rate ε taken from the literature. Moreover, kinetic and thermal dissipation rates ε and $\chi c_p/T$ were compared. The first one specifies the entropy production due to friction, while the second one characterises the entropy production due to thermal diffusion. This is the first time that ε and χ from simultaneous observations in the stratosphere were compared. In the LITOS data, ε_T and $\chi c_p/T$ are highly correlated because they are computed from the same spectrum—when, e. g., no temperature fluctuations are observed, ε_T is zero although wind fluctuations and kinetic dissipation may be present. ε_v and $\chi c_p/T$ are less correlated with a correlation coefficient of 0.56. The ratio $\varepsilon/(\chi c_p/T)$ shows strong local variations and its distribution is broad—the full width at half maximum is approximately one order of magnitude. These results confirm direct numerical simulations by Fritts and Wang [2013] who found that correlations between both fields strongly depend on event character and stage of evolution, being generally large, but weak where strong mixing has occurred. Taking into account that LITOS is expected to measure events of different origins and stages, a medium correlation is consistent.

An important part of this work was the comparison to turbulence evaluation of temperature profiles observed by radiosondes (Thorpe analysis). Such an analysis is commonly used in the literature. It uses static instabilities as proxy for turbulence. The key assumption for the computation of dissipation rates is a proportionality between Thorpe length L_T and Ozmidov scale L_O. Such proportionality was observed in the ocean, but rarely tested for atmospheric conditions. Knowledge of the value of the proportionality constant is very limited. Nevertheless, such a proportionality is widely assumed with a value of the constant mostly taken from oceanic observations. As LITOS measures ε directly, a check of the proportionality is possible and was performed, and the constant was computed. Surprisingly, no proportionality between L_O and L_T can be seen in the LITOS data. The value of $(L_O/L_T)^2$, the "constant" used in the Thorpe analysis, varies over more than two orders of magnitude for individual unstable layers. Even the most probable value deviates for different flights by nearly two orders of magnitude. That hints at a geophysical dependency of the relation between L_O and L_T. The deviation of dissipation rates from both methods depends on the choice of the constant. For 0.3 as chosen by Clayson and Kantha [2008], ε deviates by up to a factor of 300. Moreover, many turbulent layers observed by LITOS have not been detected by the radiosonde at all. This questions the applicability of the Thorpe method for individual turbulent layers. Moreover, mean values critically depend on the choice of the proportionality constant, which seems to depend on the geophysical situation.

Outlook

New insights have been gained into stratospheric turbulence. The assumption for the extraction of dissipation rates from radiosondes, namely a general proportionality between Thorpe and Ozmidov scales, has been falsified. The actual relation seems to depend on the geophysical situation, thus further LITOS flights are worthwhile to examine such a potential dependence. Moreover, new flights will improve the statistical basis. Knowledge of such a relation seems necessary to interpret Thorpe analyses of operational radiosondes. Direct numerical simulations may also help gaining such knowledge.

LITOS results have not been compared with those of remote sensing instruments observing turbulence in the same volume, e. g. the OSWIN radar in Kühlungsborn. Such a comparison would be worthwhile.

By complementing LITOS observations with model data, a connection between gravity waves and turbulence was examined. These results can be extended by measurements of gravity waves with other instruments, e. g. by aircraft or lidar, or by a gravity wave analysis of radiosondes.

Calculation of ε from first simultaneous high-resolution observations of wind and temperature were inconsistent and revealed potential problems of the turbulence theory used for data evaluation. Reviewing the theory seems necessary. Future flights with both sensor types may hint at the origin of the discrepancies and help answering these fundamental questions. Moreover, further measurements can contribute to the understanding of the relation between kinetic and thermal dissipation.

With further improvements of the small LITOS payload, flights could be performed on a regular basis. Furthermore, measurements targeted at specific geophysical questions are planned.

A Statistical theory of turbulence

In this chapter, the basics of the statistical theory of turbulence are introduced and the function to be fitted to experimental data for the extraction of turbulence parameters is derived.

As mentioned before, the velocity fluctuations $\boldsymbol{u}'(\boldsymbol{x}, t)$ and temperature fluctuations $T'(\boldsymbol{x}, t)$ are treated as random fields. By definition they have zero mean. A measurement is one realisation of the random process.

A.1 Correlations

A common approach is to relate values at two different points in time or space. These relations are described by the correlation function, one of the most important characteristic quantities. For a real-valued field the *correlation tensors* in space (superscript (s)) and time (superscript (t)) are defined as

$$B_{ij}^{(\mathrm{t})}(\boldsymbol{x}, t_1, t_2) := \left\langle u_i'(\boldsymbol{x}, t_1) u_j'(\boldsymbol{x}, t_2) \right\rangle \tag{A.1}$$

$$B_{ij}^{(\mathrm{s})}(\boldsymbol{x}_1, \boldsymbol{x}_2, t) := \left\langle u_i'(\boldsymbol{x}_1, t) u_j'(\boldsymbol{x}_2, t) \right\rangle \tag{A.2}$$

[Tatarskii, 1971, (2.5); Mathieu and Scott, 2000, (3.5), (6.4)] (remember $\boldsymbol{u}'$ has zero mean). It is positive definite and for a real field $\boldsymbol{u}$ symmetric [Tatarskii, 1971, §2].

If the statistics of a field is independent of time, it is called *stationary*, and the temporal correlation depends on the time difference $\tau := t_2 - t_1$ only. Conversely, if the temporal correlation function does not depend on time, the field is stationary [Tatarskii, 1971, §2]. Similarly, if the statistical properties do not depend on the location in space, the field is named *homogeneous*, and the spatial correlation function depends on the difference $\boldsymbol{r} := \boldsymbol{x}_2 - \boldsymbol{x}_1$ only. If it additionally is *isotropic*, i. e. the statistics are independent of the direction in space, the dependence of $\boldsymbol{B}$ reduces to the norm $r = |\boldsymbol{r}|$. For a stationary, homogeneous and isotropic field, the temporal and spatial correlation functions are thus for any unit vector $\boldsymbol{e}$

$$B_{ij}^{(\mathrm{t})}(\tau) = \left\langle u_i'(\boldsymbol{x}, t + \tau) u_j'(\boldsymbol{x}, t) \right\rangle \tag{A.3}$$

$$B_{ij}^{(\mathrm{s})}(r) = \left\langle u_i'(\boldsymbol{x} + r\boldsymbol{e}, t) u_j'(\boldsymbol{x}, t) \right\rangle \tag{A.4}$$

[Tatarskii, 1971, (2.7), (8.1); Mathieu and Scott, 2000, (6.5)]. $\boldsymbol{B}^{(\mathrm{t})}$ and $\boldsymbol{B}^{(\mathrm{s})}$ are independent of t due to stationarity and independent of $\boldsymbol{x}$ due to homogeneity.

The correlation function for a stationary process has its maximum at zero separation,

$$B_{ij}^{(\mathrm{t})}(\tau) \leq B_{ij}^{(\mathrm{t})}(0) = \left\langle u_i' u_j' \right\rangle \tag{A.5}$$

[Tatarskii, 1971, (2.12)]. For large separations, the values of turbulent velocity or temperature fluctuations typically decorrelate,

$$B_{ij}^{(\mathrm{t})}(\tau) \to 0 \quad \text{for } |\tau| \to \infty \tag{A.6}$$

$$B_{ij}^{(\mathrm{s})}(\boldsymbol{r}) \to 0 \quad \text{for } |\boldsymbol{r}| \to \infty \tag{A.7}$$

[Mathieu and Scott, 2000, Chapter 3]. This empirical behaviour turns out to be useful as it is necessary for the application of spectral methods (see below).

A.2 Spectral analysis of homogeneous turbulence

The reduction of the number of variables of $\boldsymbol{B}^{(\mathrm{t})}$ to one by stationarity, together with the assumption of decorrelation for large times increments (A.6), enables a Fourier transform:

$$W(\omega) := \frac{1}{2\pi} \int_{-\infty}^{\infty} B^{(\mathrm{t})}(\tau)\, \exp(\mathrm{i}\omega\tau)\, \mathrm{d}\tau = \frac{1}{2\pi} \int_{-\infty}^{\infty} B^{(\mathrm{t})}(\tau)\, \cos(\omega\tau)\, \mathrm{d}\tau \tag{A.8}$$

[Tatarskii, 1971, (2.16), (2.16')], where the second equality holds because $B^{(\mathrm{t})}$ is a symmetric function. W is called *(temporal) spectrum* and can be shown to be real and non-negative [Tatarskii, 1971, (2.16)]. On the other hand, if $W(\omega) \geq 0$ for all ω, then the inverse transform of (A.8) defines the correlation function of some stationary random process [Tatarskii, 1971, §2]. Analogous, the spatial spectrum of a homogeneous field satisfying (A.7) is

$$\Phi_{ij}(\boldsymbol{k}, t) := \frac{1}{(2\pi)^3} \int_{\mathbb{R}^3} B_{ij}^{(\mathrm{s})}(\boldsymbol{r}, t)\, \cos(\boldsymbol{k} \cdot \boldsymbol{r})\, \mathrm{d}^3 r \tag{A.9}$$

[Tatarskii, 1971, (4.8); Mathieu and Scott, 2000, (6.7)].

A Fourier transform can also be performed in one spatial dimension only. This is interesting because in-situ measurements are typically along a single trajectory and do not have three-dimensional resolution. For isotropic fields, where all directions are equivalent, one can regard an arbitrary line in space in the direction of the unit vector $\boldsymbol{e}$ to define the one-dimensional spatial spectrum by

$$V(k) := \frac{1}{\pi} \int_{0}^{\infty} B^{(\mathrm{s})}(r\boldsymbol{e}, t) \cos(kr)\, \mathrm{d}r \tag{A.10}$$

[Tatarskii, 1971, (4.3), (4.11)]. It is related to the three-dimensional spectrum by

$$\Phi(k) = -\frac{1}{2\pi k}\frac{\mathrm{d}V}{\mathrm{d}k}(k) \tag{A.11}$$

[Tatarskii, 1971, (4.13)].

A.3 Structure functions

A concept related to the correlation function is the *structure function*

$$D_{ij}(\boldsymbol{r}) := \left\langle (u_i'(\boldsymbol{x}+\boldsymbol{r}) - u_i'(\boldsymbol{x}))((u_j'(\boldsymbol{x}+\boldsymbol{r}) - u_j'(\boldsymbol{x}))\right\rangle \tag{A.12}$$

[Tatarskii, 1971, (8.2)]. It describes correlation of the *difference* of velocity fluctuations at separation $\boldsymbol{r}$ and mainly depends on scales smaller than $|\boldsymbol{r}|$ [Lübken, 1993, p. 28]. For a homogeneous field, it is independent of the location $\boldsymbol{x}$ and connected to the spatial correlation function by

$$D_{ij}(\boldsymbol{r}) = 2B_{ij}^{(\mathrm{s})}(0) - 2B_{ij}^{(\mathrm{s})}(\boldsymbol{r}) \tag{A.13}$$

[Tatarskii, 1971, (8.3)]. Thereby it is also connected to the spectrum,

$$D_{ij}(\boldsymbol{r}) = 2\int_{\mathbb{R}^3} \left(1 - \cos(\boldsymbol{k}\cdot\boldsymbol{r})\right)\Phi_{ij}(\boldsymbol{k})\,\mathrm{d}^3k \tag{A.14}$$

[Tatarskii, 1971, (8.18)]. (A.14) and its inversion is also well-defined for fields that are only *locally* homogeneous, i. e. the spectrum is defined more generally via the structure function [Tatarskii, 1971, §3, §5].

In the case of isotropy, several components of the structure function tensor can be shown to be equal [Tatarskii, 1971, §8], so that (A.12) reduces to

$$D_{ij}(\boldsymbol{r}) = D_{\mathrm{tt}}(\boldsymbol{r})\delta_{ij} + (D_{\mathrm{rr}}(\boldsymbol{r}) - D_{\mathrm{tt}}(\boldsymbol{r}))n_i n_j \tag{A.15}$$

[Tatarskii, 1971, (8.5')] with the transversal and longitudinal components $D_{\mathrm{tt}} = D_{\mathrm{ll}} = D_{22}$ and $D_{\mathrm{rr}} = D_{33}$, respectively, the normal vector $\boldsymbol{n} = \frac{\boldsymbol{r}}{r}$, and the Kronecker delta

$$\delta_{ij} := \begin{cases} 1, & \text{if } i = j, \\ 0, & \text{if } i \neq j. \end{cases}$$

Now the form of the structure function for turbulent fluctuations is deduced. Therefrom important relations for measured spectra can be obtained.

In the viscous subrange, i. e. for small r, a Taylor expansion around 0 can be performed. Due to the properties $D_{ii}(0) = 0$ and $\frac{\mathrm{d}D_{ii}}{\mathrm{d}r}(0) = 0$ it starts with the quadratic term. All higher terms

can be neglected. For velocity fluctuations, the relation $\varepsilon = \frac{\nu}{2}\nabla^2 D_{ii}(0)$ [Tatarskii, 1971, (10.5)] (stemming from the definition of ε) leads to

$$D_{ii}(r) = \underbrace{\frac{\varepsilon}{3\nu}}_{=:\tilde{C}_\mathrm{v}} r^2 \quad \text{in the viscous subrange} \tag{A.16}$$

[Tatarskii, 1971, (10.7)]. The longitudinal and transversal components are given by

$$D_{\mathrm{rr}}(r) = \frac{\varepsilon}{15\nu} r^2 \tag{A.17}$$

$$D_{\mathrm{tt}}(r) = \frac{2\varepsilon}{15\nu} r^2 \quad \text{in the viscous subrange} \tag{A.18}$$

[Pope, 2000, (6.39), (6.40)]. For temperature fluctuations in a steady-state distribution one obtains

$$D_\mathrm{T}(r) = \underbrace{\frac{\chi}{3\alpha}}_{=:\tilde{C}_\mathrm{T}} r^2 \quad \text{in the viscous subrange} \tag{A.19}$$

[Tatarskii, 1971, (13.28)].

In the inertial subrange, Kolmogorov's second similarity hypothesis states that the structure function is independent of the kinematic viscosity ν or the thermal diffusivity α, respectively, i. e. it depends on the dissipation rates and r only [Tatarskii, 1971, §12]. Using dimensional analysis, one obtains for velocity fluctuations

$$D_{\mathrm{rr}}(r) = \underbrace{a_\mathrm{v}^2 \varepsilon^{2/3}}_{=:C_\mathrm{v}^2} r^{2/3} \quad \text{in the inertial subrange} \tag{A.20}$$

[Kolmogorov, 1941a, (23); Tatarskii, 1971, (12.7)] with a dimensionless constant a_v^2. Using the relation $D_{\mathrm{tt}} = \frac{1}{2r}\frac{\mathrm{d}}{\mathrm{d}r} r^2 D_{\mathrm{rr}}(r)$ [Tatarskii, 1971, (8.10)], results in

$$D_{\mathrm{tt}}(r) = \frac{4}{3} a_\mathrm{v}^2 \varepsilon^{2/3} r^{2/3} \quad \text{in the inertial subrange} \tag{A.21}$$

[Tatarskii, 1971, p. 54]. Therewith, the trace is

$$D_{ii}(r) = 2D_{\mathrm{tt}}(r) + D_{\mathrm{rr}}(r) = \frac{11}{3} a_\mathrm{v}^2 \varepsilon^{2/3} r^{2/3} \quad \text{in the inertial subrange} \tag{A.22}$$

[Tatarskii, 1971, eq. (12.14)]. For temperature fluctuations, an analogous reasoning yields

$$D_\mathrm{T}(r) = \underbrace{a_\mathrm{T}^2 \frac{\chi}{\varepsilon^{1/3}}}_{=:C_\mathrm{T}^2} r^{2/3} \quad \text{in the inertial subrange} \tag{A.23}$$

[Obukhov, 1949, (21); Tatarskii, 1971, (13.33)] with a dimensionless constant a_{T}^2. C_i^2, $i \in \{\mathrm{v}, \mathrm{T}\}$, is called *structure function constant*.

For a structure function of such a form $D(r) = A\, r^{2/3}$ with arbitrary constant A, the one-dimensional spectral density is

$$V(k) = A \frac{\Gamma(\frac{5}{3}) \sin(\frac{\pi}{3})}{2\pi} k^{-\frac{5}{3}} \tag{A.24}$$

[Tatarskii, 1971, (5.37)] and the three-dimensional spectral density

$$\Phi(k) = A \frac{\Gamma(\frac{8}{3}) \sin(\frac{\pi}{3})}{4\pi^2} k^{-\frac{11}{3}} = A \frac{5}{3} \frac{\Gamma(\frac{5}{3}) \sin(\frac{\pi}{3})}{4\pi^2} k^{-\frac{11}{3}} \tag{A.25}$$

[Tatarskii, 1971, (5.38)], where the second equality uses $\Gamma(5/3 + 1) = 5/3\, \Gamma(5/3)$.

A.4 Energetics

Finally, the energetics is examined. A distribution of turbulent kinetic energy in wave vector space is obtained by looking at the inverse transform of (A.9) and setting $\boldsymbol{r} = 0$ and $i = j$, yielding

$$E_{\mathrm{TK}} = \frac{1}{2} \langle u_i' u_i' \rangle = \frac{1}{2} B_{ii}^{(\mathrm{s})}(0, t) = \frac{1}{2} \int_{\mathbb{R}^3} \Phi_{ii}(\boldsymbol{k}, t)\, \mathrm{d}^3 k \tag{A.26}$$

[Mathieu and Scott, 2000, (6.9); Tatarskii, 1971, §9]. Assuming isotropy, spherical symmetry yields

$$\frac{1}{2} \langle u_i' u_i' \rangle = \int_0^\infty \underbrace{2\pi k^2 \Phi_{ii}(k, t)}_{=: E(k,t)}\, \mathrm{d}k \tag{A.27}$$

[Mathieu and Scott, 2000, (6.14), (6.15); Tatarskii, 1971, (9.2)]. $E(k)$ is called the *energy spectrum*. If the field is stationary, Φ_{ii} and E are independent of t.

A relation to the one-dimensional spatial spectrum $V(k)$ can be deduced by inserting (A.11) in $E(k) = 2\pi k^2 \Phi_{ii}(k)$ defined in (A.27) to yield

$$E(k) = -k \frac{\mathrm{d}V}{\mathrm{d}k}(k). \tag{A.28}$$

Within a subrange (e. g. the inertial or viscous one), the spectrum can be described by a power law $V(k) = c\, k^\mu$ where μ depends on the range in question (see below). For such a spectral form with arbitrary $\mu \in \mathbb{R}$, inserting in (A.28) yields $E(k) = -\mu c k^\mu$, i. e. $E(k)$ and $V(k)$ have the same power law.

For the inertial subrange, Tatarskii [1971, (12.15)] deduces the form of the energy spectrum to

$$E(k) = \frac{55}{27\pi}\Gamma\left(\frac{2}{3}\right)\cos\left(\frac{\pi}{6}\right)a_{\mathrm{v}}^2\varepsilon^{2/3}k^{-5/3} = \frac{11}{3}\frac{5}{3}\frac{\Gamma\left(\frac{5}{3}\right)\sin\left(\frac{\pi}{3}\right)}{2\pi}\underbrace{a_{\mathrm{v}}^2\varepsilon^{2/3}}_{C_{\mathrm{v}}^2}k^{-5/3}, \tag{A.29}$$

where the second equality uses $\Gamma(2/3+1) = 2/3\,\Gamma(2/3)$ and $\cos(\pi/6) = \sin(\pi/3)$. Primarily, the $k^{-5/3}$ dependence originates from Kolmogorov's similarity hypothesis.

For the viscous subrange, Heisenberg [1948] used similarity considerations to infer the form $E(k) \propto k^{-7}$. He also gave an interpolation formula describing the transition between the inertial and viscous subranges, i. e. between slopes −5/3 and −7,

$$E(k) = E_0\,k^{-\frac{5}{3}}\left(1+\left(\frac{k}{k_0}\right)^{\frac{8}{3}}\right)^{-2} \qquad \text{for the inertial and viscous subranges} \tag{A.30}$$

[Heisenberg, 1948, (28)] where E_0 is a constant and k_0 the breakpoint between the subranges. The length scale corresponding to k_0 is called the *inner scale* $l_0 = 2\pi/k_0$. As in the viscous subrange viscosity is important, Kolmogorov [1941a] assumed in his first similarity hypothesis that l_0 depends on the kinematic viscosity and the energy dissipation rate only. Thus with dimensional reasoning

$$k_0 \propto \sqrt[4]{\frac{\varepsilon}{\nu^3}} \quad \text{or} \quad l_0 = c_{l_0}\sqrt[4]{\frac{\nu^3}{\varepsilon}} \tag{A.31}$$

[Kolmogorov, 1941a, (17); Tatarskii, 1971, (12.4)]. This form is only valid for velocity fluctuations.

For larger scales or smaller wavenumbers, the energy spectrum is dominated by buoyancy effects and thus called the buoyancy subrange. Therein, assuming that $E(k)$ depends on the Brunt-Väisälä frequency N and the wave number k only, one finds that $E(k) \propto N^2k^{-3}$ [Lübken, 1993, (3.63); Lumley, 1964]. The breakpoint k_{b} between the buoyancy subrange and the inertial subrange can be deduced by equalising the turbulent kinetic energy with the buoyancy energy, i. e.

$$k_{\mathrm{b}}\,\varepsilon^{2/3}\,k_{\mathrm{b}}^{-5/3} \asymp k_{\mathrm{b}}\,E(k_{\mathrm{b}}) \asymp E_{\mathrm{turb}} = E_{\mathrm{pot}} \propto N^2/k_{\mathrm{b}}^2,$$

yielding

$$k_{\mathrm{b}} \propto \sqrt{\frac{N^3}{\varepsilon}} \quad \text{or} \quad l_{\mathrm{b}} = c_{l_{\mathrm{b}}}\sqrt{\frac{\varepsilon}{N^3}}. \tag{A.32}$$

The length scale l_{b} is called *outer scale*. Ozmidov [1965] made a similar calculation considering the vertical size of the largest eddies in a stably stratified fluid [cf. Thorpe, 2005, p. 175] and thus

introduced the *Ozmidov scale*

$$L_\mathrm{O} = c_\mathrm{O}\sqrt{\frac{\varepsilon}{N^3}}. \tag{A.33}$$

Note that in the literature the constants for l_b and L_O are often chosen differently [Hocking, 1999]. Particularly, for L_O, c_O is often set to 1 [e. g. Gavrilov et al., 2005, Clayson and Kantha, 2008, Wilson et al., 2014]. For the outer scale l_b, Weinstock [1978, (29b)] set $c_{l_\mathrm{b}} = 2\pi/0.62$. Barat [1982a, Table 1] finds the transition between inertial and buoyancy subranges mostly in good agreement with l_b. Lumley [1964, (13)] gave a Heisenberg type interpolation formula between inertial and buoyancy subrange,

$$E(k) = c_\mathrm{L}\varepsilon^{2/3}\left(1+\left(\frac{k}{k_\mathrm{b}}\right)^{-4/3}\right)k^{-5/3} \quad \text{for the buoyancy and inertial subranges.} \tag{A.34}$$

To plot the energy spectrum, the constants c_{l_0}, E_0 and c_L have to be determined. E_0 can be deduced from the fact that for the inertial subrange (A.30) has to equal Kolmogorov's well-known formula (A.29). For $k \ll k_0$, (A.30) reduces to

$$E(k) = E_0 k^{-\frac{5}{3}} \quad \text{for the inertial subrange}$$

and a comparison with (A.29) gives

$$E_0 = \frac{11}{3}\frac{5}{3}\frac{\Gamma(\frac{5}{3})\sin(\frac{\pi}{3})}{2\pi}C_\mathrm{v}^2 \tag{A.35}$$

with the structure function constant $C_\mathrm{v}^2 = a_\mathrm{v}^2\varepsilon^{2/3}$. A similar argument holds for (A.34) and $k \gg k_\mathrm{b}$; therewith one obtains $c_\mathrm{L}\varepsilon^{2/3} = E_0$.

For the determination of the constant c_{l_0}, another constraint is needed. Lübken [1993, Section 3.3.10] and Theuerkauf [2012, Sections 2.2.6 and 2.2.7] used the condition of the structure function at the origin

$$\frac{\mathrm{d}^2 D_{ii}}{\mathrm{d}r^2}(0) = \frac{4}{3}\int_0^\infty k^2 E(k)\,\mathrm{d}k \tag{A.36}$$

[Tatarskii, 1971, p.50]. Into this equation, the form for the structure function for small r, i. e. in the viscous subrange, $D_{ii}(r) = \tilde{C}_\mathrm{v} r^2$ (see (A.16)) is inserted. However, a problem arises because the integration on the right hand side goes over all wavenumbers. To the author's knowledge, no formula for the whole range exists. Furthermore, new parameters such as the outer scale k_b would be introduced. Lübken [1993] and Theuerkauf [2012] used a form of Heisenberg's model for the integration and therewith implicitly extended the inertial range to $k = 0$ (i. e. to all scales larger than l_0). Presumably that was due to practical reasons and because they wanted to use the

turbulent part only. A similar approach with (A.30) yields

$$2\frac{\varepsilon}{3\nu} = 2\tilde{C}_\mathrm{v} = \frac{\pi}{4}E_0 k_0^{4/3} = \frac{55}{72}\Gamma\left(\frac{5}{3}\right)\sin\left(\frac{\pi}{3}\right)a_\mathrm{v}^2\varepsilon^{2/3}\,k_0^{4/3}. \tag{A.37}$$

Solving for $l_0 = 2\pi/k_0$ gives the result

$$l_0 = 2\pi\left(\frac{55}{48}\Gamma\left(\frac{5}{3}\right)\sin\left(\frac{\pi}{3}\right)a_\mathrm{v}^2\right)^{3/4}\left(\frac{\nu^3}{\varepsilon}\right)^{1/4}. \tag{A.38}$$

Using $a_\mathrm{v}^2 = 2.0$ [Bertin et al., 1997, (8); Antonia et al., 1981, p. 580; Pope, 2000, p. 194] one finds

$$c_{l_0,\mathrm{v}} \approx 9.73. \tag{A.39}$$

A theoretical energy spectrum for typical stratospheric conditions is plotted in Figure A.1.

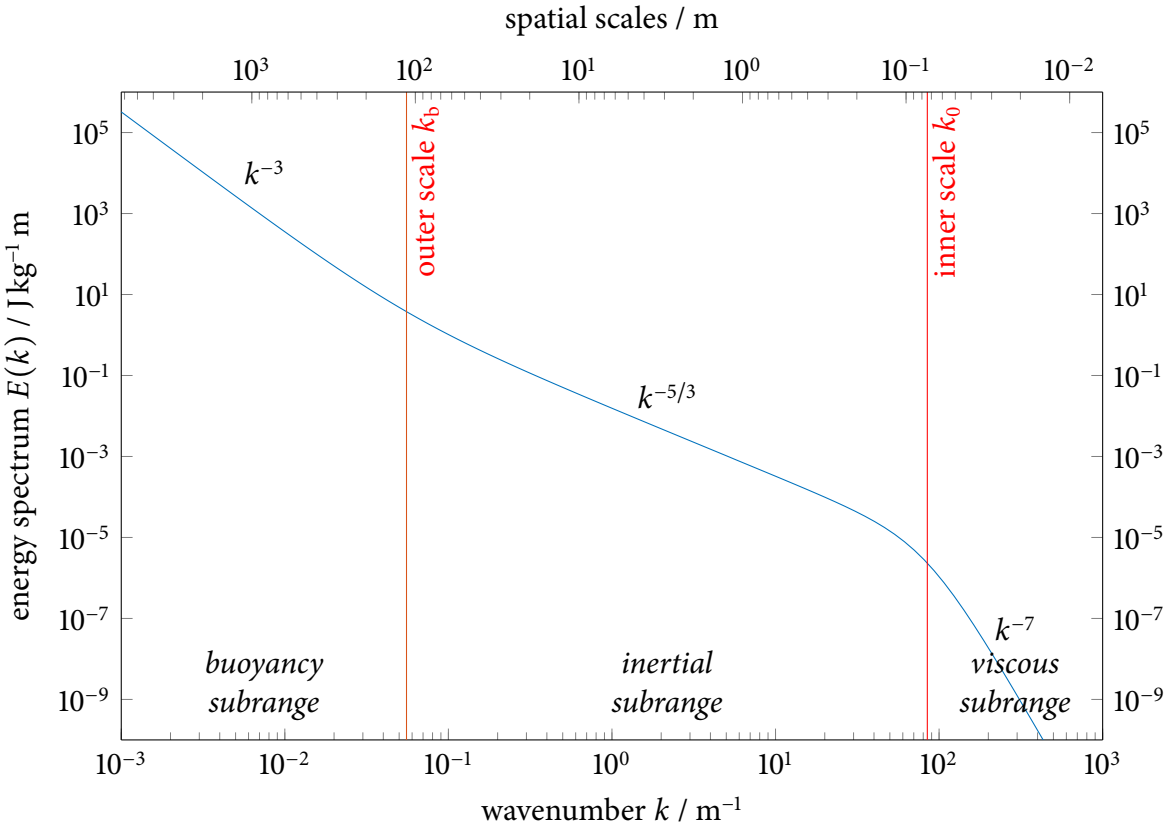

Figure A.1: Theoretical energy spectrum $E(k)$ for typical stratospheric conditions (20 km altitude, $\varepsilon = 1 \times 10^{-3}\,\mathrm{W\,kg^{-1}}$, $\nu = 1.5 \times 10^{-4}\,\mathrm{m^2\,s^{-1}}$, $N = 0.02\,\mathrm{s^{-1}}$) based on Heisenberg [1948, (28)] and Lumley [1964, (13)]

A.5 A form of the spectrum that can be fitted to experimental data

In order to derive energy dissipation rates ε from measurements, the theoretical spectrum is needed in a form that can be fitted to observed power spectra. For a one-dimensional measurement as is done with LITOS, the power spectral density of observed velocity fluctuations corresponds to the spectrum $V(k)$, which is related to the energy spectrum by (A.28). To obtain $V(k)$, thus $E(k)/k$ has to be integrated. LITOS measures in the inertial and viscous subrange so that the Heisenberg spectrum (A.30) is taken for $E(k)$. A possible solution for the integral is[1]

$$V(k) = \frac{3}{5}E_0\left(k^{-5/3}{}_2F_1\left[2, -\frac{5}{8}; \frac{3}{8}; -\left(\frac{k}{k_0}\right)^{8/3}\right] - \Gamma\left(\frac{21}{8}\right)\Gamma\left(\frac{3}{8}\right)\right) \tag{A.40}$$

with the hypergeometric function ${}_2F_1$.

Lübken and Hillert [1992, (4)] and Lübken [1993] used the form (A.30) of $E(k)$ directly for the spatial spectrum $V(k)$. Taking into account that for power laws E and V have the same power (see Section A.4, (A.28)), this can be justified with the argument that the transition is an interpolation anyway so that the specific form is irrelevant. Therewith he obtained

$$V(k) = V_0\, k^{-\frac{5}{3}}\left(1 + \left(\frac{k}{k_0}\right)^{\frac{8}{3}}\right)^{-2} \tag{A.41}$$

with

$$V_0 = C^2\frac{\Gamma(\frac{5}{3})\sin(\frac{\pi}{3})}{2\pi} \tag{A.42}$$

and, by inserting into the relation (A.11) between the three-dimensional and one-dimensional spectra,

$$\Phi(k) = \frac{1}{2\pi k}\frac{V_0}{3}k^{-8/3}\frac{5 + 21\left(\frac{k}{k_0}\right)^{8/3}}{\left(1 + \left(\frac{k}{k_0}\right)^{8/3}\right)^3}. \tag{A.43}$$

The advantage is the simpler form of V.

The constant c_{l_0} derived with this choice of V is different from the one deduced in (A.39). To be consistent, one has to use the constant derived from the form of the spectrum that is actually used. The value is needed because the spectrum contains both the inner scale k_0 and the energy dissipation rate ε (in the structure function constant C^2), but both are related by (A.31).

1 The author would like to thank Urs Schäfer-Rolffs for finding the solution for the integral.

Similarly to above, the condition of the structure function at the origin

$$\frac{\mathrm{d}^2 D_{ii}}{\mathrm{d}r^2}(0) = \frac{8\pi}{3} \int_0^\infty \Phi_{ii}(k) k^4 \,\mathrm{d}k \tag{A.44}$$

[Tatarskii, 1971, p. 49f, p. 65; Lübken, 1993, (3.108)] together with the form of the structure function in the viscous subrange $D_{ii}(r) = \tilde{C} r^2$ is used. Again, the problem arises that the integration of the right-hand side goes over all wavenumbers. Lübken [1993, p. 43] and Theuerkauf [2012] inserted the three-dimensional Heisenberg spectrum (A.43) and performed the integration. Therewith they implicitly extended (A.43) to $k = 0$. The result is

$$2\tilde{C} = \frac{4}{3} \pi V_0 k_0^{4/3}. \tag{A.45}$$

Substituting $l_0 = 2\pi/k_0$ and solving for l_0 yields

$$l_0 = 2\pi \left(\frac{3\pi}{8} \frac{V_0}{\tilde{C}} \right)^{3/4} = 2\pi \left(\frac{3\Gamma(5/3)\sin(\pi/3)}{16} \frac{C^2}{\tilde{C}} \right)^{3/4}. \tag{A.46}$$

At this point it has to be distinguished between velocity and temperature fluctuations. For velocity fluctuations, $C^2 = a_\mathrm{v}^2 \varepsilon^{2/3}$ ((A.20) or Tatarskii [1971, (12.7)]) and $\tilde{C} = \frac{\varepsilon}{3\nu}$ ((A.16) or Tatarskii [1971, (10.7)]). Thus,

$$\frac{C^2}{\tilde{C}} = \frac{3 a_\mathrm{v}^2 \nu}{\varepsilon^{1/3}} \tag{A.47}$$

and

$$l_0 = \underbrace{2\pi \left(\frac{9\Gamma(5/3)\sin(\pi/3)}{16} a_\mathrm{v}^2 \right)^{3/4}}_{=: c_{l_0,\mathrm{v}}} \left(\frac{\nu^3}{\varepsilon} \right)^{1/4} \tag{A.48}$$

[cf. Theuerkauf, 2012, (B.13)]. The value of a_v^2 is usually determined from measurements. Theuerkauf [2012, Appendix B] used $a_\mathrm{v}^2 = 2.0$ [Bertin et al., 1997, (8); Antonia et al., 1981, p. 580; Pope, 2000, p. 194] yielding

$$\boxed{c_{l_0,\mathrm{v}} = 5.7}. \tag{A.49}$$

This value is used for the evaluation performed in this thesis.

The empirical constant a_v^2 can also be determined with renormalisation group analysis techniques. Yakhot and Orszag [1986, (2.62)] obtained for the energy spectrum

$$E(k) = 1.617 \varepsilon^{2/3} k^{-5/3}$$

which, using (A.29), results in $a_\mathrm{v}^2 = 2.13$ and thus $c_{l_0,\mathrm{v}} = 5.98$.

In contrast, Wilson [2004, Section 2.1] gave $c_{l_0,\mathrm{v}} = 12.8$. Altogether, the different values of the constant vary by a factor of ~ 2.2; due to the $c_{l_0,\mathrm{v}}^4$ dependence of the inversion of (A.48), that results in an uncertainty in ε of a factor of ~ 25!

For temperature fluctuations, $C^2 = a_\mathrm{T}^2 \frac{\chi}{\varepsilon^{1/3}}$ ((A.23) or Tatarskii [1971, (13.33)]) and $\tilde{C} = \frac{\chi}{3\alpha}$ ((A.19) or Tatarskii [1971, (13.28)]), so that

$$\frac{C^2}{\tilde{C}} = \frac{3a_\mathrm{T}^2\alpha}{\varepsilon^{1/3}} \tag{A.50}$$

and with $Pr_\mathrm{mol} := \nu/\alpha$

$$l_0 = \underbrace{2\pi\left(\frac{9\Gamma(5/3)\sin(\pi/3)}{16Pr_\mathrm{mol}}a_\mathrm{T}^2\right)^{3/4}}_{=:c_{l_0,\mathrm{T}}}\left(\frac{\nu^3}{\varepsilon}\right)^{1/4} \tag{A.51}$$

[cf. Lübken, 1993, (3.110); Theuerkauf, 2012, (A.23)].

Theuerkauf [2012, Appendix A] used $a_\mathrm{T}^2 = 1.74 \times 2$ [Lübken, 1992, (37)] (the factor 2 is the normalisation factor f_α from Lübken [1992]) and $Pr_\mathrm{mol} = 0.73$ [Lübken, 1993, Appendix A]. This yields

$$\boxed{c_{l_0,\mathrm{T}} = 10.9}. \tag{A.52}$$

Wilson et al. [2014, Section 3.3.4] used $a_\mathrm{T}^2 = 3.2$ which results in $c_{l_0,\mathrm{T}} = 10.3$, i. e. a value quite similar to (A.52). Hill and Clifford [1978, (7)] gave a different value of $c_{l_0,\mathrm{T}} = 7.4$.

The different values of $c_{l_0,\mathrm{T}}$ cause an uncertainty in ε by a factor of ~ 4.7.

LITOS measures a time series while flying through the turbulent field. Thus, the fit to the measured spectra has to be done with the *temporal* spectrum. Using Taylor's frozen field hypothesis for the balloon flying through the turbulent patch with constant velocity u_b, spatial and temporal spectra are related by

$$W(\omega) = \frac{2\pi}{u_\mathrm{b}}\int_{|\omega|/u_\mathrm{b}}^{\infty}\Phi(k)\,k\,\mathrm{d}k \tag{A.53}$$

[Tatarskii, 1971, eq. (6.13)] and

$$\Phi(k) = -\frac{u_\mathrm{b}^2}{2\pi k}\frac{\mathrm{d}W}{\mathrm{d}\omega}(ku_\mathrm{b}) \tag{A.54}$$

[Tatarskii, 1971, eq. (6.14)]. Inserting (A.11) into (A.53) results in

$$W(\omega) = \frac{1}{u_\mathrm{b}} V\left(\frac{\omega}{u_\mathrm{b}}\right) \tag{A.55}$$

which gives for the Heisenberg spectrum (A.41)

$$\boxed{W(\omega) = C^2 \frac{\Gamma\left(\frac{5}{3}\right)\sin\left(\frac{\pi}{3}\right)}{2\pi u_\mathrm{b}} \frac{(\omega/u_\mathrm{b})^{-5/3}}{\left(1+\left(\frac{\omega}{u_\mathrm{b} k_0}\right)^{8/3}\right)^2}} \tag{A.56}$$

[Lübken, 1993, (3.109)]. To eliminate the interrelation between k_0 and ε, the formula (A.31) for the breakpoint, $\varepsilon = c_{l_0}^4 \nu^3 / l_0^4$, is inserted into that for the structure function constant C^2, i. e. $C_\mathrm{v}^2 = a_\mathrm{v}^2 \varepsilon^{2/3}$ for velocity fluctuations or $C_\mathrm{T}^2 = a_\mathrm{T}^2 \frac{\chi}{\varepsilon^{1/3}}$ for temperature fluctuations. The result is plugged into (A.56). The ascent velocity u_b and the kinematic viscosity ν are known from the radiosonde measurement. That way, the only remaining parameters are l_0 for velocity fluctuations or l_0 and χ for temperature fluctuations. Thus the resulting equation can readily be used to fit to experimental data.

B A new family of wavelets for spectral analysis using the continuous wavelet transform

As mentioned in Section 4.1.3, the general advantage of wavelets compared to the Fourier transform is that the window size is adapted to the scale. To visualise this advantage, notice that the analysing function for the windowed Fourier transform of a signal g with window w,

$$(\mathcal{F}_w g)(\omega) = \int_{\mathbb{R}} g(t) w(t) \exp(\mathrm{i}\omega t)\, \mathrm{d}t$$

is in fact $w \exp(\mathrm{i}\omega \cdot)$, where the centre dot denotes the active variable. For the wavelet transform (4.2) it is the scaled mother wavelet $\psi\left(\frac{\cdot - b}{a}\right)$. Figure B.1 depicts both analysing functions for two different resolutions. Therein it can clearly be seen that the wavelet transform resolves *local* details at high frequencies, while the windowed Fourier transform "averages" high-frequency features over the fixed window length.

For spectral analysis of geophysical data with wavelets, a common choice is the Morlet wavelet

$$\psi_{\omega_0}(t) = \pi^{-1/4} \exp(\mathrm{i}\omega_0 t) \exp(-t^2/2) \tag{B.1}$$

[Grossmann and Morlet, 1984] which consists of a plane wave modulated by a Gaussian. That means using that wavelet is related to a windowed Fourier transform with a Gaussian window. However, the Morlet wavelet has infinite support,

$$\operatorname{supp} \psi_{\omega_0} := \{t \in \mathbb{R} : \psi_{\omega_0}(t) \neq 0\} = \mathbb{R},$$

which is problematic for numerical applications because computers cannot handle infinite domains (which would comprise of an infinite amount of numbers). Furthermore, shorter support means less "smoothing" of local details of the time series. As wavelet theory has substantially advanced over the last decades, wavelets with compact support have become standard.

The problem with infinite support can be remedied while still keeping the spectral properties; the solution is to construct new wavelets by modulating a plane wave with a finite window. In light of the differences between windowed Fourier and wavelet transform described above, use of such a wavelet with compact support is more related to the classical (finite) windowed Fourier

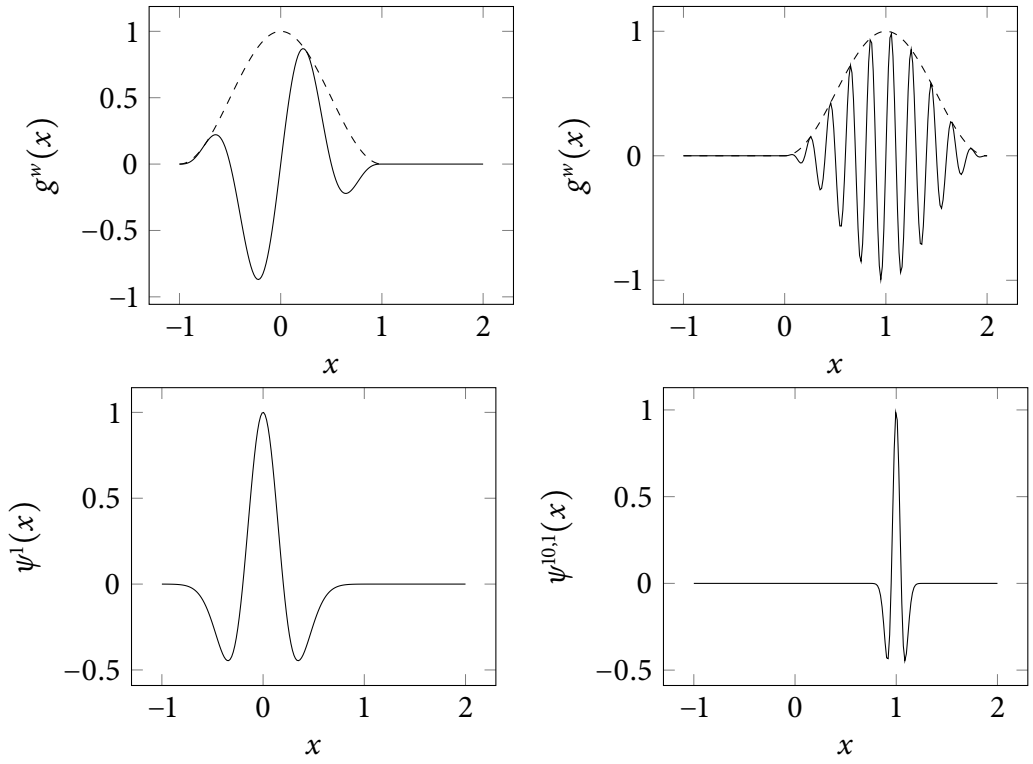

Figure B.1: Typical shapes of windowed Fourier transform (top) and wavelets (bottom) for coarse (left) and fine (right) resolutions. Figure analogous to Daubechies [1992, Fig. 1.2].

transform than the Morlet choice.

An example of a finite window is the von Hann or raised cosine window for $[-1,1]$,

$$w(t) = \begin{cases} \frac{1}{2}\left(1+\cos(\pi t)\right), & \text{if } t \in [-1,1], \\ 0, & \text{otherwise.} \end{cases} \tag{B.2}$$

The resulting wavelet is

$$\psi_{\nu_0}(t) = \sqrt{\frac{8}{3}}\cos(\pi\nu_0 t)\, w(t) = \begin{cases} \sqrt{\frac{2}{3}}\cos(\pi\nu_0 t)(1+\cos(\pi t)), & \text{if } t \in [-1,1], \\ 0, & \text{otherwise,} \end{cases} \tag{B.3}$$

for the frequency parameter $2 \leq \nu_0 \in \mathbb{N}$. It is normalised such that $\|\psi_{\nu_0}\|_{L_2} = 1$. Its Fourier

transform is

$$\begin{aligned}\mathcal{F}\psi_{\nu_0}(\omega) &= -\sqrt{\frac{2}{3}}\pi^2\left(\frac{\sin(\pi\nu_0+\omega)}{(\pi\nu_0+\omega)(\pi\nu_0+\pi+\omega)(\pi\nu_0-\pi+\omega)}\right.\\ &\quad\left.+\frac{\sin(\pi\nu_0-\omega)}{(\pi\nu_0-\omega)(\pi\nu_0-\pi-\omega)(\pi\nu_0+\pi-\omega)}\right)\\ &= \frac{(-1)^{\nu_0+1}2\sqrt{\frac{2}{3}}\,\pi^2\sin(\omega)\omega(3\pi^2\nu_0^2-\pi^2+\omega^2)}{(\omega-\pi\nu_0)(\omega-\pi\nu_0-\pi)(\omega-\pi\nu_0+\pi)(\omega+\pi\nu_0)(\omega+\pi\nu_0-\pi)(\omega+\pi\nu_0+\pi)}.\end{aligned} \tag{B.4}$$

Plots of the mother wavelet and its Fourier transform are shown in Figure B.2.

Each wavelet function must satisfy the admissibility condition [Daubechies, 1992, (2.4.1)] to ensure that the continuous wavelet transform is an isomorphism. That means the condition enables the reconstruction of the original function from the wavelet transform. For the mother wavelet (B.3) it is

$$\begin{aligned}C_{\psi_{\nu_0}} &= \int_{-\infty}^{\infty}\frac{|\mathcal{F}\psi_{\nu_0}(\omega)|^2}{|\omega|}\mathrm{d}x\\ &= \frac{1}{3\pi^2\nu_0(4\nu_0^2-1)(\nu_0^2-1)}\big(\ln(\nu_0-1)-\ln(\nu_0+1)+8\nu_0\ln(\nu_0-1)+11\nu_0^2\ln(\nu_0-1)\\ &\quad-8\nu_0^3\ln(\nu_0+1)-11\nu_0^2\ln(\nu_0+1)-12\nu_0^4\ln(\nu_0-1)+12\nu_0^4\ln(\nu_0+1)\\ &\quad+16\nu_0^3\ln(\nu_0)+8\nu_0\ln(\nu_0+1)-16\nu_0\ln(\nu_0)-8\nu_0^3\ln(\nu_0-1)\\ &\quad+16\nu_0\,\mathrm{Ci}(2\pi\nu_0)-16\nu_0^3\,\mathrm{Ci}(2\pi\nu_0)+8\nu_0^3\,\mathrm{Ci}(2\pi\nu_0-2\pi)\\ &\quad+12\nu_0^4\,\mathrm{Ci}(2\pi\nu_0-2\pi)+8\nu_0^3\,\mathrm{Ci}(2\pi\nu_0+2\pi)-12\nu_0^4\,\mathrm{Ci}(2\pi\nu_0+2\pi)\\ &\quad-11\nu_0^2\,\mathrm{Ci}(2\pi\nu_0-2\pi)-8\nu_0\,\mathrm{Ci}(2\pi\nu_0-2\pi)-8\nu_0\,\mathrm{Ci}(2\pi\nu_0+2\pi)\\ &\quad+11\nu_0^2\,\mathrm{Ci}(2\pi\nu_0+2\pi)+8\pi\,\mathrm{Si}(2\pi\nu_0)+32\pi\nu_0^4\,\mathrm{Si}(2\pi\nu_0)\\ &\quad+\mathrm{Ci}(2\pi\nu_0+2\pi)+2\pi\nu_0\,\mathrm{Si}(2\pi\nu_0+2\pi)-2\pi\nu_0\,\mathrm{Si}(2\pi\nu_0-2\pi)\\ &\quad-2\pi\nu_0^2\,\mathrm{Si}(2\pi\nu_0+2\pi)-\mathrm{Ci}(2\pi\nu_0-2\pi)+8\pi\nu_0^3\,\mathrm{Si}(2\pi\nu_0-2\pi)-40\pi\nu_0^2\,\mathrm{Si}(2\pi\nu_0)\\ &\quad-8\pi\nu_0^3\,\mathrm{Si}(2\pi\nu_0+2\pi)-2\nu_0^2\pi\,\mathrm{Si}(2\pi\nu_0-2\pi)+8\pi\nu_0^4\,\mathrm{Si}(2\pi\nu_0+2\pi)\\ &\quad+8\pi\nu_0^4\,\mathrm{Si}(2\pi\nu_0-2\pi)\big)\\ &< \infty\end{aligned} \tag{B.5}$$

where

$$\mathrm{Si}(x) := \int_0^x\frac{\sin(t)}{t}\mathrm{d}t \tag{B.6}$$

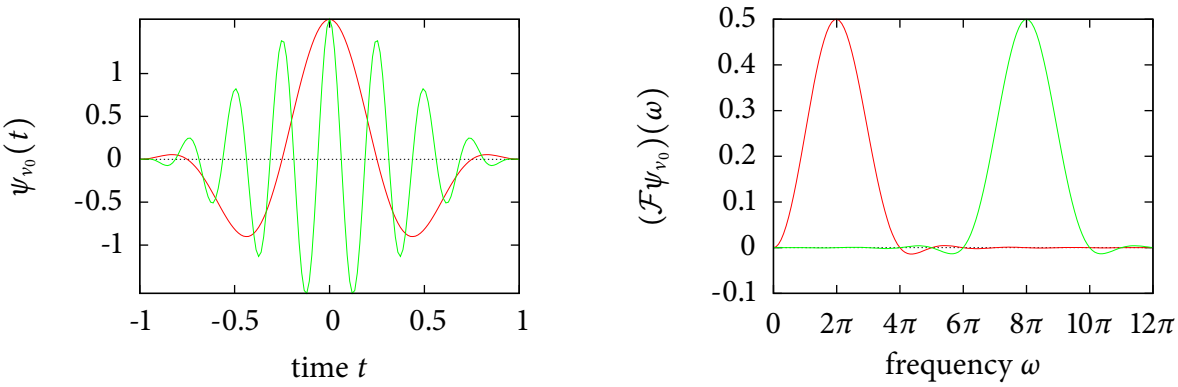

Figure B.2: Plot of the mother wavelet (left) and its Fourier transform (right) for $\nu_0 = 2$ (red) and $\nu_0 = 8$ (green)

and

$$\mathrm{Ci}(x) := -\int_x^\infty \frac{\cos(t)}{t}\mathrm{d}t = \gamma + \ln(x) + \int_0^x \frac{\cos(t)-1}{t}\mathrm{d}t \quad \text{with } \gamma = -\int_0^\infty \exp(-t)\mathrm{d}t \tag{B.7}$$

are the sine and cosine integral functions, respectively.

An important property of a wavelet is its smoothness. Classically it is given as continuous differentiability; the symbol C^n denotes that a function is n times continuously differentiable. Each branch of the piecewise definition of the wavelet (B.3) is C^∞, thus it is sufficient to check the condition at the critical points −1 and 1. Since

$$\left.\frac{\mathrm{d}\psi_{\nu_0}}{\mathrm{d}t}\right|_{[-1,1]} = -\frac{\sqrt{6}}{3}\pi\nu_0\,\sin(\pi\nu_0 t)(1+\cos(\pi t)) - \frac{\sqrt{6}}{3}\pi\,\cos(\pi\nu_0 t)\sin(\pi t) \overset{t\to\pm1}{\longrightarrow} 0$$

but

$$\begin{aligned}\left.\frac{\mathrm{d}^2\psi_{\nu_0}}{\mathrm{d}t^2}\right|_{[-1,1]} &= -\frac{\sqrt{6}}{3}\pi^2\nu_0^2\cos(\pi\nu_0 t)(1+\cos(\pi t)) + \frac{2\sqrt{6}}{3}\pi^2\nu_0\sin(\pi\nu_0 t)\sin(\pi t)\\ &\quad - \frac{\sqrt{6}}{3}\pi^2\cos(\pi\nu_0 t)\cos(\pi t) \overset{t\to\pm1}{\longrightarrow} (-1)^{\nu_0}\frac{\sqrt{6}}{3}\pi^2 \neq 0\end{aligned}$$

ψ_{ν_0} from (B.3) is C^1 but not C^2. The smoothness is of courses given by that of the window w at the boundaries. For a smoother wavelet that is, e. g., C^2, a window function with vanishing first and second derivative at the boundaries is necessary. This is not possible with standard windows that are designed with piecewise sine and cosine functions.

Summarising, the new wavelets for the CWT introduced above combine similar spectral properties as the Morlet ones with compact support. Short support is favourable for resolving local

details without unwanted smoothing. This make the new construction a promising choice for spectral analysis. However, due to the chosen window the new wavelet is only C^1. More regularity, e. g. C^2, would be better. Potentially that can be improved by using a smoother (non-trivial) window function. Such a construction would be not as straight forward and effortless as the one at hand. A quantitative comparison of the performance of the Morlet wavelet (B.1) and the new wavelet (B.3) would be complicated and is outside the scope of this work.

C Validation of attitude reconstruction

As mentioned in Section 3.3, gondola movements disturb the measurement. Thus the attitude is reconstructed. To this end, rotation, acceleration and magnetometer are measured, and the data are post-processed after flight. The algorithm from Claussen [2008] was implemented. For each time step, the displacement and azimuth angles defined in Figure 3.9 are computed.

To validate the results, the electronics box was put in known attitudes on a table. When correcting temperature-induced drifts of the gyroscope, the angles were reconstructed with a precision of $\lesssim 2°$.

As a more realistic test, the box was attached to a 3 m cord, pulled back to an angle of 40° and then let go to perform pendulum motions (see Figure C.1). The result of the algorithm is plotted in Figure C.2.

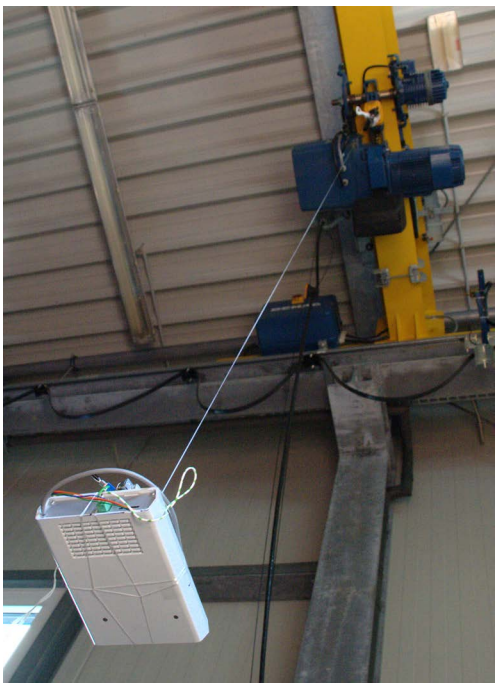

Figure C.1: Photograph of the pendulum test performed as validation for the attitude reconstruction

Bearing in mind that the manual displacement with a set square is not that precise, the initial displacement is reconstructed with satisfactory accuracy. During the pendulum motions, the displacement angle is larger because the attachment of box to the rope allows bending. The amplitude decreases as expected, and the oscillation period in the reconstructed data differs by ~0.1 s to the theoretical one of 3.5 s (assuming a mathematical pendulum with small displacements). Furthermore, the duration of 10 periods was measured with a stop watch to be 36 s; the deviation from the theoretical value is 0.1 s for a period. The variation of the azimuth angle is small, just as observed by the experimenter. All results fit together. Other tests consisted e. g. in rotation around the azimuth axis. The results had a similar accuracy.

Summing up, the validation tests confirmed that the attitude reconstruction works with the expected accuracy of 1° to 2°. During balloon flight, additional pseudo forces may occur which complicate things, but these are difficult to test.

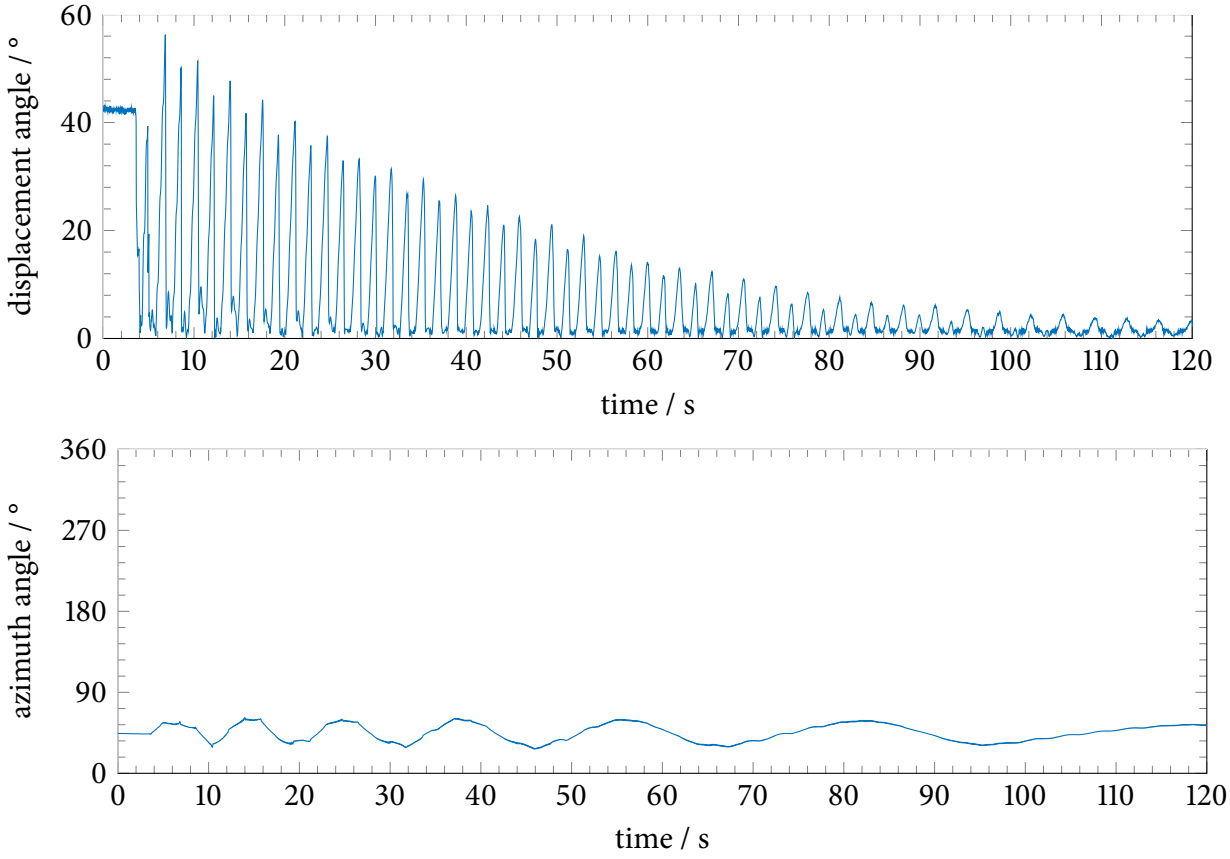

Figure C.2: Results of the pendulum test for attitude reconstruction validation

Bibliography

Ulrich Achatz. On the role of optimal perturbations in the instability of monochromatic gravity waves. *Physics of Fluids*, 17(9):094107, 2005. doi: 10.1063/1.2046709.

Jean-Rémi Alisse, Peter H. Haynes, Jacques Vanneste, and Claude Sidi. Quantification of stratospheric mixing from turbulence microstructure measurements. *Geophysical Research Letters*, 27(17):2621–2624, 2000. doi: 10.1029/2000GL011386.

Robert A. Antonia, A. J. Chambers, and B. R. Satyaprakash. Kolmogorov constants for structure functions in turbulent shear flows. *Quarterly Journal of the Royal Meteorological Society*, 107 (453):579–589, 1981. doi: 10.1002/qj.49710745308.

Ben B. Balsley, Dale A. Lawrence, David C. Fritts, Ling Wang, and Kam Wan. Fine structure, instabilities, and turbulence in the stable boundary layer, part 1: High-resolution in-situ measurements with the DataHawk UAV and comparisons with numerical modeling. *submitted to the Journal of Atmospheric and Oceanic Technology*, 2015.

Jean Barat. Some characteristics of clear-air turbulence in the middle stratosphere. *Journal of the Atmospheric Sciences*, 39(11):2553–2564, 1982a. doi: 10.1175/1520-0469(1982)039<2553:SCOCAT>2.0.CO;2.

Jean Barat. A high-resolution ionic anemometer for boundary-layer measurements. *Journal of Applied Meteorology*, 21(10):1480–1488, 1982b. doi: 10.1175/1520-0450(1982)021<1480:AHRIAF>2.0.CO;2.

Francois Bertin, Jean Barat, and Richard Wilson. Energy dissipation rates, eddy diffusivity, and the Prandtl number: An in situ experimental approach and its consequences on radar estimate of turbulent parameters. *Radio Science*, 32(2):791–804, 1997. doi: 10.1029/96RS03691.

Thomas Birner, Andreas Dörnbrack, and Ulrich Schumann. How sharp is the tropopause at midlatitudes? *Geophysical Research Letters*, 29(14):45–1–45–4, 2002. doi: 10.1029/2002GL015142.

W. Bögel and R. Baumann. Test and calibration of the DLR Falcon wind measuring system by maneuvers. *Journal of Atmospheric and Oceanic Technology*, 8(1):5–18, 1991. doi: 10.1175/1520-0426(1991)008<0005:TACOTD>2.0.CO;2.

Guy Brasseur and Susan Solomon. *Aeronomy of the middle atmosphere: chemistry and physics of the stratosphere and mesosphere*. Atmospheric sciences library. Reidel, Dordrecht, 2nd edition, 1986. ISBN 90-277-2344-3.

Hans H. Bruun. *Hot-Wire Anemomentry: Principles and Signal Analysis*. Oxford University Press, 1995. ISBN 0-19-856342-6.

V. M. Canuto, A. Howard, Y. Cheng, and M. S. Dubovikov. Ocean turbulence. Part I: One-point closure model—momentum and heat vertical diffusivities. *Journal of Physical Oceanography*, 31(6):1413–1426, 2001. doi: 10.1175/1520-0485(2001)031<1413:OTPIOP>2.0.CO;2.

Cornelius Claussen. A fixed-wing unmanned aerial vehicle for environmental physics. Diploma thesis, University of Heidelberg, 2008.

Carol Anne Clayson and Lakshmi Kantha. On turbulence and mixing in the free atmosphere inferred from high-resolution soundings. *Journal of Atmospheric and Oceanic Technology*, 25 (6):833–852, 2008. doi: 10.1175/2007JTECHA992.1.

Ingrid Daubechies. *Ten Lectures on Wavelets*. Society for Industrial and Applied Mathematics, Philadelphia, 1992. doi: 10.1137/1.9781611970104.

Timothy DelSole and Michael K. Tippett. Statistical methods in climate research. Lecture notes, 2014. URL `ftp://cola.gmu.edu/pub/delsole/clim762/chapters/`. Vis 10 Jul 2015.

Thomas M. Dillon. Vertical overturns: A comparison of Thorpe and Ozmidov length scales. *Journal of Geophysical Research: Oceans*, 87(C12):9601–9613, 1982. doi: 10.1029/JC087iC12p09601.

Franz Durst. *Fluid mechanics: An introduction to the theory of fluid flows*. Springer, Berlin, 2008. ISBN 3-540-71342-5. doi: 10.1007/978-3-540-71343-2.

William T. Eadie, D. Dryard, F. E. James, M. Roos, and B. Sadoulet. *Statistical methods in experimental physics*. North-Holland, Amsterdam, 1971. ISBN 0-7204-0239-5.

Eric L. Fleming, Sushil Chandra, Mark R. Schoeberl, and John J. Barnett. Monthly mean global climatology of temperature, wind, geopotential height, and pressure for 0–120 km. Nasa technical memorandum 100697, 1988. URL `http://ntrs.nasa.gov/archive/nasa/casi.ntrs.nasa.gov/19880013119.pdf`. Vis 10 Jul 2015.

Rod Frehlich, Yannick Meillier, Michael L. Jensen, and Ben Balsley. Turbulence measurements with the CIRES tethered lifting system during CASES-99: Calibration and spectral analysis of temperature and velocity. *Journal of the Atmospheric Sciences*, 60(20):2487–2495, 2003. doi: 10.1175/1520-0469(2003)060<2487:TMWTCT>2.0.CO;2.

Carl Freytag. Statistical properties of energy dissipation. *Boundary-Layer Meteorology*, 14(2): 183–198, 1978. doi: 10.1007/BF00122618.

Uriel Frisch. *Turbulence: The legacy of A. N. Kolmogorov*. Cambridge University Press, Cambridge, 1995. ISBN 0-521-45713-0.

David C. Fritts and M. Joan Alexander. Gravity wave dynamics and effects in the middle atmosphere. *Reviews of Geophysics*, 41(1), 2003. doi: 10.1029/2001RG000106.

David C. Fritts and Ling Wang. Gravity wave–fine structure interactions. Part II: Energy dissipation evolutions, statistics, and implications. *Journal of the Atmospheric Sciences*, 70(12): 3735–3755, 2013. doi: 10.1175/JAS-D-13-059.1.

David C. Fritts, Ling Wang, and Joseph A. Werne. Gravity wave–fine structure interactions. Part I: Influences of fine structure form and orientation on flow evolution and instability. *Journal of the Atmospheric Sciences*, 70(12):3710–3734, 2013. doi: 10.1175/JAS-D-13-055.1.

David C. Fritts, Ling Wang, Marvin A. Geller, Dale A. Lawrence, Joe Werne, and Ben B. Balsley. Numerical modeling of multi-scale dynamics at a high reynolds number: Instabilities, turbulence, and an assessment of Ozmidov and Thorpe scales. *Journal of the Atmospheric Sciences*, in press, 2015. doi: 10.1175/JAS-D-14-0343.1.

Shoichiro Fukao, Manabu D. Yamanaka, Naoki Ao, Wayne K. Hocking, Toru Sato, Mamoru Yamamoto, Takuji Nakamura, Toshitaka Tsuda, and Susumu Kato. Seasonal variability of vertical eddy diffusivity in the middle atmosphere: 1. three-year observations by the middle and upper atmosphere radar. *Journal of Geophysical Research: Atmospheres*, 99(D9):18973–18987, 1994. doi: 10.1029/94JD00911.

Boris Galperin, Semion Sukoriansky, and Philip S. Anderson. On the critical Richardson number in stably stratified turbulence. *Atmospheric Science Letters*, 8(3):65–69, 2007. doi: 10.1002/asl.153.

Almut Gaßmann and Hans-Joachim Herzog. How is local material entropy production represented in a numerical model? *Quarterly Journal of the Royal Meteorological Society*, 2014. doi: 10.1002/qj.2404.

Nikolai M. Gavrilov. Estimates of turbulent diffusivities and energy dissipation rates from satellite measurements of spectra of stratospheric refractivity perturbations. *Atmospheric Chemistry and Physics*, 13(23):12107–12116, 2013. doi: 10.5194/acp-13-12107-2013.

Nikolai M. Gavrilov, Hubert Luce, Michel Crochet, Francis Dalaudier, and Shoichiro Fukao. Turbulence parameter estimations from high-resolution balloon temperature measurements of the MUTSI-2000 campaign. *Annales Geophysicae*, 23(7):2401–2413, 2005. doi: 10.5194/angeo-23-2401-2005.

Marvin A. Geller. Remarks on the effects of atmospheric dynamics. In *Aeronomy Report No. 48: COSPAR symposium on d- and e-region ion chemistry—an informal symposium record*. University of Illinois Urbana, June 1972.

Jochen Giebeler, Franz-Josef Lübken, and M. Nägele. CONE – a new sensor for in-situ observations of neutral and plasma density fluctuations. *Proceedings of the 11th ESA Symposium on European Rocket and Balloon Programmes and Related Research, Montreux, Switzerland (ESA SP)*, ESA-SP-355:311–318, 1993.

Todd S. Glickman, editor. *Glossary of meteorology*. American Meteorological Society, Boston, Massachusetts, 2nd edition, 2000. ISBN 1-878220-34-9.

John A. Goff. Saturation presssure of water on the new Kelvin temperature scale. *Transaction of the American Society of Heating and Air-Conditioning Engineers*, 63:347–354, 1957.

Alexander Grossmann and Jean Morlet. Decomposition of hardy functions into square integrable wavelets of constant shape. *SIAM Journal on Mathematical Analysis*, 15(4):723–736, 1984. doi: 10.1137/0515056.

I. Gultepe and D. O'C. Starr. Dynamical structure and turbulence in cirrus clouds: Aircraft observations during FIRE. *Journal of the Atmospheric Sciences*, 52(23):4159–4182, 1995. doi: 10.1175/1520-0469(1995)052<4159:DSATIC>2.0.CO;2.

A. S. Gurvich and A. M. Yaglom. Breakdown of eddies and probability distributions for small-scale turbulence. *Physics of Fluids (1958–1988)*, 10(9):S59–S65, 1967. doi: 10.1063/1.1762505.

Anne Haack, Michael Gerding, and Franz-Josef Lübken. Characteristics of stratospheric turbulent layers measured by LITOS and their relation to the Richardson number. *Journal of Geophysical Research: Atmospheres*, 119(18):10605–10618, 2014. ISSN 2169-8996. doi: 10.1002/2013JD021008.

Werner Heisenberg. Zur statistischen Theorie der Turbulenz. *Zeitschrift für Physik*, 124:628–657, 1948. doi: 10.1007/BF01668899.

R. J. Hill and S. F. Clifford. Modified spectrum of atmospheric temperature fluctuations and its application to optical propagation. *Journal of the Optical Society of America*, 68(7):892–899, 1978. doi: 10.1364/JOSA.68.000892.

Wayne K. Hocking. Measurement of turbulent energy dissipation rates in the middle atmosphere by radar techniques: A review. *Radio Science*, 20(6):1403–1422, 1985. doi: 10.1029/RS020i006p01403.

Wayne K. Hocking. The dynamical parameters of turbulence theory as they apply to middle atmosphere studies. *Earth, Planets and Space*, 51(7–8):525–541, 1999. doi: 10.1186/BF03353213.

Louis N. Howard. Note on a paper of John W. Miles. *Journal of Fluid Mechanics*, 10(4):509–512, 1961. doi: 10.1017/S0022112061000317.

Fred James and Matthias Winkler. *MINUIT User's Guide*. CERN, Geneva, 2004. URL `http://seal.cern.ch/documents/minuit/mnusersguide.pdf`. Vis 10 Jul 2015.

Lakshmi Kantha and Wayne K. Hocking. Dissipation rates of turbulence kinetic energy in the free atmosphere: MST radar and radiosondes. *Journal of Atmospheric and Solar-Terrestrial Physics*, 73(9):1043–1051, 2011. doi: 10.1016/j.jastp.2010.11.024.

Andrey Nikolaevich Kolmogorov. The local structure of turbulence in incompressible viscous fluid for very large Reynolds numbers. *Akademiia Nauk SSSR Doklady*, 30:301–305, 1941a. URL `http://www.astro.puc.cl/~rparra/tools/PAPERS/kolmogorov_1951.pdf`. Vis 10 Jul 2015. English translation: Proc. R. Soc. Lond. A July 8, 1991 434 1890 9–13.

Andrey Nikolaevich Kolmogorov. On the logarithmical normal particle size distribution caused by particle crushing. *Doklady Akademii Nauk SSSR*, 31:99–102, 1941b.

Andrey Nikolaevich Kolmogorov. A refinement of previous hypotheses concerning the local structure of turbulence in a viscous incompressible fluid at high reynolds number. *Journal of Fluid Mechanics*, 13:82–85, 1962. doi: 10.1017/S0022112062000518.

Edgar Kraft. Ein Sensorsystem zur Bestimmung räumlicher Orientierungen in Echtzeit. Diplomarbeit, Universität Bonn, 8 2002. URL `http://hep1.physik.uni-bonn.de/fileadmin/Publications/Mqube/Dipl_Kraft.pdf`. Vis 10 Jul 2015.

S. Kurosaki, M.D. Yamanaka, H. Hashiguchi, T. Sato, and S. Fukao. Vertical eddy diffusivity in the lower and middle atmosphere: A climatology based on the MU radar observations during 1986–1992. *Journal of Atmospheric and Terrestrial Physics*, 58(6):727–734, 1996. doi: 10.1016/0021-9169(95)00070-4.

Hans-Joachim Lange. *Die Physik des Wetters und des Klimas*. Dietrich Reimer Verlag, Berlin, 2002. ISBN 3-496-02747-9. Free e-book version under `http://www.hajolange.de` (vis 10 Jul 2015).

D. K. Lilly, D. E. Waco, and S. I. Adelfang. Stratospheric mixing estimated from high-altitude turbulence measurements. *Journal of Applied Meteorology*, 13(4):488–493, 1974. doi: 10.1175/1520-0450(1974)013<0488:SMEFHA>2.0.CO;2.

Peter T. Love and Marvin A. Geller. Research using high (and higher) resolution radiosonde data. *Eos, Transactions American Geophysical Union*, 93(35):337–338, 2012. doi: 10.1029/2012EO350001.

Franz-Josef Lübken. On the extraction of turbulent parameters from atmospheric density fluctuations. *Journal of Geophysical Research: Atmospheres*, 97(D18):20385–20395, 1992. doi: 10.1029/92JD01916.

Franz-Josef Lübken. *Experimental Results on the Role of Turbulence for the Heat Budget of the Upper Atmosphere*. Habilitationsschrift, University of Bonn, January 1993.

Franz-Josef Lübken. Seasonal variation of turbulent energy dissipation rates at high latitudes as determined by in situ measurements of neutral density fluctuations. *Journal of Geophysical Research: Atmospheres*, 102(D12):13441–13456, 1997. ISSN 2156-2202. doi: 10.1029/97JD00853.

Franz-Josef Lübken and Wolfgang Hillert. Measurements of turbulent energy dissipation rates applying spectral models. In *Coupling Processes in the Lower and Middle Atmosphere*, pages 345–351, Loen, Norway, 1992. NATO Advanced Research Workshop, Kluwer Press.

Franz-Josef Lübken, Josef Höffner, Timo P. Viehl, Bernd Kaifler, and Raymond John Morris. Winter/summer mesopause temperature transition at Davis (69°S) in 2011/2012. *Geophysical Research Letters*, 41(14):5233–5238, 2014. doi: 10.1002/2014GL060777.

Hubert Luce, Shoichiro Fukao, Francis Dalaudier, and Michel Crochet. Strong mixing events observed near the tropopause with the MU radar and high-resolution balloon techniques. *Journal of the Atmospheric Sciences*, 59(20):2885–2896, 2002. doi: 10.1175/1520-0469(2002)059<2885:SMEONT>2.0.CO;2.

John Leask Lumley. The spectrum of nearly inertial turbulence in a stably stratified fluid. *Journal of the Atmospheric Sciences*, 21(1):99–102, 1964. doi: 10.1175/1520-0469(1964)021<0099:TSONIT>2.0.CO;2.

Jean Mathieu and Julian Scott. *An introduction to turbulent flow*. Cambridge University Press, Cambridge, 2000. ISBN 0-521-77538-8.

John W. Miles. On the stability of heterogeneous shear flows. *Journal of Fluid Mechanics*, 10(4):496–508, 1961. doi: 10.1017/S0022112061000305.

Daniel M. Murphy and Thomas Koop. Review of the vapour pressures of ice and supercooled water for atmospheric applications. *Quarterly Journal of the Royal Meteorological Society*, 131(608):1539–1565, 2005. doi: 10.1256/qj.04.94.

Carmen J. Nappo. *An Introduction to Atmospheric Gravity Waves*, volume 85 of *International Geophysics Series*. Academic Press, San Diego, 2002. ISBN 0-12-514082-7.

Alexander Mikhailovich Oboukhov. Some specific features of atmospheric tubulence. *Journal of Fluid Mechanics*, 13:77–81, 1962. doi: 10.1017/S0022112062000506.

Alexander Mikhailovich Obukhov. Structure of the temperature field in turbulent flow. *Izvestiia Akademii Nauk SSSR, Ser. Geogr. i. Geofiz.*, 13(1):58–69, 1949. URL `http://www.dtic.mil/dtic/tr/fulltext/u2/683016.pdf`. Vis 10 Jul 2015. Translated to English.

Rostislav Vsevolodovich Ozmidov. On the turbulent exchange in a stably stratified ocean. *Izvestia Acad. Sci. USSR, Atmospheric and Oceanic Physics*, 1(8):853–860, 1965. Translated from Russian to English by Danielle and Victor Barcilon.

Hans A. Panofsky and John A. Dutton. *Atmospheric turbulence: models and methods for engineering applications*. Wiley, New York, 1984. ISBN 0-471-05714-2.

Olle Persson, Andreas Stamminger, Helen Page, Mark Fittock, and Mark Uitendaal. *BEXUS User Manual*. EuroLaunch, Aug. 2010.

Stephen B. Pope. *Turbulent Flows*. Cambridge University Press, Cambridge, 2000. ISBN 0-521-59886-9.

Lewis Fry Richardson. *Weather prediction by numerical process*. Cambridge University Press, Cambridge, 1922.

Andreas Roloff. Entwicklung einer Messdatenerfassungskarte für einen Höhenballon mit 32bit PIC Controller und Speicherung auf SD-Karte. Bachelor's thesis, Hamburg University of Applied Sciences, 2011.

Rick Salmon. *Lectures on Geophysical Fluid Dynamics*. Oxford University Press, Oxford, 1998. ISBN 0-19-510808-6.

Andreas Schneider, Michael Gerding, and Franz-Josef Lübken. Comparing turbulent parameters obtained from LITOS and radiosonde measurements. *Atmospheric Chemistry and Physics*, 15 (4):2159–2166, 2015. doi: 10.5194/acp-15-2159-2015.

U. Schumann, P. Konopka, R. Baumann, R. Busen, T. Gerz, H. Schlager, P. Schulte, and H. Volkert. Estimate of diffusion parameters of aircraft exhaust plumes near the tropopause from nitric oxide and turbulence measurements. *Journal of Geophysical Research: Atmospheres*, 100(D7): 14147–14162, 1995. doi: 10.1029/95JD01277.

Holger Siebert, Katrin Lehmann, and Raymond A. Shaw. On the use of hot-wire anemometers for turbulence measurements in clouds. *Journal of Atmospheric and Oceanic Technology*, 24 (6):980–993, 2007. doi: 10.1175/JTECH2018.1.

William C. Skamarock, Joseph B. Klemp, Jimy Dudhia, David O. Gill, Dale M. Barker, Michael G. Duda, Xiang-Yu Huang, Wei Wang, and Jordan G. Powers. A description of the advanced research WRF version 3. Technical report, National Center for Atmospheric Research, Boulder, Colorado, USA, 2008. URL `http://www2.mmm.ucar.edu/wrf/users/docs/arw_v3.pdf`. Vis 10 Jul 2015.

Igor Smalikho, Friedrich Köpp, and Stephan Rahm. Measurement of atmospheric turbulence by 2 µm Doppler lidar. *Journal of Atmospheric and Oceanic Technology*, 22(11):1733–1747, 2005. doi: 10.1175/JTECH1815.1.

William D. Smyth and James N. Moum. Length scales of turbulence in stably stratified mixing layers. *Physics of Fluids*, 12(6):1327–1342, 2000. doi: 10.1063/1.870385.

Jens Söder. Development of a small-scale litos payload for turbulence measurements in the stratosphere. Master's thesis, Leibniz-Institute of Atmospheric Physics at the University of Rostock, 2014. URL `http://www.iap-kborn.de/fileadmin/user_upload/MAIN-abteilung/optik/Forschung/Master/Soeder-Master-2014.pdf`. Vis 10 Jul 2015.

V. F. Sofieva, A. S. Gurvich, F. Dalaudier, and V. Kan. Reconstruction of internal gravity wave and turbulence parameters in the stratosphere using GOMOS scintillation measurements. *Journal of Geophysical Research: Atmospheres*, 112(D12):D12113, 2007. doi: 10.1029/2006JD007483.

Olga Alicja Sumińska. Application of a constant temperature anemometer for balloon-borne stratospheric turbulence soundings. Master's thesis, Leibniz-Institute of Atmospheric Physics at the University of Rostock, 2008. URL `https://www.iap-kborn.de/fileadmin/user_upload/MAIN-abteilung/optik/Forschung/DIpl_Bachelor/Suminska_master.pdf`. Vis 10 Jul 2015.

Valerian Iljitsch Tatarskii. *The effects of the turbulent atmosphere on wave propagation*. Israel Program for Scientific Translations, Jerusalem, 1971. ISBN 0-7065-0680-4. translated from Russian.

Anne Theuerkauf. *Stratospheric turbulence observations with the new balloon-borne instrument LITOS*. PhD thesis, Leibniz-Institute of Atmospheric Physics at the University of Rostock, 2012. URL `http://www.iap-kborn.de/fileadmin/user_upload/MAIN-abteilung/optik/Forschung/Doktorarbeiten/Theuerkauf-Diss-2012.pdf`. Vis 10 Jul 2015.

Anne Theuerkauf, Michael Gerding, and Franz-Josef Lübken. LITOS – a new balloon-borne instrument for fine-scale turbulence soundings in the stratosphere. *Atmospheric Measurement Techniques*, 4(1):55–66, 2011. doi: 10.5194/amt-4-55-2011.

Stephen A. Thorpe. Turbulence and mixing in a Scottish loch. *Philosophical Transactions of the Royal Society of London. Series A, Mathematical and Physical Sciences*, 286(1334):125–181, 1977. doi: 10.1098/rsta.1977.0112.

Stephen A. Thorpe. *The Turbulent Ocean*. Cambridge University Press, Cambridge, 2005. ISBN 0-521-83543-7.

Chenning Tong and Zellman Warhaft. Passive scalar dispersion and mixing in a turbulent jet. *Journal of Fluid Mechanics*, 292:1–38, 1995. doi: 10.1017/S0022112095001418.

Christopher Torrence and Gilbert P. Compo. A practical guide to wavelet analysis. *Bulletin of the American Meteorological Society*, 79(1):61–78, 1998. doi: 10.1175/1520-0477(1998)079<0061:APGTWA>2.0.CO;2.

Jerome Weinstock. Vertical turbulent diffusion in a stably stratified fluid. *Journal of the Atmospheric Sciences*, 35(6):1022–1027, 1978. doi: 10.1175/1520-0469(1978)035<1022:VTDIAS>2.0.CO;2.

Joseph A. Werne and David C. Fritts. Anisotropy in a stratified shear layer. *Physics and Chemistry of the Earth, Part B: Hydrology, Oceans and Atmosphere*, 26(4):263–268, 2001. doi: 10.1016/S1464-1909(01)00004-1.

James R. Wertz, editor. *Spacecraft attitude determination and control*. Astrophysics and space science library. D. Reidel Publishing Company, Dordrecht, 1978. ISBN 90-277-0959-9. doi: 10.1007/978-94-009-9907-7.

Hemantha W. Wijesekera, Thomas M. Dillon, and Laurie Padman. Some statistical and dynamical properties of turbulence in the oceanic pycnocline. *Journal of Geophysical Research: Oceans*, 98(C12):22665–22679, 1993. doi: 10.1029/93JC02352.

Richard Wilson. Turbulent diffusivity in the free atmosphere inferred from MST radar measurements: a review. *Annales Geophysicae*, 22(11):3869–3887, 2004. doi: 10.5194/angeo-22-3869-2004.

Richard Wilson, Francis Dalaudier, and Francois Bertin. Estimation of the turbulent fraction in the free atmosphere from MST radar measurements. *Journal of Atmospheric and Oceanic Technology*, 22(9):1326–1339, 2005. doi: 10.1175/JTECH1783.1.

Richard Wilson, Hubert Luce, Francis Dalaudier, and Jacques Lefrère. Turbulence patch identification in potential density or temperature profiles. *Journal of Atmospheric and Oceanic Technology*, 27(6):977–993, 2010. doi: 10.1175/2010JTECHA1357.1.

Richard Wilson, Francis Dalaudier, and Hubert Luce. Can one detect small-scale turbulence from standard meteorological radiosondes? *Atmospheric Measurement Techniques*, 4(5):795–804, 2011. doi: 10.5194/amt-4-795-2011.

Richard Wilson, Hubert Luce, Hiroyuki Hashiguchi, Masato Shiotani, and Francis Dalaudier. On the effect of moisture on the detection of tropospheric turbulence from in situ measurements. *Atmospheric Measurement Techniques*, 6(3):697–702, 2013. doi: 10.5194/amt-6-697-2013.

Richard Wilson, Hubert Luce, Hiroyuki Hashiguchi, Noriyuki Nishi, and Y. Yabuki. Energetics of persistent turbulent layers underneath mid-level clouds estimated from concurrent radar and radiosonde data. *Journal of Atmospheric and Solar-Terrestrial Physics*, 118, Part A(0):78–89, 2014. doi: 10.1016/j.jastp.2014.01.005.

Victor Yakhot and Steven A. Orszag. Renormalization group analysis of turbulence. I. Basic theory. *Journal of Scientific Computing*, 1(1):3–51, 1986. doi: 10.1007/BF01061452.

Hidekatsu Yamazaki and Rolf Lueck. Why oceanic dissipation rates are not lognormal. *Journal of Physical Oceanography*, 20(12):1907–1918, 1990. doi: 10.1175/1520-0485(1990)020<1907:WODRAN>2.0.CO;2.

Jinqiang Zhang, Hongbin Chen, Zhanqing Li, Xuehua Fan, Liang Peng, Yu Yu, and Maureen Cribb. Analysis of cloud layer structure in Shouxian, China using RS92 radiosonde aided by 95 GHz cloud radar. *Journal of Geophysical Research: Atmospheres*, 115(D7), 2010. doi: 10.1029/2010JD014030.

Nomenclature

α thermal diffusivity, page 7

χ thermal dissipation rate of the turbulent fluctuations, see equation (2.17), page 9

δ_{ij} Kronecker delta $\delta_{ij} = 1$, if $i = j$ and $\delta_{ij} = 0$ otherwise, page 107

$\hat{W}$ periodogram of measured fluctuations, page 35

$\boldsymbol{\Phi}$ spatial three-dimensional spectrum, see equation (A.9), page 106

$\boldsymbol{D}$ structure function, see equation (A.12), page 107

ν kinematic viscosity, page 6

$\overline{\zeta}$ mean trend-to-noise ratio for the Thorpe analysis, see equation (4.17), page 58

ϕ gravitational potential, page 6

ρ density, page 6

$\boldsymbol{B}^{(\mathrm{s})}$ spatial correlation function, see equation (A.1), page 105

$\boldsymbol{B}^{(\mathrm{t})}$ temporal correlation function, see equation (2.19), page 11, and equation (A.1), page 105

$\boldsymbol{F}$ deformation tensor, page 6

Θ potential temperature, page 52

$\tilde{\chi}_{\mathrm{f}}$ thermal dissipation rate of the turbulent fluctuations, see equation (2.16), page 9

$\tilde{\chi}_{\mathrm{m}}$ thermal dissipation rate of the mean flow, see equation (2.16), page 9

$\tilde{\chi}_{\mathrm{t}}$ thermal dissipation rate of the total flow, see equation (2.10), page 7

ε kinetic energy dissipation rate of the turbulent fluctuations, see equation (2.15), page 9

ε_{f} kinetic energy dissipation rate of the turbulent fluctuations, see equation (2.13), page 8

ε_{m} kinetic energy dissipation rate of the mean flow, see equation (2.13), page 8

ε_{t} kinetic energy dissipation rate of the total flow, see equation (2.7), page 7

$\boldsymbol{J}_Q$ heat flux, page 6

$\boldsymbol{u}$ fluid velocity, page 6

D_T Thorpe displacement, page 52

e_i internal energy, page 6

e_i saturation pressure of water over ice, page 55

e_k kinetic energy per unit mass, page 6

e_w saturation pressure of water over liquid water, page 55

g acceleration of gravity, page 6

I_n Index set $I_n := \{1, \ldots, n\}$, page 52

K eddy diffusivity, page 68

l_0 Inner scale $l_0 = c_{l_0} \sqrt[4]{\frac{\nu^3}{\varepsilon}}$, see equation (2.22), page 12, and equation A.31, page 110

L_T Thorpe length $L_T := \mathrm{rms}(D_T)$, page 53

L_O Ozmidov length scale $L_O := c_O \sqrt{\frac{\varepsilon}{N^3}}$, see equation (2.29), page 13, and equation (A.33), page 111

p pressure, page 6

Re Reynolds number, see equation (2.1), page 5

Ri Richardson number, page 65

Ri_f Flux Richardson number, see equation (5.2), page 68

S wind shear, page 65

s Entropy per unit mass, page 7

S_T Thorpe signal, page 52

T fluid temperature, page 6

V spatial one-dimensional spectrum, see equation (A.10), page 107

W temporal spectrum, see equation (2.20), page 11, and equation (A.8), page 106

Acknowledgements

First of all, I would like to thank Prof. Franz-Josef Lübken for giving me the opportunity to work in his group and for his friendly and pragmatic way of leadership. A big thanks goes to Michael Gerding for his supervision of my work and many discussions. He was always there when I needed his advice. I would like to thank Anne Theuerkauf for teaching me many things about preparing payloads and launching balloons. She also provided the data of the BEXUS 8 flight. I thank Jens Söder, who joined the team during autumn 2013 starting with his masters thesis, for the good teamwork. I am indebted to Almut Gaßmann for sharing her profound knowledge about the theoretical point of view and for many discussions. I would like to thank Torsten Köpnick and Reik Ostermann for developing electronics used in the project and generally helping with all sorts of problems regarding data acquisition, and Hans-Jürgen Heckl and Jens Wedrich from the institute's mechanics workshop for being helpful when it came to building stuff. The chair of fluid mechanics at the University of Rostock provided access to their wind tunnel facility. The German Aerospace Centre (DLR) and the Swedish National Space Board (SNSB) gave me the opportunity to participate in the BEXUS programme. I thank the BEXUS student team members Andreas Roloff, Kevin Lehmann and Markus Kayser for their commitment that ensured the success of the measurements on the flight. I would like to thank Johannes Wagner (University of Innsbruck) for providing WRF model runs and Christoph Zülicke (IAP) for helping to interpret them. I thank Thorsten Raasch (University of Mainz) for helpful discussions about the interpretation of my newly designed wavelets. For proof-reading I thank Klaus Schneider-Zapp and Jochen Schneider. Last but not least I want to thank all my colleges for the excellent atmosphere at the institute. A friendly environment is important for creativity and success while doing research.

Erklärung

Hiermit versichere ich an Eides statt, dass ich die vorliegende Arbeit selbstständig angefertigt und ohne fremde Hilfe verfasst habe. Dazu habe ich keine außer den von mir angegebenen Hilfsmitteln und Quellen verwendet und die den benutzten Werken inhaltlich und wörtlich entnommenen Stellen als solche kenntlich gemacht.

Die Arbeit wurde bisher weder im Inland noch im Ausland in gleicher oder ähnlicher Form einer anderen Prüfungsbehörde vorgelegt. Weiterhin erkläre ich, dass ich ein Verfahren zur Erlangung des Doktorgrades an keiner anderen wissenschaftlichen Einrichtung beantragt habe.

Kühlungsborn, den 28. 08. 2015

(Andreas Schneider)